

Joint Doctoral Dissertation



Polyurethane in Biofabrication and Flexible Electronics
for Healthcare Applications

Institute of Polymer Science and Engineering

College of Engineering

National Taiwan University

&

Department of Chemistry

Faculty of Mathematics, Informatics and Natural Sciences

University of Hamburg

Shin-Da Wu

吳欣達


Supervisors: Prof. Shan-hui Hsu

Prof. Dr. Horst Weller

PD Dr. Tobias Vossmeier

March 2024





Dissertation title:	Polyurethane in Biofabrication and Flexible Electronics for Healthcare Applications
博士論文標題:	聚胺酯於生物製造與柔性電子之醫療應用研究
Dissertation titel (deu.):	Polyurethan in der Biofabrikation und flexiblen Elektronik für Gesundheitsanwendungen
Author:	Shin-Da Wu (吳欣達)
Registration number:	f06549004 (National Taiwan University) 7138893 (University of Hamburg)
Email:	f06549004@ntu.edu.tw Shin-Da.Wu@chemie.uni-hamburg.de
Working group:	Prof. Shan-hui Hsu (National Taiwan University) Prof. Dr. Horst Weller (University of Hamburg)
Institute:	Institute of Polymer Science and Engineering Institute of Physical Chemistry
University at:	National Taiwan University (Taiwan) University of Hamburg (Germany)
Examiners (assessors):	Prof. Shan-hui Hsu Prof. Dr. Horst Weller PD Dr. Tobias Vossmeier Prof. Dr. Volker Abetz Prof. Shu-Wei Chang Prof. Jia-Shing Yu
Date of oral defense:	March 26, 2024





國立臺灣大學雙聯博士學位論文
口試委員會審定書

JOINT DOCTORAL DISSERTATION ACCEPTANCE CERTIFICATE
NATIONAL TAIWAN UNIVERSITY AND UNIVERSITY OF HAMBURG

聚胺酯於生物製造與柔性電子之醫療應用研究

**Polyurethane in Biofabrication and Flexible Electronics
for Healthcare Applications**

本論文係吳欣達在國立臺灣大學高分子科學與工程學研究所(學號: F06549004)與漢堡大學化學系(學號: 7138893)完成之雙聯博士學位論文，於民國 113 年 3 月 26 日承下列考試委員審查通過及口試及格，特此證明。

The undersigned, appointed by the Institute of Polymer Science and Engineering, National Taiwan University (Student ID: F06549004), and the Department of Chemistry, Faculty of Mathematics, Informatics and Natural Sciences, University of Hamburg (Matriculation number: 7138893) on March 26, 2024 have examined a Joint Doctoral Dissertation entitled above presented by Shin-Da Wu candidate and hereby certify that it is worthy of acceptance.

口試委員 Oral examination committee:

Prof. Shan-hui Hsu: 徐善慧 (signature)

Prof. Jia-Shing Yu: 游佳聲 (signature)

Prof. Shu-Wei Chang: 張守偉 (signature)

Prof. Dr. Horst Weller: Horst Weller (signature)

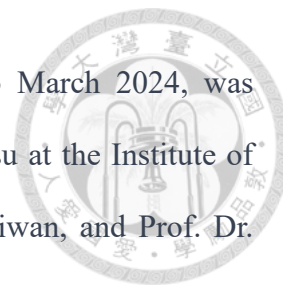
Prof. Dr. Volker Abetz: Volker Abetz (signature)

PD Dr. Tobias Vossmeier: T. Vossmeier (signature)

系所主管 Institute Director: 鄭如忠 (signature)



The joint doctoral research project, spanning from June 2018 to March 2024, was collaboratively carried out under the guidance of Prof. Shan-hui Hsu at the Institute of Polymer Science and Engineering, National Taiwan University, Taiwan, and Prof. Dr. Horst Weller and PD Dr. Tobias Vossmeier, at the Institute of Physical Chemistry in the Department of Chemistry, University of Hamburg, Germany.





List of Publications

The list below presents peer-reviewed journal articles and conference proceedings, arranged in chronological order, that have been published as part of this research project. Additionally, it includes a patent that has been granted.

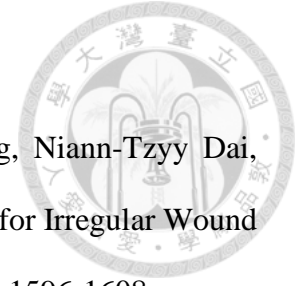


Journal article

1. Shin-Da Wu and Shan-hui Hsu. 4D Bioprintable Self-Healing Hydrogel with Shape Memory and Cryopreserving Properties. *Biofabrication* **2021**; 13: 045029.
2. Shin-Da Wu, Niann-Tzyy Dai, Chao-Yaug Liao, Lan-Ya Kang, Yu-Wen Tseng, Shan-hui Hsu. Planar-/Curvilinear-Bioprinted Tri-Cell-Laden Hydrogel for Healing Irregular Chronic Wounds. *Advanced Healthcare Materials* **2022**; 11: 2201021. (Front cover)
3. Shan-hui Hsu, Junpeng Xu, Shih-Ho Lin, Shin-Da Wu, Qian-Pu Cheng, Chui-Wei Wong. Creative Transformation of Biomedical Polyurethanes: from Biostable Tubing to Biodegradable Smart Materials. *Journal of Polymer Research* **2022**; 29: 70.
4. Bendix Ketelsen, Hendrik Schlicke, Verena R. Schulze, Sophia C. Bittinger, Shin-Da Wu, Shan-hui Hsu, and Tobias Vossmeier. Nanoparticle-Based Strain Gauges: Anisotropic Response Characteristics, Multidirectional Strain Sensing, and Novel Approaches to Healthcare Applications. *Advanced Functional Materials* **2022**; 33(7): 2210065.
5. Shin-Da Wu, Wei-Tsung Chuang, Jo-Chen Ho, Hsuan-Chen Wu, and Shan-hui Hsu. Self-Healing of Recombinant Spider Silk Gel and Coating. *Polymers* **2023**; 15(8): 1855. (Front cover)
6. Shin-Da Wu, Shan-hui Hsu, Bendix Ketelsen, Sophia C. Bittinger, Hendrik Schlicke, Horst Weller, and Tobias Vossmeier. Fabrication of Eco-friendly Wearable Strain Sensor Arrays via Facile Contact Printing for Healthcare Applications. *Small Methods*

2023; 7(9): 2300170. (Back cover)

7. Chao-Yaug Liao, Yu-Wen Tseng, Shin-Da Wu, Lan-Ya Kang, Niann-Tzyy Dai, Shan-hui Hsu. Non-Planar Bioprinting with Molding Assistance for Irregular Wound Shape. *Journal of Materials Research and Technology* **2023**; 26: 1596-1608.



Conference Proceedings

Shin-Da Wu, Bendix Ketelsen, Shan-hui Hsu, Tobias Vossmeier. Towards Nanomaterials-Based Biocompatible and Biodegradable Strain Sensors for Healthcare and Medical Applications. *Proceedings* **2020**; 56(1): 17.

Patent

Shin-Da Wu and Shan-hui Hsu. Bioink Containing Nutritional Composition and Use of the Nutrient Composition for Enhancing Self-Healing Capability of Bioink. Taiwanese Patent I720425 (2021/03/01~2039/02/14)

Contents



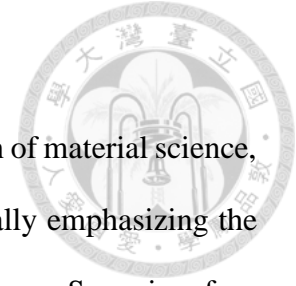
List of Publications.....	i
Abstract (English).....	vi
中文摘要	viii
Abstrakt (Deutsch).....	x
1. Introduction	1
1.1. Hydrogel	1
1.1.1. Environmental-responsive hydrogel.....	3
1.1.2. Self-healing hydrogel	7
1.1.3. Shape memory hydrogel.....	9
1.2. 3D printing.....	10
1.2.1. 3D bioprinting	11
1.2.2. Thermo-responsive bioink.....	14
1.2.3. Photo-responsive bioink	15
1.2.4. Self-healing bioink	15
1.2.5. Cryopreservable bioink.....	16
1.2.6. 4D bioprinting	18
1.3. Polyurethane (PU)	19
1.3.1. Biodegradable PU.....	22
1.3.2. Biocompatible PU	24
1.3.3. PU for bioprinting.....	26



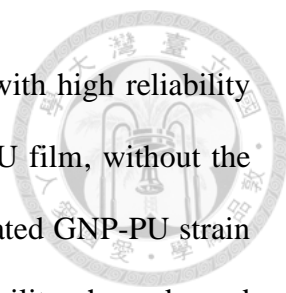
1.4.	Gold nanoparticles (GNPs).....	28
1.4.1.	Synthesis.....	29
1.4.2.	Optical properties	31
1.5.	GNP films.....	33
1.5.1.	Fabrication.....	33
1.5.2.	Charge transport properties	35
1.5.3.	Resistive strain sensing.....	38
2.	Aim of the work	44
3.	Cumulative part of the dissertation	48
3.1.	Publication 1 (first project): 4D bioprintable self-healing hydrogel with shape memory and cryopreserving properties	48
3.2.	Publication 2 (second project): Self-healing of recombinant spider silk gel and coating	111
3.3.	Publication 3 (third project): Fabrication of eco-friendly wearable strain sensor arrays via facile contact printing for healthcare applications	130
4.	Unpublished work (fourth project): Biocompatible and highly sensitive strain sensor integration in a heart-on-a-chip with 3D cardiomyocyte spheroids.....	150
4.1.	Introduction	150
4.2.	Materials and methods.....	154
4.2.1.	Synthesis and characterization of the GNPs.....	154
4.2.2.	Fabrication and characterization of the GNP-PU film	154
4.2.3.	Fabrication and characterization of the GNP-PU strain sensor.....	156

4.2.4.	Preparation and characterization of the self-healing hydrogel.....	157
4.2.5.	Preparation of 3D cardiomyocyte spheroids	158
4.2.6.	Construction of the heart-on-a-chip platform.....	160
4.3.	Results	160
4.4.	Discussion.....	171
5.	Conclusion and outlook.....	178
6.	Bibliography.....	182
7.	Appendix	220
7.1.	Supporting information	220
7.1.1.	Publication 1 (first project): 4D bioprintable self-healing hydrogel with shape memory and cryopreserving properties.....	220
7.1.2.	Publication 3 (third project): Fabrication of eco-friendly wearable strain sensor arrays via facile contact printing for healthcare applications	221
7.2.	Safety.....	238
7.2.1.	List of hazardous substances according to GHS	238
7.2.2.	CMR substance.....	239
8.	Acknowledgement.....	240
9.	Declaration on oath	242

Abstract (English)



This dissertation presents interdisciplinary research at the intersection of material science, biofabrication, flexible electronics, and tissue engineering, specifically emphasizing the role of polyurethane (PU) in revolutionizing healthcare applications. Spanning four distinct but interrelated projects, this research not only demonstrates the development of smart biomaterials but also introduces novel fabrication methods and diverse applications for strain sensors. The first project introduces a novel smart hydrogel, comprising biodegradable PU and gelatin-based biomaterials. This hydrogel exhibited an environmental-responsive behavior, which makes it suitable for high-resolution (80 μm) three-dimensional (3D) bioprinting. Additionally, the hydrogel showed an ionic self-healing property, which is instrumental in ensuring the good structural integrity of bioprinted constructs. Further, the hydrogel demonstrated good stackability (> 80 layers), structural stability, elasticity, biocompatibility, and tunable modulus (1-60 kPa). These characteristics collectively underscore its vast potential in diverse tissue engineering applications. In addition, the shape memory and cryopreservation properties of the hydrogel make it a promising candidate for four-dimensional (4D) bioprinting in minimally invasive surgery and biobanking. The second project focuses on recombinant spider silk hydrogel, chosen due to its structural similarity with PU (i.e., alternating arrangement of soft and hard segments). This work showed the autonomous self-healing property and cytocompatibility of the recombinant spider silk hydrogel. In situ small-angle x-ray scattering (SAXS) analyses revealed that the self-healing mechanism was associated with the stick-slip behavior of the β -sheet nanocrystals. These results, first identified in my research, mark an important advancement in the biomedical field of self-healing hydrogels. The third project expands into advanced wearable eco-friendly electronics, integrating biodegradable PU films with crosslinked gold nanoparticle (GNP)



films. A facile, clean, rapid, and scalable contact printing method with high reliability was developed for transferring the patterned GNP films onto the PU film, without the need of a sacrificial polymer carrier or organic solvents. The fabricated GNP-PU strain sensor with low Young's modulus (~17.8 MPa) and high stretchability showed good stability and durability (10000 cycles) as well as degradability. The GNP-PU strain sensor arrays with spatiotemporal strain resolution are applied as wearable eco-friendly electronics for monitoring subtle physiological signals and large-strain actions. The fourth project introduces a heart-on-a-chip platform as the in vitro cardiac model, comprising the 3D human induced pluripotent stem cell (hiPSC)-derived cardiomyocyte spheroid-laden gel matrix and the GNP-PU cantilever-based strain sensor. The clean contact printing method developed in the third project was used for fabricating the GNP-PU cantilever-based strain sensor to preserve the biocompatibility. The fabricated cantilever-based GNP-PU strain sensor demonstrated a high gauge factor (~50). The developed heart-on-a-chip platform was capable of detecting the contractile behavior of the cardiomyocyte spheroids.

Keywords: Polyurethane, bioprinting, smart hydrogel, self-healing, strain sensor, heart-on-a-chip

中文摘要



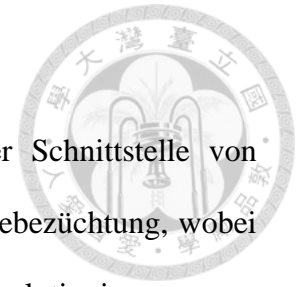
本篇論文呈現了涉及材料科學、生物製造、柔性電子和組織工程等多個領域的跨學科研究，其中特別焦點於聚胺酯材料於前瞻醫療應用革新扮演的重要角色。整個研究分為四個各具重點特色、相互關聯的主題，成功展示了創新智能性生物材料發展與新穎應變感測器製備方法及其應用。首先第一個主題介紹了一種由可生物降解聚胺酯與明膠基生物材料製成的多智能性水凝膠，具備之環境響應特性使其可用於高精度 (80 微米) 3D 生物列印，具備之自我修復特性使其可確保生物列印之結構具有良好的結構一體性。此外，水凝膠具有之良好的堆疊性 (80 層以上)、結構穩定性、彈性、生物相容性及可調整的機械模量 (1-60 千帕) 使其可應用於各種組織工程發展。另外，此水凝膠還具有良好的形狀記憶特性及冷凍保存能力，可應用於 4D 生物列印、臨床微創手術、及生物銀行長期保存與運輸發展。第二個主題選擇探討與聚胺酯具結構相似性 (軟硬鏈段交替排列) 的重組蜘蛛絲水凝膠。研究結果發現此水凝膠具有自我修復特性與好的細胞相容性。透過原位小角度 X 光散射分析，揭示了其自我修復機制與結構內部之 β 摺疊奈米晶體的黏滑行為相關，此研究成果對自我修復水凝膠於生物醫學領域發展具重要意義。第三個主題將可生物降解聚胺酯薄膜與交聯之奈米金薄膜結合，朝向發展具環境保護特性之可穿戴應變感測器。在此，我發展了一種乾淨、簡易、快速且可擴展的接觸列印新方法，不需使用犧牲性高分子載體或有機溶劑即可完整地將圖案化之奈米金薄膜轉移至聚胺酯薄膜上。製作之奈米金-聚胺酯應變感測器具低楊氏模量 (~17.8 兆帕)、高可拉伸性、良好應變穩定性與耐久性 (10000 個週期)、及可降解特性。進一步發展之應變感測器陣列具時空間應變解析度，作為可穿戴感測器可實時監測人體的微小生理訊號或大範圍的肢體動作行為。第四個主題發展了一新的心臟晶片平台，其含人類誘導多能幹細胞衍生的 3D 心肌細胞球、具自我修復特性之水凝膠、及奈米金-聚胺酯懸臂式應變傳感器，作為人體外的心臟模型。第三個主題中開發的乾淨接觸列印方法在此被使用來製備奈米金-聚胺酯懸臂式應變傳感器以確保其生物相容性。

製作之奈米金-聚胺酯懸臂式應變傳感器具高應變係數 (~50)，可於發展的心臟晶片平台中有效監測心肌細胞球的收縮與舒張行為。

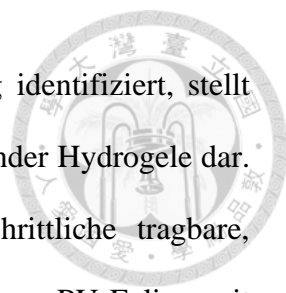


關鍵字: 聚胺酯、生物列印、智能水凝膠、自我修復、應變感測器、心臟晶片平台

Abstrakt (Deutsch)



Diese Dissertation präsentiert interdisziplinäre Forschung an der Schnittstelle von Materialwissenschaft, Biofabrikation, flexibler Elektronik und Gewebezüchtung, wobei insbesondere die Rolle von Polyurethan (PU) bei der Revolutionierung von Gesundheitsanwendungen hervorgehoben wird. Über vier unterschiedliche, jedoch eng miteinander verbundene Projekte erstreckend, demonstriert diese Arbeit nicht nur die Entwicklung intelligenter Biomaterialien, sondern führt auch innovative Herstellungsmethoden und vielseitige Anwendungen für Dehnungssensoren ein. Das erste Projekt stellt ein neuartiges, intelligentes Hydrogel vor, bestehend aus biologisch abbaubarem PU und auf Gelatine basierenden Biomaterialien. Dieses Hydrogel zeigte ein stimulisresponsives Verhalten, was es für hochauflösendes (80 μm) dreidimensionales (3D) Bioprinting geeignet macht. Zudem wies das Hydrogel Selbstheilungseigenschaften auf, die entscheidend für die strukturelle Integrität der biogedruckten Konstrukte sind. Weiterhin demonstrierte das Hydrogel eine gute Stapelfähigkeit (> 80 Schichten), strukturelle Stabilität, Elastizität, Biokompatibilität und einen anpassbaren Modulus (1-60 kPa). Diese Eigenschaften unterstreichen sein enormes Potenzial für vielfältige Anwendungen im Bereich der Gewebezüchtung. Zusätzlich machen das Formgedächtnis und die Kryokonservierungseigenschaften des Hydrogels es zu einem vielversprechenden Kandidaten für vierdimensionales (4D) Bioprinting in minimalinvasiver Chirurgie und Biobanking. Das zweite Projekt fokussiert auf rekombinantes Spinnenseide-Hydrogel, das aufgrund seiner strukturellen Ähnlichkeit mit PU (d.h., abwechselnde Anordnung von weichen und harten Segmenten) gewählt wurde. Diese Studie offenbarte die autonome Selbstheilungsfähigkeit und Zytokompatibilität des rekombinanten Spinnenseide-Hydrogels. In-situ-Kleinwinkel-Röntgenstreuanalysen zeigten, dass der Selbstheilungsmechanismus mit dem Stick-Slip-Verhalten der β -Faltblatt-Nanokristalle



zusammenhängt. Diese Ergebnisse, erstmalig in meiner Forschung identifiziert, stellt einen wichtigen Fortschritt im biomedizinischen Bereich selbstheilender Hydrogele dar. Im dritten Projekt wurden die Forschungsaktivitäten auf fortschrittliche tragbare, umweltfreundliche Elektronik erweitert, indem biologisch abbaubare PU-Folien mit vernetzten Goldnanopartikelfilmen (GNP-Filmen) kombiniert wurden. Es wurde ein einfaches, sauberes, schnelles und skalierbares Kontaktdruckverfahren mit hoher Zuverlässigkeit entwickelt, um die gemusterten GNP-Filme auf die PU-Folie zu übertragen, ohne einen Opferpolymerträger oder organische Lösungsmittel zu benötigen. Der hergestellte GNP-PU-Dehnungssensor, mit einem niedrigen Elastizitätsmodul ($\sim 17,8$ MPa) und hoher Dehnbarkeit, zeigte eine gute Stabilität und Haltbarkeit (10.000 Zyklen) sowie eine gute Abbaubarkeit. Die GNP-PU-Dehnungssensor-Arrays mit räumlich-zeitlicher Dehnungsauflösung können als tragbare, umweltfreundliche Elektronik zur Überwachung und Detektion subtiler physiologischer Signale aber auch großer Dehnungsbewegungen eingesetzt werden. Das vierte Projekt stellt eine Heart-on-a-Chip-Plattform als in vitro Herzmodell vor, bestehend aus einer 3D-Gelmatrix, beladen mit Sphäroiden aus Kardiomyozyten, die aus human indizierten pluripotenten Stammzellen abgeleitet sind, sowie einem GNP-PU-Cantilever-basierten Dehnungssensor. Das im dritten Projekt entwickelte saubere Kontaktdruckverfahren wurde zur Herstellung des Cantilever-basierten GNP-PU-Dehnungssensors verwendet, um die Biokompatibilität zu gewährleisten. Der gefertigte Cantilever-basierte GNP-PU-Dehnungssensor wies einen hohen Gauge-Faktor (~ 50) auf. Die entwickelte Heart-on-a-Chip-Plattform war in der Lage, das kontraktile Verhalten der Kardiomyozyten-Sphäroide zu erkennen.

Schlüsselwörter: Polyurethan, Biodruck, intelligentes Hydrogel, Selbstheilung, Dehnungssensor, Heart-on-a-Chip-Plattform

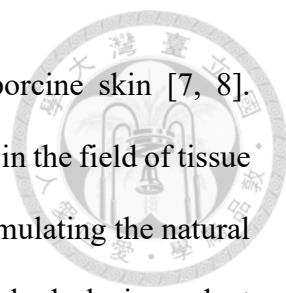


1. Introduction

1.1. Hydrogel

Hydrogels are three-dimensional (3D) network structures produced through the crosslinking of hydrophilic polymer chains [1]. Within the network structures, water molecules are readily entrapped, creating high water content and leading to the formation of gel states that exhibit viscoelastic characteristics, intermediate between those of solids and liquids [2]. Hydrogels can be categorized based on the crosslinking method and the source of the material [3]. In terms of the crosslinking method, hydrogels can be divided into chemically crosslinked and physically crosslinked types [4]. Chemically crosslinked hydrogels are created by the addition of chemical crosslinking agents that form covalent bonds between polymers under appropriate stimuli (e.g., light and enzyme catalysis) to form a permanent structure with good long-term mechanical stability. However, the chemical crosslinking agents are frequently composed of toxic compounds, and the unreacted agents must be removed from the gels prior to their application [4]. In addition, chemical crosslinking agents may engage in undesired reactions with the bioactive constituents within the hydrogel matrix. By contrast, physically crosslinked hydrogels are non-permanent network structures formed by secondary forces (e.g., electrostatic interaction, hydrogen bonding, and hydrophobic association) without the use of crosslinking agents. Although physically crosslinked hydrogels have the advantage of low toxicity, their inherent mechanical weakness and long crosslinking time are notable disadvantages [5].

In terms of the source of the material, hydrogels can be classified into natural and synthetic types [3]. Natural hydrogels, made from natural polymers, typically possess good biocompatibility [6]. Meanwhile, owing to the abundance and easy accessibility of natural polymers, natural hydrogels are cost-effective. For instance, chitosan can be



extracted from crustaceans, while gelatin can be obtained from porcine skin [7, 8]. Furthermore, natural hydrogels feature inherent biodegradability, and in the field of tissue engineering, they can serve as potential development materials for simulating the natural extracellular matrix (ECM) of tissues. A notable example is gelatin, a hydrolysis product of collagen, which shares components with the animal body's ECM, thereby showcasing superb biocompatibility and biodegradability [8]. Meanwhile, gelatin contains the arginine–glycine–aspartic acid (RGD) sequence, a crucial constituent for fostering stable interactions between cells and the surrounding ECM. Furthermore, its low cost has led to wide biomedical applications. However, challenges persist in the application of natural hydrogels, as they may degrade too rapidly, and their thermal and mechanical properties can be insufficient [9]. This leads to poor stability of the degraded network structure. By contrast, synthetic hydrogels produced through chemical synthesis can offer higher mechanical strength and long-term stability, compensating for the weaknesses of natural hydrogels [1]. Furthermore, synthetic hydrogels offer reproducibility, mass production potential, and adjustable performance to meet specific requirements [10]. As compared to natural hydrogels, their applications are more diverse and extensive. Common synthetic hydrogel constituents include poly(ethylene glycol) (PEG), poly(methyl methacrylate) (PMMA), polycaprolactone (PCL), and poly(lactic acid) (PLA) [7]. However, synthetic hydrogels may present problems such as potential cytotoxicity and difficulty in biodegradation [11]. Meanwhile, most synthetic hydrogels lack bioactive moieties (i.e., RGD) that promote the adhesion of cells. Therefore, the development of hydrogels that can simultaneously encompass the advantages of natural hydrogels, such as biodegradability and biocompatibility, and synthetic hydrogels, such as tunable mechanical strength and long-term stability, is the goal for future biomedical applications [12].

In recent decades, the development of smart hydrogels, capable of responding to external stimuli (such as temperature, light, electrical fields, pH, pressure, ionic strength, and solvents), and modulating their behavior in response to environmental cues, has emerged as a burgeoning area in the field of biomedical applications [13]. These characteristics of smart hydrogels enable the design of materials to be tailored to meet specific requirements. For instance, Wichterle and Lím designed the first smart hydrogel for clinical use in the early 1960s [14]. In 2021, over 2800 papers directly related to the synthesis and applications of smart hydrogels have been published [15]. To date, there are three representative types of smart hydrogels: environmental-responsive hydrogels, self-healing hydrogels, and shape memory hydrogels (**Figure 1**).

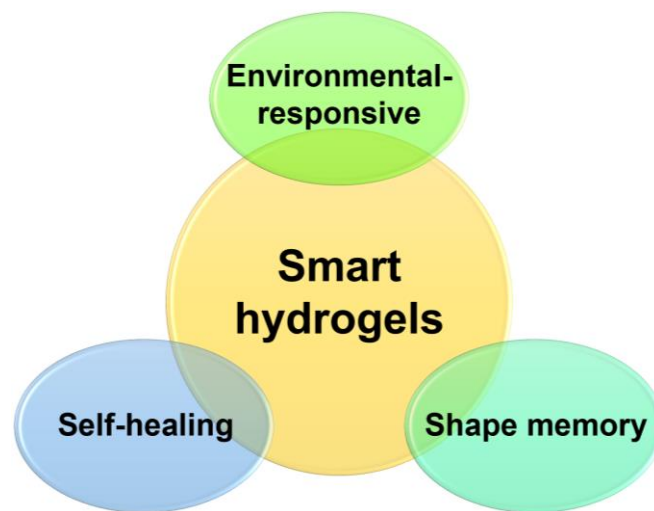
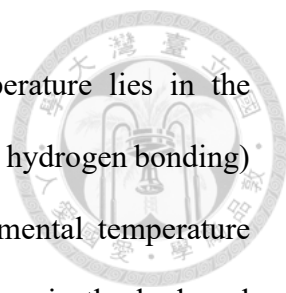


Figure 1. Schematic diagrams showing representative types of smart hydrogels.

1.1.1. Environmental-responsive hydrogel

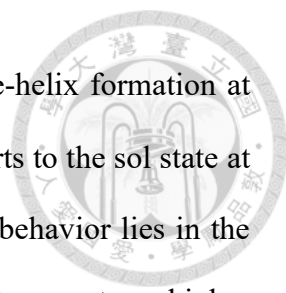
Environmental-responsive hydrogels alter their physical or chemical properties (e.g., crosslinking density, the degree of swelling, or phase transitions) when exposed to environmental stimuli. Among the environmental-responsive hydrogels, those that respond specifically to temperature fluctuations are termed thermo-responsive hydrogels.



The underlying principle governing their responsiveness to temperature lies in the interactions (e.g., van der Waals forces, hydrophobic interactions, and hydrogen bonding) among polymer chains within the hydrogels [16]. As the environmental temperature changes, the interactions are affected, leading to a significant change in the hydrogel volume. This responsiveness can be further characterized by two distinct phenomena, namely the lower critical solution temperature (LCST) and upper critical solution temperature (UCST), which govern the different behavior of thermo-responsive hydrogels [17].

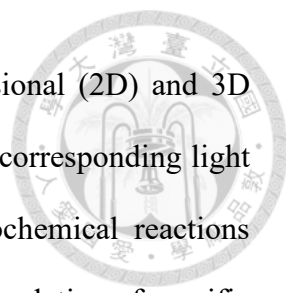
The LCST refers to a specific temperature threshold in certain polymer solutions [16]. Below this temperature, the solution remains in a single phase, while above it, phase separation occurs, resulting in two immiscible phases (i.e., gel state). This phenomenon is governed by the balance between solvent-polymer interactions and repulsive forces between polymer chains [18]. For instance, poly(N-isopropylacrylamide) (PNIPAM) is a synthetic thermo-responsive polymer governed by the LCST [16]. PNIPAM hydrogel undergoes a sol-gel transition as it crosses the LCST (~ 32 °C), causing a sharp decrease in its solubility. This is attributed to a balance of hydrophobic and hydrophilic interactions, leading to the formation of a more compact structure as the temperature rises. The LCST property of PNIPAM hydrogel makes it suitable for various biomedical applications in the human body. For example, its sharp phase transition allows targeted drug delivery or controlled release mechanisms [19]. Moreover, its responsiveness to slight temperature changes has proven useful in the fabrication of thermo-responsive biosensors [20].

On the other hand, UCST is the opposite concept of LCST. The polymer solution exists in a single phase when the temperature is above the UCST, while it transitions into two immiscible phases (i.e., gel state) when the temperature is below the UCST [21]. One of the typical biomaterials governed by the UCST is gelatin [22]. Gelatin as a naturally-



derived thermo-responsive polymer is in the gel state through triple-helix formation at temperatures lower than the UCST (i.e., ~ 27 °C), while the gel reverts to the sol state at temperatures higher than the UCST [23]. The principle behind this behavior lies in the weakening of the hydrogen bonds and other intermolecular forces at temperatures higher than the UCST, leading to the dissolution of the helical structure. While gelatin hydrogel possesses excellent biocompatibility, its melting behavior at physiological temperatures (i.e., ~ 37 °C) poses a challenge for biomedical applications. In order to address the inherent limitations of pure gelatin, the combination of gelatin with other polymers showcases a stable gel state under physiological temperatures, aligning effectively with the prerequisites of biomedical applications [24]. By harnessing the inherent biocompatibility of gelatin and elevating its thermal stability, this strategic blending introduces avenues for various applications such as wound healing and tissue engineering [25-27].

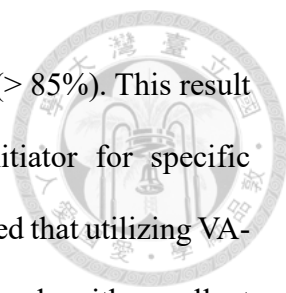
Another common type of environmental-responsive hydrogel is the photo-responsive hydrogel. Photo-responsive hydrogels are polymeric networks imbued with the distinct capability to alter their physical or chemical properties in response to light stimuli [28]. This remarkable characteristic is achieved through the integration of photoreactive functional moieties within the hydrogel matrix, facilitating controlled changes in aspects such as mechanical strength, swelling, or degradation [29]. The photo-responsive property of the hydrogel is attractive owing to the inherent advantages of light as a stimulus. The noninvasive nature of light provides the possibilities for the remote manipulation of photo-responsive hydrogels without the need of additional reagents, thereby reducing the generation of undesirable byproducts. Furthermore, by fine-tuning irradiation parameters such as intensity and exposure duration, it is feasible to exert precise control over the irradiation dosage and consequently the extent of the



photoreactions. This allows for spatial control in both two-dimensional (2D) and 3D domains, as well as temporal control by the simple actuation of the corresponding light source. Additionally, the utilization of wavelength-selective photochemical reactions facilitates orthogonal photomediation, allowing for the targeted manipulation of specific hydrogel properties. Collectively, these features emphasize the importance of photo-responsive hydrogels as externally tunable materials, substantially enhancing their contribution to the development of bioinks, smart actuators, or chemical sensors [28, 30, 31].

A typical illustrative example of photo-responsive hydrogels is gelatin methacryloyl (GelMA). GelMA was developed in 2000 by Van den Bulcke et al [32]. GelMA is a photo-responsive biomaterial derived from the modification of gelatin with methacryloyl groups. Under ultraviolet (UV) radiation, the methacryloyl groups can crosslink to form a 3D network. This allows precise control over mechanical properties and makes GelMA suitable for diverse applications, particularly in the creation of complex 3D structures, such as vascular networks or organ models [33, 34]. Its biocompatibility with various cells and biological environments further underscores its potential as a transformative technology in biomedical applications.

In the synthesis of photo-responsive hydrogels, photoinitiators are utilized to initiate crosslinking reactions [28]. Photoinitiators are chemical compounds that can absorb photons from a specific wavelength of light and subsequently produce reactive species, such as free radicals [35]. These reactive species can initiate polymerization by reacting with monomers or oligomers present within the hydrogel. The diverse nature of photoinitiators provides various options for the field of biomedical applications [36]. The commonly used photoinitiators have Irgacure 1870, Irgacure 2959, V-50, VA-044, and VA-086. Rouillard et al. compared the cell viability of these photoinitiators [37].

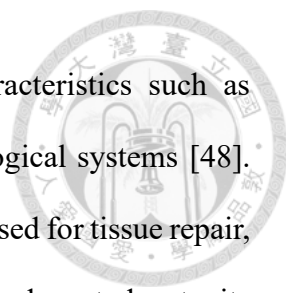


According to their findings, VA-086 displayed the best cell viability (> 85%). This result underscores the importance of selecting the appropriate photoinitiator for specific biomedical applications. Another example, Occhetta et al. demonstrated that utilizing VA-086 as the photoinitiator for GelMA leads to the formation of hydrogels with excellent biocompatibility [38].

1.1.2. Self-healing hydrogel

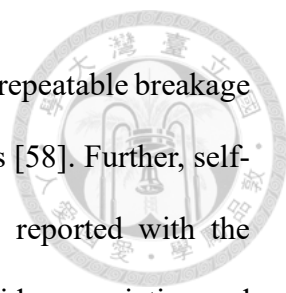
The concept of self-healing is derived from the natural wound healing process in living organisms. It refers to materials that can restore their structure and functionality after undergoing mechanical damage. There have been developments in microcapsule-laden hydrogels that release healing agents at damaged locations [39, 40]. However, challenges like irreversible healing methods and the potential negative effects of added fillers have restricted their broader application [40, 41]. Besides, many dynamic hydrogels often need external triggers like light, high heat, or acidic conditions to activate dynamic crosslinking [42, 43]. Such triggers might negatively impact cells and living tissue. In this dissertation, I focus on intrinsic self-healing hydrogels that can automatically and reversibly repair themselves and recover their original functions without external stimulation. Such natural tissue-like features offer promising potential in biomedical applications [44].

Intrinsic self-healing hydrogels can be divided into two categories based on the type of reversible interaction: dynamic covalent bonding and dynamic non-covalent bonding. The self-healing hydrogels obtained from dynamic covalent bonding exhibit stable and slow equilibriums [45]. Dynamic covalent bonding includes imine bonds, disulfide bonds, oxime bonds, boronate bonds, acylhydrazone bonds, and Diels-Alder reaction [46]. The imine bond, also known as a Schiff base, is formed by the nucleophilic attack of primary



amine on imide carbonyl [47]. Schiff base linkages exhibit characteristics such as reversibility, sensitivity to pH changes, and compatibility with biological systems [48]. Various self-healing hydrogels based on imine bonds have been proposed for tissue repair, biosensing, and drug delivery [49-51]. Among them, chitosan stands out due to its possession of primary amine groups, biocompatibility, biodegradability, antibacterial properties, and hemostatic activity, rendering it an exceptionally suitable option for the fabrication of imine bond-based self-healing hydrogels in biomedical applications [52]. Meanwhile, chitosan provides the benefit of functionalization, allowing the hydrogel to have tunable material properties. For instance, a strategy to enhance the solubility and adhesion property of chitosan is to graft phenolic acid onto chitosan chains [53]. To further crosslink chitosan to form a self-healing hydrogel, telechelic difunctional poly(ethylene glycol) (DF-PEG) is commonly used as the crosslinker [53, 54]. The dynamic imine bonds formed between the amine on the chitosan chains and the benzaldehyde on DF-PEG crosslinkers endow the resulting chitosan-based hydrogel with an intrinsic self-healing property.

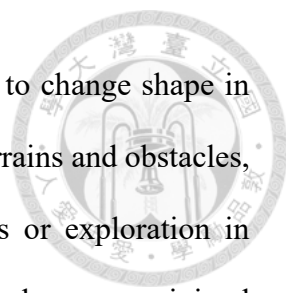
The self-healing hydrogels obtained from dynamic non-covalent bonding exhibit a better self-healing performance compared to those from dynamic covalent bonding due to their lower bond energy [55]. Dynamic non-covalent bonding includes hydrogen bonding, electrostatic ionomeric interaction, host-guest interaction, and hydrophobic interaction. Among them, hydrogen bonding is a special type of intermolecular force that occurs between molecules when a hydrogen atom bonded to a highly electronegative atom (such as nitrogen, oxygen, or fluorine) is attracted to another electronegative atom in a different molecule (or in a different part of a polymer chain). Meanwhile, hydrogen bonding is known for its distinctive characteristics, including inherent reversibility, rapid healing speed, and high healing efficiency [56, 57]. For instance, the self-healing behavior



of the recombinant squid ring teeth protein hydrogel was based on the repeatable breakage and reformation of the hydrogen bonding within β -sheet nanocrystals [58]. Further, self-healing hydrogels that utilize hydrogen bonding have often been reported with the integration of diverse chemical moieties, such as 2-ureido-4-pyrimidone moieties and gallol moieties [59, 60]. In addition, electrostatic interactions also play a significant role in the field of self-healing hydrogels. Electrostatic interactions occur between two oppositely charged polymer chains or between a charged polymer chain and an oppositely charged ion/polyelectrolyte/polyampholyte [61-63]. These electrostatic interactions within the hydrogel serve as crosslinkers and can break and reform reversibly, resulting in the self-healing property.

1.1.3. Shape memory hydrogel

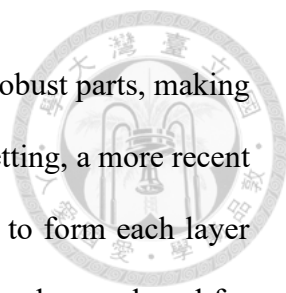
Shape memory hydrogels, which are classified as smart materials, have garnered significant attention in recent years due to their unique ability to change shape in response to external stimuli [64]. These hydrogels can be programmed to "remember" a temporary shape and revert to their original shape upon exposure to specific triggers, such as temperature, pH, or light. This property has opened up a lot of applications in various fields, including biomedical engineering, soft robotics, and wearable devices [65]. For biomedical applications, the natural temperature differential between the human body and its surroundings can act as a trigger for these materials [66]. When applied or implanted into the body, this temperature difference enables the hydrogel to undergo transformations, allowing it to adapt or change into the desired shape to serve its intended function. Such adaptability not only underscores its potential in biomedical applications but also highlights its role in the future of personalized medical tools and treatments. In the realm of soft robotics, shape memory hydrogels offer a promising avenue for creating robots



that can navigate through complex environments [67]. Their ability to change shape in response to external stimuli allows these robots to adapt to various terrains and obstacles, making them ideal for tasks such as search and rescue operations or exploration in challenging terrains. Moreover, soft and flexible nature of the hydrogel ensures minimal damage to the environment and the objects they interact with, setting them apart from traditional rigid robots. In the context of wearable devices, shape memory hydrogels can be integrated into smart textiles and wearables that adapt to the wearer's needs [68]. For instance, a garment made from shape memory hydrogels could adjust its fit based on the wearer's body temperature or activity level [69]. Such innovations could revolutionize the fashion industry by introducing clothing that is not only functional but also highly adaptive and personalized. In conclusion, shape memory hydrogels, with their unique properties and adaptability, are poised to play a pivotal role in the advancement of various fields.

1.2. 3D printing

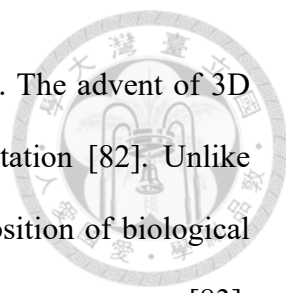
3D printing, a technology that emerged in the late 20th century, has revolutionized the way we design, produce, and implement various tools and structures [70]. The earliest 3D printing method, stereolithography (SLA), was introduced by Chuck Hull in 1986 [71]. SLA operates by employing a UV laser to solidify layers of liquid resin in a vat, gradually building the object [72]. Due to its ability to achieve high precision, SLA is popular in the dental and jewelry sectors [73]. Fused deposition modeling (FDM) is another foundational technology. In FDM, a thermoplastic filament is melted and extruded through a nozzle, layer by layer. It is favored for prototyping and research purposes due to its affordability and accessibility [74]. Selective laser sintering and direct metal laser sintering are technologies that use lasers to sinter powdered materials, such as



nylon or metal [75]. These technologies are preferred for producing robust parts, making them indispensable in aerospace and automotive industries. Binder jetting, a more recent technology that disperses a liquid binding agent onto a powder bed to form each layer [76]. It is a versatile method suitable for full-color prototypes and can be employed for metal casting molds. The 3D printing methods mentioned above are mainly focused on the manufacturing of non-biological items. The last couple of decades have witnessed an increased interest in its applications in the biomedical realm [77]. One of the primary reasons that 3D printing technology has gained prominence in biomedical applications is its ability to produce patient-specific tissues and organs. Traditional methods such as molding and casting often provide standardized solutions, which might not always be the perfect fit for every patient [70]. In contrast, 3D printing technology can create personalized items tailored to individual anatomies, ensuring higher compatibility for broader applications such as tissue engineering and regenerative medicine [78].

1.2.1. 3D bioprinting

Traditionally, the repair or replacement of damaged organs in humans has been accomplished through organ transplants [79]. One approach has been to use organs from other mammals, such as pigs, known as xenotransplantation [80]. While this method offers a potential solution to the shortage of human organs, it comes with its set of challenges. Firstly, the availability of suitable organs from animals that are both safe and effective for transplantation into humans is a concern. Consistently sourcing these organs in the needed quantities can be difficult, and the ethical considerations surrounding the use of animals for this purpose also pose challenges. Moreover, a primary medical concern with using organs from different species is the potential for immune rejection [81]. The patient's immune system can recognize the transplanted organ as foreign,



leading to immune responses that can attack and damage the organ. The advent of 3D bioprinting presents a revolutionary approach to address this limitation [82]. Unlike traditional 3D printing, bioprinting involves the layer-by-layer deposition of biological materials, notably cells, to create 3D structures resembling native tissues or organs [83]. The promise of 3D bioprinting lies in its potential to overcome limitations associated with traditional tissue engineering strategies, such as scaffold-based approaches or the manual assembly of cells [84]. With the precision of bioprinting, there is potential for fabricating tissues with intricate microarchitectures and heterogeneous cell compositions similar to those found in native tissues [83]. By utilizing the patient's specific cells, it is feasible to bioprint customized tissues or organs that are genetically matched to the patient, minimizing the risk of immune rejection and enhancing therapeutic outcomes [85]. Therefore, 3D bioprinting offers a promising alternative to traditional organ transplants, especially in cases where a compatible human donor is not available. With advances in this technology, the possibility of creating fully functional, patient-specific organs is on the horizon.

Central to the advancement of 3D bioprinting in tissue engineering is the discovery and utilization of suitable printing materials. In recent years, one material, in particular, has caught the attention of researchers in this field: hydrogels. Hydrogels are water-swollen polymer networks with high-water-content, closely mimicking the soft and hydrated environment of many biological tissues such as cartilage, skin, and even the brain [86]. Their resemblance to the physiological environment is not just in their hydration level but also in their mechanical properties, which are crucial for tissue integration. “Bioinks” are specially formulated hydrogels that contain living cells and other biological factors. For an ideal bioink, several characteristics are vital (**Figure 2**). First and foremost, biocompatibility is paramount. The material must not elicit adverse

immune responses and should support cellular attachment, proliferation, and differentiation. This ensures that the printed structures can function as intended when implanted or used for various applications. Next, the viscosity of the bioink plays an essential role. It should have a shear-thinning property, meaning that it becomes less viscous under stress, ensuring smooth extrusion during the printing process but regains its shape immediately post-extrusion. Additionally, the bioink should provide mechanical stability to maintain the structural integrity of the printed construct. Furthermore, it's important for the bioink to possess suitable degradation kinetics, aligning with tissue remodeling and ensuring that the printed structure does not degrade prematurely or remain longer than necessary.

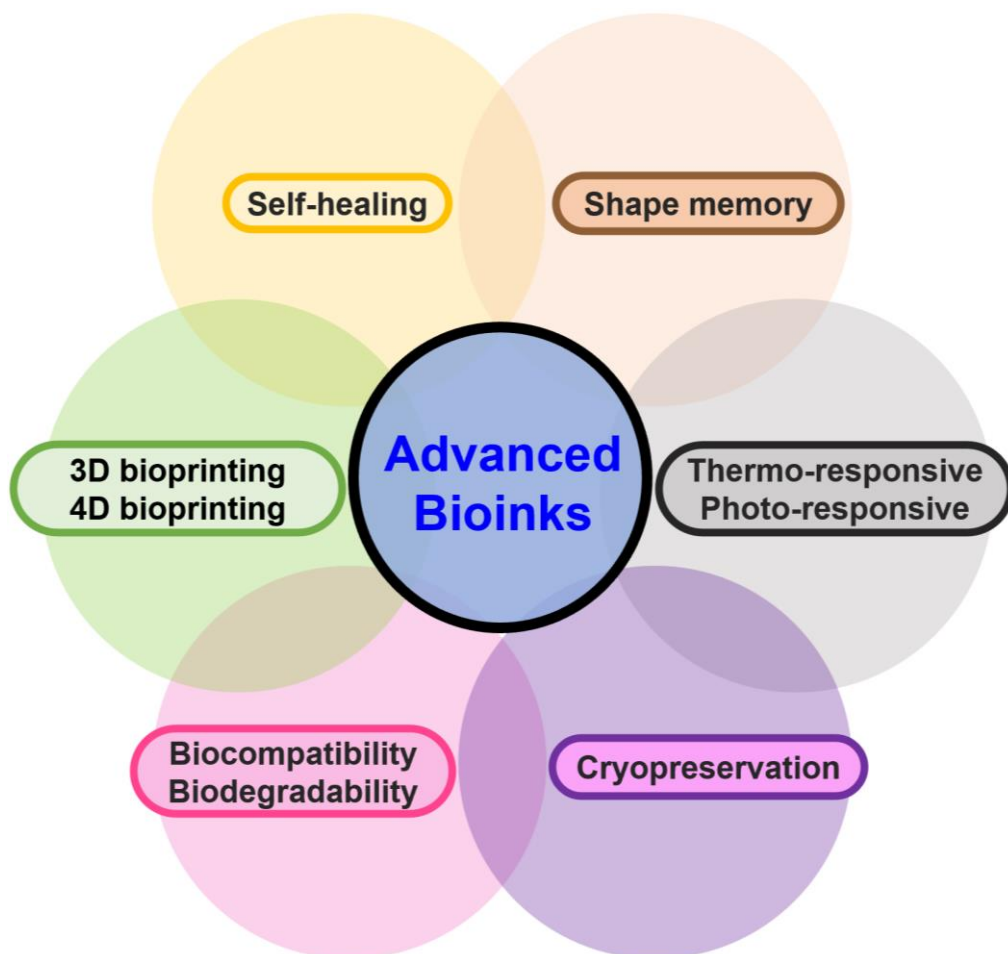
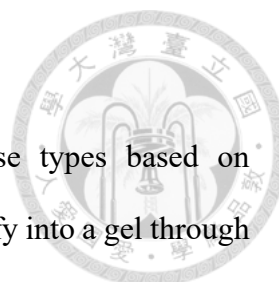


Figure 2. Schematic diagrams showing the key properties of advanced bioinks.



1.2.2. Thermo-responsive bioink

The versatility of bioinks can be attributed to their diverse types based on responsiveness to external stimuli. Thermo-responsive bioinks solidify into a gel through temperature changes. The advantage is that the gelation process causes minimal damage to cells compared to other responsiveness (e.g., pH), and the appropriate gelation temperature is conducive to cell survival and maintaining their normal functions [87]. For instance, PNIPAM as the representative thermo-responsive bioink can undergo a phase transition from liquid to solid in response to temperature changes, ensuring that the bioink remains fluid during the printing process but solidifies post-printing when subjected to human body temperature [88]. Although PNIPAM can exhibit thermo-responsive behavior, making it an attractive candidate for various applications, there are reports suggesting potential cytotoxicity and adverse cellular responses when interfaced with biological systems [89]. Meanwhile, the non-biodegradability of PNIPAM is a disadvantage for tissue engineering applications, as the persistent presence of the material can interfere with tissue regeneration or cause long-term issues [90]. Another representative thermo-responsive bioink is gelatin. Gelatin exists in a liquid state at temperatures higher than the UCST (i.e., $\sim 28^{\circ}\text{C}$), while it solidifies to form a gel at temperatures lower than the UCST [91]. This property is advantageous because it can be easily extruded for printing at room temperature, and when printed onto a low-temperature platform, it exhibits good shape fidelity and stackability. However, this property makes gelatin unsuitable for use in physiological conditions (i.e., 37°C) because it will dissolve. To overcome this inherent limitation of pure gelatin, it is often blended with other polymers to form stable gels that can stably exist at physiological temperatures for use in 3D printing [24].

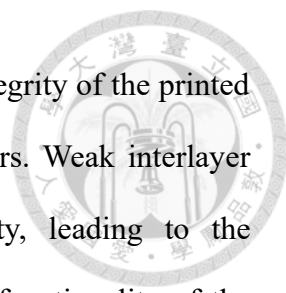


1.2.3. Photo-responsive bioink

Photo-responsive bioinks introduce another type to the field of bioprinting by taking advantage of light-induced crosslinking mechanisms to transform the bioink from a liquid state to a gel state [28]. This methodology provides precise spatiotemporal control over gelation, offering the capability to create highly defined structures that are essential for fabricating complex tissue architectures. A prominent example of a photo-responsive bioink is GelMA [33]. GelMA is synthesized from gelatin by introducing methacryloyl groups, which allows for photo-crosslinking when exposed to UV light in the presence of a photoinitiator. The unique property of GelMA enables it to retain the biocompatibility and cell-friendly characteristics of gelatin while also providing the capability to form stable hydrogels upon exposure to UV light. Hence, during the bioprinting process, GelMA can remain fluid, and post-printing, targeted UV light exposure solidifies the structure, ensuring spatial accuracy and structural stability. Importantly, GelMA hydrogels can exist stably at physiological temperatures without dissolving, unlike pure gelatin, which makes them suitable for various tissue engineering applications [92]. Moreover, the degradation rate of GelMA can be tuned by controlling the degree of methacryloyl substitution, providing added flexibility in designing for different tissue types. However, while the use of UV light offers precision in crosslinking, it is imperative to consider the potential detrimental effects of UV exposure on encapsulated cells and ensure that exposure durations are optimized to prevent cytotoxicity [93].

1.2.4. Self-healing bioink

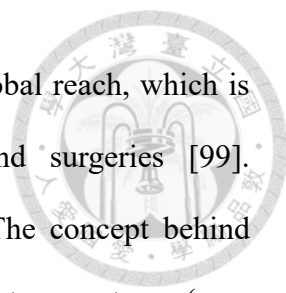
The quest for perfecting 3D bioprinted structures does not end merely at their fabrication. Post-fabrication, one of the primary concerns is ensuring good interlayer adhesion [94]. As 3D bioprinting involves the layer-by-layer deposition of bioinks to



build a structured tissue construct, the mechanical and functional integrity of the printed tissue largely relies on the interactions between these printed layers. Weak interlayer interactions have the potential to undermine structural integrity, leading to the delamination of layers, which in turn can significantly impact the functionality of the bioprinted tissue. To address this challenge, the development of self-healing bioinks has emerged as a promising strategy [95]. Self-healing materials have the intrinsic capability to recover their structural and functional integrity post-damage. By utilizing this property in bioinks, it becomes possible to fabricate 3D bioprinted tissues capable of self-healing damages or inconsistencies at the interlayer interfaces [96, 97]. This not only enhances the mechanical strength of the printed tissues but also extends their functional durability. However, while the potential benefits are vast, the development and optimization of self-healing bioinks present a complex interplay of material science, cell biology, and bioprinting technology. The challenge lies not only in achieving self-healing properties but also in ensuring that these properties do not come at the expense of other vital parameters such as biocompatibility, printability, and mechanical stability. Moreover, the incorporation of cells within these bioinks demands careful consideration of how the self-healing mechanisms might impact cell viability, proliferation, and differentiation. To date, only a limited number of research studies have been published on the utilization of self-healing materials within the realm of 3D bioprinting [98]. Therefore, there is a pressing need for the development of new self-healing bioinks to propel advancements in this field.

1.2.5. Cryopreservable bioink

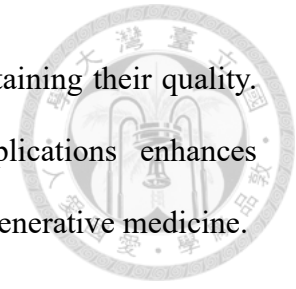
The realm of 3D bioprinting is continuously expanding, with researchers constantly innovating to meet specific requirements and challenges presented by various applications. One such imperative requirement is the long-term storage and transportation



of bioprinted constructs, facilitating an extended shelf-life and a global reach, which is critical in medical settings for ensuring timely treatments and surgeries [99]. Cryopreservable bioinks offer a solution to this dilemma [100]. The concept behind cryopreservation is to store biological constructs at deep cryogenic temperatures (e.g., with liquid nitrogen), thereby reducing the metabolic rates of the cells within the bioink, which in turn can potentially prolong the viability and functionality of the bioprinted tissues or organs over extended durations [101, 102]. By allowing bioinks to be cryopreserved, researchers and clinicians can print the necessary structures well in advance and store them for subsequent use without the concern of the material degrading or the cells losing their functionality. This is particularly beneficial in settings where bioprinted tissues or organs are needed on-demand, or where there is a requirement to transport the constructs across long distances, ensuring that they reach the end-users in optimal condition. Moreover, the cryopreservation of bioinks presents an opportunity to establish a standardized biobank of bioprinted constructs [103]. Such a bank would be a repository of various tissue types, all preserved and ready for transplantation when needed. This standardized approach not only ensures quality and consistency but also significantly reduces the lead time from when a tissue is needed to when it can be implanted.

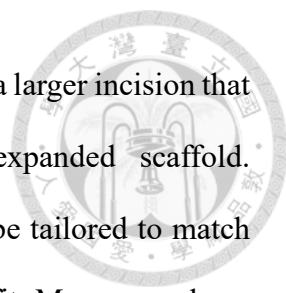
It's crucial to ensure that the cryopreservation process does not compromise the structural integrity of the bioprinted construct or the cell viability within the construct. This means that the cooling rates, the choice of cryoprotective agents, and the thawing process all need to be meticulously optimized. A poorly executed cryopreservation can lead to the formation of ice crystals within the bioprinted construct, which can disrupt cellular membranes and compromise cell viability [104]. Therefore, while the ability to cryopreserve bioinks is significant, it is accompanied by its own set of challenges that need to be addressed. Overall, bioinks capable of cryopreservation offer a solution for

preserving bioprinted constructs over extended periods while maintaining their quality. This bridge between bioprinting laboratories and clinical applications enhances accessibility and timeliness in the field of tissue engineering and regenerative medicine.



1.2.6. 4D bioprinting

As the field of bioprinting continues to evolve, it has given rise to a novel concept known as four-dimensional (4D) bioprinting. Going beyond the static 3D structures fabricated using conventional 3D bioprinting, the fourth dimension in 4D bioprinting is time. This implies that the bioprinted structures undergo transformations, typically in response to external stimuli, after their initial fabrication [105]. Essentially, 4D bioprinted materials can change shape, mechanical properties, or functionality over time, adding dynamicity to the otherwise static constructs. A pivotal element in the realm of 4D bioprinting is the use of shape memory hydrogels as bioinks. These hydrogels can remember their original shape and revert to it in response to specific triggers, such as temperature, pH, or moisture [106]. The appeal of shape memory hydrogels lies in their potential to mimic the dynamic behaviors observed in native tissues. For instance, a bioprinted blood vessel might be designed to expand or contract in response to changes in blood flow [107]. Using shape memory hydrogels in 4D bioprinting offers numerous advantages. One of the significant advantages lies in its potential applications in minimally invasive surgery. In minimally invasive surgery, smaller incisions are made, resulting in reduced trauma to the patient, quicker recovery times, and less visible post-surgical scars. The 4D bioprinted shape memory hydrogels can be implanted in a compressed, shape-fixed state through small incisions. Once inside the body, these hydrogels can expand and recover to their original shapes to perform the desired function, such as supporting damaged tissue, serving as tissue-engineered implants for regenerative

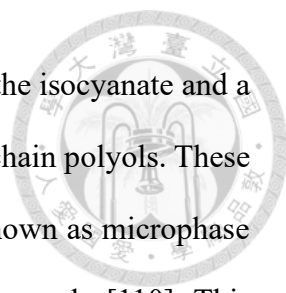


medicine, or delivering drugs [105]. This eliminates the necessity for a larger incision that would conventionally be required to accommodate a fully expanded scaffold. Additionally, due to the bioprinting capability, these hydrogels can be tailored to match an individual patient's personalized anatomy, guaranteeing an ideal fit. Moreover, shape memory hydrogels can bring an added level of functionality to bioprinted tissues, allowing them to interact and adapt more realistically within the body. This adaptive behavior can improve tissue integration, healing, and overall therapeutic efficacy [108].

While 4D bioprinting offers promising benefits, it is crucial to highlight the accompanying challenges. The design of bioinks, in particular shape memory hydrogels, requires a good balance between retaining their shape memory property while also ensuring biocompatibility [109]. Furthermore, ensuring consistent and predictable transformations *in vivo* also requires further research and optimization. Overall, 4D bioprinting with shape memory hydrogels as bioinks offers broader application opportunities in tissue engineering and regenerative medicine. While there are numerous challenges to overcome, the prospect of fabricating dynamic, adaptable tissue structures marks a thrilling evolution in bioprinting advancements.

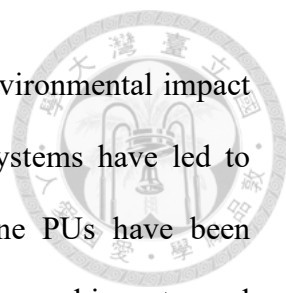
1.3. Polyurethane (PU)

PU stands as a critical class of polymers distinguished by its versatile range of mechanical and chemical properties. Central to its molecular architecture is the urethane functional group, typically synthesized through the nucleophilic addition reaction between an isocyanate moiety ($R-N=C=O$) and a hydroxyl group ($R-OH$) [110]. This basic building block can be modulated through the employment of a diverse composition of monomers, granting PU the ability to exhibit properties ranging from highly elastic to rigid. The distinctive behavior of PU can be linked to the balance in composition between



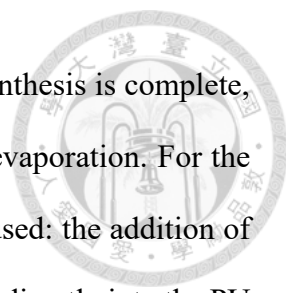
its rigid and flexible segments. The hard segment usually comprises the isocyanate and a short chain extender, whereas the soft segment is derived from long-chain polyols. These segments are intrinsically incompatible, leading to a phenomenon known as microphase separation, where hard and soft domains segregate at the nanometer scale [110]. This segregation manifests as distinct physical regions within the polymer matrix, resembling the behavior observed in block copolymers. Elasticity in PU arises primarily due to the soft segments, which act as entropic springs. These chains prefer a coiled, random conformation but can be elongated under stress. Once the stress is removed, they return to their original state, contributing to the elastic behavior [111]. On the other hand, hard segments contribute to tensile strength and thermal stability, assembling into hard domains that act as physical crosslinks [112]. The characteristics of microphase separation can be tuned to create PU materials with targeted properties. For instance, a higher proportion of hard segments usually results in increased tensile strength but decreased elasticity [113]. Conversely, a high percentage of soft segments results in more flexible but weaker materials [114]. Through microphase separation, PU materials achieve a wide range of mechanical properties, making them suitable for diverse applications such as medical elastomers, automotive components, and even adhesives [115].

The adaptability of PU is demonstrated not only in its adjustable structure but also in its varied forms and solubilities, particularly its presence in both oil-based and water-based systems. Traditional oil-based PUs have dominated the market for years, especially in the development of automotive finishes, furniture coatings, and industrial applications [116]. These are often solvent-borne systems in which the polymer chains are dissolved in organic solvents. Solvent-borne PUs are renowned for their outstanding weather resistance, capable of withstanding harsh environmental conditions such as humidity,



sunlight, and high and low temperatures. While widely used, the environmental impact and volatile organic compound emissions associated with these systems have led to increasing scrutiny [117]. To address these challenges, waterborne PUs have been developed. In contrast to solvent-borne PUs, waterborne PUs are dispersed in water and can be formulated as either dispersions or emulsions [118, 119]. The hydrophilic segments in waterborne PU can be designed to interact with water molecules, ensuring stable dispersion and reducing the need for harmful solvents.

The preparation of waterborne PU in the beginning involves the reaction of isocyanate groups with hydroxyl groups to form a pre-polymer structure. However, the isocyanate groups are highly reactive and susceptible to undesirable side reactions, particularly with water. To avoid the undesirable side reactions, the pre-polymerization process is typically conducted in an environment devoid of moisture and shielded with nitrogen gas [119]. Furthermore, maintaining an appropriate reaction temperature during whole waterborne PU synthesis is crucial. If the temperature is too low, the reaction will not happen, while excessive heat can lead to the decomposition of raw materials. Meanwhile, additional side reactions at elevated temperatures could occur between isocyanate groups and the carboxylic acid groups (which come from the functional groups of compounds used in making waterborne PU) within the system. This divergence impacts the properties of the end product, making temperature control a key factor in PU synthesis [119]. Viscosity also needs to be controlled as the molecular weight of the polymer increases, making it harder for the polymer to disperse in subsequent water phases. Various solvents have been used to control this, such as tetrahydrofuran (THF) by Santamaria-Echart et al. and methyl ethyl ketone (MEK) by Hsu et al. [119, 120]. However, the use of toxic organic solvents contradicts the original intention of a water-based system, posing environmental and biological risks. Therefore, the amount of

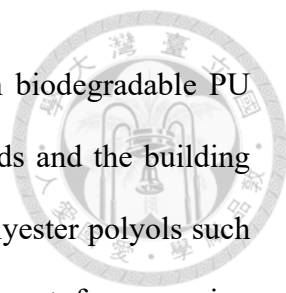


organic solvent added needs to be strictly controlled, and after the synthesis is complete, the organic solvent must be removed using methods such as rotary evaporation. For the stabilization of PU particles in water, two approaches are generally used: the addition of external emulsifiers or the incorporation of charged functional groups directly into the PU structure [119, 121].

Furthermore, the versatility of PU extends to its physical form, notable examples being hydrogels and films [119]. Waterborne PU-based hydrogels are of significant interest in the biomedical field due to their elasticity, biocompatibility, and adjustable mechanical properties. These hydrogels can be synthesized via a variety of techniques, including physical or chemical crosslinking with other polymers, to form a 3D network that can hold a significant amount of water for various applications [25]. On the other hand, PU films are utilized in a wide range of industries, such as packaging, where their barrier properties are crucial, and in biomedical applications, where their flexibility and tunable mechanical properties are advantageous [122]. These films can be processed via various methods such as extrusion, casting, and electrospinning, each of which can be optimized to achieve desired properties. Overall, the adaptability of PU manifests in both its solubility—ranging from traditional oil-based to eco-friendly waterborne forms—and its physical forms, which include hydrogels and films. These features underscore the suitability of PU for a multitude of applications, from industries to biomedicine.

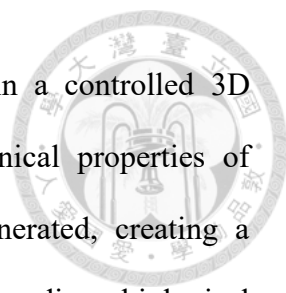
1.3.1. Biodegradable PU

Biodegradable PU represents a significant advancement in the realm of materials science, offering a groundbreaking solution to some of the most pressing challenges we face in environmental protection and medical applications [123]. Unlike traditional PU, which can persist in the environment for decades or even centuries, biodegradable PU



undergoes biodegradation processes. The major difference between biodegradable PU and its non-biodegradable counterpart is the types of chemical bonds and the building blocks from which the polymer is synthesized. Hydrolysis-prone polyester polyols such as PCL diol and PLA diol are commonly used as the soft segment for preparing biodegradable PU [124]. The hydrolysis rate for PCL diol-based PU was approximately ten times higher than that of polyether diol-based PU [125]. The ester bonds within the biodegradable PU undergo hydrolysis when exposed to natural conditions such as water and microbial activity, breaking the polymer chain and leading to its degradation into smaller molecules that can be metabolized or further broken down by microorganisms [126]. The decomposition into water, carbon dioxide, and innocuous by-products essentially leaves no trace, thereby reducing landfill waste and eliminating the detrimental long-term effects on aquatic and terrestrial ecosystems [127].

Biodegradable PU has found significant utility in the field of medical applications, notably in the specialized area of implantable devices [128]. Conventionally, implants made from non-biodegradable materials often need a second surgical procedure for removal. This not only subjects the patient to additional physical and psychological stress but also increases the risk of complications such as foreign body reaction and infection. Biodegradable PU materials offer a unique advantage in this regard; once they serve their purpose, the material naturally degrades within the body, eliminating the need for a second, invasive surgery to remove the implant [129]. Moreover, the importance of biodegradable PU extends further into the realm of tissue engineering. In tissue engineering, scaffolds made from biodegradable materials play a critical role [130]. Unlike the non-biodegradable counterparts, the biodegradable scaffolds offer a key advantage: they gradually degrade over time, freeing up space for proliferating cells to populate and form functional tissues. This “room-making” capability is important for

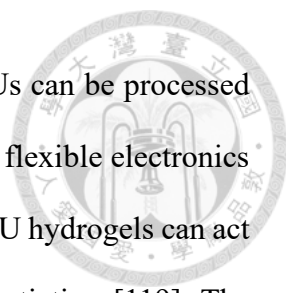


effective tissue regeneration and repair, allowing cells to grow in a controlled 3D environment [131]. The controlled degradation rates and mechanical properties of biodegradable PU can be tuned to match the tissue being regenerated, creating a harmonious relationship between the scaffold and the surrounding biological environment. The degradation products of the biodegradable PU can be biocompatible, meaning they are safely metabolized or excreted by the body, minimizing inflammation or other adverse reactions [126, 131].

1.3.2. Biocompatible PU

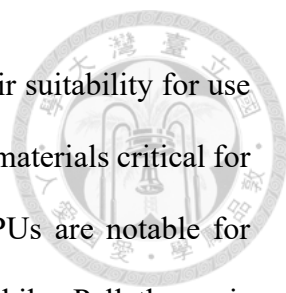
Biocompatibility is an essential consideration in the development of materials for biomedical applications, and PU has been significantly researched for its biocompatible properties [132]. Biocompatible PUs are designed to interact with biological systems, minimizing adverse reactions such as inflammation, immune response, or tissue damage. Biocompatible PUs can be tailored to display a broad range of mechanical and chemical properties. This adaptability makes them suitable for a wide variety of biomedical applications. For example, softer forms of biocompatible PUs are often used in medical devices and products that require flexibility and comfort, such as catheters, wound dressings, and flexible implants [133]. These softer forms are generally engineered to be highly elastic, flexible, and porous, thereby facilitating essential biological functions like tissue contraction/relaxation or fluid transfer. On the other hand, more rigid forms of biocompatible PUs can serve as structural components in medical applications where greater mechanical strength is necessary [133]. These might include prosthetic devices or components in medical implants like hip or knee replacements.

In the realm of biocompatible PU, particular attention has been given to waterborne PU. Unlike traditional solvent-borne PUs, the preparation process of waterborne PUs is



more eco-friendly and generally less cytotoxic [119]. Waterborne PUs can be processed into hydrogels or films for applications such as tissue engineering or flexible electronics [132, 134]. In the applications of tissue engineering, the waterborne PU hydrogels can act as the necessary constructs for cell attachment, growth, and differentiation [119]. The mechanical properties of these constructs can be fine-tuned to closely mimic the native tissues they are targeted to replace. For instance, the elastic modulus of biocompatible, waterborne PU hydrogel can be adjusted to mimic the soft nature of the nerve, making it a promising material for nerve tissue engineering [135, 136]. In the applications of flexible electronics, the inherent flexibility of PU films makes them ideal candidates for wearables, as they can easily conform to the contours and movements of the human body [134]. Further, the issue of skin compatibility is crucial in the realm of wearable electronics, as these devices require direct skin contact. While conventional materials may sometimes cause skin irritation or allergies, biocompatible PUs are engineered to mitigate these risks. The biocompatibility of PU films makes them safe for direct skin contact, thus opening up new avenues for their application in various health-monitoring wearable electronics.

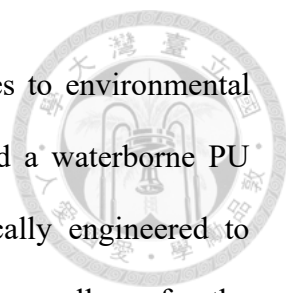
Another typical biocompatible PU is Pellethane, a family of medical-grade thermoplastic PU (TPU) elastomers. Pellethane distinguishes itself through its superior biocompatibility, biostability, and processing versatility [137]. In particular, the Pellethane 2363 Series TPU, which is an aromatic polyether-based variant within this family, stands out for its outstanding hydrolytic stability as well as its mechanical and chemical resistance properties [138]. Further, Pellethane 2363 Series TPU can be processed using a conventional molding method, offering flexibility in manufacturing and design [139]. Importantly, the Lubrizol Corporation, an American provider of specialty chemicals, has a master file on record with the United States Food and Drug



Administration (FDA) for this range of products. This highlights their suitability for use in biomedical applications. Overall, biocompatible PUs are versatile materials critical for biomedical applications, from wearables to implants. Waterborne PUs are notable for their eco-friendliness and suitability for tissue engineering, while Pellethane is distinguished by its mechanical strength and biostability. Both types are approved for various medical uses, showing the promise and adaptability of biocompatible PUs in healthcare applications.

1.3.3. PU for bioprinting

3D bioprinting technology offers the potential to fabricate customized, tissue-engineered constructs with intricate architectures and tailored cellular arrangements. Central to the success of this technology is the choice of bioink, which must not only support the viability and function of encapsulated cells but also possess the appropriate rheological properties for high-fidelity printing. Waterborne PU with good biocompatibility and tunable biodegradability stands as a promising candidate for bioprinting applications. For instance, Ho et al. investigated the potential of 3D bioprinting in cell reprogramming, demonstrating that fibroblasts could be reprogrammed into neural-like constructs when embedded within the waterborne PU hydrogel [124]. Similarly, Huang et al. developed a waterborne PU-graphene composite hydrogel as the bioink for 3D bioprinting [136]. The introduction of graphene imparted conductive properties to the bioink, supporting the proliferation and differentiation of neural stem cells. This PU-based composite, therefore, has significant potential for applications in neural tissue engineering. These two examples underscored the potential of waterborne PU not just as a tissue-engineered construct but also as a conducive environment for cellular differentiation and function.



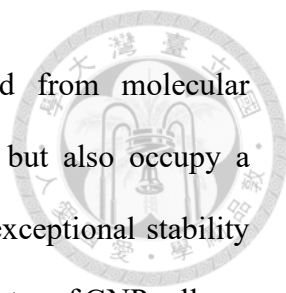
To endow PU bioinks with smart property, responsive features to environmental stimuli have been developed. For example, Hsiao et al. introduced a waterborne PU bioink with photo-responsive properties, which has been specifically engineered to respond to UV light [135]. This innovation in PU bioink technology allows for the fabrication of constructs whose structural strength can be enhanced post-bioprinting, playing a crucial role in creating high-fidelity constructs. Despite these advancements, there are aspects of this bioink that do not meet expectations, including its printing window, printing resolution, and biocompatibility. To address these limitations, further modifications and integrations have been explored. In particular, by blending PU with other biomaterials, its bioprinting properties and biocompatibility could be further improved. For instance, Hsieh et al. blended PU with gelatin to develop a double-network PU-gelatin hydrogel as the thermo-responsive bioink [25]. This bioink not only exhibits the advantageous rheological properties of PU but also incorporates the biocompatibility and cell-adhesiveness of gelatin. Owing to the thermo-responsive property of gelatin, the bioink can achieve suitable rheological characteristics by adjusting the surrounding temperature, enabling high-resolution 3D bioprinting. Because of its tunable modulus, this bioink can be used for a wide range of tissue engineering applications. However, this Ca^{2+} -crosslinked approach reduces the elasticity of the bioprinted constructs, thereby limiting their applicability. Moreover, the use of Ca^{2+} notably impacts the application for cell types that are highly sensitive to ions, such as cardiomyocytes. Therefore, it is crucial to develop a new smart PU bioink that possesses good biocompatibility, bioprinting properties, excellent elasticity, and wide applicability in various tissue engineering applications.



1.4. Gold nanoparticles (GNPs)

Since ancient times, the captivating glow and lustrous yellow of bulk gold have drawn human fascination. The initial endeavors to extract gold can be traced back to the 5th millennium B.C. near the vicinity of Varna, Bulgaria [140]. From then on, gold has ascended to prominence, becoming the most esteemed noble metal, widely utilized for crafting exquisite artworks, decor, and coveted jewelry, and evolving as a precious commodity in trade. Moreover, the remarkable electrical conductivity of gold, combined with its unwavering resistance to corrosion, designates it as an essential component in the field of electronics. Its applications are wide-ranging, encompassing corrosion-resistant contact platings, semiconductor package bond wires, hybrid circuits, solderable coatings designed for printed circuit boards, gold-based solders, conductor tracks, and contact pads [141, 142]. Furthermore, its biocompatibility has led to its adoption in the dental industry, particularly in the fabrication of bridges, crowns, porcelain enamel inlays, and onlays [141].

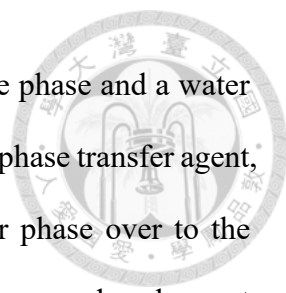
The emergence of nanotechnology has garnered increasing attention for materials sized between 1 and 100 nm, which exhibit properties unique from their bulk counterparts [143]. This difference opens doors to unique effects and phenomena, unveiling new possibilities for various applications. For instance, the quantum size effect becomes evident when reducing semiconductor particles to the nanoscale. This allows for the manipulation of the electronic band gap simply by altering the particle size, without the need to modify the material composition [144, 145]. In another example, GNPs are notable for their variety of remarkable electronic and optical effects. Efforts have been made to comprehend and harness the fascinating characteristics and potential uses of the GNPs, involving extensive research into various fabrication methods. The research encompasses both top-down strategies, like photo-/electron-beam lithography, and



bottom-up approaches grounded in chemical syntheses initiated from molecular precursors [146]. Further, GNPs not only fascinate on their own but also occupy a distinctive position within the realm of nanomaterials due to their exceptional stability when compared to other metal nanoparticles [147]. The surface chemistry of GNPs allows for controlled ligand exchange, making it possible to decorate the nanoparticles with a wide range of molecules ranging from simple to complex, including biomolecules like DNA functionalized with thiol groups, which facilitates strong gold-sulfur bonds [147, 148]. Through the use of GNPs adorned with various complementary DNA strands, researchers can engineer specifically designed arrangements of GNPs [149]. With their unique surface chemistry and optical properties, GNPs provide a promising area for investigation in biological detection, medical diagnostics, and therapeutic applications [150, 151].

1.4.1. Synthesis

GNPs have a rich history dating back to the Roman Empire when they were used, albeit unknowingly, to stain glasses for decorative purposes, resulting in red glasses or ruby glass [152]. This early technique involved incorporating colloidal gold and stannic hydroxide into the molten glass [153]. The synthesis of GNPs as we understand it today began in the 1850s with Michael Faraday, who synthesized colloidal GNPs by reducing gold chloride with phosphorus [154]. In 1951, Turkevich et al. introduced a pioneering method for synthesizing ligand-stabilized GNPs using citric acid as a stabilizer and reducing agent, establishing a foundation for the development of various GNP synthesis methods that utilize different stabilizers and solvents [155-157]. The Brust-Shiffrin method, developed in 1994, was groundbreaking as it first facilitated the facile synthesis of thermally and air stable GNPs of reduced dispersity and controlled size [140]. Shiffrin's



group implemented a two-phase system, incorporating both a toluene phase and a water phase. Within this system, tetraoctylammonium bromide, serving as a phase transfer agent, was employed to transfer dissolved $[\text{AuCl}_4]^-$ anions from the water phase over to the organic toluene phase. It was in this organic phase that the gold compound underwent reduction, facilitated by NaBH_4 , and in the presence of dodecanethiol ligands. GNPs were observed to possess diameters that ranged from 1 to 3 nm, with the majority of the distribution peaking at a size range of 2.0 to 2.5 nm.

Leff et al. reported a modification to the original Brust-Schiffrin method that results in GNPs possessing a controlled diameter of ~ 4 nm [158]. Leff's method employed 1-dodecylamine as the stabilizing ligand due to its inherently weaker bond with gold compared to the gold-thiol bond [159, 160]. This feature is beneficial for the subsequent fabrication of crosslinked GNP films, as it allows for feasible ligand-linker exchange reactions with dithiols. In contrast to the synthesis method outlined by Leff et al., the method by Peng et al. was conducted entirely within a single organic phase. The reduction of $[\text{AuCl}_4]^-$ was achieved through the injection of the tert-butylamine-borane complex in tetralin in the presence of oleylamine at the specified temperature (2–40 °C), allowing for the adjustment of particle sizes. At higher temperatures, the rapid reduction of Au^{3+} ions occurs when the reduction solution was injected, depleting most of the precursor material at once and resulting in the formation of small particles. Conversely, at lower temperatures, the precursor was not rapidly consumed due to a slower reduction rate, enabling the growth of larger particles [161]. By manipulating the reaction temperature, it became possible to control the GNP diameter, which can range from 2 to 10 nm. Importantly, this method resulted in the production of GNPs characterized by a remarkably narrow size distribution, with less than 10% variation.



1.4.2. Optical properties

GNPs distinctively exhibit unique optical properties in contrast to their bulk counterpart, finding applications in various realms such as art. While bulk gold is renowned for its lustrous yellow hue, GNPs display an intense red-pink color due to their pronounced absorption band within the visible spectral range [162]. This particular characteristic has been utilized in artistic creations such as the “Purple of Cassius” pigment and the Lycurgus Cup [162, 163]. The latter, a remarkable piece of 4th-century art, is embedded with gold and silver nanoparticles as confirmed through transmission electron microscopy (TEM). Interestingly, the Lycurgus Cup exhibits a dynamic color change, appearing red under transmitted light and green under reflected light, a phenomenon attributed to the unique optical properties of GNPs. This absorption phenomenon observed in GNPs is attributed to surface plasmon resonance (SPR). SPR involves the coherent oscillation of free conduction band electrons within the GNPs when interacting with incident electromagnetic waves. This interaction results in polarizations and oscillations of electrons. When the frequency of these oscillations aligns with that of the incident light, it leads to the strong absorption of electromagnetic radiation, observable through the characteristic absorption bands in the spectra of GNPs [162].

In 1908, Gustav Mie provided a theoretical framework to understand these observations. He solved Maxwell's equations for spherical particles, describing the extinction coefficient as a summation of electric and magnetic multipole oscillations contributing to light absorption and scattering [140, 162, 164]. In cases where the particle diameter is significantly smaller than the wavelength of the incident light, the absorption is predominantly attributed to the dipolar term. For GNPs within the quasi-static approximation regime, the Mie theory can be simplified into the following equation (1) to describe the extinction cross section σ_{ext} [162, 165]:



$$\sigma_{ext} = \frac{9V_p \varepsilon_m^{3/2}}{c_0} \frac{\omega \varepsilon_2(\omega)}{[\varepsilon_1(\omega) + 2\varepsilon_m]^2 + \varepsilon_2(\omega)^2} \quad (1)$$

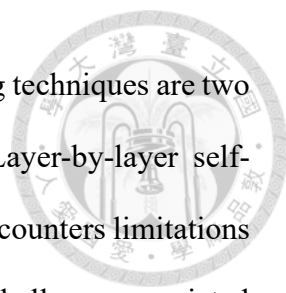
Here, V_p represents the volume of a spherical particle. The speed of light is denoted by c_0 , while the angular frequency of the exciting light is represented by ω . Additionally, ε_m refers to the dielectric constant of the medium surrounding the particle. ε_m is assumed to be frequency-independent. The complex dielectric function of GNP, $\varepsilon(\omega)$, is assumed to be frequency-dependent and can be expressed as $\varepsilon_1 + i\varepsilon_2$, where ε_1 and ε_2 are the real and imaginary parts, respectively. According to equation (1), the quasi-static approximation suggests that the spectral position and the bandwidth of the plasmon absorption do not depend on the particle size. However, this stands in opposition to what has been observed through experimentation. In the case of particles with a diameter less than 20 nm, the plasmon bandwidth is inversely proportional to the particle radius [165]. Therefore, adjustments to the Mie theory have been proposed due to observed size dependence. These modifications consider a size-dependent dielectric function $\varepsilon(\omega, D)$ for the GNPs, where D is the diameter of GNP. The SPR in GNPs is susceptible to changes in the interparticle distance. This sensitivity makes GNPs valuable in detecting molecular recognition and sensing applications [166]. For instance, a red-shift in the absorption bands is observable when GNPs undergo aggregation. Jain et al. demonstrated an exponential decay in fractional plasmon wavelength shift for polarization along the interparticle axis with increasing interparticle distances [167]. Sonnichsen et al. introduced a "plasmonic ruler", employing it to examine the kinetics involved in DNA hybridization events [168].



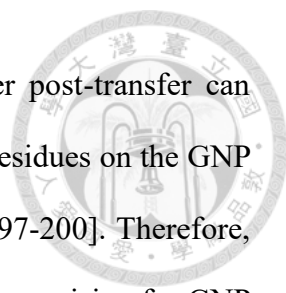
1.5. GNP films

1.5.1. Fabrication

Nanoparticles, often obtained in colloidal solutions, have become promising candidates for flexible wearable electronics due to the low-cost and various deposition techniques available for applying them on different substrates. Techniques such as spray coating, drop-casting, Langmuir-Blodgett deposition, inkjet-printing, layer-by-layer self-assembly, and layer-by-layer spin coating allow precise tuning of the thickness, crystallinity, and spatial dimensions of nanoparticle films, by adjusting the size, shape, concentration, solvent, and ligand [169-174]. GNP films, often crosslinked with organic ligands like amines, thiols, phosphines, or carboxylates, present unique functionalities due to the inherent hybrid nature of the composite network and the ability to tailor material properties by choosing specific organic molecules [175]. Such composites have demonstrated potential for various applications including sensors and have been extensively studied with respect to their film properties, applications, and deposition methods [172, 174-176]. Thiols and dithiols, in particular, play a crucial role due to the strong bond they form with gold and their ability to crosslink GNPs effectively [177]. Furthermore, the literature reveals a diverse range of GNP composites differing in physical parameters, including assemblies ranging from disordered structures to highly ordered supercrystals and superlattices [160, 176, 178-180]. The charge transport in these composites is highly dependent on the interparticle matrix, which is vital for various sensing applications. However, some composites, such as those with GNPs capped with long-chain 1-alkanethiols, tend to exhibit extremely low conductivities. To overcome this issue, our group's previous research employed GNPs crosslinked with short dithiol ligands, such as 1,6-hexanedithiol or 1,9-nonanedithiol (9DT), to offer an appropriate range of resistance variation for sensing purposes [174, 181].



The layer-by-layer self-assembly and layer-by-layer spin-coating techniques are two prominent methods for fabricating GNP films [160, 174, 176]. Layer-by-layer self-assembly, while enabling the creation of highly ordered structures, encounters limitations such as the necessity for surface functionalization and the intrinsic challenge associated with film transfer to different substrates, particularly since the first layer of the film is covalently bound to the surface of its original substrate, thereby hampering lift-off and transfer procedures [173]. By contrast, layer-by-layer spin-coating presents a faster way for depositing solutions on substrates as there is no need for a complete immersion of the substrates, i.e., only μL volumes of the GNP/ligand solutions are necessary. In 2011, our group introduced a versatile protocol for the rapid fabrication of crosslinked GNP films using layer-by-layer spin-coating [176]. Spin-coated GNP films, which are not covalently bound to the substrate (i.e., glass or silicon), can be feasibly transferred to different target substrates with the assistance of various methods. Common transfer methods include the wedging transfer process, peel-and-stick process, lift-off by etching, and PMMA-mediated transfer printing [174, 176, 182-193]. However, these methods encounter respective challenges. For example, the GNP films transferred via the wedging process often form wrinkles and the undesired wrinkles or cracks induced can degrade the performance of the fabricated devices [194, 195]. Moreover, the wedging process does not permit the transfer of an array of GNP films. The peel-and-stick process, which involves the annealing of protection layers and baking of thermal release tapes, can degrade organic components within the GNP film and alter the properties of the flexible substrate due to harsh thermal conditions [119, 184, 185, 196]. Furthermore, the use of a chemical etchant limits the types of crosslinked GNP films and flexible substrates that can be selected [184, 187]. For example, GNP films can be transferred onto different substrates using a sacrificial PMMA layer [174, 193]. However, utilizing organic solvents,



such as dichloromethane and acetone, to remove the PMMA layer post-transfer can degrade chemically non-resistant substrates, and remaining PMMA residues on the GNP film can impair sensor performance after fabrication is complete [197-200]. Therefore, the development of a new method that is convenient, clean, and high-precision for GNP film transfer is of paramount importance.

1.5.2. Charge transport properties

In composite materials like the crosslinked GNP film, GNPs serve as active conductive centers, while ligands as the crosslinkers separating GNPs establish tunneling barriers for charge carriers to tunnel through. In other words, the electrical characteristics of the crosslinked GNP film are primarily determined by tunneling of charge carriers through the organic matrix, which can be explained as a thermally activated tunneling process. Based on this model, the composite materials commonly show non-metallic conduction behavior, meaning their conductivity rises when subjected to heat [201]. In 1986, Van Staveren et al. investigated the electrical transport characteristics of tiny pellets made from ligand-stabilized 55-atom gold clusters [202]. Their findings highlighted a conductivity that was temperature-dependent, showcasing a linear relationship of logarithmic conductivity ($\ln \sigma$) on $T^{-\frac{1}{2}}$. This agrees with previous studies on granular metals [203]. In subsequent studies, the electrical properties of drop-cast films from ligand-stabilized gold clusters and pellets made from alkanedithiol crosslinked GNPs composites were explored by Terrill et al. and Brust et al., respectively [170, 201]. Both research groups also observed a non-metallic conduction behavior. The temperature effect on conductivity was aptly described using a formula initially introduced by Neugebauer and Webb for metal films formed from a multitude of discrete metal islands [201, 204]. This formula, represented as equation (2), details an Arrhenius-type correlation between

conductivity (σ) and temperature (T):

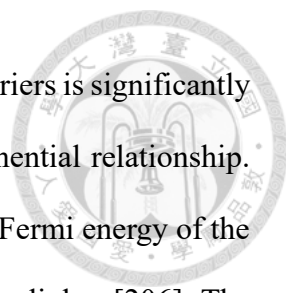
$$\sigma = \sigma_0^* \exp\left(\frac{-E_A^*}{k_b T}\right) \quad (2)$$



Here, σ_0^* stands as the preexponential factor. E_A^* is the activation energy, and k_b is the Boltzmann constant. Considering the expected decrease in electron transfer rates as the distance increases, Terrill et al. formulated an equation that incorporates an exponential tunneling term to account for the interparticle spacing, represented as δ [170]. This equation, denoted as (3), was applied in detailing the temperature-influenced conductivities of thin films that were either alkanethiol stabilized or alkanedithiol crosslinked GNPs [160, 170, 205-207]:

$$\sigma(\delta, T) = \sigma_0 \exp(-\beta\delta) \exp\left(\frac{-E_A}{k_b T}\right) \quad (3)$$

Here, β is the tunneling decay constant. The first exponential term outlines the tunneling of the electrons through the organic matrix between the GNPs [206]. The movement (i.e., tunneling probability) of the charge carriers between two GNPs largely depends on the molecular structure of the ligands/crosslinkers. For the alkanedithiol crosslinked GNP composite, the term can be presented in relation to the number of methylene units and the tunneling decay constant in reciprocal units of the methylene group count [160, 207]. The alkanedithiol crosslinkers have a number of methylene units, which are often considered to act as insulators [206]. The Fermi level of the GNP falls in the gap between the highest occupied molecular orbital (HOMO) and the lowest unoccupied molecular orbital (LUMO) of the alkanedithiol crosslinker. The side orbitals provide a superexchange



pathway for electron transfer [206]. The conductivity of the charge carriers is significantly influenced by the length of the crosslinker, showing a notable exponential relationship. In contrast, a weaker distance dependence can be observed when the Fermi energy of the GNP becomes resonant with the molecular orbital energy of the crosslinker [206]. The tunneling decay constant of the alkanedithiol crosslinked GNP film was found to be ~ 0.61 per methylene unit [160]. The result agrees well with other findings from different alkanedithiols embedded in a monothiol layer on flat gold surfaces, as studied by Lindsay et al., who reported a tunneling decay constant of ~ 0.57 [208]. Interestingly, when examining alkanethiol-capped GNPs and alkanethiol molecule monolayers on gold surfaces, the tunneling decay constant noted was considerably higher, with ~ 1.2 and ~ 0.8 per methylene unit, respectively [207, 209]. These data suggest that when GNPs are crosslinked with alkanedithiols, the conductivity of the resultant composites is enhanced. Moreover, Joseph et al. demonstrated that the conductivity strongly relies on the alkylene chain length of the crosslinker, a significant increase in conductivity, approximately an order of magnitude, is observed when the chain length of the alkanedithiol is shortened by three methylene units [160].

The second exponential term of the equation describes the above-mentioned temperature dependence [204]. E_A represents the activation energy associated with charge transport, signifying the energy required to generate charge carriers by extracting an electron from a neutral metal particle and transferring it to another neutral particle. Various theories can be utilized to characterize the corresponding E_A . Abeles et al. put forth an electrostatic perspective for granular metals [203]. The granular metal theory indicates a temperature-dependent conductivity given by $\sigma \propto \exp(-2\sqrt{\frac{C}{kT}})$, where C is equal to $\beta\delta E_A$, and E_A is associated with the following equation [203, 206]:

$$E_A = \frac{e^2}{8\pi\epsilon_r\epsilon_0} \left(\frac{1}{R_{GNP}} - \frac{1}{R_{GNP+\delta}} \right) \quad (4)$$



R_{GNP} indicates the radius of the particle. δ is the spacing between particles. ϵ_r and ϵ_0 are the relative permittivity of the organic matrix material and the vacuum permittivity, respectively. According to this equation, larger-sized GNPs are anticipated to have greater conductivity. When GNPs reach a threshold of small size, the activation barrier becomes too significant for the thermal energy to surpass, leading to an observable Coulomb blockade effect [210]. Brust et al. and Vossmeier et al. employed equation (4) to compute the E_A of alkanedithiol crosslinked GNP films. They made an assumption of an Arrhenius-type activation, as referred to in equations (2) and (3). Their findings were consistent with the experimental data [201, 211].

1.5.3. Resistive strain sensing

As captured in equation (3), under isothermal conditions, the conductivity of crosslinked GNP films is exponentially dependent on the distance δ between GNPs and the activation energy E_A for charge transport. For a GNP composite sensor with a defined geometry and an initial resistance R_0 , the relative change of R_0 due to changes of δ and E_A can be computed by the rearrangement of equation (3) to equation (5) [212, 213]:

$$\frac{\Delta R}{R_0} = \exp\left(\frac{\Delta E_A}{kT}\right) \exp(\beta\Delta\delta) - 1 \quad (5)$$

Here, ΔR represents the change in resistance. The strong dependence of the resistance of the crosslinked GNP film on the interparticle spacing makes it a valuable material for the

design of strain sensors. Herrmann et al. were among the first to develop highly sensitive strain sensors based on a GNP film [214]. They reported that the dependence of the activation energy E_A on δ can be neglected for systems with particles of a diameter ~ 10 nm and an interparticle spacing of $\delta \sim 1$ nm. Considering these parameters, the equation (5) can be simplified to equation (6):

$$\frac{\Delta R}{R_0} = \exp(\beta\Delta\delta) - 1 \quad (6)$$

ΔR is governed by the tunneling current between GNPs depending exponentially on the interparticle distance δ . Equation (6) accounts for the variation of the interparticle spacing $\Delta\delta$, which correlates with the elongation Δl of the GNP film. When stretching the GNP film in the direction of tunneling current the resulting strain is defined as $\varepsilon = \Delta l/l_0$, where l_0 is the initial length of the film. Considering the GNPs in a primitive cubic packing arrangement, l_0 can be expressed as $N(D + \delta_0)$, where N is the number of GNPs in the certain direction, D is the diameter of the GNPs, and δ_0 is the initial interparticle spacing of GNP. Thus, the elongation of the GNP film, Δl , is proportional to $N\Delta\delta$, as the ligands/crosslinkers can deform more readily than the GNPs [214]. The relevant schematic illustration is shown in **Figure 3**.

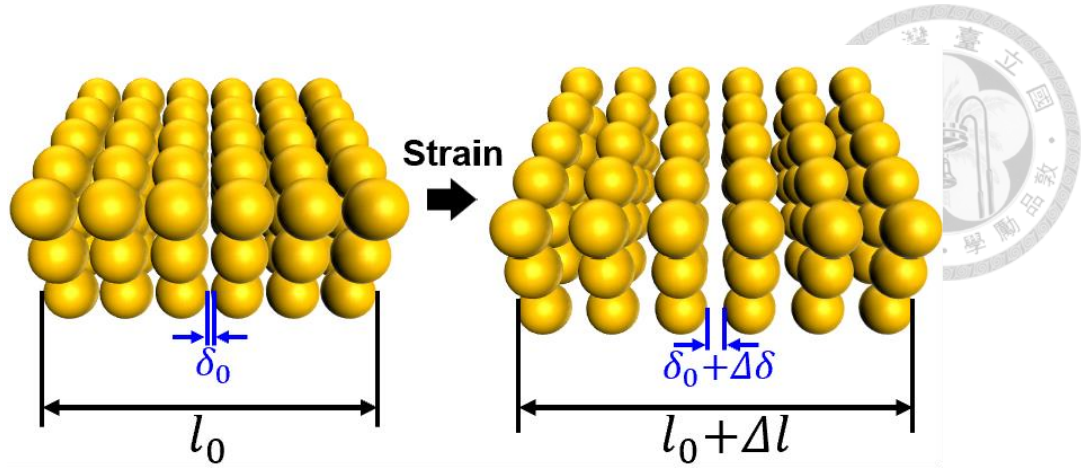


Figure 3. Tensile strain applied to the crosslinked GNP film results in expanded interparticle spacing between GNPs along the strain direction, attenuating the tunneling currents.

Based on these concepts, equation (7) correlates the change of interparticle distance with the strain applied to the material.:

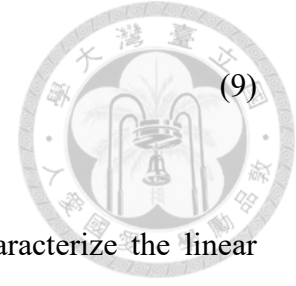
$$\Delta\delta = (D + \delta_0) \frac{\Delta l}{l_0} = (D + \delta_0) \varepsilon \quad (7)$$

Based on equation (7), equation (6) can then be represented as equation (8) [214]:

$$\frac{\Delta R}{R_0} = \exp [\beta(D + \delta_0) \varepsilon] - 1 \quad (8)$$

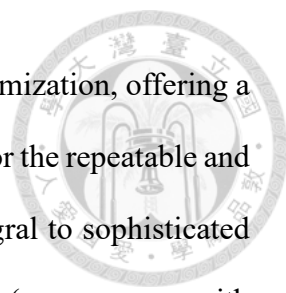
According to equation (8), the resistive behavior of the crosslinked GNP film under strain ε is predominantly non-linear, influenced by variations in both the diameter D of the GNPs and the initial interparticle spacing δ_0 . Nonetheless, for small strains, one can deduce an approximately linear response according to a first-order Maclaurin expansion of equation (8), resulting in equation (9) [214]:

$$\frac{\Delta R}{R_0} = \beta(D + \delta_0)\varepsilon = g\varepsilon \quad (9)$$



Here, $g = \beta(D + \delta_0)$, where g is the gauge factor used to characterize the linear sensitivity of resistive strain gauges. Traditional metal foil strain gauges commonly exhibit a gauge factor of ~ 2 [215]. To enhance the gauge factor of the strain gauge, Herrmann et al. proposed the use of GNP films as highly sensitive strain gauges ($g \sim 50$ -200). The experimental results closely matched the simulation using the above-presented model with a β of 10 nm^{-1} and $D + \delta_0$ of 10 nm, resulting in $g \sim 100$ [214]. However, subsequent studies of our group revealed that GNP films crosslinked with 9DT have gauge factors in the range of 10 to 25 when subjected to bending tests [211]. It is proposed that the comparatively smaller gauge factors in these cases are due to the disordered 3D arrangement of the GNP networks fabricated through a layer-by-layer spin-coating process, as confirmed by TEM images.

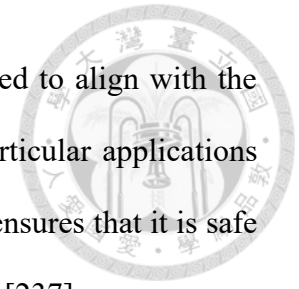
Flexible nanomaterials-based strain sensors, which transduce mechanical deformation to electrical signals, have garnered significant interest within the realm of wearable healthcare electronics, attributable to their adaptability and diverse design options [216]. These sensors represent a paradigm shift from conventional, rigid strain sensors by eliminating the interface mismatch between the transducer and human tissues, thereby enabling the detection of nuanced physiological cues and facilitating accurate assessment of deep tissues [217, 218]. A typical flexible strain sensor consists of two components: the active conductive layer and the flexible substrate [219]. Crosslinked GNP films serving as the active conductive layer have found extensive application in the fabrication of high-performance strain sensors. This is based on the advantage to precisely adjust their charge transport properties in response to parameters such as GNP size, interparticle distances, and the composition of the organic matrix [174, 212, 220, 221].



The strategic patterning of the GNP films is paramount in sensor optimization, offering a path toward the fine-tuning of sensor attributes and is indispensable for the repeatable and scalable production of intricately patterned transducers that are integral to sophisticated electronic systems [222]. For example, fractal geometry design (e.g., curves with tortuosity morphology) of the active conductive layer can enhance their mechanical performance for the burgeoning field of stretchable electronics [223]. Furthermore, patterned strain sensor arrays enable spatial resolution, thereby addressing issues stemming from the positional inaccuracies typically encountered with traditional single-point sensors, particularly in applications such as arterial sensing [224].

The flexible substrate of the strain sensor acts as a base to hold the active conductive layer in place [219]. Polydimethylsiloxane (PDMS), polyimide (PI), poly(ethylene terephthalate) (PET), and TPU are among the typically utilized flexible base materials [174, 225-228]. Yet, it is critical to select a flexible substrate with a minimal environmental impact to minimize environmental stress after the operational period of the sensor [229]. Biodegradable polymers are becoming favored alternatives for flexible substrate materials due to their natural degradability, which diminishes harmful waste and the carbon footprint [230]. For instance, the biodegradable PLA is exemplified in the fabrication of disposable sensors for wearable applications and devices for implantable biomedical use, suitable for both *in vitro* and *in vivo* environments [231, 232]. However, the fragility and high elastic modulus (~ 4 GPa) of PLA restrict its stretchability and flexibility, consequently impacting its ability to detect subtle physiological signals or large strain movements [233, 234]. By contrast, biodegradable PU films that present a significantly lower Young's modulus and higher stretchability are employed as flexible substrates for wearable strain sensors that efficiently track physiological signals and human movement across an extensive strain range [235]. Additionally, the mechanical

characteristics and degradability of biodegradable PU can be tailored to align with the features of various human tissues and the precise necessities of particular applications [119, 236]. Furthermore, the biocompatibility of biodegradable PU ensures that it is safe for long-term contact with human skin in skin-mounted applications [237].



2. Aim of the work

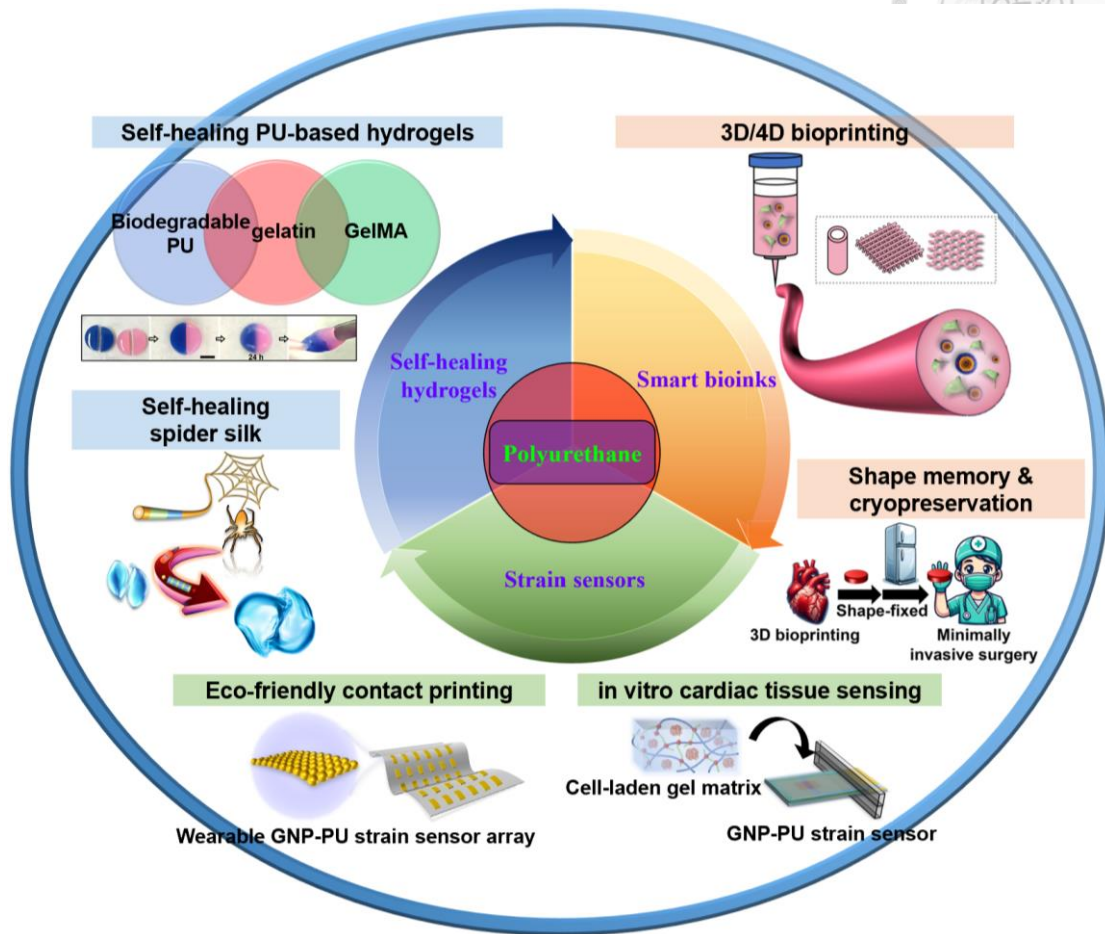
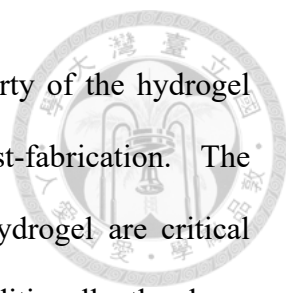


Figure 4. The research concept map of this dissertation.

The aim of my work is an interdisciplinary endeavor to address the challenges at the convergence of material science, biofabrication, flexible electronics, and tissue engineering for the advancement of healthcare applications (**Figure 4**).

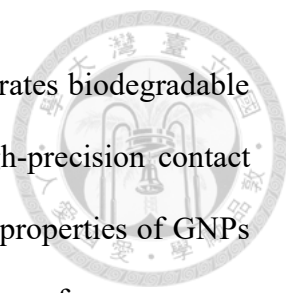
In the first project (publication 1), I developed an innovative smart hydrogel composed of biodegradable PU, gelatin, and GelMA, abbreviated as PUGG, which can serve as a bioink. This material exhibited self-healing properties that ensured the integrity of bioprinted structures, making it an ideal bioink for fabricating reliable tissue constructs. The PUGG hydrogel also showed the thermo-responsive property, allowing for high-resolution 3D bioprinting applications where precise control of the rheological behavior



of the bioink is essential. Furthermore, the photo-responsive property of the hydrogel enhanced the long-term stability of printed constructs post-fabrication. The biocompatibility and adjustable degradation rates of the PUGG hydrogel are critical features that allow for its use in various biomedical applications. Additionally, the shape memory property of the PUGG hydrogel opens the possibility for 4D bioprinting, which is beneficial for compact transportation and minimally invasive clinical procedures. The cryopreservation property of the PUGG hydrogel demonstrated that cells embedded within the matrix can proliferate effectively post-thawing, a crucial consideration for biobanking and tissue engineering applications.

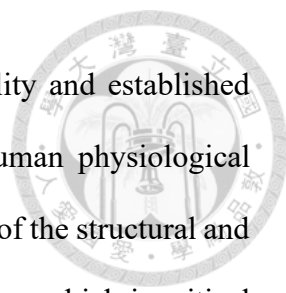
The second project (publication 2) strategically focused on the recombinant spider silk hydrogel due to its unique chemical structure, which intriguingly resembles the arrangement of PU. Biodegradable PU typically comprises alternating soft and hard segments. Similarly, spider silk consists of a repeating arrangement of alanine-rich and proline-rich motifs. This parallel segmented arrangement suggests both materials may share desirable mechanical properties like elasticity and toughness. Exploring the potential similarities between spider silk and PU could reveal new ways to leverage these traits in biomedical applications. Results showed that I achieved a discovery by identifying for the first time that the recombinant spider silk hydrogel exhibits self-healing property. To unravel the self-healing mechanism, I utilized in situ Small Angle X-ray Scattering (SAXS) technology combined with the rheometer to monitor and analyze the structural evolution during the healing process of the recombinant spider silk hydrogel. This project is not only pivotal for the advancement of recombinant spider silk applications in biomedicine but also contributes significantly to the field of material science, setting the stage for the development of self-healing biomimetic biomaterials.

In the third project (publication 3), I expanded the scope of my work into wearable



technology by developing an advanced strain sensor array that integrates biodegradable PU with crosslinked GNP films via a facile, clean, rapid, and high-precision contact printing method. This combination takes advantage of the electrical properties of GNPs and the environmental benefits of biodegradable PU to create a high-performance, eco-friendly sensor that is both sensitive to physiological signals and aligned with ecological principles. Meanwhile, the sensor is designed to be biocompatible and can be safely applied to the skin for continuous health monitoring. The significance of this work lies in the successful creation of a strain sensor array capable of detecting human pulse waveforms. This development addresses and overcomes the limitations associated with traditional single-point sensors by providing a more comprehensive and detailed monitoring system. The flexible strain sensor array allows for the acquisition of data from multiple points, offering a richer and more nuanced picture of cardiovascular health. This enhanced functionality is crucial for the precise monitoring of various physiological parameters, including pulse rate, which can be pivotal in the diagnosis and management of cardiovascular diseases. The application of the GNP-PU strain sensor array in detecting subtle changes in pulse waveforms signifies a substantial leap forward in wearable health monitoring technology, providing both patients and healthcare professionals with a powerful tool for non-invasive and continuous health assessment.

The progression of my research endeavors, beyond the development of wearable sensors in the third project, aspires to advance towards implantable sensors for diverse medical applications. However, a critical issue arose with the use of polyester-based biodegradable PU, which failed to provide adequate waterproofing at the physiological temperature of 37 °C in the cell culture medium. This deficiency led to the breakage of the GNP film. Confronted with this challenge, the fourth project pivoted to utilizing a polyether-based biocompatible PU, specifically Pellethane 2363 Series TPU. This



material was strategically chosen for its enhanced hydrolytic stability and established biocompatibility, which is indispensable for applications in the human physiological system. The adoption of this waterproof PU ensured the maintenance of the structural and functional integrity of the GNP films at the physiological temperature, which is critical for the performance of the GNP-PU strain sensor. The fabricated cantilever-based GNP-PU strain sensor exhibited the capability for *in vitro* cardiac monitoring, i.e., sensing the beating of cardiomyocyte spheroids. This application demonstrates the potential utility of the sensor as a tool for the development of *in vitro* cardiac tissue models. The aim of this project is to provide a platform that can study the dynamic behavior of cardiac tissues, offering a more accurate and ethical alternative for cardiac research, drug testing, and the future design of implantable cardiac sensors.

Overall, my work aims to integrate smart material design with biofabrication and biomedical engineering techniques to produce advanced biomaterials that are tailored for next-generation healthcare applications. The smart PUGG hydrogel marks a significant step in biofabrication with its self-healing and environmental-responsive properties, tailored for tissue engineering and biobanking. Exploring the properties of recombinant spider silk hydrogels has unveiled the self-healing ability that echoes the beneficial traits of PU, underscoring its potential for biomedical innovation. Transitioning into wearable technology, the GNP-PU strain sensor array I developed demonstrated the feasibility of PU in developing electronic devices that can monitor health in a non-invasive manner. The move towards the biocompatible cantilever-based GNP-PU strain sensor demonstrated the application for *in vitro* cardiac sensing, setting a foundation for the next generation of implantable sensors.

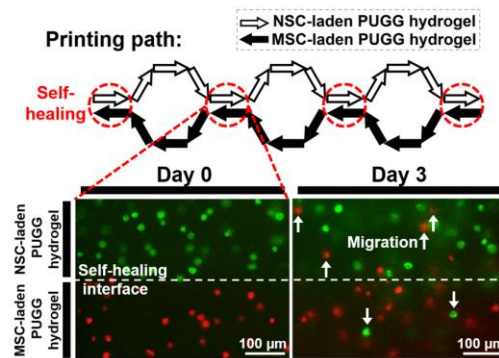
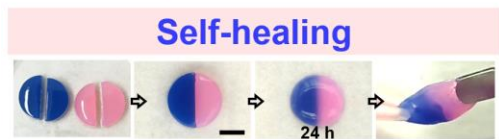
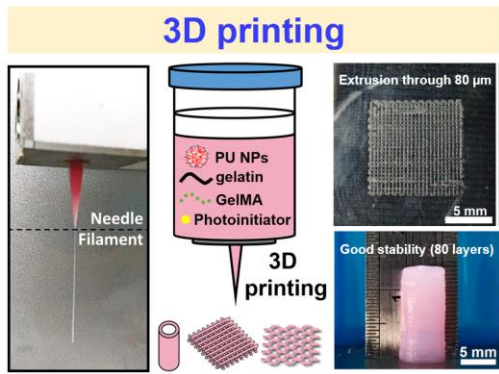
3. Cumulative part of the dissertation

Each publication is interconnected to present a central theme, which has already been described in the “2. Aim of the work” section.

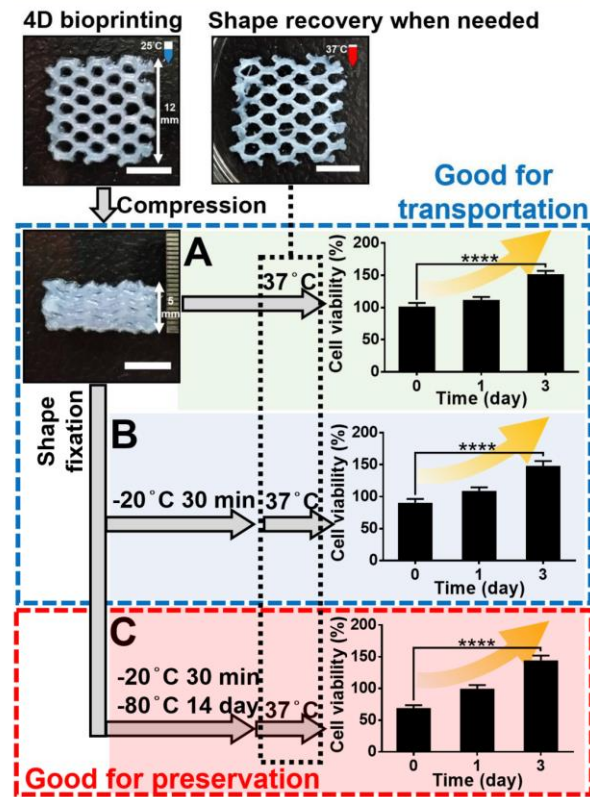


3.1. Publication 1 (first project): 4D bioprintable self-healing hydrogel with shape memory and cryopreserving properties

Reprinted from “Shin-Da Wu and Shan-hui Hsu. 4D Bioprintable Self-Healing Hydrogel with Shape Memory and Cryopreserving Properties. *Biofabrication* **2021**; 13: 045029.” with permission from IOP Publishing Ltd. The corresponding supporting information is available at the following digital object identifier (DOI): <https://doi.org/10.1088/1758-5090/ac2789>



Shape memory & cryopreserving properties





ACCEPTED MANUSCRIPT

4D bioprintable self-healing hydrogel with shape memory and cryopreserving properties

To cite this article before publication: Shin-Da Wu *et al* 2021 *Biofabrication* in press <https://doi.org/10.1088/1758-5090/ac2789>

Manuscript version: Accepted Manuscript

Accepted Manuscript is "the version of the article accepted for publication including all changes made as a result of the peer review process, and which may also include the addition to the article by IOP Publishing of a header, an article ID, a cover sheet and/or an 'Accepted Manuscript' watermark, but excluding any other editing, typesetting or other changes made by IOP Publishing and/or its licensors"

This Accepted Manuscript is © 2021 IOP Publishing Ltd.

During the embargo period (the 12 month period from the publication of the Version of Record of this article), the Accepted Manuscript is fully protected by copyright and cannot be reused or reposted elsewhere.

As the Version of Record of this article is going to be / has been published on a subscription basis, this Accepted Manuscript is available for reuse under a CC BY-NC-ND 3.0 licence after the 12 month embargo period.

After the embargo period, everyone is permitted to use copy and redistribute this article for non-commercial purposes only, provided that they adhere to all the terms of the licence <https://creativecommons.org/licenses/by-nc-nd/3.0>

Although reasonable endeavours have been taken to obtain all necessary permissions from third parties to include their copyrighted content within this article, their full citation and copyright line may not be present in this Accepted Manuscript version. Before using any content from this article, please refer to the Version of Record on IOPscience once published for full citation and copyright details, as permissions will likely be required. All third party content is fully copyright protected, unless specifically stated otherwise in the figure caption in the Version of Record.

View the [article online](#) for updates and enhancements.



1
2
3
4
5
6
7
8
9
10
11
12
13
14
15
16
17
18
19
20
21
22
23
24
25
26
27
28
29
30
31
32
33
34
35
36
37
38
39
40
41
42
43
44
45
46
47
48
49
50
51
52
53
54
55
56
57
58
59
60

**4D Bioprintable Self-healing Hydrogel with Shape Memory and
Cryopreserving Properties**

Shin-Da Wu¹ and Shan-hui Hsu^{1,2,*}

¹Institute of Polymer Science and Engineering, National Taiwan University, No. 1, Sec.

4 Roosevelt Road, Taipei 10617, Taiwan, Republic of China

²Institute of Cellular and System Medicine, National Health Research Institutes, Miaoli,

Taiwan Republic of China

* Corresponding author: Shan-hui Hsu

Institute of Polymer Science and Engineering, National Taiwan University, No. 1, Sec.

4 Roosevelt Road, Taipei 10617, Taiwan, Republic of China;

Phone: +886-2-3366-5313;

Fax: +886-2-3366-5237;

E-mail: shhsu@ntu.edu.tw

Accepted Manuscript

Abstract

Four-dimensional (4D) bioprinting is an emerging biofabrication technology that integrates time as a fourth dimension with 3D bioprinting for fabricating customizable tissue-engineered implants. 4D bioprinted implants are expected to possess self-healing and shape memory properties for new application opportunities, for instance, fabrication of devices with good shape integrity for minimally invasive surgery. Herein, we developed a self-healing hydrogel composed of biodegradable polyurethane (PU) nanoparticles and photo-/thermo-responsive gelatin-based biomaterials. The self-healing property of hydrogel may be associated with the formation of reversible ionic interaction between the COO^- group of PU nanoparticles and NH_3^+ group on the gelatin chains. The self-healing hydrogel demonstrated excellent 3D printability and filament resolution. The UV-crosslinked printed hydrogel showed good stackability (> 80 layers), structural stability, elasticity, and tunable modulus (1–60 kPa). The shape-memorizable 4D printed constructs revealed good shape fixity (~ 95%) and shape recovery (~ 98%) through the elasticity as well as forming and collapsing of water lattice in the hydrogel. The hydrogel and the printing process supported the continuous proliferation of neural stem cells (~ 3.7-fold after 14 days). Moreover, the individually bioprinted neural stem cells and mesenchymal stem cells in the adjacent, self-healed filaments showed mutual migration and such interaction promoted the cell differentiation behavior. The cryopreserved ($-20\text{ }^\circ\text{C}$ or $-80\text{ }^\circ\text{C}$) 4D bioprinted hydrogel after awakening and shape recovery at $37\text{ }^\circ\text{C}$ demonstrated cell proliferation similar to that of the non-cryopreserved control. This 4D bioprintable, self-healable hydrogel with shape memory and cryopreserving properties may be employed for customized biofabrication.



1
2
3
4
5
6
7
8
9
10
11
12
13
14
15
16
17
18
19
20
21
22
23
24
25
26
27
28
29
30
31
32
33
34
35
36
37
38
39
40
41
42
43
44
45
46
47
48
49
50
51
52
53
54
55
56
57
58
59
60

Keywords: 4D bioprinting, biodegradable polyurethane, self-healing, shape memory, cryopreservation

Accepted Manuscript

1
2
3
4
5
6
7
8
9
10
11
12
13
14
15
16
17
18
19
20
21
22
23
24
25
26
27
28
29
30
31
32
33
34
35
36
37
38
39
40
41
42
43
44
45
46
47
48
49
50
51
52
53
54
55
56
57
58
59
60

1. Introduction

Three-dimensional (3D) bioprinting is a promising biofabrication technology for making customizable tissue-engineered implants [1]. In 3D bioprinting, cells are mixed with hydrogel materials of high water contents that mimic the extracellular matrix of a real tissue. Hydrogel used as bioink must be biocompatible and possess suitable rheological properties and good interlayer adhesion for printing; besides, they should have tunable degradation rates and mechanical properties to meet the properties of different tissues as well as cryopreservable properties in order for long-term storage and transportation [2-4]. Gelatin is a naturally-derived thermo-responsive hydrogel and widely used for bioprinting because of its excellent biocompatibility and low immunogenicity as well as the ability to promote cell attachment and remodeling [5]. Gelatin forms a gel at temperatures lower than $\sim 27^\circ\text{C}$ but melts at the physiological temperature. Gelatin methacryloyl (GelMA) undergoes rapid crosslinking under UV exposure and is one of the most popular bioink [6], but GelMA bioinks suffer from poor processability at lower concentrations (i.e., $\leq 5\%$ w/v) [7]. To enhance the processability and shape fidelity, GelMA was mixed with gelatin and crosslinked to obtain proper rheology from reversible thermo-responsive gelatin as well as shape stability from irreversible photo-responsive GelMA [8]. However, the GelMA-based hydrogels degraded rather quickly (with $\sim 80\%$ degradation in PBS buffer at 28 days)

1
2
3
4
5
6
7
8
9
10
11
12
13
14
15
16
17
18
19
20
21
22
23
24
25
26
27
28
29
30
31
32
33
34
35
36
37
38
39
40
41
42
43
44
45
46
47
48
49
50
51
52
53
54
55
56
57
58
59
60

[9]. Biodegradable polyurethanes (PUs) are a family of tough synthetic elastomers with tunable degradation rates and mechanical properties, and are commonly used in biomedical applications [10]. Hydrogels from the mixture of biodegradable polyurethane nanoparticles (PU NPs) and gelatin can possess a range of degradation time for 3D bioprinting of various tissues [11], but need to be post-fixed by divalent cations. Meanwhile, the printed hydrogel constructs may delaminate upon large deformation due to the lack of interlayer adhesiveness.

One of the approaches to increase the interlayer adhesion is to use self-healing materials for 3D printing. Self-healing materials have the ability to repair structural damage and restore the original functions [12]. Intrinsic self-healing hydrogels as bioink may reassemble automatically via dynamic reversible interaction after extrusion through the nozzle and deposition onto the platform [13]. Interlayer adhesion was achieved by the self-healing properties of the printed constructs between “weld lines” to improve structural integrity [14, 15]. This advantage makes self-healing hydrogels possible to fabricate more durable products for numerous applications such as biomedicine, tissue therapies, and flexible electronics [16]. Moreover, 3D bioprintable self-healing hydrogel can be used to fabricate modular heterogeneous structures from assembly of the individually printed constructs [17]. 3D bioprintable self-healing hydrogels, however, face several challenges such as printing resolution, stackability,

1
2
3
4 and shape stability [18]. Self-healing hydrogels for 3D bioprinting have difficulty in
5
6
7 passing through nozzles smaller than 200 μm because they quickly self-heal and lack
8
9
10 self-supporting ability [19-22]. A self-healing hydrogel composed of biodegradable PU
11
12
13 NPs and chitosan demonstrated intrinsic self-healing properties and injectability [23],
14
15
16 but was not printable due to insufficient self-supporting ability and poor stackability.
17
18
19 Self-healing hydrogels can be printed into support materials to maintain the desired
20
21
22 shape [24], but a post-processing step after printing is needed for removing the support
23
24
25 materials. A few printable self-healing hydrogels have sufficient self-supporting ability
26
27
28 and do not require support materials during printing, but a secondary crosslinking (e.g.
29
30
31 UV exposure) is still needed to stabilize the construct after printing [16, 25, 26].
32
33
34 Meanwhile, there is still room for improvement in shape fidelity, stackability, and
35
36
37 elasticity of the self-healing hydrogel.

38
39
40 3D bioprinting considers only the initial state of the printed object and assumes it
41
42
43 to be static and inanimate [27]. However, the dynamic functional and conformational
44
45
46 changes as well as the sophisticated 3D structures of native tissues cannot be fully
47
48
49 mimicked through 3D bioprinting [28]. Four-dimensional (4D) bioprinting is an
50
51
52 emerging biofabrication technology that integrates time as a fourth dimension with 3D
53
54
55 bioprinting, where the bioprinted constructs are able to change the shapes or
56
57
58 functionalities with time when an external stimulus is imposed [27, 29]. Shape memory
59
60



1
2
3
4
5
6
7
8
9
10
11
12
13
14
15
16
17
18
19
20
21
22
23
24
25
26
27
28
29
30
31
32
33
34
35
36
37
38
39
40
41
42
43
44
45
46
47
48
49
50
51
52
53
54
55
56
57
58
59
60

materials that vary their shape in response to environmental changes are commonly used for 4D bioprinting [30]. 4D bioprintable material with shape memory property is utilized to fabricate the stimulus-responsive dynamic construct corresponding to physiological activities, which enables mimicking the complex geometry of natural tissues and compacting the size for minimally invasive surgery [31]. For example, the GelMA-based hydrogels were printed and morphed into tubular constructs to mimic vascularized skeletal muscle tissue, but the folded constructs did not have sufficient structural integrity to prevent blood leakage [32]. The PU-based hydrogels with shape memory properties were printed, shape-fixed, and employed in minimally invasive surgery for bone tissue engineering [33], but the constructs may delaminate upon significant deformation due to the absence of adhesion between layers. To increase the structural integrity and interlayer adhesion of the printed constructs, self-healing properties are highly desired for 4D bioprintable hydrogels [16, 34]. For instance, the vessel fabricated by 4D printable self-healing material demonstrated rapid reconnection at the cut position, regained blood circulation, and showed high-strain affordability [35]. In addition, the stimulus-responsive conditions of shape memory hydrogels are critical for cell survival and proliferation in 4D bioprinting. For instance, cells are sensitive to the temperature variation of the surroundings [4]. Therefore, the temperature setting during printing and preservation of the cell-laden constructs before the clinical use is

1
2
3
4 important.

5
6
7 Bioprinted functional implants for fundamental research and clinical therapies
8
9
10 may face the difficulty in worldwide conveyance due to in situ biofabrication and
11
12 hierarchical complexity [36, 37]. Cryopreservation of the biofabricated implants is a
13
14 solution to escape in situ manufacturing and long-term cell maturation process because
15
16 cryopreservation technology allows the ready-to-use storage in biobanks and on-
17
18 demand transportation for fulfilling international standards [38]. Recent researches
19
20 demonstrated the possibility of cryopreservation of the 3D bioprinted constructs [39,
21
22 40]. In 4D bioprinting, the cryopreserved shape memory hydrogel may provide a
23
24 protective surrounding for cells and be fixed to a minimized size when the
25
26 cryopreservation temperature matches the stimulus-responsive conditions of the
27
28 hydrogel [41]. The small volume of the shape-fixed hydrogels is conducive to
29
30 transportation, storage, and minimally invasive surgery. Furthermore, the 4D
31
32 bioprintable and cryopreservable hydrogels with self-healing properties may possess
33
34 greater structural integrity and reliability for better long-term storage and manipulation
35
36 [37]. Herein, we design the combination of gelatin, GelMA, and PU nanoparticles to
37
38 formulate an elastic multi-intelligent (thermo-responsive, photo-responsive, self-
39
40 healing, and shape-memorizable) hybrid bioink that is successfully employed in 4D
41
42 bioprinting with good printability (shear thinning), resolution (80 μm nozzle), and
43
44
45
46
47
48
49
50
51
52
53
54
55
56
57
58
59
60



1
2
3
4 stackability (> 80 layers). The shape-fixed cell-laden constructs after cryopreservation
5
6
7 (-20 °C or -80 °C) and shape recovery are examined to highlight the potential for
8
9
10 storage of the 4D printed constructs until use on-demand in tissue engineering and
11
12
13 regenerative medicine applications.
14
15
16
17
18
19

20 **2. Materials and Methods**

21 **2.1. Synthesis of waterborne biodegradable PU dispersion**

22
23
24
25
26 The detailed synthetic procedure has been described previously [42]. Briefly, the
27
28
29 waterborne biodegradable PU dispersion had the soft segment composed of two
30
31
32 different oligodiols, polycaprolactone (PCL) diol ($M_n \sim 2000$ Da, Sigma-Aldrich, USA)
33
34
35 and poly(D,L-lactide) (PDLLA) diol ($M_n \sim 1500$ Da), in 4:1 molar ratio. PCL diol and
36
37
38 PDLLA diol were reacted with isophorone diisocyanate (IPDI, Evonik Degussa GmbH,
39
40
41 Germany) for 3 h in the presence of 0.03% tin(II) 2-ethylhexanoate (T-9, Alfa Aesar)
42
43
44 as the catalyst. After pre-polymerization, 2,2-bis(hydroxymethyl)propionic acid
45
46
47 (DMPA, Sigma) and methyl ethyl ketone (MEK, J. T. Baker, Phillipsburg, USA) were
48
49
50 added to the reactor under reflux. After 1 h, the reaction temperature was cooled down
51
52
53 to 50 °C and triethylamine (TEA, R.D.H., USA) was dripped to neutralize the
54
55
56 carboxylic group of DMPA for 30 min. Subsequently, deionized water was quickly
57
58
59 added to the reactor with vigorous stirring (1100 rpm) for 2 min. Finally, the chain
60

1
2
3
4 extender ethylenediamine (EDA, Tedia) was added to complete the reaction. The molar
5
6
7 ratio of IPDI/oligodiols/DMPA/EDA/TEA was 3.52:1:1:1.52:1 [10]. Residual solvents,
8
9
10 MEK and TEA, were removed by vacuum distillation under reduced pressure.
11
12
13
14
15

16 **2.2. Preparation and characterization of GelMA**

17
18
19 The experimental procedure for GelMA synthesis followed earlier literature [43].
20
21
22 In short, 10% (w/v) gelatin solution (Porcine skin, Type A, 300 bloom) was dissolved
23
24
25 in 0.25 M carbonate-bicarbonate buffer, and the pH was 9. Subsequently, methacrylic
26
27
28 anhydride (MAA, Sigma-Aldrich) was added to the gelatin solution under vigorous
29
30
31 stirring (500 rpm) at 45 °C and allowed to react for 1.5 h. The solution was adjusted to
32
33
34 pH 7.4 to stop the reaction and dialyzed with a dialysis tubing (12–14 kDa cutoff
35
36
37 membranes) at an ambient temperature of 40 °C. After dialysis for 5 days, the solution
38
39
40 was filtered through a membrane filter (0.22 µm pore diameter) and lyophilized to
41
42
43 obtain GelMA product. The sample was stored at –20 °C until further use.
44
45

46
47 The degree of functionalization (DoF) was determined by quantifying the
48
49 concentration of residual free amine groups using ninhydrin assay as previously
50
51 described in the synthesized GelMA relative to gelatin [44]. The corresponding value
52
53
54 of GelMA absorbance on the gelatin standard curve was recorded (X) to obtain the DoF
55
56
57 (100%–X). The characterization of GelMA was measured by ¹H-NMR [45]. GelMA
58
59
60

1
2
3
4
5
6
7
8
9
10
11
12
13
14
15
16
17
18
19
20
21
22
23
24
25
26
27
28
29
30
31
32
33
34
35
36
37
38
39
40
41
42
43
44
45
46
47
48
49
50
51
52
53
54
55
56
57
58
59
60

was first dissolved in 99.9 atom % deuterium oxide (D_2O) and the proton resonance signal of H_2O at 4.7 ppm was used as the internal standard. The 1H -NMR spectra were rescaled by normalization to the signal value of the internal standard with water suppression.

2.3. Preparation and characterization of self-healing PUGG hydrogel

The PUGG hydrogel consisted of PU dispersion, gelatin, and GelMA. The ingredients were completely dissolved in the low glucose Dulbecco's modified Eagle's medium (LG-DMEM, Gibco, USA) with 1% sodium bicarbonate (Sigma-Aldrich) at 37 °C, and the photoinitiator 2,2'-azobis[2-methyl-n-(2-hydroxyethyl)propionamide] (VA-086, Wako Chemicals Co., Ltd.) was then added to the prepolymer solution at 1.5 w/v % of total solid content. The weight percentage of PU, gelatin, GelMA, and VA-086 in the mixture was 12%, 3%, 4%, and 0.285%, respectively. The photocrosslinkable PUGG hydrogel was irradiated by UV light (5W, 365 nm) for 1 min at 4 °C. The irradiation distance was 2.6 cm between the sample and the UV lamp.

To demonstrate the self-healing properties of PUGG hydrogel, the pre-UV and post-UV PUGG hydrogels were cut into two pieces by a sharp blade and then kept in physical contact together without external intervention at 4 or 25 °C to test if they formed a united construct. The morphology of PU nanoparticles, gelatin, and GelMA

1
2
3
4 in the pre-UV PUGG hydrogel was examined by transmission electron microscopy
5
6
7 (TEM) (JEM-1200EX II, JEOL, Tokyo, Japan) using 120 kV electron beam. The
8
9
10 hydrogel was diluted to a concentration of 2500 ppm with distilled water, stained with
11
12
13 phosphotungstic acid for 1 min, and cast on a copper grid before the examination. In
14
15
16 addition, the microstructures of PU suspension, PU/gelatin mixture, and pre-UV PUGG
17
18
19 hydrogel in water and in cell culture medium at 25 °C were investigated by the small
20
21
22 angle X-ray scattering (SAXS) measurements using the coherent X-ray at the beamline
23
24
25 25A1 of the National Synchrotron Radiation Research Center (NSRRC) at Hsinchu,
26
27
28 Taiwan.

29
30
31 The dynamic compressive moduli of UV-crosslinked PUGG hydrogel were
32
33
34 measured by a dynamic mechanical analyzer (DMA, Q-800, TA, USA) at a
35
36
37 compressive strain of 1% and a frequency of 1 Hz. The measurements were conducted
38
39
40 at 20 °C and 37 °C in order to demonstrate the hydrogel characteristics at room
41
42
43 temperature and human physiological condition, respectively. The elasticity of UV-
44
45
46 crosslinked PUGG hydrogel was analyzed through the cyclic loading/unloading test
47
48
49 with lateral compression in 20–40% strain. For the latter test, the hydrogel was
50
51
52 preloaded to a compressive force of 0.01 N.

53 54 55 56 57 58 **2.4. Rheological properties of self-healing PUGG hydrogel** 59 60



1
2
3
4 For rheological evaluation, the dynamic phase transition behavior of self-healing
5
6 PUGG hydrogel was measured with a rheometer (HR-2, TA Instrument, New Castle,
7
8 DE, USA). All measurements were performed on the cone plate (40 mm diameter) with
9
10
11
12
13 2° angle in this study. The setting temperatures were 25 °C and 4 °C to demonstrate the
14
15
16
17
18
19
20
21
22
23
24
25
26
27
28
29
30
31
32
33
34
35
36
37
38
39
40
41
42
43
44
45
46
47
48
49
50
51
52
53
54
55
56
57
58
59
60

For rheological evaluation, the dynamic phase transition behavior of self-healing PUGG hydrogel was measured with a rheometer (HR-2, TA Instrument, New Castle, DE, USA). All measurements were performed on the cone plate (40 mm diameter) with 2° angle in this study. The setting temperatures were 25 °C and 4 °C to demonstrate the rheology of hydrogel when extruded through the nozzle and when deposited onto the platform, respectively. For time-dependent measurement, the storage (G') and loss (G'') moduli of pre-UV and post-UV PUGG hydrogels were measured against time with an oscillatory strain of 1% and a frequency of 1 Hz. In strain-dependent measurement, the shear moduli of pre-UV and post-UV PUGG hydrogels were measured against different strains (1–500%) at 1 Hz to obtain the critical strain value for the gel-to-sol transition to occur. The self-healing properties of pre-UV and post-UV PUGG hydrogels were evaluated by switching the amplitude of oscillatory strain (damaging-healing cycles). Structure destruction was measured at a strain greater than the critical strain for 5 min and structure recovery was evaluated by reducing strain to the initial small strain for 5 min. Continuous step changes of oscillatory strain are between the small strain (1%) and the subsequent larger strain under 1 Hz. For the temperature sweep tests, temperature was set at 4 °C for 1200 s prior to the measurement. The tests were performed before UV exposure with an oscillation temperature ramp from 4 to 32 °C in a rate of 0.2 °C per minute, at the constant strain of 1% and angular frequency of 1

1
2
3
4 Hz. The shear-thinning properties of pre-UV PUGG hydrogel were investigated by a
5
6
7 steady shear experiment at 25 °C. The steady shear viscosity of the PUGG hydrogel
8
9
10 was determined against the increase in the strain rate (0.1–1000 s⁻¹).
11
12
13
14
15

16 **2.5. 3D printing of self-healing PUGG hydrogel**

17
18
19 The self-healing PUGG hydrogel was loaded into a cylindrical syringe as the
20
21 bioink and extruded through two different nozzles (80 μm needle-like nozzle and 160
22
23 μm cone-like nozzle) for printing by a commercial 3D bioprinter (Regenovo, Bio-
24
25 Printer-WS, China). The printing pressure was 45 kPa and the printing velocity was 4
26
27 mm/s at 25 °C. The PUGG bioink was printed as mesh-like, hollow cylindrical, sheet-
28
29 like, flower, and honeycomb constructs with the temperature of the printing stage at 4
30
31 °C. The printed PUGG constructs were exposed to the UV light for 1 min. The internal
32
33 structure of the printed mesh-like PUGG construct (cross-section) was examined by
34
35 SEM (Hitachi TM3000, Japan) operated in 3 kV. The construct was freeze-dried at –50
36
37 °C for 48 h and coated with platinum prior to the SEM observation.
38
39
40
41
42
43
44
45
46
47
48
49
50
51

52 **2.6. Shape memory property of the printed PUGG hydrogel**

53
54 The shape memory property of printed sheet-like PUGG constructs (7 layers) was
55
56 evaluated by the U-bending test and twisting test. The UV-crosslinked constructs were
57
58
59
60



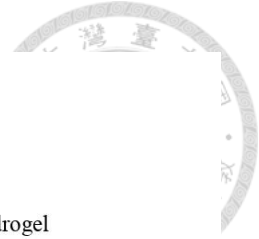
1
2
3
4 placed in 25 °C water for 15 min before the test. The constructs were then removed
5
6
7 from water and bent into the U-shape (0 degrees to 180 degrees) or twisted into the
8
9
10 helical shape at 25 °C. Subsequently, the constructs were placed in a -20 °C refrigerator
11
12
13 for 15 min to fix the shape. To recover the shape, the deformed constructs were quickly
14
15
16 transferred to 37 °C water. The shape memory performance of the U-bent construct was
17
18
19 quantified by the shape fixity ratio S_f and shape recovery ratio S_r using the following
20
21
22 equations. $S_f = [\theta_f/180] \times 100$ (%) and $S_r = [(\theta_f - \theta_r)/\theta_f] \times 100$ (%), where θ_f is the fixed
23
24
25 angle at unloading state and θ_r is the recovery angle at 37 °C [33]. On the other hand,
26
27
28 the shape memory performance of the printed flower (4-layer) and honeycomb (4-layer)
29
30
31 PUGG constructs was assessed under load-free and constrained conditions with the
32
33
34 same operating temperature. The shape fixity ratio H_f and shape recovery ratio H_r of
35
36
37 the honeycomb construct was quantified by the following equations: $H_f = [L_r/L_t] \times 100$
38
39
40 (%), where L_t and L_r are the target compressed length and the actual compressed length
41
42
43 of the construct, respectively; and $H_r = [L_r/L_o] \times 100$ (%), where L_o and L_r are the
44
45
46 original length and the recovered length of the construct, respectively.
47
48
49
50
51

52 **2.7. Cell viability and proliferation in printed PUGG hydrogel**

53
54
55 Mouse neural stem cells (NSCs) and human induced pluripotent stem cell-derived
56
57
58 mesenchymal stem cells (MSCs) were used in this study. NSCs derived from adult
59
60

1
2
3
4 mouse brain were cultured in high glucose DMEM and Ham's F-12 (1:1) (Gibco, USA)
5
6
7 with 3.7 g/L sodium bicarbonate (NaHCO₃, Sigma), 10% fetal bovine serum (FBS,
8
9
10 Caisson), 400 mg/ml G418 (Invitrogen), and 1% penicillin–streptomycin (Caisson) in
11
12
13 a 5% CO₂ incubator at 37°C [46]. Human induced pluripotent stem cells were derived
14
15
16 from human umbilical vein endothelial cells (Bioresource Collection and Research
17
18
19 Center, Hsinchu, Taiwan) transfected through lentiviral induction with Sox 2 and Oct
20
21
22 4 as previously reported [47]. The induced pluripotent stem cells were further
23
24
25 differentiated into MSCs by replacing the culture medium with the MSC culture
26
27
28 medium. MSCs were cultured in low glucose DMEM with 3.7 g/L sodium bicarbonate,
29
30
31 10% FBS, 1% L-glutamine (Gibco, USA), and 1% penicillin–streptomycin in the
32
33
34 incubator. All culture media were refreshed every 2 days.
35
36

37
38 To evaluate the immediate cell viability in the self-healing PUGG hydrogel, NSCs
39
40 with a density of 3×10^6 cells per mL were mixed with the cell culture medium, pristine
41
42
43 PU hydrogel, or pre-UV PUGG hydrogel. The viability of NSCs was determined by
44
45
46 staining with Solution 5, which contained 1.2 µg/mL acridine orange (AO) and 500
47
48
49 µg/mL propidium iodide (PI) [48]. AO stains nucleated living cells to generate green
50
51
52 fluorescence and PI stains dead cells to generate red fluorescence. After staining, cells
53
54
55 were examined by an inverted Leica (DM IRB) fluorescence microscope. The cell
56
57
58 viability was evaluated by counting the number of live cells and dead cells.
59
60

1
2
3
4
5
6
7
8
9
10
11
12
13
14
15
16
17
18
19
20
21
22
23
24
25
26
27
28
29
30
31
32
33
34
35
36
37
38
39
40
41
42
43
44
45
46
47
48
49
50
51
52
53
54
55
56
57
58
59
60

The long-term cell proliferation in the 3D printed self-healing PUGG hydrogel was evaluated by the CCK-8 (Sigma-Aldrich) assay [49]. The self-healing PUGG hydrogel was mixed with NSCs (density 5×10^5 cells per mL) as the cell-laden bioink. After 3D bioprinting, the printed cell-laden bioink was exposed to UV light for 1 min and cultured in the incubator. The culture media were refreshed every other day. At 0, 3, 7, and 14 days, all samples were washed and immersed with the mixture of CCK-8 reagent and cell culture medium in 1:9 at 37 °C for 2 h. Supernatants were then taken in 96-well plates and measured by a microplate reader (SpectraMax M5, Molecular Devices) at absorbance 450 nm. The absorbance was deducted from that of a blank control (same construct but without NSCs) and normalized to the initial absorbance at day 0 (4 h after bioprinting).

2.8. Interaction of NSCs and MSCs in bioprinted PUGG hydrogel

NSCs and MSCs were respectively labeled with green PKH67 and red PKH26 fluorescent dyes (Sigma-Aldrich). The PUGG hydrogels were individually printed and interlaid as the contacting filaments in the honeycomb pattern. Cell migration across the self-healed border of the honeycomb filaments was examined by the fluorescence microscope. After the bioprinted NSC-/MSC-laden PUGG hydrogels were cultured for 3 days, the gene expression of NSCs was investigated by quantitative real-time reverse

1
2
3
4 transcription polymerase chain reaction (qRT-PCR). The cell-laden hydrogels were
5
6
7 harvested by 0.25% trypsin (Sigma) and Trizol reagent (Invitrogen, USA). The
8
9
10 expressions of marker genes including nestin (neural stemness), Tubb3 (neuronal
11
12 marker), and glial fibrillary acidic protein (GFAP, astrocyte marker) were analyzed by
13
14
15 DyNAmo Flash SYBR Green qPCR Kit (Finnzymes Oy, Espoo, Finland). The
16
17
18 expression level of each neural-related gene was normalized to that of glyceraldehyde
19
20
21 3-phosphate dehydrogenase (GAPDH) and then presented as the relative ratio to the
22
23
24 group of NSCs on tissue culture polystyrene (TCPS).

2.9. Cryopreserving properties of bioprinted PUGG hydrogel

31
32
33
34 The mixture of 7% (v/v) dimethyl sulphoxide (DMSO; Sigma) and 93% (v/v) cell
35
36
37 growth culture medium was used as the cell cryopreservation agent. The bioprinted
38
39
40 MSC-laden PUGG honeycomb-shaped construct was immersed in the cell
41
42
43 cryopreservation agent for 20 min at 4 °C. Subsequently, the hydrogels were laterally
44
45
46 compressed, shape fixed, and maintained at one of the conditions: 37 °C; -20 °C for 30
47
48
49 min; -20 °C for 30 min and -80 °C for 3 days; or -20 °C for 30 min and -80 °C for 14
50
51
52 days. After rapid thawing at 37 °C, cell proliferation in the shape-recovered constructs
53
54
55 was evaluated by the CCK-8 assay as previously described.
56
57
58
59
60

1
2
3
4
5
6
7
8
9
10
11
12
13
14
15
16
17
18
19
20
21
22
23
24
25
26
27
28
29
30
31
32
33
34
35
36
37
38
39
40
41
42
43
44
45
46
47
48
49
50
51
52
53
54
55
56
57
58
59
60

2.10. Statistical analysis

All experiments were reproduced independently three times and quantitative values were presented as mean \pm standard deviation. The statistical variances among the experimental groups were performed with the Student's t-test. Results were considered statistically significant when p values were < 0.05 .

3. Results and Discussion

3.1. Synthesis of PUGG hydrogel

The PUGG hydrogel was prepared from mixing waterborne PU, gelatin, and GelMA in culture medium (Figure 1). The PU was synthesized with the soft segment containing two oligodiols, i.e. PCL diol and PDLLA diol, in 4 :1 molar ratio. The photocrosslinkable GelMA was prepared from the reaction of gelatin and MAA. ^1H NMR spectroscopy confirmed the functionalization of GelMA (Figure S1). The degree of substitution in GelMA was 93.3% based on the ninhydrin assay (Figure S2). One of the optimized contents of the hydrogel contained 12 wt % of PU, 3 wt % of gelatin, and 4 wt % of GelMA. The components were dissolved in cell culture medium (LG-DMEM) to prepare the hydrogel.

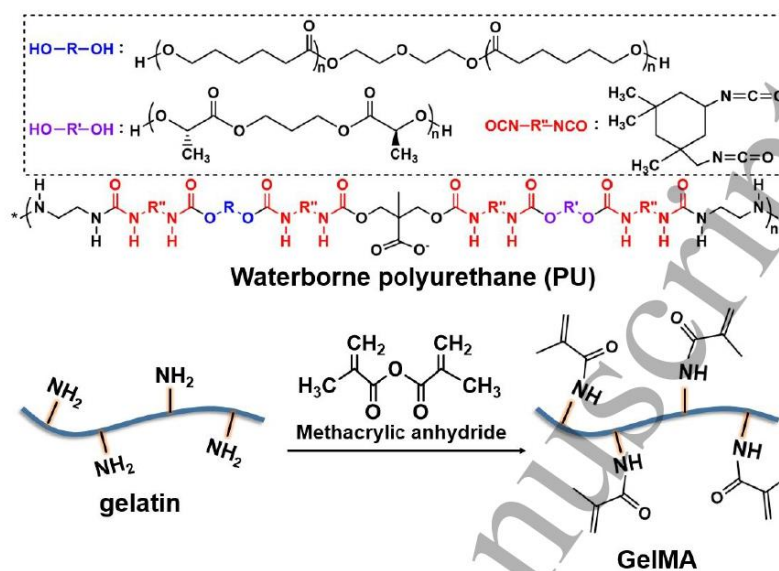
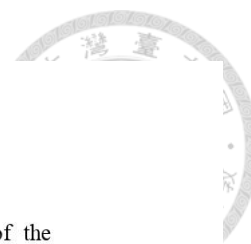


Figure 1. Chemical structures of the three components (i.e., PU, gelatin, and GelMA) in the PUGG hydrogel.

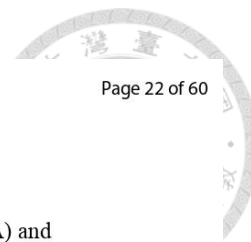
3.2. Self-healing property of PUGG hydrogel

The macroscopic self-healing behavior of the PUGG hydrogel is demonstrated in Figure 2 (A, B). The original hydrogel sample, when cut into two halves and kept in physical contact, was healed after 24 h at 25 °C. Healing of the two separate pieces was verified by the ability of the integrated sample to support the weight and to swing without being broken (Movie S1). The PUGG hydrogel showed self-healing ability either before or after UV exposure. Besides, the self-healed hydrogel was not split by



1
2
3
4 stretching with a pair of tweezers (Movie S2). Although the boundaries of the
5
6 differently colored pieces became obscured gradually, the two pieces did not turn into
7
8 a mingled color even after 24 h. Based on the observation, we proposed that self-healing
9
10 occurred only near the interface of the hydrogel.
11
12

13
14
15 The rheological properties of the PUGG hydrogel are shown in Figure 2 (C-H).
16
17 The G' value of the hydrogel at equilibrium was ~ 120 Pa without UV exposure (Figure
18
19 2C). After the hydrogel was cured by UV exposure for 1 min, the G' increased to ~ 1.2
20
21 kPa (Figure 2F). The critical strain for gel-to-sol transition (structure damage) was
22
23 determined by the strain sweep experiment, and the values were $\sim 350\%$ and $\sim 260\%$
24
25 for pre- and post-UV samples, respectively [Figure 2 (D, G)]. The self-healing
26
27 properties of the PUGG hydrogel were evaluated by giving continuous and alternative
28
29 strains between a higher strain that exceeded the critical strain and a lower strain (1%)
30
31 [Figure 2 (E, H)]. The testing temperature was $25\text{ }^{\circ}\text{C}$, which is the expected printing
32
33 temperature of the PUGG hydrogel. At the lower strain (1%), G' was higher than G''
34
35 and both moduli stayed constant with time. When the higher strains were applied, G' -
36
37 G'' crossover occurred (i.e. $G'' > G'$) and the bioink was in the sol state. Upon reversal
38
39 of the strain, the G' and G'' values returned rapidly to their initial values. The
40
41 reproducible rheological behavior after repeated damaging-healing cycles confirmed
42
43 the self-healing nature of the PUGG hydrogel. A series of self-healing PUGG hydrogels
44
45
46
47
48
49
50
51
52
53
54
55
56
57
58
59
60



1
2
3
4 can be prepared with different ratios among the components (PU/gelatin/GelMA) and
5
6
7 different chemical composition of PU (Figures S3 and S4). In addition to PUGG
8
9
10 hydrogel, the two-component of PU/gelatin hydrogel also showed self-healing (Figure
11
12
13 S5). The self-healing phenomenon of this hydrogel was not observed in the absence of
14
15
16 culture medium, suggesting that the ionic interaction may play a key role in self-healing.
17
18
19 Besides, pure gelatin hydrogel in culture medium did not have self-healing property.
20
21
22 These results indicate that the interaction force between PU and gelatin may take a
23
24
25 crucial role in the self-healing property of PU/gelatin hydrogel.
26
27
28
29
30
31
32
33
34
35
36
37
38
39
40
41
42
43
44
45
46
47
48
49
50
51
52
53
54
55
56
57
58
59
60

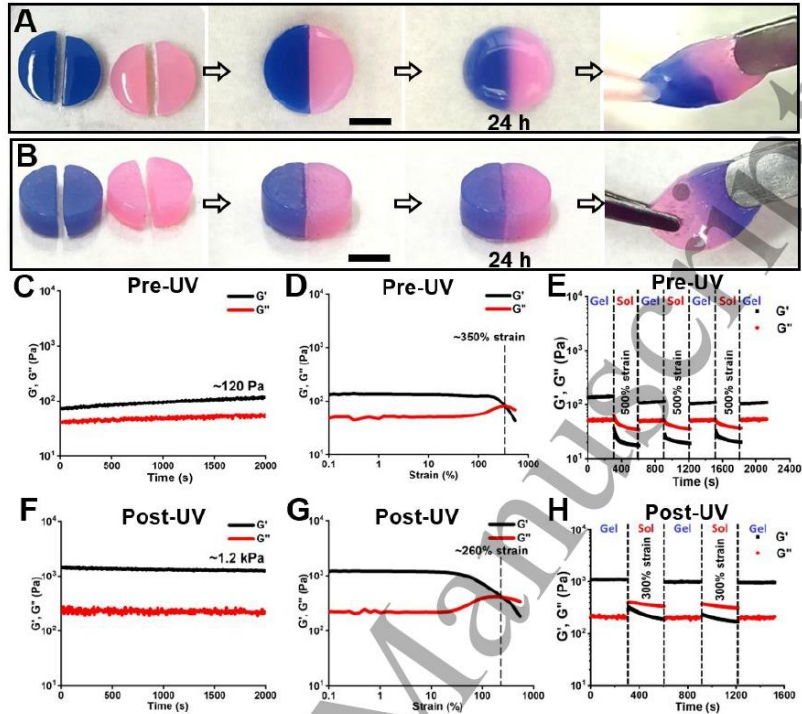


Figure 2. The self-healing behavior of the PUGG hydrogel before UV exposure (“pre-UV”) and after UV exposure (“post-UV”), demonstrated by gross tests (A, B) and rheological properties (C-H) at 25 °C. (A, B) The gross tests showed broken hydrogels (either pre-UV or post-UV) could heal automatically and be stretched by a pair of tweezers. (C, F) Time-dependent moduli (G' and G'') after sample loading, measured at 1% strain and 1 Hz. The values of G' increased ten times after UV curing. (D, G) Strain-dependent moduli (G' and G'') after gel stabilization, measured at 1 Hz. Structure damage occurred at $\sim 350\%$ strain for pre-UV samples and $\sim 260\%$ for post-UV

1
2
3
4 samples. (E, H) The damaging-healing cycles measured through the continuous step
5
6
7 strain changes at 1 Hz. The reproducible cycles confirm the self-healing properties of
8
9
10 pre-UV and post-UV samples of the PUGG hydrogel.
11
12
13
14
15

16 **3.3. Self-healing mechanism of PUGG hydrogel**

17
18
19 A possible mechanism for the autonomic self-healing of PUGG hydrogel is
20
21 depicted in Figure 3. PU nanoparticles as one component of PUGG hydrogel have many
22
23 COO⁻ functional groups located on the spherical surface of nanoparticles. The
24
25 electrolytes in cell culture medium may interact with the COO⁻ groups of PU
26
27 nanoparticles and produce an electron shielding effect (Figure 3Ai) [50]. The reduced
28
29 electrostatic repulsive forces among the PU nanoparticles probably result in
30
31 aggregation to form the "multiplet" structure [51]. Meanwhile, the NH₂ group in gelatin
32
33 chains could be protonated to NH₃⁺ in cell culture medium (pH = 7.2-7.4) [52]. The
34
35 COO⁻ group in PU multiplets may further interact through electrostatic attractive forces
36
37 with the NH₃⁺ group in gelatin chains, forming the "cluster" structure (Figure 3Aii).
38
39 The aggregated clusters could facilitate self-healing through reversible ionomeric
40
41 interactions [53]. Once the hydrogel is broken, the intermolecular forces are recruited
42
43 because gelatin chains may move from one PU multiplet to another through ion hopping,
44
45 which allows the clusters to reform at the broken area and achieve the self-healing
46
47
48
49
50
51
52
53
54
55
56
57
58
59
60



1
2
3
4 behavior (Figure 3Aiii, iv) [54]. The best self-healing result was observed when PU and
5
6
7 gelatin were mixed at an 80/20 weight ratio. If PU nanoparticles were more than 80 wt
8
9
10 %, the self-healing effect would decrease probably because of insufficient gelatin
11
12
13 chains to form clusters with PU multiplets. If gelatin accounted for more than 20 wt %,
14
15
16 the ion hopping effect of gelatin would be limited due to more intra-/inter-molecular
17
18
19 interaction.

20
21
22 The aforementioned self-healing mechanism was partially supported by TEM and
23
24
25 SAXS results. The TEM image of PUGG hydrogel confirmed the existence of larger
26
27
28 PU nanoparticles and aggregated PU multiplets (Figure 3B). The morphology of PU in
29
30
31 hydrogel was different from that in pure water suspension (~ 30 nm) [55]. The PU
32
33
34 multiplets were attracted to the gelatin aggregate through electrostatic attractive forces
35
36
37 to form clusters. The SAXS curves of the pure PU nanoparticle suspension alone and
38
39
40 PU/gelatin mixture (Figure S6) revealed curve humps that represent the diameter of PU
41
42
43 nanoparticles and inter-particle distance among the PU nanoparticles. When the solvent
44
45
46 was switched to the culture medium from water, the intensities of the humps decreased,
47
48
49 i.e., with a reduced structure factor. Such reduction in structure factor may be attributed
50
51
52 to the formation of PU multiplets. In the presence of culture medium, the SAXS curve
53
54
55 of PUGG hydrogel showed a different hump signal at $q \sim 0.009$ which was broadened
56
57
58 and shifted more toward the low- q region (Figure 3C). This broad hump may be
59
60

ascribed to the untangled PU molecular chains and newly formed PU nanoparticles in the hydrogel. In addition, the scattering intensity and slope in low q region (q 0.002 – 0.007 \AA^{-1}) increased, suggesting the formation of cluster structure with larger size and polydispersity.

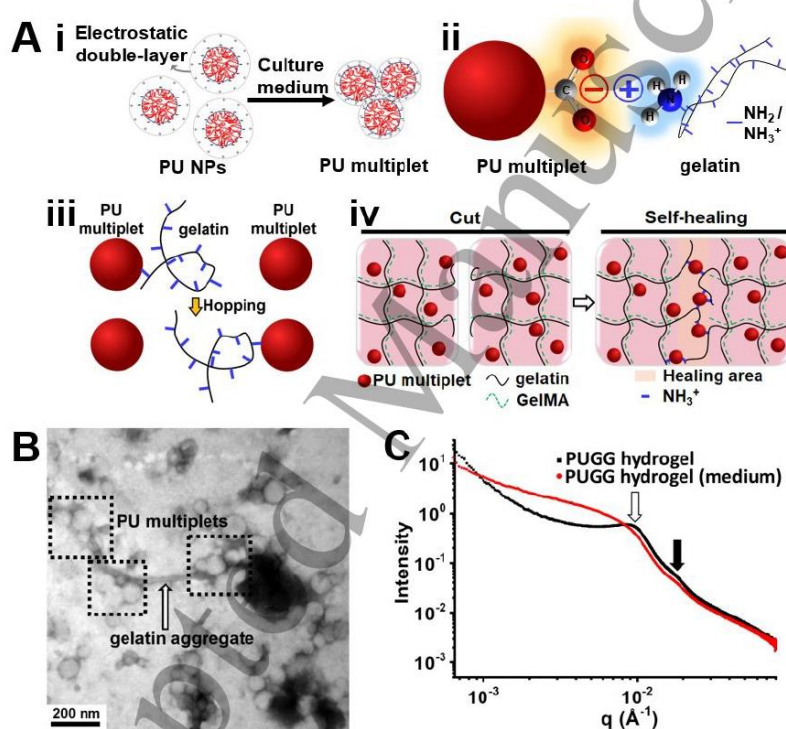


Figure 3. The hypothetical mechanism for self-healing of the PUGG hydrogel, based on the morphological and microstructure examination. (A) Schematic illustration for possible interaction forces of each component in the healing hydrogel: (i) PU



1
2
3
4 nanoparticles may form PU multiplets. (ii) The COO^- group in PU multiplets may
5
6
7 interact through electrostatic forces with NH_3^+ on gelatin chains. (iii) Gelatin chain may
8
9
10 move from one PU multiplet to another through ion hopping. (iv) In the cut area of the
11
12
13 hydrogel where the intermolecular forces are broken, the re-aggregation of PU
14
15
16 multiplets and ion hopping of gelatin chains may account for the interfacial self-healing
17
18
19 behavior. (B) The TEM image of the PUGG hydrogel. The morphology shows that PU
20
21
22 multiplets are linked by gelatin aggregate. (C) SAXS profiles for the PUGG hydrogel
23
24
25 in water and in cell culture medium at 25 °C. The solid arrow (black) at $q \sim 0.018 \text{ \AA}^{-1}$
26
27
28 indicates the size ($\sim 35 \text{ nm}$) of the PU nanoparticles; the hollow arrow (white) at $q \sim$
29
30
31 0.009 \AA^{-1} corresponds to the distance ($\sim 70 \text{ nm}$) between the PU nanoparticles.

3.4. 3D printing of the PUGG hydrogel

32
33
34
35
36
37
38
39
40
41 Self-healing PUGG hydrogel was applied as the bioink. The shear thinning
42
43
44 property of the hydrogel is shown in Figure 4A. The slope of the log-log plot of
45
46
47 viscosity vs. shear rate was about -1.1 , suggesting good printability [11]. The gelatin
48
49
50 and GelMA components were both thermo-responsive with sol-gel transition at ~ 27
51
52
53 °C and $\sim 19 \text{ °C}$, respectively (Figure S7A). The rheology of the PUGG bioink can be
54
55
56 simply adjusted by the printing temperature. One of the optimized conditions was the
57
58
59 bioink with 19 wt % (12:3:4 wt % of PU, gelatin, and GelMA) printed using a $160 \mu\text{m}$
60

1
2
3
4 (or 80 μm) nozzle controlled at 25 $^{\circ}\text{C}$ (Figure 4B). Such PUGG bioink underwent
5
6
7 gelation and had a low (~ 120 Pa) modulus and relatively high $\tan \delta$ (~ 0.46) at the
8
9
10 printing temperature of 25 $^{\circ}\text{C}$ (Figure S7B), which facilitated continuous extrusion
11
12
13 through the small printing nozzle [56].
14

15
16 The bioink was printed through the 160 μm nozzle with the temperature set at 25
17
18 $^{\circ}\text{C}$. The printed mesh-like constructs were deposited on the platform with the
19
20 temperature set at 4 $^{\circ}\text{C}$ (Figure 4C). High-resolution printing of mesh-like constructs
21
22 was verified using the 80 μm nozzle. The dimension was 10 mm \times 10 mm \times 0.64 mm.
23
24
25 Meanwhile, the structure kept good integrity because the self-healing phenomenon
26
27 between the stacked layers remained to be effective at 4 $^{\circ}\text{C}$ (Figure S8). After UV
28
29 curing for 1 min, the photo-crosslinkable GelMA in the bioink polymerized and formed
30
31 covalently crosslinked constructs. The compressive modulus of the UV-crosslinked
32
33 PUGG hydrogel was ~ 1.4 kPa at 37 $^{\circ}\text{C}$, partially attributed to the secondary force
34
35 interaction among PU nanoparticles [57]. The diameters of the UV-crosslinked
36
37 filaments were ~ 180 μm (from the 160 μm nozzle) and ~ 120 μm (from the 80 μm
38
39 nozzle). The internal structure of the UV-crosslinked constructs was observed by SEM
40
41 (Figure S9). The constructs exhibited interconnected grid structures without collapse
42
43 (Figure S9Aii). Meanwhile, the structure demonstrated good integrity probably because
44
45 of the self-healing phenomenon of PUGG hydrogel that occurred at the stacking sites.
46
47
48
49
50
51
52
53
54
55
56
57
58
59
60

1
2
3
4
5
6
7
8
9
10
11
12
13
14
15
16
17
18
19
20
21
22
23
24
25
26
27
28
29
30
31
32
33
34
35
36
37
38
39
40
41
42
43
44
45
46
47
48
49
50
51
52
53
54
55
56
57
58
59
60

The cross-sectional outline of the printed filament was an ellipse (Figure S9Bii). The filament height was $\sim 154 \mu\text{m}$ and the diameter was $\sim 180 \mu\text{m}$ (printed from the $160 \mu\text{m}$ nozzle), indicating slight swelling and spreading after extrusion. The crosslinked constructs were strong enough to be picked up from the printing stage and used for subsequent operations (for example, moving into cell incubator). When placed in PBS buffer at 37°C for 7 days, constructs maintained their shape fidelity and the diameters of the filaments were reduced to $\sim 160 \mu\text{m}$ (printed from the $160 \mu\text{m}$ nozzle) and $\sim 100 \mu\text{m}$ (printed from the $80 \mu\text{m}$ nozzle), respectively. Finally, the compressive modulus of UV-crosslinked hydrogels can be tuned through changing the content of GelMA in a rather wide range of 1–60 kPa (Figure S10).

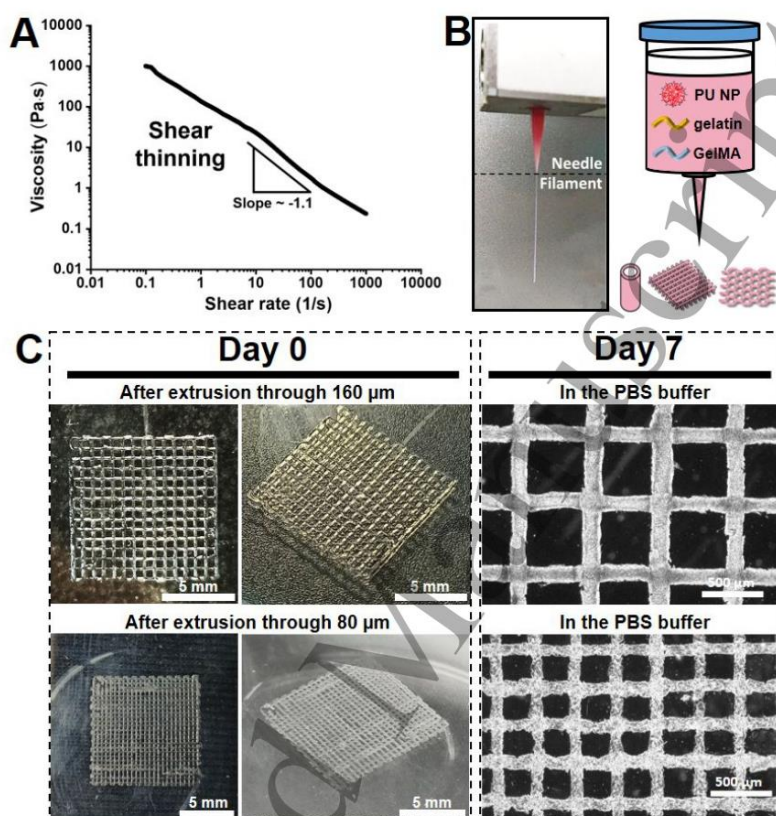
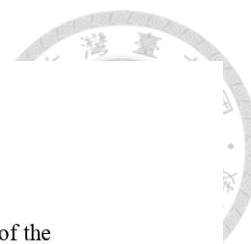


Figure 4. Printability of the PUGG bioink, and stability of the printed hydrogels. (A) The shear thinning property demonstrated by the steady shear experiment suggested the printability of the PUGG bioink. (B) A smooth filament of the PUGG bioink extruded through a nozzle controlled at 25 °C can be deposited on the platform to form 3D constructs. (C) The gross appearance of 3D printed mesh-like constructs from the



1
2
3
4
5
6
7
8
9
10
11
12
13
14
15
16
17
18
19
20
21
22
23
24
25
26
27
28
29
30
31
32
33
34
35
36
37
38
39
40
41
42
43
44
45
46
47
48
49
50
51
52
53
54
55
56
57
58
59
60

PUGG bioink through 160 μm or 80 μm nozzles after UV curing. The integrity of the constructs was maintained after 7 days in 37 $^{\circ}\text{C}$ PBS buffer.

3.5. Stackability of the 3D printed PUGG hydrogel

To show the stackability, a hollow cylinder with an outer diameter of 6.5 mm and an internal diameter of 4 mm was printed through the 160 μm nozzle (Figure 5A). The extruded filaments were continuously stacked for up to 80 layers to the designed height of 12.8 mm. After UV crosslinking, the actual dimension of the hollow cylinder was 13 mm high with an outer diameter of 6.6 mm and an internal diameter of 3.9 mm. The slightly larger dimension indicated swelling of the hydrogel after extrusion. The structure of the printed hollow cylinder was stable without delamination or collapse.

The mechanical stability and flexibility of the 3D printed PUGG hollow cylinder were verified by gross observation and mechanical testing [Figure 5 (B-D)]. The printed hollow cylinder was compressed laterally to 3 mm with tweezers at room temperature, and when the lateral compression force was released, the construct rapidly recovered to the original shape (Figure 5B and Movie S3). The elasticity of the hollow cylinder and the ability to withstand repeated cycles of lateral compression strain (20–40%) were confirmed by DMA (Figure 5D). The shape recovery ratio remained $\sim 100\%$ (full recovery) after the continuous eighteen cycles. Another sheet-like construct (5 mm \times



1
2
3
4 10 mm × 0.64 mm) was shown to endure bending of 80° angle (Figure 5C and Movie
5
6
7 S4). The elastic recovery of the printed constructs without obvious permanent
8
9
10 deformation may be associated with formation of interpenetrating polymer network
11
12 (IPN) in the UV-crosslinked network [58]. The relatively lower content (4 wt %) of
13
14 GelMA (vs. PU) in the hydrogel may produce a moderate extent of crosslinking and
15
16
17 provide fixation points required for elastic recovery.
18
19
20
21
22
23
24
25
26
27
28
29
30
31
32
33
34
35
36
37
38
39
40
41
42
43
44
45
46
47
48
49
50
51
52
53
54
55
56
57
58
59
60

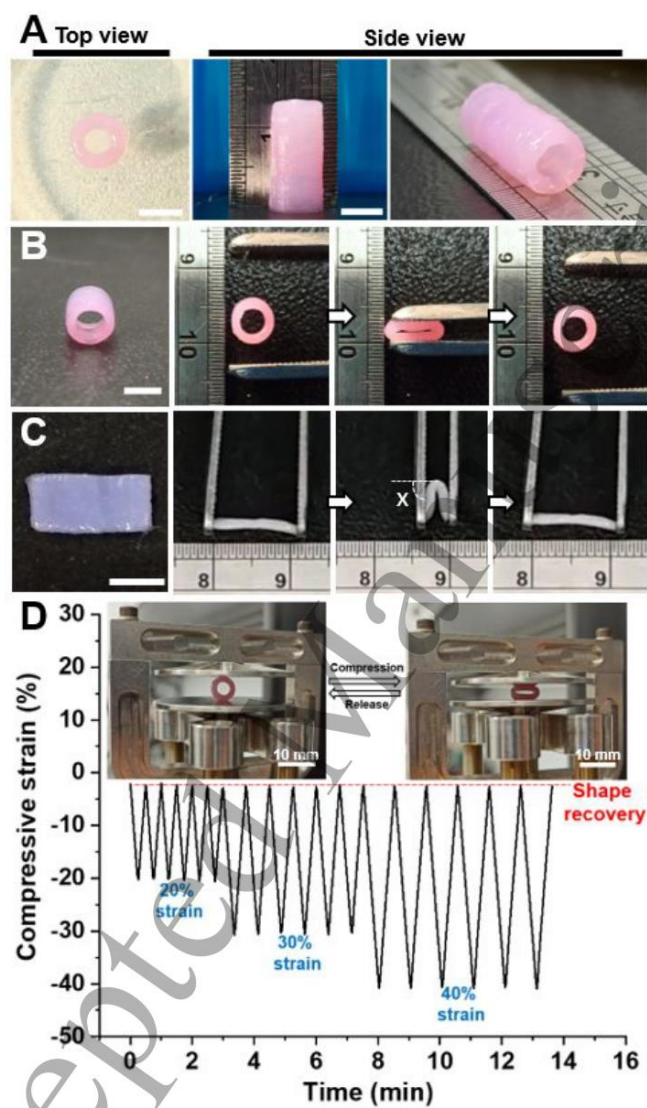


Figure 5. Stackability, flexibility, and recovery capacity of the 3D printed PUGG constructs. (A) Images of the printed hollow cylinder (stacked 80 layers). (B, C) Images

1
2
3
4 showing the elastic recovery of the (B) hollow cylinder and (C) sheet after squeezing
5
6
7 and subsequent release. Symbol “x” indicates a bending angle of 80°. Scale bars (A-C)
8
9
10 represent 5 mm. (D) Dynamic compression cycles of the hollow cylinder measured by
11
12
13 DMA with 20–40% compressive at 20 °C. The preload of the measurements was 0.01
14
15
16 N, which caused an initial compressive strain of ~ 2% (not exactly zero).
17
18
19
20
21
22

23 **3.6. 4D printed constructs with shape memory properties**

24
25
26 Shape memory properties were introduced to the self-healable PUGG hydrogel
27
28 after printing, as shown in Figure 6. First, the sheet-like, flower, and honeycomb
29
30
31 constructs were printed through the 160 μm nozzle at 25 °C and exposed to UV for 1
32
33
34 min. The printing path/patterns and expected self-healing sites of the bioinks are
35
36
37 sketched in dotted panels of Figure 6. The quick structural recovery of self-healing
38
39
40 bioink after extrusion can improve the adhesions between the adjacent fibers and
41
42
43 between the stacked layers in printed constructs [15]. To install the shape memory, the
44
45
46 printed constructs were deformed and fixed to the temporary shape in a -20 °C
47
48
49 refrigerator. The shape fixity ratio of the U-bent sheet-like construct (11.5 mm long in
50
51
52 water) was ~ 95% based on the maintenance of the angle for bending deformation
53
54
55 (Figure 6Ai). The shape recovery was activated by immersion in 37 °C water. The shape
56
57
58 recovery ratio was ~ 98% (from bent to sheet-like). Meanwhile, the twisted sheet-like
59
60

1
2
3
4
5
6
7
8
9
10
11
12
13
14
15
16
17
18
19
20
21
22
23
24
25
26
27
28
29
30
31
32
33
34
35
36
37
38
39
40
41
42
43
44
45
46
47
48
49
50
51
52
53
54
55
56
57
58
59
60

construct and “closed” flower construct also demonstrated good shape fixity and shape recovery under constrained and load-free conditions with the same operating temperature [Figure 6(Aii, B) and Movie S5, S6]. Besides, the 3D printed honeycomb construct (12 mm longitudinal size in water) was laterally compressed and fixed at a shorter length of 5 mm (shape fixity ratio ~ 100%, Figure 6C). After immersion in 37 °C water, the compressed honeycomb construct rebound to a length of 12.1 mm, i.e., had a shape recovery ratio ~ 100% (Movie S7). The structural integrities of the printed constructs after shape fixation and recovery indicated the feasibility of 4D printing using the self-healing and shape memory characters of PUGG hydrogel.

The PUGG hydrogel is shape-fixable at subzero temperature probably because the rigid water lattice in the hydrogel can restrict the movement of polymer chains by hydrogen bonding [59]. Meanwhile, the shape recovery of PUGG hydrogel may be attributed to the elasticity of PU and crosslinked GelMA in the network. When the hydrogel is placed in 37 °C water, the polymer chains can relax and return to their unrestricted states owing to the collapse of water lattice. The hydrogel may quickly recover the original shape as a result of the interaction between the diffused water and the polymer chains [33]. During the process, water swelling may occur to account for the small length increase (~ 0.83%) of the honeycomb construct.

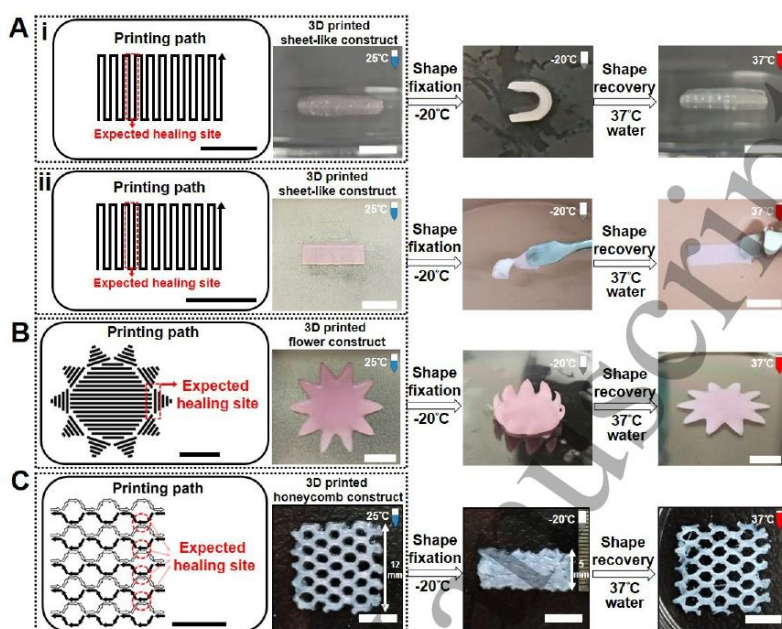


Figure 6. Self-healing and shape memory properties of the 3D printed PUGG constructs.

The printing path/patterns and images of the 3D printed (A) sheet-like (7 layers), (B) flower (4 layers), and (C) honeycomb (4 layers) constructs, showing self-healing between adjacent fibers as indicated on the expected healing sites. After UV exposure for 1 min, the constructs were deformed and shape-fixed at -20°C . Full shape recovery was triggered by 37°C water. Scale bars represent 5 mm in (Ai, C) and 1 cm in (Aii, B).

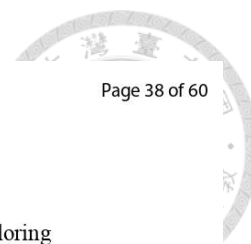
3.7. Cell viability and proliferation in the bioprinted PUGG hydrogel



1
2
3
4 The immediate viability of NSCs after embedding in PUGG bioink was assessed
5
6
7 by live (AO)/dead (PI) staining at 37 °C, as shown in Figure S11 (A, B). Cells in the
8
9
10 culture medium served as the control. Based on the live/dead assay, the average
11
12 percentage of cell viability was 97.3%, 93.8%, and 94.8% for the culture medium
13
14 control, PU bioink, and PUGG bioink, respectively. These values were not significantly
15
16 different. The long-term proliferation of NSCs in the 3D printed PUGG hydrogels (160
17
18 μm nozzle and post-UV) during a period of 14 days is shown in Figure S11C. The cell
19
20 viability was increased by 237%, 280%, and 366% in PUGG hydrogel after 3, 7, and
21
22 14 days, respectively. Meanwhile, the cell viability in PU hydrogel was 101%, 105%,
23
24 and 96% after 3, 7, and 14 days, respectively. These results confirmed the
25
26 cytocompatibility of the hydrogel and the printing process.
27
28
29
30
31
32
33
34
35
36
37
38
39
40

41 **3.8. Interaction of NSCs and MSCs in the bioprinted hydrogel**

42
43 Cell interaction in the adjacent, self-healed area of the honeycomb construct is
44
45 illustrated in Figure 7. The printing path and pattern of the NSC-/MSC-laden PUGG
46
47 hydrogel in the honeycomb construct are sketched in Figure 7A. The adjacent filaments
48
49 of the printed hydrogels were expected to heal and integrate. In the enlarged self-healed
50
51 zone, the fluorescence labeled NSCs (green color) and MSCs (red color) both migrated
52
53 to the other side of the adjacent filaments through the self-healing interface (Figure 7B)
54
55
56
57
58
59
60



1
2
3
4 in 3 days. This finding can be useful for printing multiple types of cells and exploring
5
6
7 the 3D cell crosstalk in the future [60, 61].
8
9

10 The effect of adjacent MSC-laden filament on the differentiation potential of
11
12 NSCs was analyzed by the gene expression of neural-related markers (Nestin, Tubb3,
13
14 and GFAP) as shown in Figure 7C. The gene expression levels of these three markers
15
16 increased for all NSC-laden and NSC/MSC-interlaid hydrogel groups at 3 days
17
18 compared to NSCs cultured on TCPS, suggesting the enhanced neurogenic activity of
19
20 NSCs. Moreover, the NSC/MSC-interlaid group expressed greater levels of Tubb3 gene
21
22 than NSCs alone in the hydrogel, indicating a tendency to differentiate toward neuronal
23
24
25
26
27
28
29
30
31
32
33
34
35
36
37
38
39
40
41
42
43
44
45
46
47
48
49
50
51
52
53
54
55
56
57
58
59
60 cells.

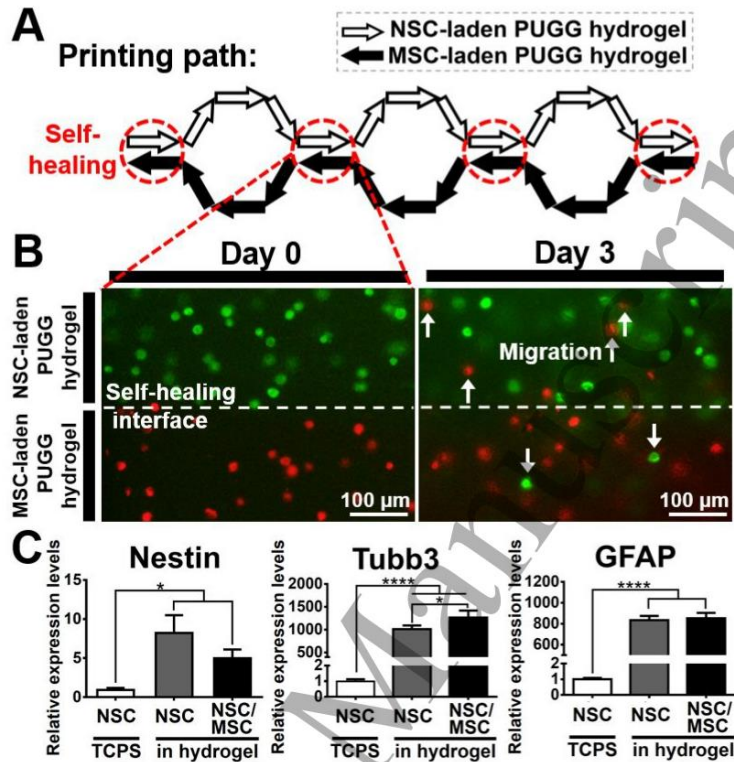


Figure 7. The migration and differentiation behavior of individually printed NSCs and MSCs in the self-healed zone of PUGG hydrogel. (A) The hollow arrow and solid arrow each indicated the printing path of NSC-laden PUGG hydrogel and MSC-laden PUGG hydrogel. Self-healing of PUGG hydrogels was expected to occur at the interface between adjacent fibers, indicated by red circles. (B) Enlarged micrographs for the self-healed interface of NSC (green) /MSC (red) -laden PUGG hydrogels revealed cell migration across the border after 3 days of cell culture. (C) The effect of adjacent MSC-

1
2
3
4 laden filament on the differentiation potential of NSCs assessed by real-time RT-PCR
5
6
7 at 3 days. NSCs on the tissue culture polystyrene (TCPS) and the constructs printed
8
9
10 with NSCs alone served as the control. The gene expression level was normalized to
11
12
13 the housekeeping gene (GAPDH) and presented as the relative expression level to that
14
15
16 of the mono-cultured NSCs on TCPS. * $p < 0.05$, **** $p < 0.0001$, among the indicated
17
18
19 groups.
20
21
22
23
24

25 **3.9. Cryopreserving properties of 4D bioprinted PUGG hydrogel**

26
27 The cryopreserving properties of 4D printed cell-laden hydrogel were investigated.
28
29 MSC-laden honeycomb constructs were laterally compressed to a smaller volume and
30
31 then immersed in the cell cryopreservation agent (a mixture of 7% DMSO and 93% cell
32
33 culture medium) for 20 min (Figure 8) [62]. To fix the shape, the constructs were placed
34
35 in the $-20\text{ }^{\circ}\text{C}$ refrigerator for 30 min before further cryopreservation ($-80\text{ }^{\circ}\text{C}$) for 3
36
37 days or 14 days (Figure 8B-D). After thawing at $37\text{ }^{\circ}\text{C}$, MSCs in the shape-recovered
38
39 constructs kept proliferating for 3 days and no significant difference in cell viability
40
41 was observed between the cryopreserved groups (either $-20\text{ }^{\circ}\text{C}$ or $-80\text{ }^{\circ}\text{C}$) and non-
42
43 cryopreserved groups, indicating the cytocompatibility and cryopreserving possibility
44
45 of the 4D bioprintable PUGG hydrogel.
46
47
48
49
50
51
52
53
54
55
56
57
58
59
60

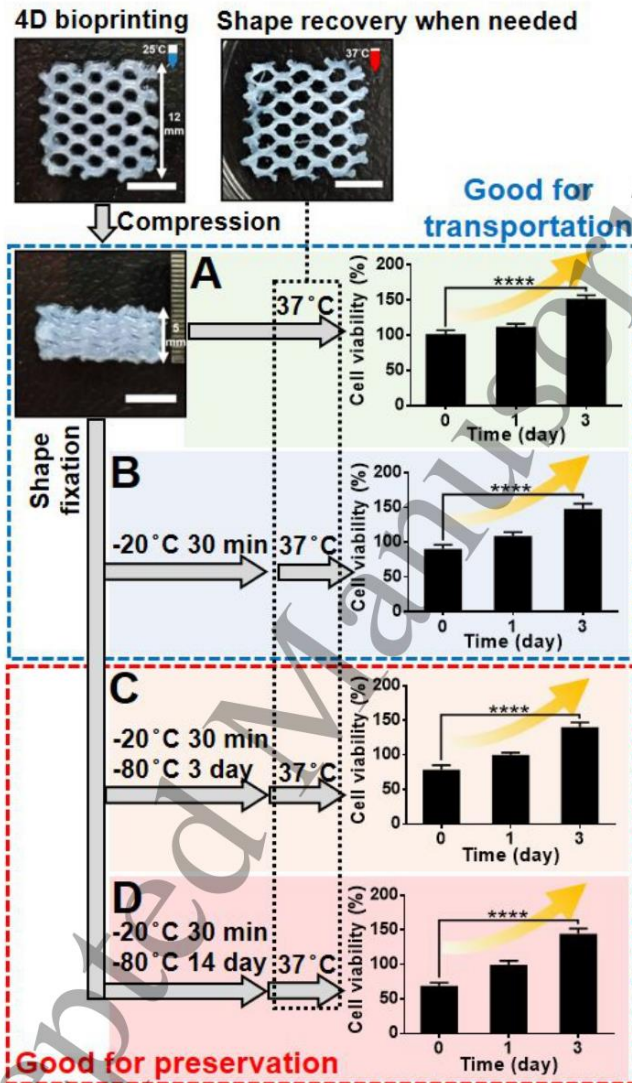


Figure 8. Cryopreserving properties of 4D printed MSC-laden PUGG constructs. The bioprinted constructs were compressed and maintained at various conditions: (A) 37 °C; (B) -20 °C for 30 min; (C) -20 °C for 30 min and -80 °C for 3 days; and (D) -20 °C

1
2
3
4 for 30 min and $-80\text{ }^{\circ}\text{C}$ for 14 days. After rapid thawing and recovery to $37\text{ }^{\circ}\text{C}$, the cell
5
6
7 proliferation in the shape-recovered constructs was evaluated by the CCK-8 assay. Cell
8
9
10 viability was normalized to the initial value of the control group [i.e. cell viability of
11
12
13 the group (A) at 0 day serving as 100%]. **** $p < 0.0001$, among the indicated groups.
14
15
16
17
18

19 The component concentration and ratio of the three-component PUGG
20
21 (PU/gelatin/GelMA) hydrogel were optimized based on self-healing property,
22
23 processing ability, and cytocompatibility. PU is the main component of the PUGG
24
25 hydrogel, which offers good elasticity and shear thinning behavior [55]. Gelatin was
26
27 chosen for two reasons. First, gelatin and PU mixed at a weight ratio of 80/20 exhibited
28
29 self-healing properties (Figure 2 and Figures S3-S5). Second, low-concentration (i.e.,
30
31 $\leq 5\text{ w/v }%$) GelMA bioink suffered from poor processability during extrusion and
32
33 deposition, while high-concentration (i.e., $30\text{ w/v }%$) GelMA bioink with better
34
35 processability showed poor cell viability [7, 63]. Gelatin mixed with low-concentration
36
37 GelMA not only significantly improves the processability to be comparable to that of
38
39 high-concentration GelMA but also maintains high cell viability [8]. The PUGG
40
41 hydrogel was optimized by selecting $4\text{ wt }%$ of GelMA on the basis of mechanical
42
43 stability. The design of structural evolution and properties of each component in the
44
45 PUGG bioink during different stages of 3D printing is demonstrated in Figure 9. The
46
47
48
49
50
51
52
53
54
55
56
57
58
59
60

1
2
3
4
5
6
7
8
9
10
11
12
13
14
15
16
17
18
19
20
21
22
23
24
25
26
27
28
29
30
31
32
33
34
35
36
37
38
39
40
41
42
43
44
45
46
47
48
49
50
51
52
53
54
55
56
57
58
59
60

three components were in sol state at 37 °C and mixed uniformly with cells. The mixture underwent thermo-gelation at 25 °C due to formation of the physical network in gelatin. PU and gelatin mixed at a weight ratio of 80/20 have been confirmed to own high-resolution printability [11]. The purpose of gelatin is to increase the viscosity of the bioink and retain the shape fidelity after deposition onto the platform. The 3D printed PUGG constructs demonstrated good stackability at 4 °C due to further gelation of gelatin and GelMA. The stackability of the printed PUGG constructs may be attributed to the high G' value (~ 6 kPa) and low $\tan \delta$ value (~ 0.08), as shown in Figure S7B. In the literature, fast gelation with the G' value above 250 Pa is necessary for stacking in 3D printing [11]. Gels with smaller $\tan \delta$ (< 0.1) often show better shape stability and allow for continuous stacking of the printed filaments [56]. After UV exposure, GelMA in the PUGG hydrogel was photo-crosslinked to produce a moderate extent of fixation points for long-term structural stability. The fixation points contributed to the elastic recovery and shape memory property of the PUGG hydrogel.

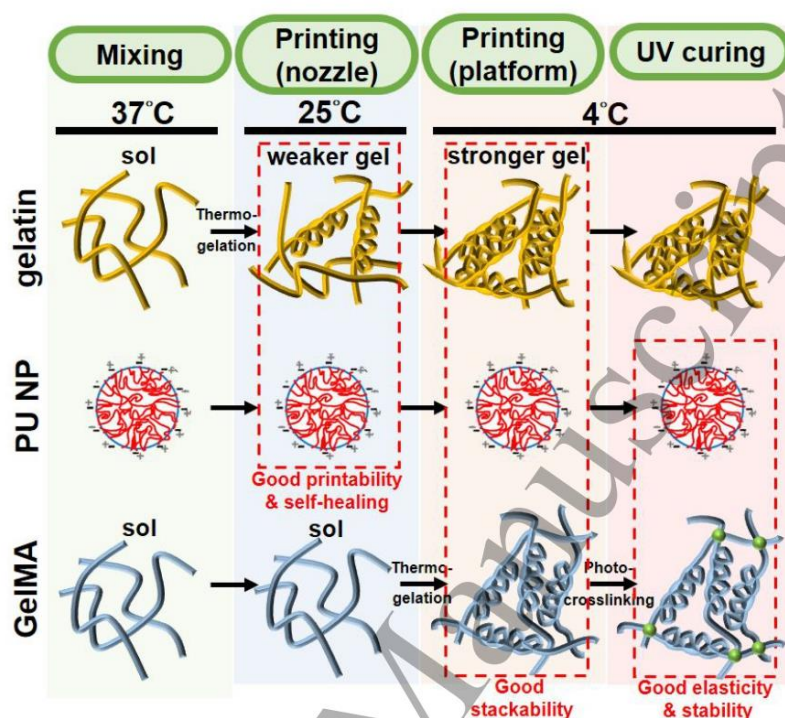


Figure 9. Schematic diagram of structural evolution and properties of each component in the PUGG hydrogel during different stages of 3D printing.

The self-healing property of the PUGG hydrogel may enhance its operation reliability during repeated elastic deformation or shape memory processes [64]. Meanwhile, the individually bioprinted NSCs and MSCs in the adjacent filaments showed mutual migration, confirming the structural integrity of the self-healed construct. The self-healing time of the PUGG hydrogel was similar to those of

1
2
3
4
5
6
7
8
9
10
11
12
13
14
15
16
17
18
19
20
21
22
23
24
25
26
27
28
29
30
31
32
33
34
35
36
37
38
39
40
41
42
43
44
45
46
47
48
49
50
51
52
53
54
55
56
57
58
59
60

numerous hybrid and nanocomposite hydrogels [65]. Besides, Leng et al. claimed shape memory materials such as space-deployable structures and vascular stents could be deformed to small size and deployed to the designed structure at the desired position and time, which overcomes the difficulty of package and transportation of large materials [66]. In addition, cryopreservation technology is considered as a solution for long-term storage of tissues because the on-demand availability of biotherapeutics is valuable for clinical use [67]. For instance, Alsberg et al. demonstrated that cryopreserved cell-laden alginate microgel bioink was conducive to 3D bioprinting of living tissues [68]. Herein, the printed MSC-laden PUGG constructs were fixed to a minimized size and cryopreserved in cell-protective surroundings for 14 days. The shape fixation condition of the PUGG hydrogel was designed to match the cryopreservation temperature ($-20\text{ }^{\circ}\text{C}$ or $-80\text{ }^{\circ}\text{C}$). The 4D shape-fixed bioprinted constructs allow ready-to-use storage in freezers/biobanks, on-demand transportation, and on-site shape recovery for biomedical applications.

The disadvantage of extrusion-based 3D bioprinting is that the high shear stress during extrusion of cell-laden bioink at the narrow nozzle may damage cells [69, 70]. One strategy to reduce cell death is to use self-healing bioink because cells are more capable of being spread in a dynamic network compared to the conventional static bioink [71]. The use of a $160\text{ }\mu\text{m}$ cone-like nozzle in this study generated relatively

1
2
3
4 high shear stress when compared to the use of a 410 μm nozzle in the previous literature
5
6
7 [55]. Nevertheless, cells in the self-healing PUGG hydrogel remained to survive and
8
9
10 proliferate well after bioprinting. Other than the shear force, employment of UV
11
12 irradiation as a post-printing reinforcement could also result in damage to cell DNA
13
14 because of creating free radicals during photo-curing [72]. In the previous study,
15
16 GelMA hydrogels with high degree of functionalization (DoF) showed higher cell
17
18 viability when compared to GelMA hydrogels with low DoF because the abundance of
19
20 photoinitiator reactive groups offered cytoprotective effects [73]. Meanwhile, the use
21
22 of low toxic photoinitiators such as VA-086 has been substantiated by evidence of
23
24 rather benign effect [74, 75]. Other groups have developed visible-light-sensitive
25
26 photoinitiation (blue and green light wavelength) to improve cell viability [76, 77]. An
27
28 attractive new approach is to use jammed microgels as the bioinks for extrusion-based
29
30 3D printing. Literature has reported the possibility of densely packed microgels to be
31
32 extruded into target locations with low shear forces because of significant shear
33
34 thinning effect that arises from microparticle interaction [78, 79]. The extruded
35
36 microgels rapidly recover and maintain viscoelastic properties upon deposition due to
37
38 interparticle adhesion forces. Moreover, any hydrogel material can have the potential
39
40 to be processed into microgels, independent of microgel composition [80]. It would be
41
42
43
44
45
46
47
48
49
50
51
52
53
54
55
56
57
58
59
60

1
2
3
4
5
6
7
8
9
10
11
12
13
14
15
16
17
18
19
20
21
22
23
24
25
26
27
28
29
30
31
32
33
34
35
36
37
38
39
40
41
42
43
44
45
46
47
48
49
50
51
52
53
54
55
56
57
58
59
60

interesting to see if the self-healing PUGG hydrogel can be processed into self-healing microgels for use in 3D bioprinting in the future.

4. Conclusion

Self-healing PUGG hydrogel with good 3D printability and stackability (> 80 layers) was prepared. The printed hydrogel exhibited good structural stability and elasticity after UV curing for 1 min. The printed hydrogel endured multiple deformation cycles and shape memory programming. The shape-memorizable 4D printed constructs revealed good shape fixity (~ 95%) and shape recovery (~ 98%). The bioink and the printing process supported the continuous cell proliferation (~ 3.7-fold after 14 days). Moreover, the individually bioprinted NSCs and MSCs in the adjacent, self-healed filaments showed mutual migration, and the cell interaction promoted the neural differentiation behavior. The cryopreserved (-20 °C or -80 °C) 4D bioprinted PUGG hydrogels after awakening and shape recovery at 37 °C demonstrated cell proliferation similar to that of the non-cryopreserved control. The unique 4D bioprintable, self-healable PUGG hydrogel with shape memory and cryopreserving properties is a promising bioink for customized biofabrication.

Declaration of competing interest

44



The authors declare no competing financial interest.

Acknowledgments

This research was supported by the Program for Additive Manufacturing and other funding from the Ministry of Science and Technology of Taiwan (MOST 109-2218-E-002-037; MOST 109-2221-E-002-031-MY3). We also thank Ms. Shou-Ling Huang of the Instrumentation Center at National Taiwan University funded by the Ministry of Science and Technology for the assistance in NMR experiments. NSCs were kindly provided by Dr. Ing-Ming Chiu (Institute of Cellular and Systems Medicine, National Health Research Institutes, Zhunan, Taiwan). We also thank the National Synchrotron Radiation Research Center (NSRRC), Taiwan (2018-1-138) and the staff of TPS beamline 25A1, particularly, Dr. Yu-Shan Huang, for providing the resources and technical support.

Supporting Information

Supporting information including supplemental figures and supplemental movies is available from the website or the author.

1
2
3
4
5
6
7
8
9
10
11
12
13
14
15
16
17
18
19
20
21
22
23
24
25
26
27
28
29
30
31
32
33
34
35
36
37
38
39
40
41
42
43
44
45
46
47
48
49
50
51
52
53
54
55
56
57
58
59
60**References**

- [1] Decante G, Costa J B, Silva-Correia J, Collins M N, Reis R L, Oliveira J M 2021 Engineering bioinks for 3D bioprinting *Biofabrication* **13** 032001
- [2] Murphy S V, Atala A 2014 3D bioprinting of tissues and organs *Nat. Biotechnol* **32** 773-785
- [3] Zhou Z, et al. 2021 An imidazolium-based supramolecular gelator enhancing interlayer adhesion in 3D printed dual network hydrogels *Materials & Design* **206** 109792
- [4] Giwa S, et al. 2017 The promise of organ and tissue preservation to transform medicine *Nat. Biotechnol* **35** 530-542
- [5] Wang X, Ao Q, Tian X, Fan J, Tong H, Hou W, Bai S 2017 Gelatin-Based Hydrogels for Organ 3D Bioprinting *Polymers* **9** 401
- [6] Loessner D, et al. 2016 Functionalization, preparation and use of cell-laden gelatin methacryloyl-based hydrogels as modular tissue culture platforms *Nat. Protoc* **11** 727-746
- [7] Colosi C, Shin S R, Manoharan V, Massa S, Costantini M, Barbetta A, Dokmeci M R, Dentini M, Khademhosseini A 2016 Microfluidic Bioprinting of Heterogeneous 3D Tissue Constructs Using Low-Viscosity Bioink *Advanced Materials* **28** 677-684
- [8] Yin J, Yan M, Wang Y, Fu J, Suo H 2018 3D Bioprinting of Low-Concentration

Cell-Laden Gelatin Methacrylate (GelMA) Bioinks with a Two-Step Cross-linking

Strategy *ACS Appl. Mater. Interfaces* **10** 6849–6857

[9] Rehman S R, Augustine R, Zahid A A, Ahmed R, Tariq M, Hasan A 2019 Reduced graphene oxide incorporated GelMA hydrogel promotes angiogenesis for wound healing applications *Int J Nanomedicine* **14** 9603

[10] Hsu S h, et al. 2014 Water-based synthesis and processing of novel biodegradable elastomers for medical applications *J. Mater. Chem. B* **2** 5083–5092

[11] Hsieh C T, Hsu S h 2019 Double-Network Polyurethane-Gelatin Hydrogel with Tunable Modulus for High-Resolution 3D Bioprinting *ACS Appl. Mater. Interfaces* **11** 32746–32757

[12] Liu Y, Hsu S h 2018 Synthesis and Biomedical Applications of Self-healing Hydrogels *Front. Chem.* **6** 449

[13] Guo B, Yu R 2020 Chapter 7 - Self-healing biomaterials based on polymeric systems *Self-Healing Polymer-Based Systems* in: S. Thomas, A. Surendran (Eds.) Elsevier p 167–207

[14] Heidarian P, Kouzani A Z, Kaynak A, Paulino M, Nasri-Nasrabadi B 2019 Dynamic Hydrogels and Polymers as Inks for Three-Dimensional Printing *ACS Biomater. Sci. Eng.* **5** 2688–2707

[15] Pekkanen A M, Mondschein R J, Williams C B, Long T E 2017 3D Printing



1
2
3
4
5
6
7
8
9
10
11
12
13
14
15
16
17
18
19
20
21
22
23
24
25
26
27
28
29
30
31
32
33
34
35
36
37
38
39
40
41
42
43
44
45
46
47
48
49
50
51
52
53
54
55
56
57
58
59
60

Polymers with Supramolecular Functionality for Biological Applications

Biomacromolecules **18** 2669–2687

[16] Loebel C, Rodell C B, Chen M H, Burdick J A 2017 Shear-thinning and self-healing hydrogels as injectable therapeutics and for 3D-printing *Nat. Protoc* **12** 1521–1541

[17] Liu Y, Wong C-W, Chang S-W, Hsu S-h 2021 An injectable, self-healing phenol-functionalized chitosan hydrogel with fast gelling property and visible light-crosslinking capability for 3D printing *Acta Biomaterialia* **122** 211-219

[18] Heidarian P, Kouzani A Z, Kaynak A, Paulino M, Nasri-Nasrabadi B 2019 Dynamic Hydrogels and Polymers as Inks for Three-Dimensional Printing *ACS Biomater. Sci. Eng.* **5** 2688–2707

[19] Nadgorny M, Xiao Z, Connal L A 2017 2D and 3D-printing of self-healing gels: design and extrusion of self-rolling objects *Mol. Syst. Des. Eng.* **2** 283–292

[20] Nadgorny M, Collins J, Xiao Z, Scales P J, Connal L A 2018 3D-printing of dynamic self-healing cryogels with tuneable properties *Polymer Chemistry* **9** 1684–1692

[21] Lee M, Bae K, Levinson C, Zenobi-Wong M 2020 Nanocomposite bioink exploits dynamic covalent bonds between nanoparticles and polysaccharides for precision bioprinting *Biofabrication* **12** 025025

- 1
2
3
4 [22] Caprioli M, Roppolo I, Chiappone A, Larush L, Piri C F, Magdassi S 2021 3D-
5
6 printed self-healing hydrogels via Digital Light Processing *Nat. Commun* **12** 2462
7
8
9
10 [23] Lin T-W, Hsu S-h 2020 Self-Healing Hydrogels and Cryogels from Biodegradable
11
12 Polyurethane Nanoparticle Crosslinked Chitosan *Advanced Science* **7** 1901388
13
14
15 [24] Highley C B, Rodell C B, Burdick J A 2015 Direct 3D Printing of Shear-Thinning
16
17 Hydrogels into Self-Healing Hydrogels *Advanced Materials* **27** 5075–5079
18
19
20
21 [25] Ouyang L, Highley C B, Rodell C B, Sun W, Burdick J A 2016 3D Printing of
22
23 Shear-Thinning Hyaluronic Acid Hydrogels with Secondary Cross-Linking *ACS*
24
25 *Biomater. Sci. Eng.* **2** 1743-1751
26
27
28
29 [26] Wang L L, Highley C B, Yeh Y C, Galarraga J H, Uman S, Burdick J A 2018
30
31 Three-dimensional extrusion bioprinting of single- and double-network hydrogels
32
33 containing dynamic covalent crosslinks *J. Biomed. Mater. Res. A* **106** 865–875
34
35
36
37 [27] Gao B, Yang Q, Zhao X, Jin G, Ma Y, Xu F 2016 4D Bioprinting for Biomedical
38
39 Applications *Trends in Biotechnol* **34** 746-756
40
41
42
43 [28] Li Y-C, Zhang Y S, Akpek A, Shin S R, Khademhosseini A 2016 4D bioprinting:
44
45 the next-generation technology for biofabrication enabled by stimuli-responsive
46
47 materials *Biofabrication* **9** 012001
48
49
50
51 [29] Yang Q, Gao B, Xu F 2020 Recent Advances in 4D Bioprinting *Biotechnology*
52
53 *Journal* **15** 1900086
54
55
56
57
58
59
60



1
2
3
4
5
6
7
8
9
10
11
12
13
14
15
16
17
18
19
20
21
22
23
24
25
26
27
28
29
30
31
32
33
34
35
36
37
38
39
40
41
42
43
44
45
46
47
48
49
50
51
52
53
54
55
56
57
58
59
60

- [30] Wan Z, Zhang P, Liu Y, Lv L, Zhou Y 2020 Four-dimensional bioprinting: Current developments and applications in bone tissue engineering *Acta Biomaterialia* **101** 26-42
- [31] Miao S, et al. 2018 Stereolithographic 4D Bioprinting of Multiresponsive Architectures for Neural Engineering *Advanced Biosystems* **2** 1800101
- [32] Yang G H, Kim W, Kim J, Kim G 2021 A skeleton muscle model using GelMA-based cell-aligned bioink processed with an electric-field assisted 3D/4D bioprinting *Theranostics* **11** 48–63
- [33] Wang Y J, Jeng U S, Hsu S h 2018 Biodegradable Water-Based Polyurethane Shape Memory Elastomers for Bone Tissue Engineering *ACS Biomater. Sci. Eng.* **4** 1397–1406
- [34] Zhang B, Zhang W, Zhang Z, Zhang Y-F, Hingorani H, Liu Z, Liu J, Ge Q 2019 Self-Healing Four-Dimensional Printing with an Ultraviolet Curable Double-Network Shape Memory Polymer System *ACS Appl. Mater. Interfaces* **11** 10328-10336
- [35] Kuang X, Chen K, Dum C K, Wu J, Li V C F, Qi H J 2018 3D Printing of Highly Stretchable, Shape-Memory, and Self-Healing Elastomer toward Novel 4D Printing *ACS Appl. Mater. Interfaces* **10** 7381-7388
- [36] Khetan S, Corey O 2019 Maintenance of stem cell viability and differentiation potential following cryopreservation within 3-dimensional hyaluronic acid hydrogels

1
2
3
4 *Cryobiology* **90** 83-88
5
6

7 [37] Hernández-Tapia L G, Fohlerová Z, Židek J, Alvarez-Perez M A, Čelko L, Kaiser
8
9

10 J, Montufar E B 2020 Effects of Cryopreservation on Cell Metabolic Activity and
11

12 Function of Biofabricated Structures Laden with Osteoblasts *Materials* **13** 1966
13
14

15 [38] Baust J M, Corwin W L, VanBuskirk R, Baust J G 2015 Biobanking: The Future
16
17

18 of Cell Preservation Strategies *Biobanking in the 21st Century* in: F. Karimi-Busheri
19

20 (Ed.) Springer International Publishing Cham p 37–53
21
22

23 [39] Pan H M, Chen S, Jang T-S, Han W T, Jung H-d, Li Y, Song J 2019 Plant seed-
24
25

26 inspired cell protection, dormancy, and growth for large-scale biofabrication
27
28

29 *Biofabrication* **11** 025008
30
31

32 [40] Lee J, Kim G 2020 A cryopreservable cell-laden GelMa-based scaffold fabricated
33
34

35 using a 3D printing process supplemented with an in situ photo-crosslinking *J. Ind.*
36
37

38 *Eng. Chem* **85** 249-257
39
40

41 [41] Huang H-J, Tsai Y-L, Lin S-H, Hsu S-h 2019 Smart polymers for cell therapy and
42
43

44 precision medicine *J. Biomed. Sci* **26** 73
45
46

47 [42] Lin H H, Hsieh F Y, Tseng C S, Hsu S h 2016 Preparation and characterization of
48
49

50 a biodegradable polyurethane hydrogel and the hybrid gel with soy protein for 3D cell-
51
52

53 laden bioprinting *J. Mater. Chem. B* **4** 6694–6705
54
55

56 [43] Shirahama H, Lee B H, Tan L P, Cho N J 2016 Precise Tuning of Facile One-Pot
57
58



1
2
3
4
5
6
7
8
9
10
11
12
13
14
15
16
17
18
19
20
21
22
23
24
25
26
27
28
29
30
31
32
33
34
35
36
37
38
39
40
41
42
43
44
45
46
47
48
49
50
51
52
53
54
55
56
57
58
59
60

Gelatin Methacryloyl (GelMA) Synthesis *Scientific Reports* **6** 31036

[44] van den Bosch E, Gielens C 2003 Gelatin degradation at elevated temperature *Int.*

J. Biol. Macromol **32** 129–138

[45] Yue K, et al. 2017 Structural analysis of photocrosslinkable methacryloyl-

modified protein derivatives *Biomaterials* **139** 163–171

[46] Hsieh F-Y, Lin H-H, Hsu S-h 2015 3D bioprinting of neural stem cell-laden

thermo-responsive biodegradable polyurethane hydrogel and potential in central

nervous system repair *Biomaterials* **71** 48–57

[47] Ho P-J, et al. 2010 Endogenous KLF4 Expression in Human Fetal Endothelial

Cells Allows for Reprogramming to Pluripotency With Just OCT3/4 and SOX2—Brief

Report *Arterio. Thromb. Vasc. Biol* **30** 1905–1907

[48] Hsu S-h, Chen C-W, Hung K-C, Tsai Y-C, Li S 2016 Thermo-Responsive

Polyurethane Hydrogels Based on Poly(ϵ -caprolactone) Diol and Amphiphilic

Poly(lactide-Poly(Ethylene Glycol) Block Copolymers *Polymers* **8** 252

[49] Huang C T, Kumar Shrestha L, Ariga K, Hsu S h 2017 A graphene–polyurethane

composite hydrogel as a potential bioink for 3D bioprinting and differentiation of neural

stem cells *J. Mater. Chem. B* **5** 8854–8864

[50] Dautzenberg H 1997 Polyelectrolyte Complex Formation in Highly Aggregating

Systems. 1. Effect of Salt: Polyelectrolyte Complex Formation in the Presence of NaCl

1
2
3
4 *Macromolecules* **30** 7810–7815

5
6
7 [51] Eisenberg A, Hird B, Moore R B 1990 A new multiplet-cluster model for the
8 morphology of random ionomers *Macromolecules* **23** 4098–4107

9
10
11
12 [52] Lee B H, Shirahama H, Cho N-J, Tan L P 2015 Efficient and controllable synthesis
13 of highly substituted gelatin methacrylamide for mechanically stiff hydrogels *RSC*
14
15
16
17
18
19 *Advances* **5** 106094–106097

20
21
22 [53] Varley R 2007 Ionomers as Self Healing Polymers *Self Healing Materials* **100**
23
24
25 106–125

26
27
28 [54] Vanhoome P, Register R A 1996 Low-Shear Melt Rheology of Partially-
29 Neutralized Ethylene–Methacrylic Acid Ionomers *Macromolecules* **29** 598–604

30
31
32 [55] Ho L, Hsu S h 2018 Cell reprogramming by 3D bioprinting of human fibroblasts
33 in polyurethane hydrogel for fabrication of neural-like constructs *Acta Biomaterialia*
34
35
36
37
38
39
40 **70** 57–70

41
42
43 [56] Vancauwenberghe V, et al. 2017 Pectin based food-ink formulations for 3-D
44 printing of customizable porous food simulants *Innov. Food Sci. Emerg. Technol* **42**
45
46
47
48
49 138–150

50
51
52 [57] Ou C W, Su C H, Jeng U S, Hsu S H 2014 Characterization of biodegradable
53 polyurethane nanoparticles and thermally induced self-assembly in water dispersion
54
55
56
57
58 *ACS Appl. Mater. Interfaces* **6** 5685-5694



1
2
3
4
5
6
7
8
9
10
11
12
13
14
15
16
17
18
19
20
21
22
23
24
25
26
27
28
29
30
31
32
33
34
35
36
37
38
39
40
41
42
43
44
45
46
47
48
49
50
51
52
53
54
55
56
57
58
59
60

- [58] Fares M M, Shirzaei Sani E, Portillo Lara R, Oliveira R B, Khademhosseini A, Annabi N 2018 Interpenetrating network gelatin methacryloyl (GelMA) and pectin-g-PCL hydrogels with tunable properties for tissue engineering *Biomaterials Science* **6** 2938–2950
- [59] Frank H S, Bernal J D 1958 Covalency in the hydrogen bond and the properties of water and ice *Proc. Math. Phys. Eng. Sci.* **247** 481–492
- [60] Han H-W, Hsu S-h 2017 Chitosan derived co-spheroids of neural stem cells and mesenchymal stem cells for neural regeneration *Colloids Surf. B Biointerfaces* **158** 527–538
- [61] Han H-W, Hou Y-T, Hsu S-h 2019 Angiogenic potential of co-spheroids of neural stem cells and endothelial cells in injectable gelatin-based hydrogel *Mater. Sci. Eng., C* **99** 140–149
- [62] Kartberg A J, Hambiliki F, Arvidsson T, Stavreus-Evers A, Svalander P 2008 Vitrification with DMSO protects embryo membrane integrity better than solutions without DMSO *Reprod. Biomed. Online* **17** 378–384
- [63] Nichol J W, Koshy S T, Bae H, Hwang C M, Yamanlar S, Khademhosseini A 2010 Cell-laden microengineered gelatin methacrylate hydrogels *Biomaterials* **31** 5536–5544
- [64] Rammal H, et al. 2021 Advances in biomedical applications of self-healing hydrogels *Mater. Chem. Front.* **5** 4368–4400

- 1
2
3
4 [65] Taylor D L, in het Panhuis M 2016 Self-Healing Hydrogels *Advanced Materials*
5
6 **28** 9060-9093
7
8
9
10 [66] Xin X, Liu L, Liu Y, Leng J 2019 Mechanical Models, Structures, and Applications
11
12 of Shape-Memory Polymers and Their Composites *Acta Mech. Solida Sin.* **32** 535–565
13
14
15 [67] Song Y C, Khirabadi B S, Lightfoot F, Brockbank K G M, Taylor M J 2000
16
17 Vitreous cryopreservation maintains the function of vascular grafts *Nat. Biotechnol* **18**
18
19 296-299
20
21
22 [68] Jeon O, Lee Y B, Hinton T J, Feinberg A W, Alsberg E 2019 Cryopreserved cell-
23
24 laden alginate microgel bioink for 3D bioprinting of living tissues *Mater. Today Chem.*
25
26 **12** 61–70
27
28
29 [69] Blaeser A, Duarte Campos D F, Puster U, Richtering W, Stevens M M, Fischer H
30
31 2016 Controlling Shear Stress in 3D Bioprinting is a Key Factor to Balance Printing
32
33 Resolution and Stem Cell Integrity *Adv. Healthc. Mater.* **5** 326–333
34
35
36 [70] Derakhshanfar S, Mbeleck R, Xu K, Zhang X, Zhong W, Xing M 2018 3D
37
38 bioprinting for biomedical devices and tissue engineering: A review of recent trends
39
40 and advances *Bioactive Materials* **3** 144–156
41
42
43 [71] McKinnon D D, Domaille D W, Cha J N, Anseth K S 2014 Biophysically Defined
44
45 and Cytocompatible Covalently Adaptable Networks as Viscoelastic 3D Cell Culture
46
47 Systems *Advanced Materials* **26** 865–872
48
49
50
51
52
53
54
55
56
57
58
59
60



1
2
3
4
5
6
7
8
9
10
11
12
13
14
15
16
17
18
19
20
21
22
23
24
25
26
27
28
29
30
31
32
33
34
35
36
37
38
39
40
41
42
43
44
45
46
47
48
49
50
51
52
53
54
55
56
57
58
59
60

[72] Sinha R P, Häder D P 2002 UV-induced DNA damage and repair: a review

Photochem. Photobiol. Sci. **1** 225–236

[73] Bartnikowski M, Bartnikowski N J, Woodruff M A, Schrobback K, Klein T J 2015

Protective effects of reactive functional groups on chondrocytes in photocrosslinkable

hydrogel systems *Acta Biomaterialia* **27** 66–76

[74] Occhetta P, Visone R, Russo L, Cipolla L, Moretti M, Rasponi M 2015 VA-086

methacrylate gelatine photopolymerizable hydrogels: A parametric study for highly

biocompatible 3D cell embedding *J. Biomed. Mater. Res A* **103** 2109–2117

[75] Billiet T, Gevaert E, De Schryver T, Cornelissen M, Dubruel P 2014 The 3D

printing of gelatin methacrylamide cell-laden tissue-engineered constructs with high

cell viability *Biomaterials* **35** 49–62

[76] Wang Z, Kumar H, Tian Z, Jin X, Holzman J F, Menard F, Kim K 2018 Visible

Light Photoinitiation of Cell-Adhesive Gelatin Methacryloyl Hydrogels for

Stereolithography 3D Bioprinting *ACS Appl. Mater. Interfaces* **10** 26859–26869

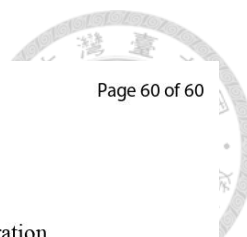
[77] Lin C H, Lin K F, Mar K, Lee S Y, Lin Y M 2016 Antioxidant N-Acetylcysteine

and glutathione increase the viability and proliferation of MG63 cells encapsulated in

the gelatin methacrylate/VA-086/blue light hydrogel system *Tissue Eng. Part C*

Methods **22** 792–800

[78] Riley L, Schirmer L, Segura T 2019 Granular hydrogels: emergent properties of



1
2
3
4 jammed hydrogel microparticles and their applications in tissue repair and regeneration

5
6
7 *Curr. Opin. Biotechnol.* **60** 1–8

8
9
10 [79] Mealy J E, Chung J J, Jeong H H, Issadore D, Lee D, Atluri P, Burdick J A 2018

11
12
13 Injectable Granular Hydrogels with Multifunctional Properties for Biomedical

14
15
16 Applications *Advanced Materials* **30** 1705912

17
18
19 [80] Highley C B, Song K H, Daly A C, Burdick J A 2019 Jammed Microgel Inks for

20
21
22 3D Printing Applications *Advanced Science* **6** 1801076

23

24

25

26

27

28

29

30

31

32

33

34

35

36

37

38

39

40

41

42

43

44

45

46

47

48

49

50

51

52

53

54

55

56

57

58

59

60

3.2. Publication 2 (second project): Self-healing of recombinant spider silk gel and coating

Reprinted from “Shin-Da Wu, Wei-Tsung Chuang, Jo-Chen Ho, Hsuan-Chen Wu, and Shan-hui Hsu. Self-Healing of Recombinant Spider Silk Gel and Coating. *Polymers* **2023**; 15(8): 1855.” with permission from Multidisciplinary Digital Publishing Institute (MDPI).





polymers

IMPACT
FACTOR
4.967

Indexed in:
PubMed

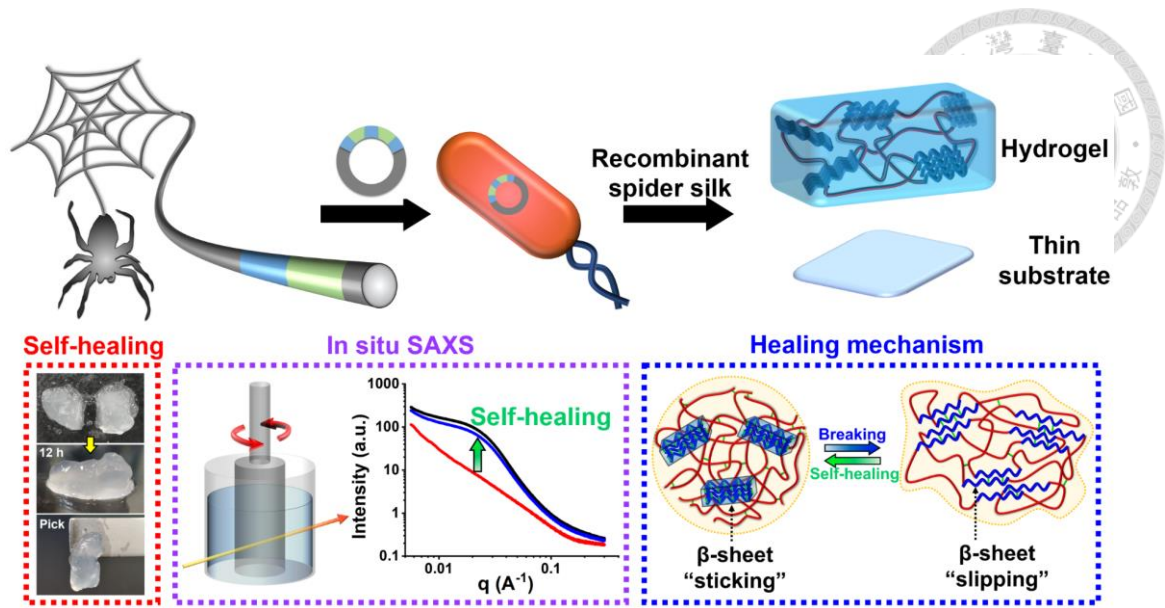


Self-Healing of Recombinant Spider Silk Gel and Coating





Volume 15 · Issue 8 | April (II) 2023



mdpi.com/journal/polymers
ISSN 2073-4360



Self-Healing of Recombinant Spider Silk Gel and Coating

Shin-Da Wu ¹, Wei-Tsung Chuang ², Jo-Chen Ho ³, Hsuan-Chen Wu ³ and Shan-hui Hsu ^{1,4,*}

¹ Institute of Polymer Science and Engineering, National Taiwan University, Taipei 10617, Taiwan
² National Synchrotron Radiation Research Center (NSRRC), Hsinchu 30076, Taiwan
³ Department of Biochemical Science and Technology, National Taiwan University, Taipei 10617, Taiwan
⁴ Institute of Cellular and System Medicine, National Health Research Institutes, Miaoli 350, Taiwan
* Correspondence: shhsu@ntu.edu.tw; Tel.: +886-2-3366-5313

Abstract: Self-healing properties, originating from the natural healing process, are highly desirable for the fitness-enhancing functionality of biomimetic materials. Herein, we fabricated the biomimetic recombinant spider silk by genetic engineering, in which *Escherichia coli* (*E. coli*) was employed as a heterologous expression host. The self-assembled recombinant spider silk hydrogel was obtained through the dialysis process (purity > 85%). The recombinant spider silk hydrogel with a storage modulus of ~250 Pa demonstrated autonomous self-healing and high strain-sensitive properties (critical strain ~50%) at 25 °C. The in situ small-angle X-ray scattering (in situ SAXS) analyses revealed that the self-healing mechanism was associated with the stick-slip behavior of the β -sheet nanocrystals (each of ~2–4 nm) based on the slope variation (i.e., ~−0.4 at 100%/200% strains, and ~−0.9 at 1% strain) of SAXS curves in the high q-range. The self-healing phenomenon may occur through the rupture and reformation of the reversible hydrogen bonding within the β -sheet nanocrystals. Furthermore, the recombinant spider silk as a dry coating material demonstrated self-healing under humidity as well as cell affinity. The electrical conductivity of the dry silk coating was ~0.4 mS/m. Neural stem cells (NSCs) proliferated on the coated surface and showed a 2.3-fold number expansion after 3 days of culture. The biomimetic self-healing recombinant spider silk gel and thinly coated surface may have good potential in biomedical applications.

Keywords: recombinant spider silk; self-healing; β -sheet nanocrystal; in situ SAXS



Citation: Wu, S.-D.; Chuang, W.-T.; Ho, J.-C.; Wu, H.-C.; Hsu, S.-h. Self-Healing of Recombinant Spider Silk Gel and Coating. *Polymers* **2023**, *15*, 1855. <https://doi.org/10.3390/polym15081855>

Academic Editor: Yen-Zen Wang

Received: 18 March 2023

Revised: 8 April 2023

Accepted: 10 April 2023

Published: 12 April 2023

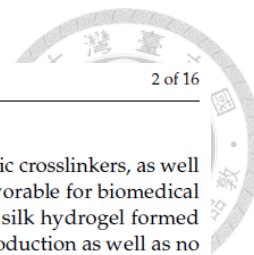


Copyright: © 2023 by the authors. Licensee MDPI, Basel, Switzerland. This article is an open access article distributed under the terms and conditions of the Creative Commons Attribution (CC BY) license (<https://creativecommons.org/licenses/by/4.0/>).

1. Introduction

Spiders are one of the oldest species on earth and have experienced evolution under various extreme conditions over hundreds of millions of years. Spider silks produced by spiders are unique protein-based biofibers possessing extraordinary properties, such as high tensile strength and toughness as well as supercontraction [1,2]. Meanwhile, spider silks are biocompatible and biodegradable [3]. These outstanding properties make spider silks an appealing natural material for use in the fields of medicine, textiles, and engineering [4]. However, the large-scale production of spider silks faces difficulty because spiders tend to kill each other when artificial breeding is carried out in a limited space. Meanwhile, the procedure of collecting spider silks from living spiders is cost-ineffective [5]. To overcome these problems, developing artificial recombinant spider silks by genetic engineering has become a promising solution for large-scale production [3,6]. For instance, *Escherichia coli* (*E. coli*), as a heterologous expression host, has widely been employed to produce recombinant spider silks via simple manipulation and cost-efficient production [7,8]. The produced recombinant spider silks can further self-assemble to form various products (e.g., hydrogel, films, microcapsules, tubes, and foams) for a wide range of applications [6].

Hydrogel, being a crosslinked three-dimensional (3D) polymeric network, is capable of retaining a large amount of water. Due to their high water content, hydrogels are appealing materials for use in biomedical applications [9]. Hydrogels based on recombinant spider silks can be formed from spider silk solutions by chemical or physical crosslinking [10].



Chemically crosslinked spider silk hydrogel involving the use of toxic crosslinkers, as well as initiators or catalysts in the crosslinking reaction, may be less favorable for biomedical applications [11,12]. In comparison, physically crosslinked spider silk hydrogel formed through the self-assembly process has the advantages of simple production as well as no need for additional toxic elements (e.g., crosslinkers, initiators, or catalysts) [12,13]. The mechanism of the self-assembly process is concentration-dependent gelation via nucleation and aggregation [12,14,15]. Upon gelation to a hydrogel, the spider silk is arranged into physically crosslinked β -sheet nanocrystal structures by chain entanglements and hydrophobic interactions [15–17]. The fabricated physically crosslinked recombinant spider silk hydrogel with semiflexible nature has a similar polymeric network to that of other biopolymers, which provides great potential for various applications [11,18,19].

Self-healing properties, originating from the natural healing process of all multicellular organisms, have received considerable attention in recent years due to the ability to heal structural damages and recover the original functions [20]. For instance, the natural spider silk fibers showed an intrinsic self-healing property, which is beneficial to restoring the morphology of spider webs after repeated damage [21]. Inspired by this fitness-enhancing functionality that has evolved under various surroundings for hundreds of millions of years, researchers have tried to develop materials with biomimetic self-healing properties [20]. The biomimetic self-healing materials are mainly classified into two categories based on the type of reversible interaction: dynamic supramolecular interactions and dynamic covalent bond interactions [22]. The dynamic supramolecular interactions have a better self-healing performance than the dynamic covalent bond interactions because of the lower bond energy [23]. Hydrogen bonding, as one of the common dynamic supramolecular interactions, has the advantages of natural reversibility as well as fast healing speed and high healing efficiency [20,24]. Due to these merits, Koga et al. developed a biomimetic spider silk-inspired film with a self-healing property based on multiple reversible hydrogen bonding [25]. However, the fabrication involved the use of toxic organic solvents, which may limit the development of biomedical applications owing to the residual solvents [26]. These things considered, to the best of our knowledge, the self-healing property and the healing mechanism of the recombinant spider silk hydrogel have not been reported.

In this study, we develop the biomimetic recombinant spider silk through genetic engineering. The biomimetic recombinant spider silk was then self-assembled into the physically crosslinked hydrogel. The recombinant spider silk hydrogel showed autonomic and reversible self-healing behavior. The possible self-healing mechanism of the hydrogel examined by in situ small-angle X-ray scattering (in situ SAXS) was identified as the reversible hydrogen bonding within the β -sheet nanocrystal. The recombinant spider silk cast coated and dried from the hydrogel demonstrated a self-healing capacity and cytocompatibility. The fabricated biomimetic self-healing recombinant spider silk hydrogel and surface coating may have good potential in terms of biomedical applications.

2. Materials and Methods

2.1. Production of Recombinant Spider Silk: Gene Construction and Protein Expression

The type 2 major ampullate silk spidroin-associated gene from the spider *Nephila pilipes* was identified by Sanger and next-generation sequencing (Illumina NovaSeq 6000; Illumina, San Diego, CA, USA). Specifically, the signature repetitive unit, containing alanine-rich and proline-rich motifs, was cloned by the Biobrick restriction enzyme assembly strategy (NheI and SpeI enzyme sets; New England BioLabs, Ipswich, MA, USA) to generate a 32-repeated synthetic spidroin gene. Subsequently, the spidroin gene was flanked by N-terminal and C-terminal domains, and the resulting constructed spidroin was cloned in the pET28 expression vector and transformed into *E. coli* BLR(DE3) cells for recombinant spider silk protein expression via 0.25 mM isopropyl β -D-1-thiogalactopyranoside (IPTG) induction at 20 °C for 16–20 h.

2.2. Purification of Recombinant Spider Silk Protein

BLR(DE3) cell pellets expressing the recombinant spider silk were resuspended in lysis buffer (10 mM Tris-HCl at pH 8.0, 1.25 mg/mL lysozyme, and 0.5% *v/v* Triton X-100) and subjected to ultrasonication for cell lysis on ice (450 W, on/off pulse cycle of 3 s/5 s for a total of 120 min). Subsequently, the samples were centrifuged and resuspended with a 5% SDS buffer (10 mM Tris-HCl at pH 8.0) with sonication (20.334 kHz) for a total of 20 min on ice, followed by four cycles of centrifugation and rinsing with deionized water. After the removal of impurities, the resultant white pellet of silk protein was frozen with liquid nitrogen and lyophilized by a vacuum freeze dryer (under a pressure of 1 Pa at $-20\text{ }^{\circ}\text{C}$). The final silk powder was kept in the desiccator at room temperature for storage.

2.3. Protein Analysis of Recombinant Spider Silk

For protein analysis, SDS-polyacrylamide gel electrophoresis (SDS-PAGE) was performed. Briefly, the dried silk was dissolved in hexafluoro-2-propanol (HFIP; Sigma-Aldrich, St. Louis, MI, USA), mixed with lithium dodecyl sulfate (LDS) sampling buffer, and heated at $95\text{ }^{\circ}\text{C}$ for 5–10 min. Subsequently, the silk samples were loaded to an 8% SDS-polyacrylamide gel and analyzed by electrophoresis using 3-(N-morpholino) propane sulfonic acid (MOPS) running buffer. Afterward, the gel was removed and stained with Commassive Blue R-250 for 20–30 min and then destained with a destaining solution for further gel imaging.

2.4. Fabrication of Recombinant Spider Silk Hydrogel and Coated Surface

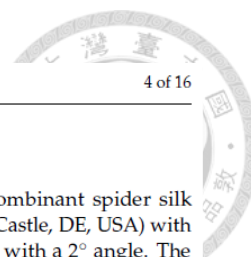
For hydrogel fabrication, the recombinant spider silk powder was first dissolved in 6 M guanidinium thiocyanate solution at the silk concentration of 8% and subsequently transferred into a dialysis tube (12–14 kDa cutoff membranes). The silk-containing tube was then dialyzed against fresh 10 mM Tris-HCl buffer at $25\text{ }^{\circ}\text{C}$, with the duration of the first two cycles being 3 h and a subsequent cycle continuing for 16 h. The dialyzed silk products were then kept at $4\text{ }^{\circ}\text{C}$ for 4 days to obtain stable silk hydrogels. For the fabrication of surface coating, the recombinant spider silk hydrogel was placed onto a plastic petri dish (Greiner). After drying for 24 h at the ambient temperature ($25\text{ }^{\circ}\text{C}$), the dry coating of recombinant spider silk was obtained.

2.5. FT-IR Analysis of Recombinant Spider Silk Hydrogel

The secondary structure analysis of spider silk hydrogel was carried out using the attenuated total reflectance-Fourier transform infrared (ATR-FTIR). Briefly, the spider silk hydrogel samples were submerged into liquid nitrogen and lyophilized by a vacuum freeze dryer. Afterward, the ATR-FTIR spectrum of the sample was detected using an FTIR spectrophotometer (Spectrum 100 model, PerkinElmer, Waltham, MA, USA) with a setup of the ATR mode. The sample was scanned 32 times with a resolution of 0.5 cm^{-1} in the wavelength range of $600\text{--}4000\text{ cm}^{-1}$. The resulting amide I area of the ATR-FTIR spectrum (wavenumber between $1580\text{ and }1720\text{ cm}^{-1}$) was chosen for Gaussian deconvolution via Origin 9.0 (OriginLab, Northampton, MA, USA), followed by the subsequent identification of secondary structures.

2.6. Self-Healing Properties of Recombinant Spider Silk Hydrogel and Coated Films

To demonstrate the self-healing property of recombinant spider silk hydrogel, the hydrogel was cut into two halves by a sharp blade and then brought into physical contact in ambient air ($25\text{ }^{\circ}\text{C}$) for 12 h without external intervention to test if they formed an integrated unit. To demonstrate the self-healing property of the recombinant spider silk coating, the surface of the dried gel coating was first gently scratched by a sharp blade. Subsequently, the scratched surface was immersed in deionized water for 10 min and then dried in ambient air ($25\text{ }^{\circ}\text{C}$) for 6 h. The self-healing property of the coated films was evaluated by an observation of the scratch variation.



2.7. Rheological Properties of Recombinant Spider Silk Hydrogel

For rheological evaluation, the dynamic behavior of the recombinant spider silk hydrogel was measured by a rheometer (HR-2, TA Instrument, New Castle, DE, USA) with a cone plate geometry. The diameter of the upper cone was 40 mm with a 2° angle. The measurements were conducted in three different modes at 25 °C. For a time-dependent measurement, the shear moduli [i.e., storage modulus (G') and loss modulus (G'')] of the hydrogel were measured against time with an oscillatory strain of 1% and a frequency of 1 Hz. For a strain-dependent measurement, the shear moduli of the hydrogel were measured against strains (1–500%) at a frequency of 1 Hz to determine the critical strain where a gel-to-sol transition occurred. For evaluating the self-healing property, the hydrogel was measured through continuous step changes of the oscillatory strain (damaging-healing cycles) at a frequency of 1 Hz to test the strain-induced structure destruction and recovery. Structure destruction was induced at a strain (60%) larger than the critical strain for a period of 5 min, and structure recovery was evaluated by decreasing the strain to the initial low strain (1%) for the same period of time (5 min).

2.8. In Situ SAXS Analysis of Recombinant Spider Silk Hydrogel

To analyze the structural variation of self-healing recombinant spider silk hydrogel under different strains, small-angle X-ray scattering (SAXS), combined with an in situ rheometer (Physica MCR-501, Anton Paar, Graz, Austria), was conducted at the beamline station 25A1 of Taiwan Photon Source (TPS 25A1) at National Synchrotron Radiation Research Center (NSRRC), Hsinchu, Taiwan. The SAXS profiles were measured under different oscillatory strains [i.e., 1% (beginning), 100%, 200%, and 1% (after 200%)] at 25 °C and a frequency of 1 Hz.

2.9. Cell Culture on Recombinant Spider Silk Substrate

Mouse neural stem cells (NSCs) were used for the cell culture test. NSCs derived from the brains of adult mice were cultured in Ham's F-12 and HG-DMEM (1:1), with 10% fetal bovine serum (FBS; Caisson), 1% penicillin-streptomycin-amphotericin (PSA; Caisson), and 400 mg/mL G418 (Invitrogen), in a humid incubator containing 5% CO₂ at 37 °C. The culture medium was refreshed every day. The recombinant spider silk-coated surface (area of 1.9 cm²), in a 24-well plate, was immersed in 75% ethanol for 1 h and irradiated with UV light for 1 h before NSC inoculation (cell density 4×10^4 cells/cm²). The proliferation of cells on the surface was evaluated by the Cell Counting Kit-8 (CCK-8; Sigma-Aldrich) assay [27]. The reacted CCK-8 solution was mixed gently to ensure uniformity and then collected into a 96-well plate. The absorbance, at a wavelength of 450 nm, was detected by a plate reader (SpectraMax M5, Molecular Devices, San Jose, CA, USA). Statistical differences between the experimental groups were performed with the student's *t*-test. The result was considered statistically significant when the *p*-value was smaller than 0.05.

2.10. Conductivity of the Recombinant Spider Silk Substrate

The electrical conductivity of the recombinant spider silk substrate was measured using a single-channel system sourcemeter (2601B, Keithley Instruments, Inc., Cleveland, OH, USA) under an applied voltage of 1 V at 25 °C.

3. Results

3.1. Fabrication of Recombinant Spider Silk

The recombinant spider silk was designed and generated via a genetic engineering approach, as shown in Figure 1A. First, the spidroin gene from the spider *Nephila pilipes* was synthesized. Subsequently, the spidroin gene was cloned in the vector and transformed into *E. coli* for recombinant spider silk protein expression. After the production and purification process, the final recombinant spider silk product containing N-terminal and C-terminal domains, as well as the tandem repetitive region in the presence of alanine-rich and proline-rich motifs, was obtained. The amino acid sequence ratio of the recombinant spider silk was

analyzed, as shown in Figure 1B. The representative amino acid sequences were Gly and Ala as well as Pro, indicating the low sequence complexity of the recombinant spider silk. The molecular weight of the recombinant spider silk protein detected by SDS-PAGE was ~120 kDa, as shown in Figure 1C. Further image analysis of spider silk protein extracted from SDS-PAGE data using ImageJ (version 1.52a, National Institutes of Health, Bethesda, MD, USA) demonstrated an overall purity of more than 85%.

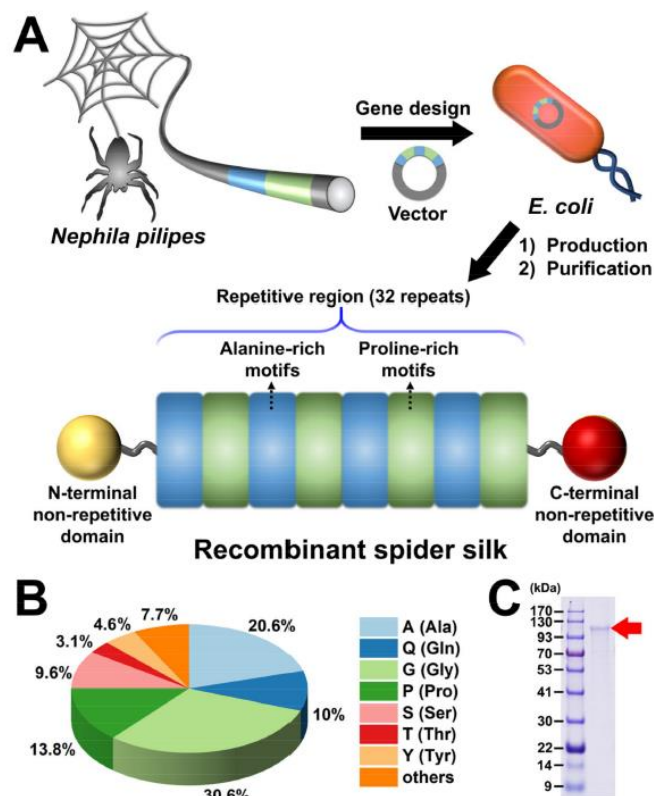


Figure 1. Schematic illustration of design for the recombinant spider silk. (A) Production and the modular structure of recombinant spider silk. (B) Amino acid sequence ratio of the recombinant spider silk. (C) The protein size of the recombinant spider silk, visualized by SDS-polyacrylamide gel electrophoresis (SDS-PAGE).

3.2. Fabrication of Recombinant Spider Silk Hydrogel

The fabrication procedure of the recombinant spider silk hydrogel is shown in Figure 2A. First, the freeze-dried recombinant spider silk powder was denatured in guanidinium thiocyanate solution to obtain the recombinant spider silk solution. The silk solution was then dialyzed against the Tris-HCl buffer for two days at 25 °C. During dialysis, the silk solution spontaneously self-assembled into hydrogel inside the dialysis tube. The stable physically crosslinked recombinant spider silk hydrogel was obtained after storage of the self-assembled hydrogel in a 4 °C fridge for 4 days.

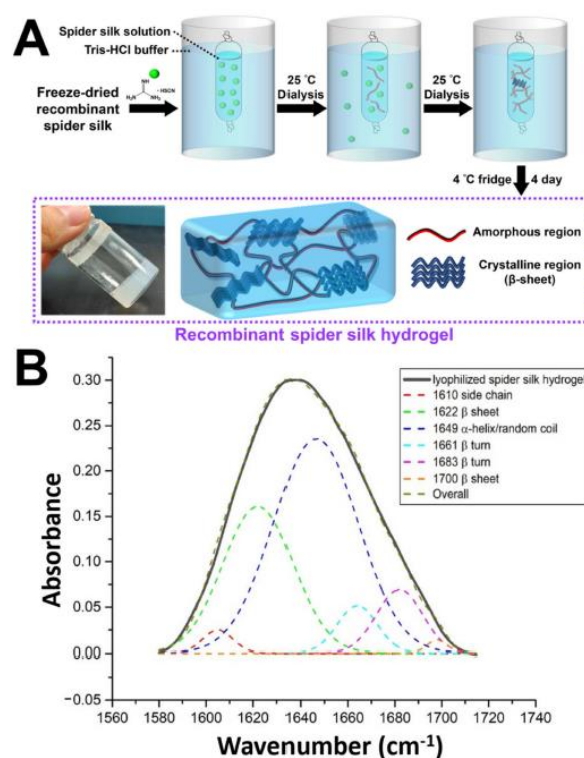


Figure 2. Fabrication and characterization of the recombinant spider silk hydrogel. (A) Schematic illustration of the fabrication procedure of the recombinant spider silk hydrogel. The inset shows the image of the fabricated recombinant spider silk hydrogel. (B) The attenuated total reflectance-Fourier transform infrared (ATR-FTIR) deconvolution analysis of lyophilized spider silk hydrogel.

3.3. FTIR Analysis of Recombinant Spider Silk Hydrogel

In spider silk structural research, the amide I region, generally between 1600 and 1700 cm^{-1} , has been widely exploited as a hallmark for estimating secondary structures [28]. According to Figure 2B, a series of peak assignments and fitting was carried out, with the β -sheet associated peak designated at 1622 cm^{-1} , random coil at 1649 cm^{-1} , and β -turn peaks at 1661 and 1683 cm^{-1} [29]. The relative content of the β -sheet structure over the total signals was estimated at around 30.9%, as an index for the crystallinity of the silk sample.

3.4. Self-Healing Property of Recombinant Spider Silk Hydrogel

The macroscopic self-healing behavior of the recombinant spider silk hydrogel is demonstrated in Figure 3. The hydrogel was cut into two halves and then brought into physical contact at $25\text{ }^{\circ}\text{C}$. After 12 h, the two hydrogel halves healed automatically and showed a smoother appearance. To verify the healing of the two hydrogel halves, the integrated unit was picked up vertically from half of it. The image showed that one half of the integrated unit could support the weight of another half without breaking. In addition, the integrated unit was stretched until breaking with a pair of tweezers. The location where the breaking occurred was different from the self-healed site of the hydrogel, verifying the self-healing ability of the recombinant spider silk hydrogel.

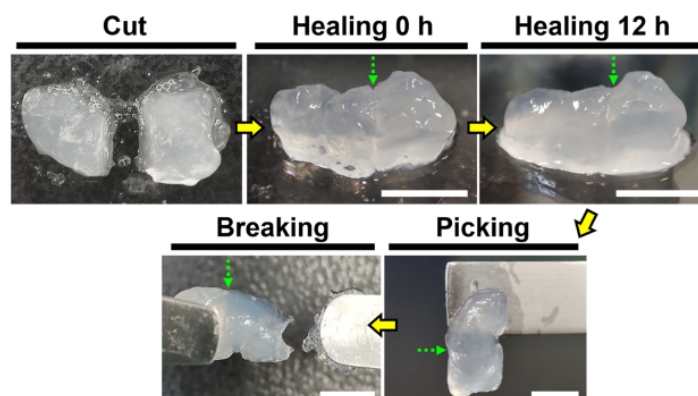


Figure 3. The self-healing behavior of the recombinant spider silk hydrogel, demonstrated by the gross test at 25 °C. The green dotted arrows show the cut section of the hydrogel. Scale bars represent 5 mm.

3.5. Rheological Properties of Self-Healing Recombinant Spider Silk Hydrogel

The rheological properties of the recombinant spider silk hydrogel are shown in Figure 4. For time-dependent measurement, the G' value of the hydrogel at equilibrium was ~ 250 Pa (Figure 4A). The critical strain for gel-to-sol transition (structure destruction) was determined by a strain-dependent measurement. The result showed that the critical strain of the hydrogel was $\sim 50\%$ (Figure 4B). The self-healing property of the recombinant spider silk hydrogel was evaluated by continuous step changes of the oscillatory strain between a lower strain (1%) and a higher strain (60%) that exceeded the critical strain (Figure 4C). At the lower strain (1%), G' was higher than G'' and both shear moduli kept steady with time. Regarding the higher strain (60%), the hydrogel showed $G'-G''$ crossover and turned into the sol state. When reversing to the lower strain (1%), both shear moduli (G' and G'') of the hydrogel recovered immediately to their initial values. The reproducible rheological property identified during multiple damaging-healing cycles confirmed the self-healing behavior of the recombinant spider silk hydrogel.

3.6. In Situ SAXS Analysis of Self-Healing Recombinant Spider Silk Hydrogel

The self-healing property of the recombinant spider silk hydrogel was further supported by in situ SAXS analyses, as shown in Figure 5. The in situ SAXS setup combined the collimated X-ray beam with the rheometer that loaded with the recombinant spider silk hydrogel (Figure 5A). The SAXS profiles were measured at different oscillatory strains to analyze the structural variation of the hydrogel (Figure 5B). At the initial low strain [i.e., 1% (beginning)], the SAXS profile revealed a broad hump signal in the q -range of $\sim 0.008\text{--}0.08 \text{ \AA}^{-1}$, which may reflect the featured spherical aggregates [30,31]. The radius of the spherical aggregates was calculated to be ~ 9 nm. The distance among the spherical aggregates was $\sim 8\text{--}80$ nm. The slope of the curve in the high q -range (i.e., $0.15\text{--}0.3 \text{ \AA}^{-1}$) was ~ -0.9 , which may be ascribed to the rod-like β -sheet nanocrystals [32]. The size of the β -sheet nanocrystals was $\sim 2\text{--}4$ nm. Upon applying the high strains (i.e., 100% and 200%) that exceeded the critical strain, the hump disappeared in the SAXS profiles. Such variation indicated that the spherical aggregates were destroyed. The fractal dimension calculated based on the power law and the slope of the curve was ~ 1.7 , which suggested an irregular shape of the aggregates. The slope of the curve in the high q -range decreased to ~ -0.4 , indicating the failure of the β -sheet nanocrystals. Afterward, when the strain was reversed from 200% to the initial low value of 1%, the hump reappeared at the same q region with a similar intensity to that of the initial SAXS profile. This finding indicated the structure recovery of the spherical aggregates. Furthermore, the slope of the curve in the

high q -range returned to a range near the initial value (i.e., ~ -0.9), indicating the repairing of the rod-like β -sheet nanocrystals.

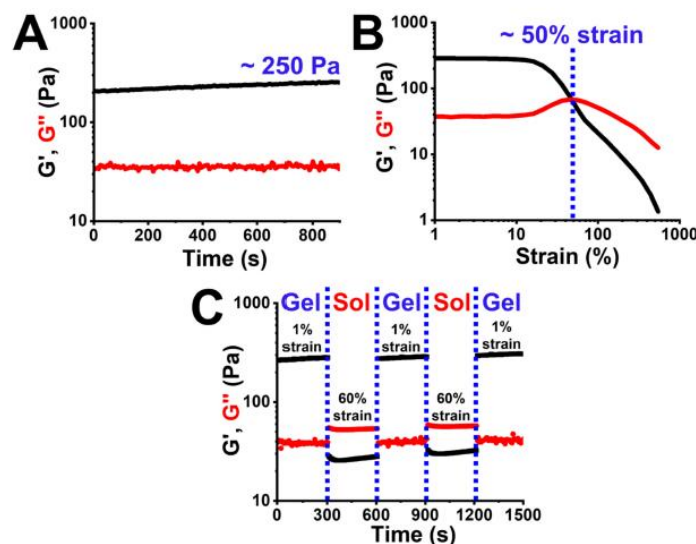


Figure 4. Rheological properties of the self-healing recombinant spider silk hydrogel at 25 °C. (A) The time-dependent moduli (G' and G'') of the hydrogel were measured at 1% strain and 1 Hz. (B) The strain-dependent moduli (G' and G'') were measured at 1 Hz. (C) The damaging-healing property of the self-healing recombinant spider silk hydrogel was measured through the continuous step changes of oscillatory strain at 1 Hz.

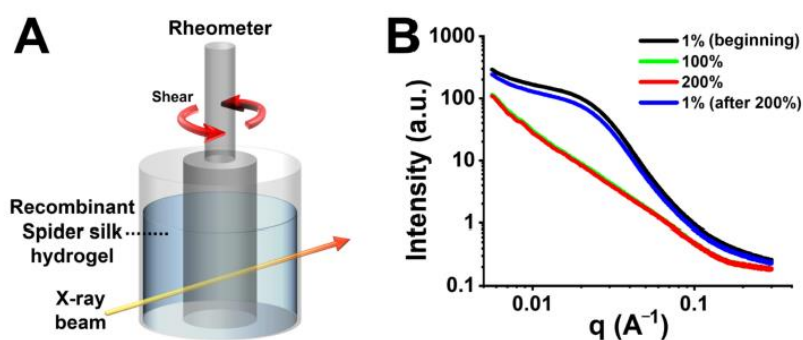


Figure 5. In situ small-angle X-ray scattering (in situ SAXS) measurements of the self-healing recombinant spider silk hydrogel at 25 °C. (A) Schematic illustration of the experimental setup for in situ SAXS measurements. (B) The small-angle X-ray scattering (SAXS) profiles of the recombinant spider silk hydrogel under different strains [i.e., 1% (beginning), 100%, 200%, and 1% (after 200%)].

3.7. Self-Healing Mechanism of Recombinant Spider Silk Hydrogel

The possible mechanism for the autonomic self-healing property of the recombinant spider silk hydrogel is illustrated in Figure 6. The recombinant spider silk consisted of segmented amino acid sequences with alanine-rich and proline-rich motifs (cf. Figure 1A). The alanine-rich and proline-rich motifs were driven to form rod-like β -sheet nanocrystals (each of ~ 2 – 4 nm) and amorphous regions, respectively, within the hydrogel. At the

lower strain (1%), the hydrogel was stable because the β -sheet nanocrystals were firmly locked by the hydrogen bonds. Meanwhile, some hydrogen bonds also existed within the amorphous regions. A large amount of hydrogen bonding allowed the formation of spherical aggregates (each of ~ 9 nm). Upon applying a higher strain that exceeded the critical strain ($>50\%$), the spherical aggregates were destroyed and became irregular aggregates (cf. Figure 5B). Such structural variation could be mainly ascribed to the rupture of hydrogen bonds within the β -sheet nanocrystals, leading to the slipping and failure of the β -sheet nanocrystals. Meanwhile, the hydrogen bonds within the amorphous regions were also broken. Upon reversing to the lower strain (1%), the spherical aggregates reformed. This structure recovery could be mainly attributed to the regaining of the hydrogen bonds within the β -sheet nanocrystals, leading to the sticking of the β -sheet nanocrystals. The stick-slip behavior of the β -sheet nanocrystals enabled the damaging and healing of the hydrogel network. In addition, some hydrogen bonds within the elastic amorphous regions may also reform and facilitate the healing of hydrogel.

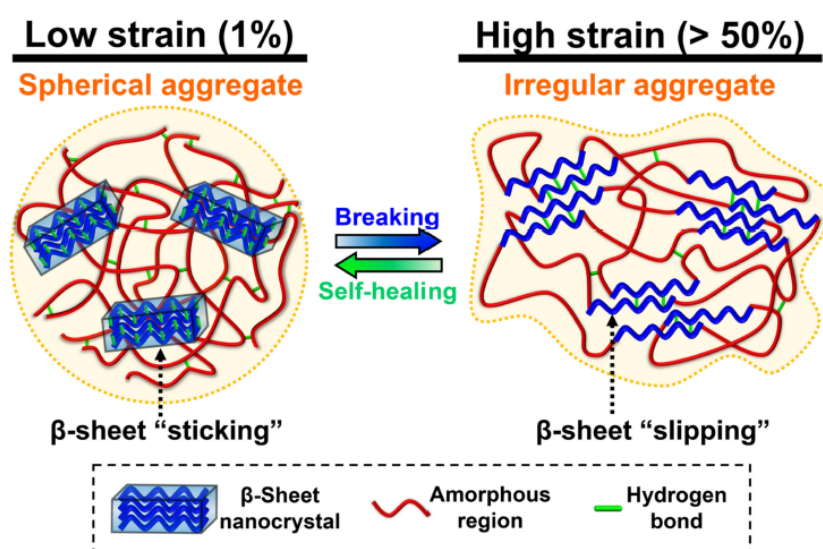


Figure 6. The hypothetical self-healing mechanism of the recombinant spider silk under low strain (1%) and high strain ($>50\%$).

3.8. Fabrication and Characterization of Recombinant Spider Silk-Coated Substrate

The recombinant spider silk substrate was fabricated by coating and drying the recombinant spider silk hydrogel at ambient air for 24 h, as shown in Figure 7A. The thickness of the dried silk substrate (thin film) was about $200\ \mu\text{m}$. The electrical conductivity of the dried silk substrate was $\sim 0.4\ \text{mS/m}$. The self-healing behavior of the recombinant spider silk thin substrate demonstrated by a scratch test is shown in Figure 7B. After the scratched surface was treated with water for 10 min and dried for 6 h, the major scratch width and the minor scratch width on the surface of the substrate were reduced from 23.2 ± 2.5 to $15.1 \pm 3.6\ \mu\text{m}$ and from 14.2 ± 1.9 to $9.9 \pm 1.3\ \mu\text{m}$, respectively. Meanwhile, the appearance of both the major and minor scratches after the treatment became less distinct than that of the initial scratches. These scratch changes verified the healing behavior of the recombinant spider silk. The cytocompatibility of the recombinant spider silk substrate is demonstrated in Figure 7C,D. The proliferation of NSCs on the spider silk substrate during a period of 3 days was observable. After 3 days of cell culture, the cell viability significantly increased to $\sim 230\%$.

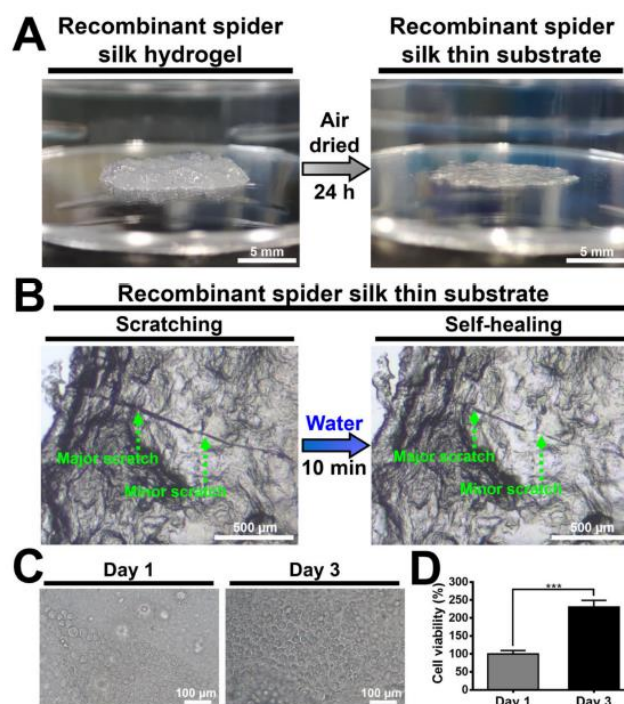


Figure 7. Fabrication, self-healing, and cytocompatibility of the recombinant spider-silk-coated films. (A) Images showing the recombinant spider silk fabricated from casting the recombinant spider silk hydrogel under ambient air and drying for 24 h at 25 °C. The thickness of the film was ~200 μm . (B) Optical microscopic images showing the healing of scratches on the surface of the recombinant spider silk after immersion in water for 10 min and then drying in ambient air for 6 h at 25 °C. The green dotted arrows show the major scratches and the minor scratches. The proliferation of neural stem cells (NSCs) on the recombinant spider silk substrate was evaluated by (C) observation under the optical microscope and (D) the Cell Counting Kit-8 (CCK-8) assay. The cell viability was deducted from that of the control group (same substrates but without cells) and normalized to the initial value (i.e., cell viability at 1 day serving as 100%). *** $p < 0.001$ between the indicated groups.

4. Discussion

Major ampullate spidroin (MaSp), also known as spider dragline silk, receives more attention than other spidroins due to its known protein sequence and desired mechanical properties [33]. MaSp includes two main types of proteins, i.e., major ampullate spidroin 1 (MaSp1) and major ampullate spidroin 2 (MaSp2). The most apparent difference between MaSp1 and MaSp2 is the proline content in the protein sequence. MaSp2 is a proline-rich protein (~9%), whereas MaSp1 contains few proline residues (<1%) [34,35]. The proline-rich motif in MaSp2 acts to form the β -turn spiral structure for providing high elasticity [36], which plays a key role in the function of the natural spider silk, such as supercontraction behavior [4,37]. For the large-scale fabrication of the biomimetic MaSp2 spider silk, various expression systems (e.g., bacteria, yeasts, plants, insects, silkworms, and animals) are used to attempt the recombinant production of spider silk [38]. *E. coli* is one of the most popular expression platforms for the large-scale genetic engineering production of recombinant spider silk due to the advantages of its well-known genetics, easy genetic manipulation, short life cycle, and easy culture [35,39]. In this study, *E. coli* was employed as a heterologous expression host to synthesize the recombinant MaSp2 spider silk.

The protein sequence of the designed recombinant MaSp2 spider silk based on the spider *Nephila pilipes* has a highly repetitive core region consisting of alternating alanine-rich and proline-rich motifs. The alanine-rich motifs dominated by A_n or $(GA)_n$ (A: Ala; G: Gly) form the β -sheet crystalline region for the high tensile strength of the spider silk, while the proline-rich motifs dominated by GPGXX (P: Pro; X: Gly, Gln, Tyr, Ala, Ser) form the amorphous region for the extensibility of the spider silk [40,41]. The two non-repetitive terminal domains (i.e., N-terminal domain and C-terminal domain) flanking the repetitive core region are important for the storage of proteins in the gland and the initiation of fiber assembly [42–44]. The synthesized recombinant MaSp2 spider silk powder was further processed to the recombinant spider silk hydrogel according to a previously published procedure [12]. The self-assembling mechanism of the recombinant spider silk hydrogel during dialysis is the nucleation-aggregation process followed by concentration-dependent gelation [11,14]. During gelation, the α -helical and random coil conformations of the spider silk protein chains are arranged into β -sheet conformations due to the hydrophobic interactions and entanglements [12,15–17]. The fabricated recombinant spider silk hydrogel in the present study involving an aqueous solution could possess greater potential for broader biomedical applications, compared to other recombinant spider silk gels derived from organic solvents [13].

The fabricated recombinant spider silk hydrogel evaluated by the rheological measurements was a soft gel ($G' \sim 250$ Pa) [45]. The critical strain of the recombinant spider silk hydrogel was low ($\sim 50\%$), indicating the high strain-sensitive property. The high strain-sensitive property is typically attributed to the supramolecular interaction of the physical hydrogel, e.g., hydrogen bonding [46–48]. The bond energy of hydrogen bonding within the physical hydrogel is much lower than that of covalent bonding within the chemical hydrogel [49,50]. Therefore, when applying a higher strain that exceeded the critical strain, the weak hydrogen bonding was easily broken, and the 3D network of the physical hydrogel was then destroyed into a sol-like state [51]. However, due to the reversible nature of hydrogen bonding, many physical hydrogels in the published literature could reconstruct their network (i.e., self-healing) after reversing to the initial low strain [52]. In this study, the self-healing behavior of the recombinant spider silk hydrogel was observed and confirmed by the gross test and the rheological damaging-healing test. It has to be noted that, the rheological damaging-healing test was conducted right after the strain-dependent measurement. Due to the large applied strain (i.e., 500%) in the strain-dependent measurement, the hydrogel was broken thoroughly and needed more time to repair. Therefore, within the rheological damaging-healing test, the initial shear moduli were slightly lower than the final shear moduli of the self-healed hydrogel. This result also confirmed the self-healing property of the recombinant spider silk hydrogel.

Self-healing materials can be categorized into extrinsic healing and intrinsic healing, or non-autonomous healing and autonomous healing [53]. The extrinsic self-healing materials employ the encapsulation of external healing agents to achieve self-healing. However, the major disadvantage of extrinsic healing is the limited one-time healing cycle [54]. In comparison, the intrinsic self-healing materials employing reversible bonds to restore the structure can heal multiple cycles without a need for healing agents or catalysts. The non-autonomous healing materials require external stimuli, such as light and heat, to trigger structural recovery. However, external stimuli could have adverse effects on the cells in biomedical applications [55]. In comparison, autonomous healing materials can automatically and reversibly repair the damages [53]. In this study, the self-healing property of the recombinant spider silk hydrogel is autonomous and intrinsic, according to the gross test and the rheological damaging-healing test.

The β -sheet nanocrystals are one of the key elements for the toughness and strength of natural silks (e.g., spider silk and silkworm silk) [30,56]. The sizes of the β -sheet nanocrystals in natural silks are typically less than 10 nm in all three dimensions [57]. According to the molecular dynamics simulations, Keten et al. demonstrated that the β -sheet nanocrystals with different sizes within the spider silk can be categorized into

two types [58]. The critical size of the β -sheet nanocrystals was 2–4 nm. During large lateral loading, the failure mechanism for the β -sheet nanocrystal with a size larger than the critical value was dominated by the bending deformation [58]. The cracks caused by the non-uniform tension were easily attacked by water molecules in the surroundings, which resulted in a large-scale rupture of the hydrogen bonds [59]. In comparison, the failure mechanism for the β -sheet nanocrystal of the smaller size was dominated by the uniform shear deformation, owing to the greater stiffness and fracture resistance [58]. Under a homogeneous shear, the cooperative rupture of the hydrogen bonds prevented the internal defects of the nanocrystals from being exposed to the surrounding water. Based on the characteristic stick-slip mechanism of the hydrogen bonds via repeatable rupturing and reformation, the self-healing behavior of the smaller β -sheet nanocrystal could occur. In this study, the failure mechanism for the β -sheet nanocrystal of the smaller size (~2–4 nm) may be dominated by the uniform shear deformation. Through the stick-slip mechanism of the β -sheet nanocrystals under low and high shear deformation, the self-healing behavior of the recombinant spider silk hydrogel was achieved.

The recombinant squid ring teeth (SRT) protein, which consisted of highly repetitive tandem polypeptides similar to the recombinant spider silk protein, also showed the self-healing behavior discussed in the published literature [60–62]. For instance, Ding et al. showed that the autonomous self-healing behavior of the SRT protein hydrogel was based on the breakage and reformation of the β -sheet nanocrystals [60]. For example, Pena-Francesch et al. fabricated the SRT protein film with the self-healing property, which mainly relied on the reversible hydrogen bonding within the β -sheet nanocrystals [61]. In the film system, water was necessarily employed for breaking the hydrogen bonding within the amorphous region, which can facilitate the chain mobility and network repair [4,61,63]. Based on the same principle and similar conditions, Koga et al. demonstrated that the spider-silk-inspired multiblock copolymer film showed the self-healing behavior, which also relied on the reversible hydrogen bonding within the β -sheet nanocrystals [25]. In this study, we infer that the self-healing mechanism of the recombinant spider silk thin surface coating was based on the chain diffusion within the amorphous region and the reversible hydrogen bonds within the β -sheet nanocrystals.

The advantage of our recombinant spider silk-coated film is the feasibility of biomedical applications due to no involvement of organic solvents in the fabrication process [26]. NSCs from the identical cell line in our previously published literature were used to evaluate the cytocompatibility of the recombinant spider silk-coated film [27]. NSCs proliferated on the coated film and a significant difference in cell viability was observed between Day 1 and Day 3. The proliferation rates of NSCs were similar to that of NSCs on other biocompatible films [27]. Based on the results, the cytocompatibility of the recombinant spider silk-coated film was confirmed. Overall, the main goal of this study focuses on the self-healing mechanism of the recombinant spider silk hydrogel and surface coating. Although the surface of the coated and dried recombinant spider silk was rough, a smoother film may be fabricated by drying the hydrogel directly in the desired container after dialysis, instead of moving it to other containers before drying.

Natural dragline spider silk has some fascinating properties when it is wetted. One of the properties is known as supercontraction, which is the ability of the silk to shrink significantly in response to changes in humidity [2]. This property plays an important role in the functional adaptation of spider webs. Under high relative humidity, the spider silk in the supercontracted state behaves as a rubber network because the hydrogen bonding within the amorphous region of the spider silk is broken [64,65]. Meanwhile, the electrical conductivity of the spider silk at this state was found to be enhanced, compared to that of the original dry sample [66]. The conductivity ranges from 10^{-4} mS/m to 10^0 mS/m, depending on the relative humidity. The enhanced conductivity of the spider silk under hydration could be attributed to the increased mobility of the silk protein chains [67,68]. Furthermore, it is worth mentioning that water can be retained in the silk even after subsequent drying [69]. In this study, the dried recombinant spider silk film fabricated from

the hydrogel showed a conductivity of ~ 0.4 mS/m, which is compatible with the previous literature. In addition, the thin recombinant spider silk coating with cytocompatibility and biodegradability has great potential for biomedical applications, such as protecting various surfaces of medical implants [70]. Overall, we expect that the self-healing property and the healing mechanism of the recombinant spider silk hydrogel and cast thin films from the hydrogel in this study will assist in the design and optimization of self-healing silk-related biomaterials for fundamental research and functional applications. The potential limitation of the fabricated recombinant spider silk hydrogel in this study was the relatively low G' (~ 250 Pa). For our future work, we plan to develop a series of recombinant spider silk hydrogels with tunable mechanical properties for broader biomedical applications. Furthermore, recombinant spider silk hydrogels incorporating different biomaterials will be developed to achieve multi-intelligent hydrogels with various functionalities (e.g., 3D printable self-healing hydrogel).

5. Conclusions

The self-healing recombinant spider silk hydrogel and thin coating were fabricated. The soft self-healing recombinant spider silk hydrogel (~ 250 Pa) demonstrated a high strain-sensitive property (critical strain $\sim 50\%$), which could be ascribed to the supramolecular interactions of the hydrogen bonding. The possible self-healing mechanism examined by in situ SAXS was mainly based on the stick-slip behavior of the β -sheet nanocrystals. Through the rupture and reformation of the reversible hydrogen bonding within the β -sheet nanocrystals, the self-healing behavior of the recombinant spider silk hydrogel was achieved. For the cast and dried coating, the possible self-healing mechanism was based on the chain diffusion within the amorphous region and the reversible hydrogen bonding within the β -sheet nanocrystals. Furthermore, the coated substrate demonstrated cytocompatibility (~ 2.3 -fold increase in the proliferation of NSCs after 3 days) and an electrical conductivity of ~ 0.4 mS/m. The developed biomimetic self-healing recombinant spider silk hydrogel, coating, and dried films may have good potential for broad biomedical applications.

Author Contributions: Conceptualization, S.-D.W., H.-C.W. and S.-h.H.; Methodology, S.-D.W., W.-T.C., J.-C.H., H.-C.W. and S.-h.H.; Resources, W.-T.C., H.-C.W. and S.-h.H.; Visualization, S.-D.W.; Validation, H.-C.W. and S.-h.H.; Writing—Original Draft Preparation, S.-D.W. and S.-h.H.; Writing—Review & Editing, H.-C.W. and S.-h.H.; Supervision, H.-C.W. and S.-h.H. All authors have read and agreed to the published version of the manuscript.

Funding: This work was supported by the National Science and Technology Council, Taiwan, R.O.C. (NSTC 111-2221-E-002-052-MY3), and partially supported by the National Taiwan University (NTU-CC-112L890801). NSCs were kindly provided by Ing-Ming Chiu (Institute of Cellular and Systems Medicine, National Health Research Institutes, Zhunan, Taiwan). We are also grateful to the National Synchrotron Radiation Research Center (NSRRC), Republic of China (2022-1-042-1). In particular, Jih-Min Lin, for providing the resources and technical support. We also thank Shih-Ho Lin for assistance in the SAXS experiment and Tsai-Yu Chen for assistance in the cell experiment.

Institutional Review Board Statement: Not applicable.

Data Availability Statement: Not applicable.

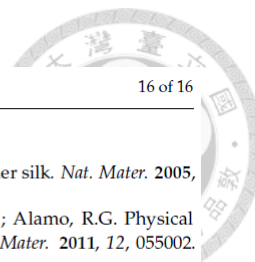
Conflicts of Interest: The authors declare no conflict of interest.

References

1. Omenetto, F.G.; Kaplan, D.L. New Opportunities for an Ancient Material. *Science* **2010**, *329*, 528–531. [[CrossRef](#)] [[PubMed](#)]
2. Bell, F.I.; McEwen, I.J.; Viney, C. Supercontraction stress in wet spider dragline. *Nature* **2002**, *416*, 37. [[CrossRef](#)] [[PubMed](#)]
3. Chung, H.; Kim, T.Y.; Lee, S.Y. Recent advances in production of recombinant spider silk proteins. *Curr. Opin. Biotechnol.* **2012**, *23*, 957–964. [[CrossRef](#)]
4. Li, J.; Li, S.; Huang, J.; Khan, A.Q.; An, B.; Zhou, X.; Liu, Z.; Zhu, M. Spider Silk-Inspired Artificial Fibers. *Adv. Sci.* **2022**, *9*, 2103965. [[CrossRef](#)]

5. Bittencourt, D.M.d.C.; Oliveira, P.; Michalczechen-Lacerda, V.A.; Rosinha, G.M.S.; Jones, J.; Rech Filho, E.L. Bioengineering of spider silks for the production of biomedical materials. *Front. Bioeng. Biotechnol.* **2022**, *10*, 958486. [[CrossRef](#)]
6. Debabov, V.G.; Bogush, V.G. Recombinant Spidroins as the Basis for New Materials. *ACS Biomater. Sci. Eng.* **2020**, *6*, 3745–3761. [[CrossRef](#)]
7. Liu, T.; Liang, A.; Liang, Z.; Li, G.; Wang, F. Construction of a synthetic Araneus ventricosus dragline silk gene multimer and its expression in *Escherichia coli*. *3 Biotech* **2018**, *8*, 252. [[CrossRef](#)]
8. Edlund, A.M.; Jones, J.; Lewis, R.; Quinn, J.C. Economic feasibility and environmental impact of synthetic spider silk production from *Escherichia coli*. *New Biotechnol.* **2018**, *42*, 12–18. [[CrossRef](#)]
9. Hoffman, A.S. Hydrogels for biomedical applications. *Adv. Drug Deliv. Rev.* **2012**, *64*, 18–23. [[CrossRef](#)]
10. Humenik, M.; Smith, A.M.; Scheibel, T. Recombinant Spider Silks—Biopolymers with Potential for Future Applications. *Polymers* **2011**, *3*, 640–661. [[CrossRef](#)]
11. Rammensee, S.; Huemmerich, D.; Hermanson, K.D.; Scheibel, T.; Bausch, A.R. Rheological characterization of hydrogels formed by recombinantly produced spider silk. *Appl. Phys. A* **2006**, *82*, 261–264. [[CrossRef](#)]
12. Schacht, K.; Scheibel, T. Controlled Hydrogel Formation of a Recombinant Spider Silk Protein. *Biomacromolecules* **2011**, *12*, 2488–2495. [[CrossRef](#)] [[PubMed](#)]
13. Neubauer, V.J.; Trossmann, V.T.; Jacobi, S.; Döbl, A.; Scheibel, T. Recombinant Spider Silk Gels Derived from Aqueous–Organic Solvents as Depots for Drugs. *Angew. Chem. Int. Ed.* **2021**, *60*, 11847–11851. [[CrossRef](#)]
14. Slotta, U.K.; Rammensee, S.; Gorb, S.; Scheibel, T. An Engineered Spider Silk Protein Forms Microspheres. *Angew. Chem. Int. Ed.* **2008**, *47*, 4592–4594. [[CrossRef](#)]
15. Kim, U.-J.; Park, J.; Li, C.; Jin, H.-J.; Valluzzi, R.; Kaplan, D.L. Structure and Properties of Silk Hydrogels. *Biomacromolecules* **2004**, *5*, 786–792. [[CrossRef](#)]
16. Matsumoto, A.; Chen, J.; Collette, A.L.; Kim, U.-J.; Altman, G.H.; Cebe, P.; Kaplan, D.L. Mechanisms of Silk Fibroin Sol–Gel Transitions. *J. Phys. Chem. B* **2006**, *110*, 21630–21638. [[CrossRef](#)]
17. Wang, X.; Kluge, J.A.; Leisk, G.G.; Kaplan, D.L. Sonication-induced gelation of silk fibroin for cell encapsulation. *Biomaterials* **2008**, *29*, 1054–1064. [[CrossRef](#)]
18. Hsu, S.-h.; Hung, K.-C.; Lin, Y.-Y.; Su, C.-H.; Yeh, H.-Y.; Jeng, U.S.; Lu, C.-Y.; Dai, S.A.; Fu, W.-E.; Lin, J.-C. Water-based synthesis and processing of novel biodegradable elastomers for medical applications. *J. Mater. Chem. B* **2014**, *2*, 5083–5092. [[CrossRef](#)]
19. Hu, X.; Liao, M.; Gong, H.; Zhang, L.; Cox, H.; Waigh, T.A.; Lu, J.R. Recent advances in short peptide self-assembly: From rational design to novel applications. *Curr. Opin. Colloid Interface Sci.* **2020**, *45*, 1–13. [[CrossRef](#)]
20. Diesendruck, C.E.; Sottos, N.R.; Moore, J.S.; White, S.R. Biomimetic Self-Healing. *Angew. Chem. Int. Ed.* **2015**, *54*, 10428–10447. [[CrossRef](#)]
21. Becker, N.; Oroudjev, E.; Mutz, S.; Cleveland, J.P.; Hansma, P.K.; Hayashi, C.Y.; Makarov, D.E.; Hansma, H.G. Molecular nanosprings in spider capture-silk threads. *Nat. Mater.* **2003**, *2*, 278–283. [[CrossRef](#)] [[PubMed](#)]
22. Roy, N.; Bruchmann, B.; Lehn, J.-M. DYNAMERS: Dynamic polymers as self-healing materials. *Chem. Soc. Rev.* **2015**, *44*, 3786–3807. [[CrossRef](#)] [[PubMed](#)]
23. Ke, R.; Lin, Z.; Zhang, H.; Zhou, S. Research Progress in Intrinsic Self-healing Polyurethane Materials Based on Dynamic Reversible Non-Covalent Bonds. *J. Phys. Conf. Ser.* **2022**, *2324*, 012007. [[CrossRef](#)]
24. Xie, Z.; Hu, B.-L.; Li, R.-W.; Zhang, Q. Hydrogen Bonding in Self-Healing Elastomers. *ACS Omega* **2021**, *6*, 9319–9333. [[CrossRef](#)] [[PubMed](#)]
25. Koga, T.; Morishita, T.; Harumoto, Y.; Nishimura, S.-n.; Higashi, N. Spider silk-inspired peptide multiblock hybrid copolymers for self-healable thin film materials. *Mater. Adv.* **2021**, *2*, 7851–7860. [[CrossRef](#)]
26. Larrañeta, E.; Henry, M.; Irwin, N.J.; Trotter, J.; Perminova, A.A.; Donnelly, R.F. Synthesis and characterization of hyaluronic acid hydrogels crosslinked using a solvent-free process for potential biomedical applications. *Carbohydr. Polym.* **2018**, *181*, 1194–1205. [[CrossRef](#)]
27. Xu, J.; Fu, C.-Y.; Tsai, Y.-L.; Wong, C.-W.; Hsu, S.-h. Thermoresponsive and Conductive Chitosan-Polyurethane Biocompatible Thin Films with Potential Coating Application. *Polymers* **2021**, *13*, 326. [[CrossRef](#)]
28. Boulet-Audet, M.; Vollrath, F.; Holland, C. Identification and classification of silks using infrared spectroscopy. *J. Exp. Biol.* **2015**, *218*, 3138–3149. [[CrossRef](#)]
29. Tso, I.M.; Wu, H.-C.; Hwang, I.-R. Giant wood spider *Nephila pilipes* alters silk protein in response to prey variation. *J. Exp. Biol.* **2005**, *208*, 1053–1061. [[CrossRef](#)]
30. Jin, H.-J.; Kaplan, D.L. Mechanism of silk processing in insects and spiders. *Nature* **2003**, *424*, 1057–1061. [[CrossRef](#)]
31. Martel, A.; Burghammer, M.; Davies, R.J.; Di Cola, E.; Vendrely, C.; Riekel, C. Silk Fiber Assembly Studied by Synchrotron Radiation SAXS/WAXS and Raman Spectroscopy. *J. Am. Chem. Soc.* **2008**, *130*, 17070–17074. [[CrossRef](#)]
32. Thomas, S.; Shanks, R.; Joy, J. *Micro- and Nanostructured Polymer Systems: From Synthesis to Applications*; CRC Press: Boca Raton, FL, USA, 2016.
33. Saric, M.; Eisoldt, L.; Döring, V.; Scheibel, T. Interplay of Different Major Ampullate Spidroins during Assembly and Implications for Fiber Mechanics. *Adv. Mater.* **2021**, *33*, 2006499. [[CrossRef](#)]

34. Tucker, C.L.; Jones, J.A.; Bringham, H.N.; Copeland, C.G.; Addison, J.B.; Weber, W.S.; Mou, Q.; Yarger, J.L.; Lewis, R.V. Mechanical and Physical Properties of Recombinant Spider Silk Films Using Organic and Aqueous Solvents. *Biomacromolecules* **2014**, *15*, 3158–3170. [[CrossRef](#)]
35. Cao, H.; Parveen, S.; Ding, D.; Xu, H.; Tan, T.; Liu, L. Metabolic engineering for recombinant major ampullate spidroin 2 (MaSp2) synthesis in *Escherichia coli*. *Sci. Rep.* **2017**, *7*, 11365. [[CrossRef](#)]
36. Hayashi, C.Y.; Lewis, R.V. Evidence from flagelliform silk cDNA for the structural basis of elasticity and modular nature of spider silks. *J. Mol. Biol.* **1998**, *275*, 773–784. [[CrossRef](#)]
37. Suzuki, Y.; Higashi, T.; Yamamoto, T.; Okamura, H.; Sato, T.K.; Asakura, T. Presence of β -Turn Structure in Recombinant Spider Silk Dissolved in Formic Acid Revealed with NMR. *Molecules* **2022**, *27*, 511. [[CrossRef](#)]
38. Ramezaniaghdam, M.; Nahdi, N.D.; Reski, R. Recombinant spider silk: Promises and bottlenecks. *Front. Bioeng. Biotechnol.* **2022**, *10*, 835637. [[CrossRef](#)]
39. Rosano, G.L.; Ceccarelli, E.A. Recombinant protein expression in *Escherichia coli*: Advances and challenges. *Front. Microbiol.* **2014**, *5*, 172. [[CrossRef](#)]
40. Hayashi, C.Y.; Shipley, N.H.; Lewis, R.V. Hypotheses that correlate the sequence, structure, and mechanical properties of spider silk proteins. *Int. J. Biol. Macromol.* **1999**, *24*, 271–275. [[CrossRef](#)]
41. Rising, A.; Nimmervoll, H.; Grip, S.; Fernandez-Arias, A.; Storckenfeldt, E.; Knight, D.P.; Vollrath, F.; Engström, W. Spider silk proteins—mechanical property and gene sequence. *Zool. Sci.* **2005**, *22*, 273–281. [[CrossRef](#)]
42. Hagn, F.; Thamm, C.; Scheibel, T.; Kessler, H. pH-Dependent Dimerization and Salt-Dependent Stabilization of the N-terminal Domain of Spider Dragline Silk—Implications for Fiber Formation. *Angew. Chem. Int. Ed.* **2011**, *50*, 310–313. [[CrossRef](#)] [[PubMed](#)]
43. Eisoldt, L.; Smith, A.; Scheibel, T. Decoding the secrets of spider silk. *Mater. Today* **2011**, *14*, 80–86. [[CrossRef](#)]
44. Hagn, F.; Eisoldt, L.; Hardy, J.G.; Vendrely, C.; Coles, M.; Scheibel, T.; Kessler, H. A conserved spider silk domain acts as a molecular switch that controls fibre assembly. *Nature* **2010**, *465*, 239–242. [[CrossRef](#)] [[PubMed](#)]
45. Yuk, H.; Wu, J.; Zhao, X. Hydrogel interfaces for merging humans and machines. *Nat. Rev. Mater.* **2022**, *7*, 935–952. [[CrossRef](#)]
46. Song, G.; Zhao, Z.; Peng, X.; He, C.; Weiss, R.A.; Wang, H. Rheological Behavior of Tough PVP-in Situ-PAAm Hydrogels Physically Cross-Linked by Cooperative Hydrogen Bonding. *Macromolecules* **2016**, *49*, 8265–8273. [[CrossRef](#)]
47. Fujikura, K.; Maeda, H.; Obata, A.; Inukai, K.; Kato, K.; Kasuga, T. Preparation and rheological characterization of imogolite hydrogels. *J. Nanomater.* **2014**, *2014*, 727254. [[CrossRef](#)]
48. Shao, C.; Chang, H.; Wang, M.; Xu, F.; Yang, J. High-Strength, Tough, and Self-Healing Nanocomposite Physical Hydrogels Based on the Synergistic Effects of Dynamic Hydrogen Bond and Dual Coordination Bonds. *ACS Appl. Mater. Interfaces* **2017**, *9*, 28305–28318. [[CrossRef](#)]
49. Maitra, J.; Shukla, V.K. Cross-linking in hydrogels—a review. *Am. J. Polym. Sci.* **2014**, *4*, 25–31.
50. Tang, S.; Liu, Z.; Xiang, X. Graphene oxide composite hydrogels for wearable devices. *Carbon Lett.* **2022**, *32*, 1395–1410. [[CrossRef](#)]
51. Hu, X.; Vatankhah-Varnoosfaderani, M.; Zhou, J.; Li, Q.; Sheiko, S.S. Weak Hydrogen Bonding Enables Hard, Strong, Tough, and Elastic Hydrogels. *Adv. Mater.* **2015**, *27*, 6899–6905. [[CrossRef](#)]
52. Quan, L.; Xin, Y.; Wu, X.; Ao, Q. Mechanism of Self-Healing Hydrogels and Application in Tissue Engineering. *Polymers* **2022**, *14*, 2184. [[CrossRef](#)]
53. Luo, J.; Wang, T.; Sim, C.; Li, Y. Mini-Review of Self-Healing Mechanism and Formulation Optimization of Polyurea Coating. *Polymers* **2022**, *14*, 2808. [[CrossRef](#)]
54. Goyal, M.; Agarwal, S.N.; Bhatnagar, N. A review on self-healing polymers for applications in spacecraft and construction of roads. *J. Appl. Polym. Sci.* **2022**, *139*, e52816. [[CrossRef](#)]
55. Liu, Y.; Hsu, S.-h. Synthesis and biomedical applications of self-healing hydrogels. *Front. Chem.* **2018**, *6*, 449. [[CrossRef](#)]
56. Chan, N.J.-A.; Gu, D.; Tan, S.; Fu, Q.; Pattison, T.G.; O'Connor, A.J.; Qiao, G.G. Spider-silk inspired polymeric networks by harnessing the mechanical potential of β -sheets through network guided assembly. *Nat. Commun.* **2020**, *11*, 1630. [[CrossRef](#)]
57. Du, N.; Yang, Z.; Liu, X.Y.; Li, Y.; Xu, H.Y. Structural Origin of the Strain-Hardening of Spider Silk. *Adv. Funct. Mater.* **2011**, *21*, 772–778. [[CrossRef](#)]
58. Keten, S.; Xu, Z.; Ihle, B.; Buehler, M.J. Nanoconfinement controls stiffness, strength and mechanical toughness of β -sheet crystals in silk. *Nat. Mater.* **2010**, *9*, 359–367. [[CrossRef](#)]
59. Ling, S.; Kaplan, D.L.; Buehler, M.J. Nanofibrils in nature and materials engineering. *Nat. Rev. Mater.* **2018**, *3*, 18016. [[CrossRef](#)]
60. Ding, D.; Guenette, P.A.; Fu, J.; Zhang, L.; Irvine, S.A.; Miserez, A. From Soft Self-Healing Gels to Stiff Films in Suckerin-Based Materials through Modulation of Crosslink Density and β -Sheet Content. *Adv. Mater.* **2015**, *27*, 3953–3961. [[CrossRef](#)]
61. Pena-Francesch, A.; Jung, H.; Demirel, M.C.; Sitti, M. Biosynthetic self-healing materials for soft machines. *Nat. Mater.* **2020**, *19*, 1230–1235. [[CrossRef](#)]
62. Gaddes, D.; Jung, H.; Pena-Francesch, A.; Dion, G.; Tadigadapa, S.; Dressick, W.J.; Demirel, M.C. Self-Healing Textile: Enzyme Encapsulated Layer-by-Layer Structural Proteins. *ACS Appl. Mater. Interfaces* **2016**, *8*, 20371–20378. [[CrossRef](#)] [[PubMed](#)]
63. Némethy, G.; Steinberg, I.Z.; Scheraga, H.A. Influence of water structure and of hydrophobic interactions on the strength of side-chain hydrogen bonds in proteins. *Biopolymers* **1963**, *1*, 43–69. [[CrossRef](#)]
64. Cohen, N.; Levin, M.; Eisenbach, C.D. On the Origin of Supercontraction in Spider Silk. *Biomacromolecules* **2021**, *22*, 993–1000. [[CrossRef](#)] [[PubMed](#)]

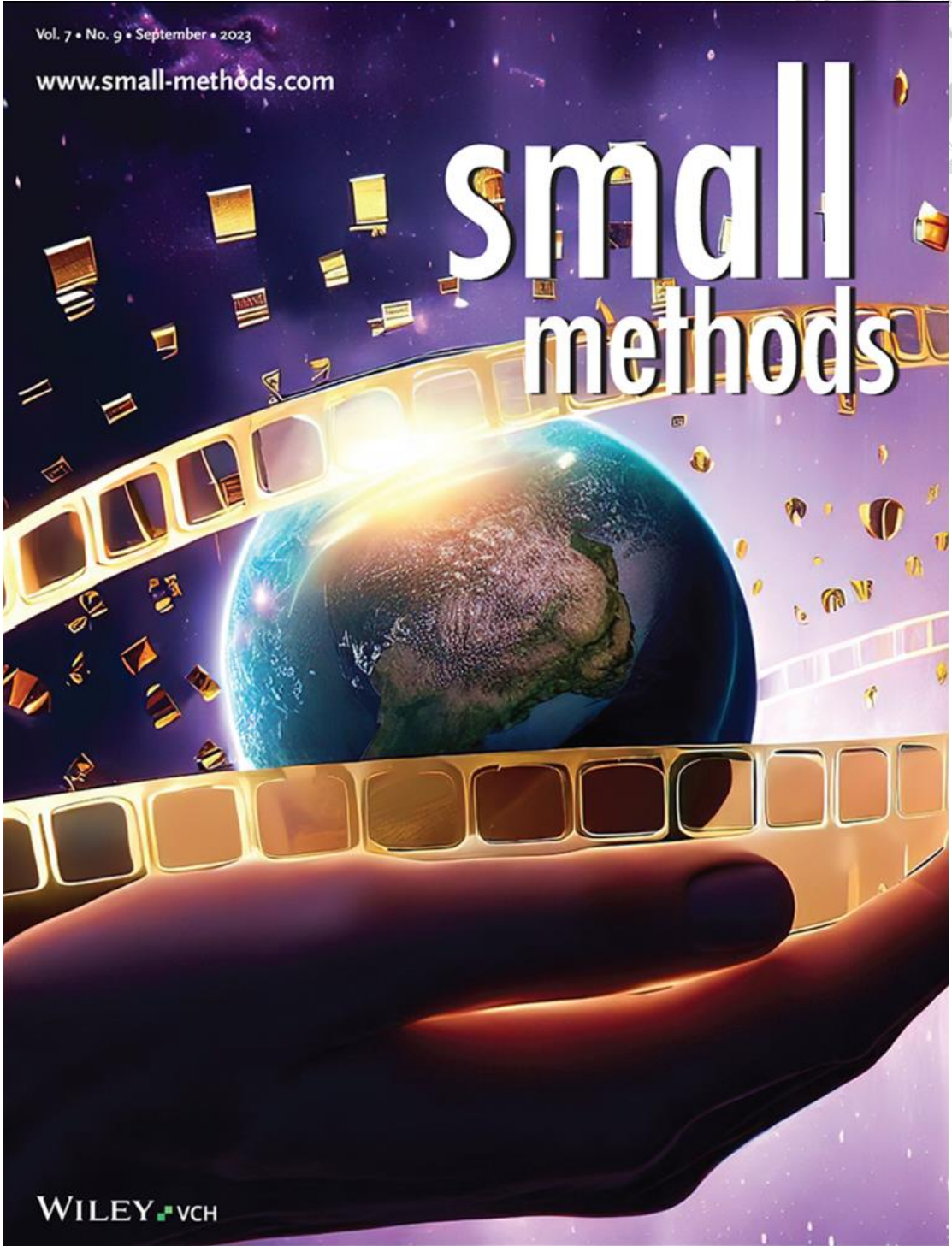


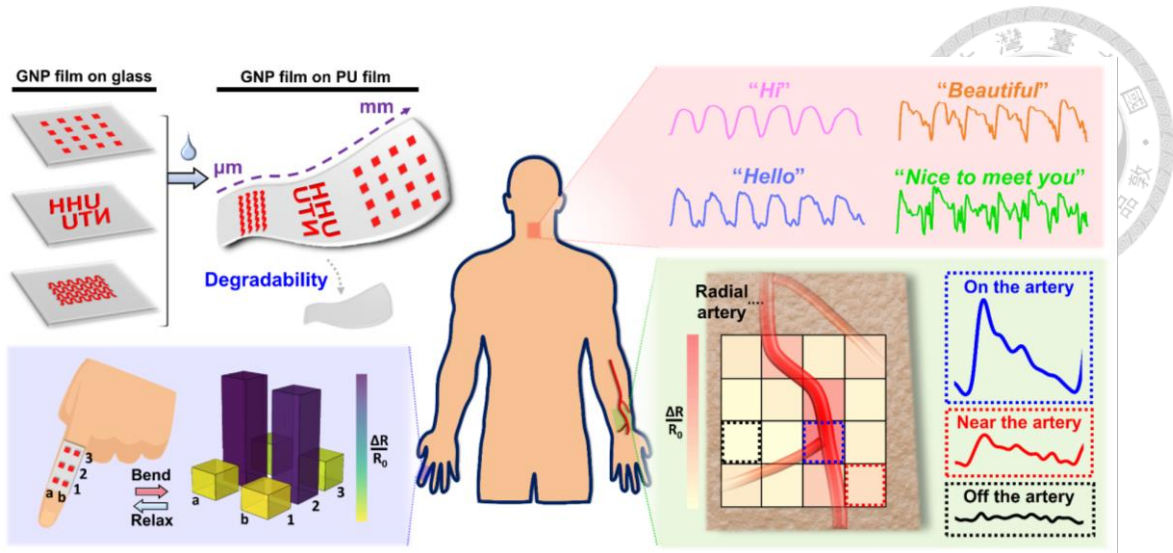
65. Liu, Y.; Shao, Z.; Vollrath, F. Relationships between supercontraction and mechanical properties of spider silk. *Nat. Mater.* **2005**, *4*, 901–905. [[CrossRef](#)] [[PubMed](#)]
66. Steven, E.; Park, J.G.; Paravastu, A.; Lopes, E.B.; Brooks, J.S.; Englander, O.; Siegrist, T.; Kaner, P.; Alamo, R.G. Physical characterization of functionalized spider silk: Electronic and sensing properties. *Sci. Technol. Adv. Mater.* **2011**, *12*, 055002. [[CrossRef](#)]
67. Yang, Z.; Liivak, O.; Seidel, A.; LaVerde, G.; Zax, D.B.; Jelinski, L.W. Supercontraction and Backbone Dynamics in Spider Silk: ¹³C and ²H NMR Studies. *J. Am. Chem. Soc.* **2000**, *122*, 9019–9025. [[CrossRef](#)]
68. Holland, G.P.; Lewis, R.V.; Yarger, J.L. WISE NMR Characterization of Nanoscale Heterogeneity and Mobility in Supercontracted *Nephila clavipes* Spider Dragline Silk. *J. Am. Chem. Soc.* **2004**, *126*, 5867–5872. [[CrossRef](#)]
69. Agnarsson, I.; Boutry, C.; Wong, S.-C.; Bajji, A.; Dhinojwala, A.; Sensenig, A.T.; Blackledge, T.A. Supercontraction forces in spider dragline silk depend on hydration rate. *Zoology* **2009**, *112*, 325–331. [[CrossRef](#)]
70. Lefèvre, T.; Auger, M. Spider silk as a blueprint for greener materials: A review. *Int. Mater. Rev.* **2016**, *61*, 127–153. [[CrossRef](#)]

Disclaimer/Publisher's Note: The statements, opinions and data contained in all publications are solely those of the individual author(s) and contributor(s) and not of MDPI and/or the editor(s). MDPI and/or the editor(s) disclaim responsibility for any injury to people or property resulting from any ideas, methods, instructions or products referred to in the content.

3.3. Publication 3 (third project): Fabrication of eco-friendly wearable strain sensor arrays via facile contact printing for healthcare applications

Reprinted from “Shin-Da Wu, Shan-hui Hsu, Bendix Ketelsen, Sophia C. Bittinger, Hendrik Schlicke, Horst Weller, and Tobias Vossmeier. Fabrication of Eco-friendly Wearable Strain Sensor Arrays via Facile Contact Printing for Healthcare Applications. *Small Methods* **2023**; 7(9): 2300170.” with permission from WILEY-VCH. The corresponding supporting information is reprinted in section 7.1.2.





Fabrication of Eco-Friendly Wearable Strain Sensor Arrays via Facile Contact Printing for Healthcare Applications

Shin-Da Wu, Shan-hui Hsu,* Bendix Ketelsen, Sophia C. Bittinger, Hendrik Schlicke, Horst Weller, and Tobias Vossmeier*

Wearable flexible strain sensors with spatial resolution enable the acquisition and analysis of complex actions for noninvasive personalized healthcare applications. To provide secure contact with skin and to avoid environmental pollution after usage, sensors with biocompatibility and biodegradability are highly desirable. Herein, wearable flexible strain sensors composed of crosslinked gold nanoparticle (GNP) thin films as the active conductive layer and transparent biodegradable polyurethane (PU) films as the flexible substrate are developed. The patterned GNP films (micrometer- to millimeter-scale square and rectangle geometry, alphabetic characters, and wave and array patterns) are transferred onto the biodegradable PU film via a facile, clean, rapid and high-precision contact printing method, without the need of a sacrificial polymer carrier or organic solvents. The GNP-PU strain sensor with low Young's modulus (≈ 17.8 MPa) and high stretchability showed good stability and durability (10 000 cycles) as well as degradability (42% weight loss after 17 days at 74 °C in water). The GNP-PU strain sensor arrays with spatiotemporal strain resolution are applied as wearable eco-friendly electronics for monitoring subtle physiological signals (e.g., mapping of arterial lines and sensing pulse waveforms) and large-strain actions (e.g., finger bending).

1. Introduction

Flexible nanomaterials-based strain sensors that convert mechanical deformations into electrical signals have gained tremendous attention in the area of wearable healthcare electronics owing to their adaptability and diverse design options.^[1] Compared to the more rigid traditional strain sensors, wearable flexible strain sensors eliminate the interface mismatch between human tissues and the transducer. Hence, they are able to sense subtle physiological signals and enable a reliable evaluation of deep tissues.^[2] A flexible resistive strain sensor typically comprises two key elements: the active conductive layer and the flexible substrate.^[3] The active conductive layer, composed of organic and/or inorganic nanomaterials, imparts functional sensing properties. Especially, gold nanoparticle (GNP) thin films have been widely used for the fabrication of high-performance strain sensors because their stimuli-responsive


charge transport properties can be tuned precisely by varying the GNP size, the interparticle distances, and the composition of the organic matrix.^[4] Patterning of GNP films plays an important role in developing their advanced sensing applications owing to beneficial effects on performance adjustment. Furthermore, patterning techniques are mandatory for the repeatable and scalable fabrication of transducers with complex patterns and their integration into advanced device architectures.^[5] For instance, fractal geometry design (e.g., curves with tortuosity morphology) of the conductive nanomaterials can enhance their mechanical performance for applications in stretchable electronics.^[6] Meanwhile, patterned strain sensor arrays enable spatial resolution and, hence, can overcome problems arising from the positional inaccuracy of conventional single-point sensors in, for example, arterial sensing.^[7]

The flexible substrate of the sensor serves as the base to support the configuration of the active conductive layer.^[3] Commonly used flexible substrates are polydimethylsiloxane (PDMS),^[4b,8] polyimide (PI),^[4b,9] polyethylene terephthalate (PET),^[10] and thermoplastic polyurethane (PU).^[11] However, the choice of the flexible substrate should take into consideration the environmental footprint to avoid an environmental burden after the sensor's lifetime.^[12] Biodegradable polymers emerge as attractive replacement substrates because they degrade naturally

S.-D. Wu, S.-hui Hsu
Institute of Polymer Science and Engineering
National Taiwan University
Taipei 10617, Taiwan
E-mail: shhsu@ntu.edu.tw

S.-D. Wu, B. Ketelsen, S. C. Bittinger, H. Weller, T. Vossmeier
Institute of Physical Chemistry
University of Hamburg
20146 Hamburg, Germany
E-mail: tobias.vossmeier@chemie.uni-hamburg.de

S.-hui Hsu
Institute of Cellular and System Medicine
National Health Research Institutes
Miaoli 35053, Taiwan
H. Schlicke, H. Weller
Fraunhofer Center for Applied Nanotechnology CAN
20146 Hamburg, Germany

 The ORCID identification number(s) for the author(s) of this article can be found under <https://doi.org/10.1002/smt.202300170>

© 2023 The Authors. Small Methods published by Wiley-VCH GmbH. This is an open access article under the terms of the Creative Commons Attribution-NonCommercial License, which permits use, distribution and reproduction in any medium, provided the original work is properly cited and is not used for commercial purposes.

DOI: 10.1002/smt.202300170

and, hence, reduce hazardous waste and the carbon footprint.^[13] For instance, biodegradable poly(lactic acid) (PLA) was used to demonstrate the design of disposable wearable sensors and implantable biomedical devices for in vitro and in vivo applications.^[14] However, the brittleness and high elastic modulus (≈ 4 GPa) of PLA limit their stretchability and flexibility and, hence, reduce their ability to detect subtle physiological signals or large strain actions.^[15] In contrast, using biodegradable PU films with much lower Young's modulus and high stretchability as the substrate enables the design of wearable strain sensors which are well suited to monitor physiological signals and human motion over a broad strain range.^[16] Meanwhile, the mechanical properties and degradability of biodegradable PU can be adjusted to match the characteristics of various human tissues and the requirements of specific applications.^[17] Furthermore, the biocompatibility of biodegradable PU provides a safe contact with human skin for long-term skin-mounted applications.^[18]

Many biodegradable flexible substrates are chemically non-resistant.^[19] The fabrication of the active conductive layers, however, usually involves the use of various chemicals and solvents. Therefore, the active layers are typically deposited first onto chemically robust substrates, such as glass or silicon.^[20] Hence, the transfer of the pre-formed active layers from their original substrates onto suitable flexible substrates plays a key role in the fabrication process of biocompatible and biodegradable flexible strain sensors.^[21] Common transfer methods include the wedging transfer process,^[22] peel-and-stick process,^[23] lift-off by etching,^[24] and poly(methyl methacrylate) (PMMA)-mediated transfer printing.^[4b,25] However, these methods have their respective limitations. For instance, the active layers transferred via the wedging process often form wrinkles.^[26] The undesired wrinkles or cracks induced during the transfer process can degrade the performance of the fabricated devices.^[27] Also, a whole array of active layers is not transferable by the wedging process. The peel-and-stick process involves annealing of protection layers and baking of thermal release tapes.^[23a,b] The harsh thermal conditions can degrade organic components of the active layer or affect the desired properties of the flexible substrate.^[17a,28] Furthermore, the use of a chemical etchant limits the types of active layers and flexible substrates that can be selected.^[23a,24a] For example, GNP films can be transferred onto flexible substrates using a PMMA mediator film.^[4b,25d] However, the use of organic solvents such as dichloromethane and acetone for removing the PMMA mediator after the transfer can degrade the chemically non-resistant substrates.^[29] Furthermore, PMMA residues remaining on the active layer after finishing the fabrication process can affect the performance of the sensors.^[30] Therefore, the development of a convenient, clean, and high-precision transfer method enabling the fabrication of nanomaterials-based biodegradable flexible strain sensors is highly desirable.

Herein, we present the combination of patternable crosslinked GNP films as active conductive layers with biodegradable PU films as flexible substrates. A facile, clean, rapid, and scalable contact printing method with high reliability was developed for transferring the patterned GNP films (micrometer- to millimeter-scale square and rectangle geometry, alphabetic characters, and wave and array patterns) onto the biodegradable PU film. Thermal release tapes, chemical etchants, a PMMA mediator, or or-

ganic solvents were not needed for the facile contact printing process. As demonstrated in this study, biodegradable GNP-PU strain sensors and sensor arrays feature high fidelity and durability, and enable spatiotemporal strain resolution. Hence, these sensors are excellently suited for the implementation in advanced wearable eco-friendly electronics, especially for healthcare applications such as highly versatile muscle action monitoring (e.g., laryngeal movement or finger joint motion) and facile mapping of arteries with precise sensing of pulse waveforms.

2. Results

2.1. Fabrication and Characteristics of the GNP-PU Film

Figure 1 presents the characterization of the two components (i.e., GNPs and biodegradable PU) of the strain sensor. A representative transmission electron microscopy (TEM) image of the synthesized GNPs is displayed in Figure 1A. The ultraviolet-visible (UV-vis) absorbance spectrum of the GNPs is shown in Figure S1, Supporting Information. According to TEM images, the GNPs were spherical with an average diameter of 7.3 ± 0.6 nm (Figure 1B). The UV-vis absorbance spectrum showed the localized surface plasmon resonance (LSPR) peak at the wavelength of ≈ 520 nm. Figure 1C shows the molecular structure of the biodegradable PU. The biodegradable PU film was fabricated by casting,^[17a] had a thickness of ≈ 250 μm , and featured high flexibility (Figure 1D(i)). A tensile test setup was used to measure the film's stress-strain curve as presented in Figure 1D(ii). Within the initial linear strain range (0–5%) the slope of the curve revealed a Young's modulus of ≈ 17.8 MPa (Figure 1D(ii), inset). Further, the PU film was colorless and highly transparent ($\approx 92\%$ transmittance) as shown by the photograph and the transmittance spectrum presented in Figure 1D(iii,iv).

The GNP film was fabricated on a glass slide via a layer-by-layer spin-coating procedure (Figure 2A).^[4b,22c] First, the glass slide was treated with air plasma. The 1,9-nonanedithiol (9DT) crosslinker solution and the GNP solution were then alternately dropped onto the rotating glass slide. The fabrication of the crosslinked GNP film was finished after completing three spin-coating cycles. Figure 2B presents a photograph of the crosslinked GNP film on the glass substrate. UV-vis absorbance spectra measured at different positions of the coated glass slide confirmed the homogeneity of the GNP film (Figure 2C). The color of the film was bluish, as shown in the figure inset. In order to transfer the crosslinked GNP film from the original glass substrate to the biodegradable PU film, we developed a clean and facile contact printing procedure (Figure 2D). First, the GNP film on the glass substrate was scratched using a sharp blade to obtain the desired size and shape. Second, a PDMS stamp was used to facilitate the transfer by contacting the surface of the GNP film. Subsequently, a small amount of water (≈ 3 μL) was dripped onto the interfacial region between the glass and the GNP film. By peeling off the glass substrate, the GNP film was transferred onto the PDMS stamp. Third, the PDMS stamp with the GNP film was placed onto the biodegradable PU film. After heating to 60 $^{\circ}\text{C}$ for 3 min and cooling to 0 $^{\circ}\text{C}$ for 3 min, the GNP film was transferred onto the PU film and the PDMS stamp was removed. The fabrication of the GNP-PU strain sensor was completed by depositing

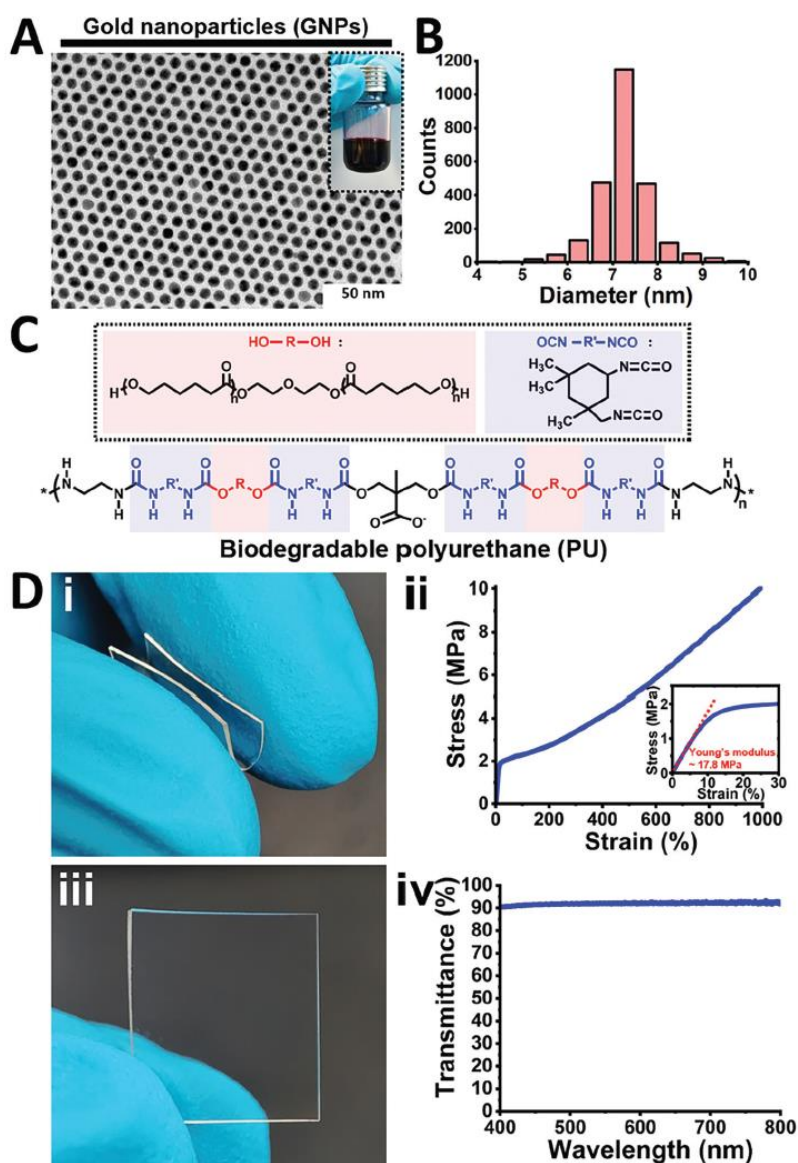


Figure 1. Characteristics of the two components [i.e., gold nanoparticles (GNPs) and biodegradable polyurethane (PU)] of the strain sensor. A) Transmission electron microscopy (TEM) image and B) the size distribution histogram of GNPs. The inset in (A) shows a photograph of the GNP solution. C) Chemical structures of the biodegradable PU and its precursors, that is, polycaprolactone (PCL) diol (red) and isophorone diisocyanate (IPDI), (blue). D) Photographs and plots showing the i) flexibility, ii) tensile stress–strain curve, iii) transparency, and iv) transmittance spectrum of the biodegradable PU film.

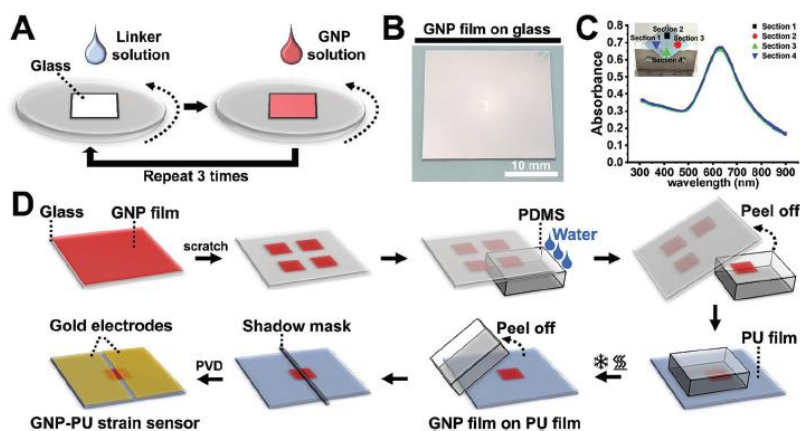


Figure 2. Preparation and characterization of the crosslinked GNP film and printing procedure used to transfer the GNP film onto the biodegradable PU film. A) Layer-by-layer spin-coating deposition of the crosslinked GNP film. B) Optical appearance of the fabricated 1,9-nananedithiol (9DT) crosslinked GNP film deposited onto the glass substrate. C) Ultraviolet–visible (UV–vis) absorbance spectra measured on different sections of the substrate confirming the homogeneity of the GNP film. D) Schematic illustration showing the clean and facile contact printing method employed for the fabrication of GNP-PU strain sensors.

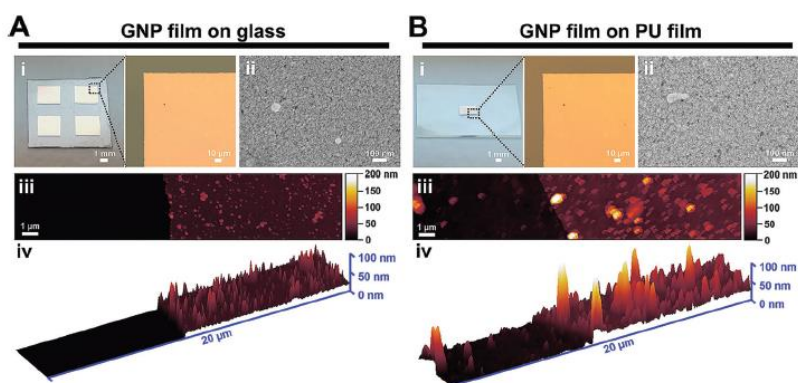


Figure 3. Surface morphology of the GNP film A) before (i.e., on the glass substrate) and B) after the contact printing process (i.e., on the PU film). For both samples the i) photographs and optical microscopy (OM) images, ii) scanning electron microscopy (SEM) images, iii) 2D atomic force microscopy (AFM) maps, and iv) 3D AFM topographic images are shown.

gold electrodes onto the GNP-PU film via physical vapor deposition (PVD) using a shadow mask. The thickness of the deposited gold electrodes was ≈ 100 nm and the gap between the two gold electrodes was ≈ 230 μm (Figure S2, Supporting Information).

The surface morphology of the GNP film before (i.e., on the glass substrate), during (i.e., on the PDMS stamp), and after contact printing (i.e., on the PU film) is shown in Figure 3, and Figure S3, Supporting Information. The optical images shown in Figure 3A(i), B(i), and Figure S3A, Supporting Information, demonstrate that the geometry of the GNP film was well preserved after the contact printing process. The GNP film was perfectly transferred onto the PU film without any visible cracks. Further, scanning electron microscopic (SEM) images reveal the granular structure of the film formed by crosslinked GNPs and

confirm a consistent surface morphology before and after contact printing (Figure 3A(ii), B(ii), and Figure S3B, Supporting Information). The atomic force microscopy (AFM) images shown in Figure 3A(iii), B(iii), and Figure S4, Supporting Information, reveal the surface roughness of the PU film and GNP film. The roughness of the PU film was higher than that of the glass substrate. Therefore, the average roughness of the GNP film on the PU film (≈ 12 nm) appeared to be higher than that of the GNP film on the glass substrate (≈ 4 nm). However, a comparison of the images confirms that the morphology of the GNP film itself was not affected by the contact printing process. The thickness of the GNP film on the glass and the PU substrate was determined by measuring AFM images at the edge of the film, revealing ≈ 22 nm for the film on both substrates (Figure 3A(iv), B(iv)).

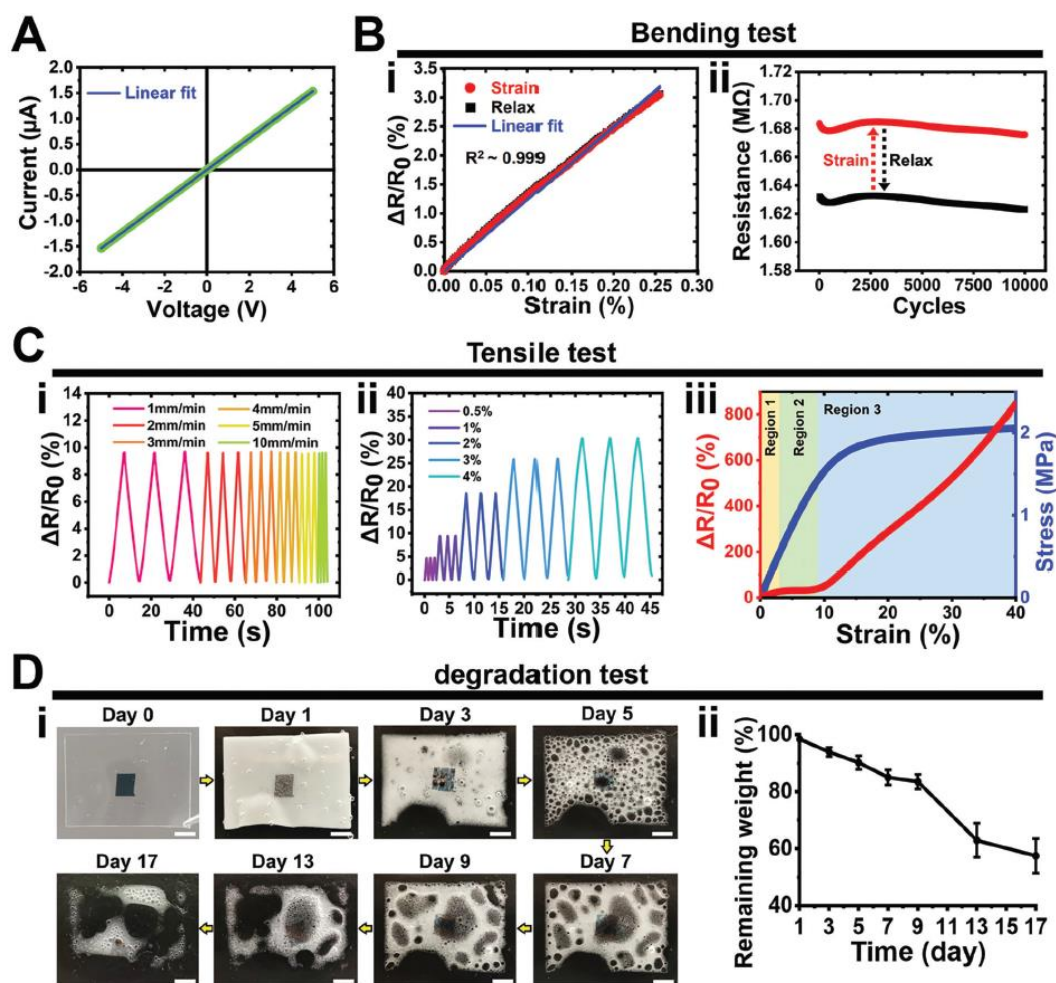


Figure 4. Characterization of the GNP-PU strain sensor. A) Current–voltage (I – V) curve. B) Results of four-point bending tests: i) relationship between relative resistance change ($\Delta R/R_0$) and applied strain from 0 to 0.25%. ii) Fatigue test consisting of 10 000 strain–relaxation cycles with a strain variation from 0 to 0.125%. Linear fits to the data in (A,B) are shown as blue solid lines. C) Results of tensile tests: i,ii) Cyclic strain–response characteristics under i) 1 to 10 mm min^{-1} tension rates with a maximum strain of 1%, and ii) 0.5% to 4% strain at a tension rate of 10 mm min^{-1} . iii) $\Delta R/R_0$ and tensile stress as a function of applied strain from 0 to 40% at a tension rate of 10 mm min^{-1} . D) Degradation behavior: i) photographs and ii) plot of weight loss versus time showing the degradation of the GNP-PU film on different days in distilled water at an accelerated-degradation temperature of 74 °C. Scale bars in (D-i) represent 2 mm.

2.2. Characterization of the GNP-PU Strain Sensor

The characterization of the GNP-PU strain sensor is presented in Figure 4. The current–voltage (I – V) curve of the sensor showed ohmic conductivity (Figure 4A) with a conductance of $\approx 0.3 \mu\text{S}$. Resistive strain responses of the sensor were characterized by four-point bending tests and tensile tests (Figure 4B,C). In the bending tests, the relative resistive response ($\Delta R/R_0$) increased nearly linearly with increasing strain from 0 to 0.25% (Figure 4B(i)). The gauge factor (i.e., the sensitivity) of the sensor

is defined by the slope of the $\Delta R/R_0$ versus strain plot, revealing a value of ≈ 13 . The sensor was subjected to 10 000 strain–relaxation cycles and displayed good stability and reversibility (Figure 4B(ii), and Figure S5 and S6, Supporting Information).

Figure 4C(i) shows typical $\Delta R/R_0$ responses of the sensor during cyclic tensile tests with a maximum strain of 1%. The response dynamics reproduce the applied tensile rates which were increased from 1 to 10 mm min^{-1} . Another set of cyclic tensile tests in the range of small strains (0.5% to 4%) confirmed that the $\Delta R/R_0$ responses were stable and reproducible

(Figure 4C(ii)). Furthermore, the $\Delta R/R_0$ response of the sensor within a broader strain range (0 to 40%) can be divided into three regions (Figure 4C(iii), and Figure S7, Supporting Information). To explain the differences between the three regions of the response curve, the surface morphology of the GNP film was examined by SEM after straining the sensor (Figure S8, Supporting Information). Within the small strain range from 0 to $\approx 3\%$ (region 1), the gauge factor of the sensor was ≈ 10 (Figure S9, Supporting Information). After loading the GNP film within this strain range (e.g., 3%), a similar surface morphology was observed as in the case of the native unstrained sensor. Within the moderate strain range from 3 to 9% (region 2), the gauge factor decreased to ≈ 1 . SEM images captured of the GNP film after straining it within the limits of this strain range (e.g., 6%) indicated the formation of initial microcracks (Figure S8, Supporting Information). Within the large strain range from 9 to 40% (region 3), the gauge factor of the sensor increased to ≈ 25 . After loading the GNP film with 12% strain, cracks with an overall perpendicular orientation to the direction of applied strain were clearly observable. The number of cracks increased as the tensile load increased from 12% to 20%. After loading the sensor with 30% tensile strain, the cracks were extended and enlarged (Figure S8, Supporting Information).

The degradation of the GNP-PU sensor was studied by placing the sensor in distilled water at 74 °C. The degradation of the sensor without and with gold electrodes is shown in Figure 4D, and Figure S10, Supporting Information, respectively. The photographs show that the PU film gradually degraded with time (Figure 4D(i)). The remaining weight of the GNP-PU film was $\approx 58\%$ after 17 days (Figure 4D(ii)).

2.3. Healthcare Applications of the GNP-PU Strain Sensor

Various applications of the GNP-PU composite film as wearable strain transducer for real-time monitoring of human physiological signals and muscle action were studied as depicted in Figure 5. The sensor was attached to the wrist artery for sensing the radial artery pulse waves (Figure 5A). The signal trace shows seven well-resolved pulse waves (i.e., percussion wave, dicrotic wave, and tricuspid valve opening). Further, the sensor fixed on the wrist showed well-reproducible signals when repeatedly bending the wrist joint (Figure 5B). The sensor attached to the face mask of an adult test person exhibited well-resolved periodic signals corresponding to inhalation and exhalation while breathing normally (Figure 5C). Furthermore, the sensor was attached to the human throat to detect swallowing and laryngeal movement during speaking (Figure 5D(i)). When swallowing, the complex signals of throat muscles were accurately captured and reproduced by the signal pattern (Figure 5D(ii)). When speaking, clearly distinguishable and characteristic signal traces corresponding to representative words (i.e., “Hi”, “Hello”, “Beautiful”, and “Nice to meet you”) were recorded, as shown in Figure 5D(iii–vi).

2.4. Fabrication of the Patterned GNP-PU Strain Sensors

Precisely patterned GNP films were successfully fabricated on the glass substrates via a deep-UV photolithography procedure (Figure 6).^[31] The glass substrate was first treated with air plasma.

The contact angle of water droplets on the glass surface was $\approx 56^\circ$ and $\approx 49^\circ$ before and after plasma treatment, respectively. A PMMA layer was deposited on the glass substrate by spin-coating. The PMMA layer was exposed to deep-UV light through a photomask for 130 min. Subsequently, the UV-exposed areas of the PMMA layer were dissolved by the PMMA developer. The contact angle of the glass substrate at the UV-exposed areas was $\approx 66^\circ$. The glass with the patterned PMMA layer was treated again with air plasma and washed with the PMMA developer. After this step, the contact angle of the glass substrate at the UV-exposed areas decreased to $\approx 50^\circ$. Afterward, the 9DT linker solution and GNP solution were alternately dropped onto the patterned PMMA covered glass substrate while performing three spin-coating cycles. Finally, the patterned GNP film on the glass substrate was obtained by dissolving the PMMA layer in acetone.

The GNP films with various patterns were transferred from the glass substrate onto the biodegradable PU film, as shown in Figure 6A–E, via the clean and facile contact printing procedure described above (cf. Figure 2D). Briefly, the patterned GNP films with square shape (10 mm²), rectangle shape (width of 35 μ m), array pattern (4 \times 4; each ≈ 1 mm²), alphabetic letters (i.e., H, U, T, and N; line width of 500 μ m), or wave-shape (line width of 100 μ m) were transferred onto a PDMS stamp by applying a small amount of water to the interface between the glass surface and the patterned GNP films. Subsequently, the patterned GNP films were successfully transferred from the PDMS stamp onto the biodegradable PU films after applying a heating/cooling cycle. The fabrication of patterned GNP-PU strain sensors was completed by depositing gold electrodes onto the patterned GNP-PU films.

2.5. Applications of GNP-PU Strain Sensor Arrays for Spatiotemporal Measurements

In order to demonstrate the broad range of possible applications, GNP-PU strain sensor arrays were used to measure human finger joint bending and pulse wave patterns with spatiotemporal resolution, as shown in Figure 7. A GNP-PU strain sensor array comprising 6 sensors was attached to the back of the index finger joint (Figure 7A(i)). The $\Delta R/R_0$ signal pattern of the sensor array was recorded while periodically bending and stretching the finger (Figure 7A(ii)). At the bending state, the color map of $\Delta R/R_0$ values along the y-axis (positions “1”, “2”, and “3”) shows the spatial sensing capability of the strain sensor array (Figure 7A(iii)). The $\Delta R/R_0$ values for position “2” were the largest and for “1” and “3” were approximately symmetrical, indicating that the position “2” sensors were located right above the finger joint. The color map of $\Delta R/R_0$ along the x-axis (positions “a” and “b”) shows consistent values, confirming the reliability of the strain sensor array. Furthermore, the GNP-PU strain sensor array featured reversible and repeatable temporal sensing capability during the bending–stretching cycles (Figure 7A(iv)).

To monitor the pulse waves and to map the arterial lines, a GNP-PU strain sensor array comprising 16 sensors was fabricated (Figure 7B(i)). This sensor array was attached above the wrist radial artery to record a spatiotemporal signal pattern (Figure 7B(ii)). The $\Delta R/R_0$ signatures of the strain sensor array were collected and are presented as a 4 \times 4 color map in

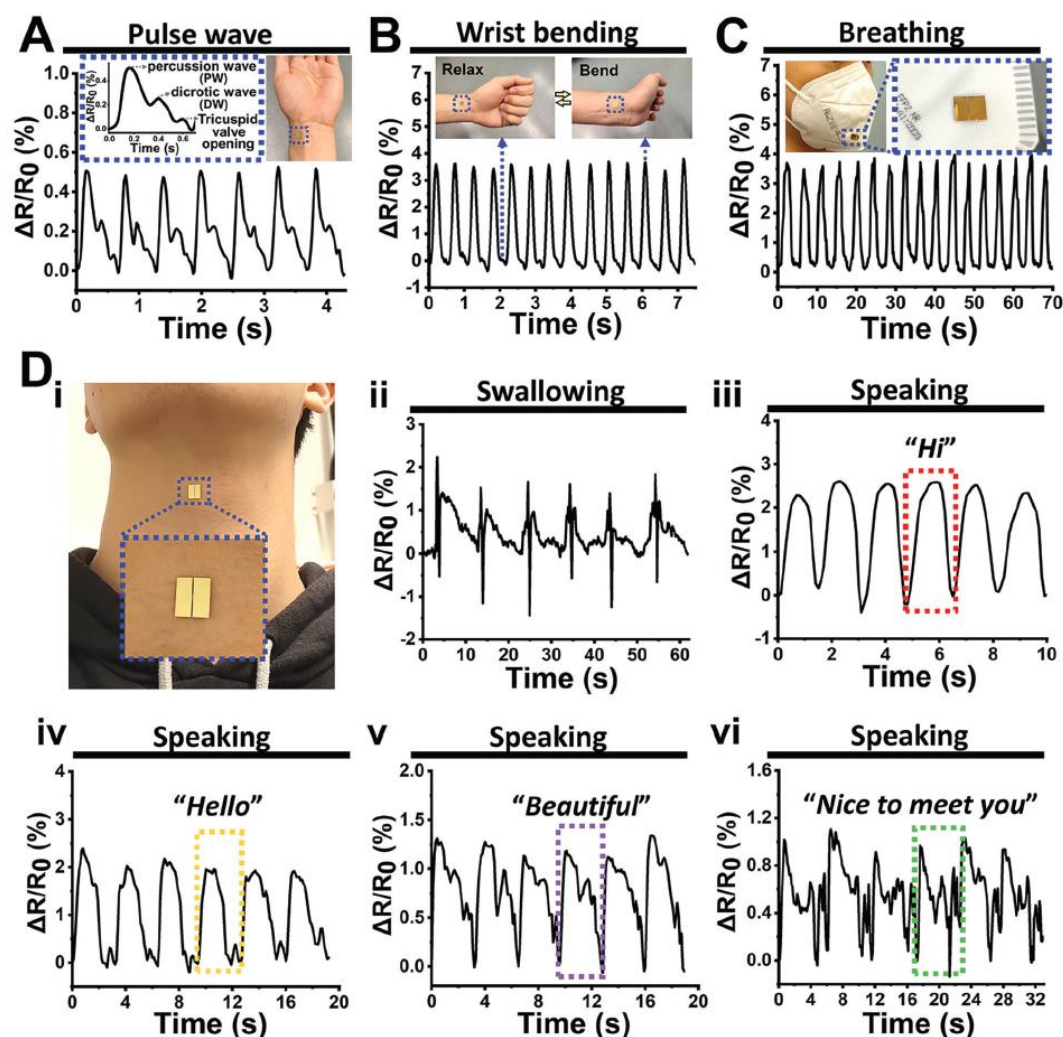


Figure 5. Application of the GNP-PU film as wearable strain sensor. $\Delta R/R_0$ signal traces representing A) pulse wave patterns, B) cyclic wrist bending-relaxation movement, C) breathing, D) swallowing, and speaking. The panels show i) the strain sensor attached to the throat of an adult male, and the $\Delta R/R_0$ signatures recorded during ii) swallowing and speaking the words: iii) "Hi", iv) "Hello", v) "Beautiful", and vi) "Nice to meet you."

Figure 7B(iii). The color map reproduces the amplitude of the pulse waves depending on the position of each sensor. As indicated in Figure 7B(ii), we interpret this pattern as a map of the arterial lines. To present the details of the pulse waveforms, representative $\Delta R/R_0$ signal traces are shown in Figure 7B(iv). The sensor at coordinates (2,c) showed the largest signal amplitudes and a well-resolved pulse waveform, suggesting that this sensor was positioned directly on the artery. The well-resolved pulse waveform features four diagnostically relevant peaks: P1 (percussion wave), P2 (tidal wave), P3 (dicotic wave), and P4 (tricuspid valve opening). The $\Delta R/R_0$ signal trace of the sensor at coordi-

nates (1,d) displayed a pulse waveform with lower signal-to-noise ratio, indicating that the sensor was near the artery. The $\Delta R/R_0$ signal trace of the sensor at coordinates (4,c) displayed only some faint signals, indicating that the sensor was off the artery.

3. Discussion

3.1. Fabrication and Characteristics of the GNP-PU Film

The biodegradable PU substrate was synthesized via a green water-based process using hydrolysis-prone polyester diol as the

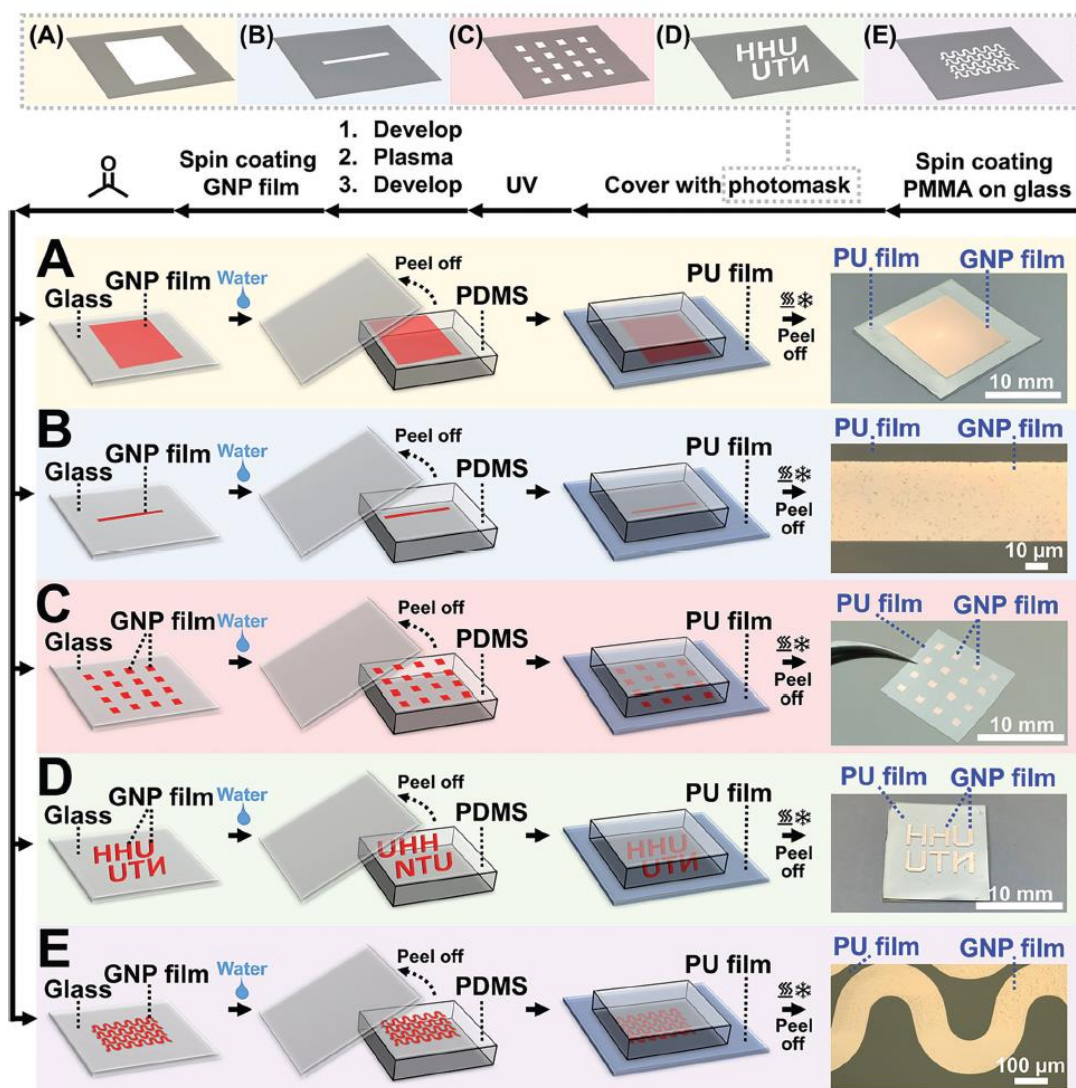


Figure 6. Schematic presenting the fabrication of precisely patterned GNP films on glass substrates via deep-UV photolithography and their transfer onto a PU film via facile contact printing. The photographs and optical microscopy images show the contact-printed GNP film patterns: A) a centimeter-scale square, B) a micrometer-scale rectangle, C) a 4×4 array of squares, D) alphabetic letters (i.e., H, U, T, and N), and E) a wave-shaped pattern.

soft segment and aliphatic diisocyanate as the hard segment (Figure 1C).^[17a] In contrast to thermoset polymers which require a remolding process to obtain the final shape of the substrate, the waterborne dispersion of the biodegradable PU with thermoplastic nature enables the economic fabrication of thin film substrates via simple casting. Based on its high flexibility (cf. Figure 1D(ii)), the fabricated PU film enables conformal contact to the human skin and other human tissues. Hence, this polymer is well suited for applications as flexible biodegradable substrate

for skin-mounted wearable and implantable sensors. In previous studies, the flexible substrates of strain sensors consisted of polyethylene (PE),^[32] PET,^[10a] PI,^[9a] and silicone polymers.^[3,33] Compared to low density PE (LDPE), PET, and PI substrates (Young's modulus of ≈ 300 MPa, ≈ 2.5 GPa, and ≈ 3.5 GPa, respectively),^[32,34] the biodegradable PU film used in our present study has a significantly lower Young's modulus (Figure 1D(ii), ≈ 17.8 MPa) matching the mechanical characteristics of human skin much better.^[17b] Therefore, the PU film enables a better

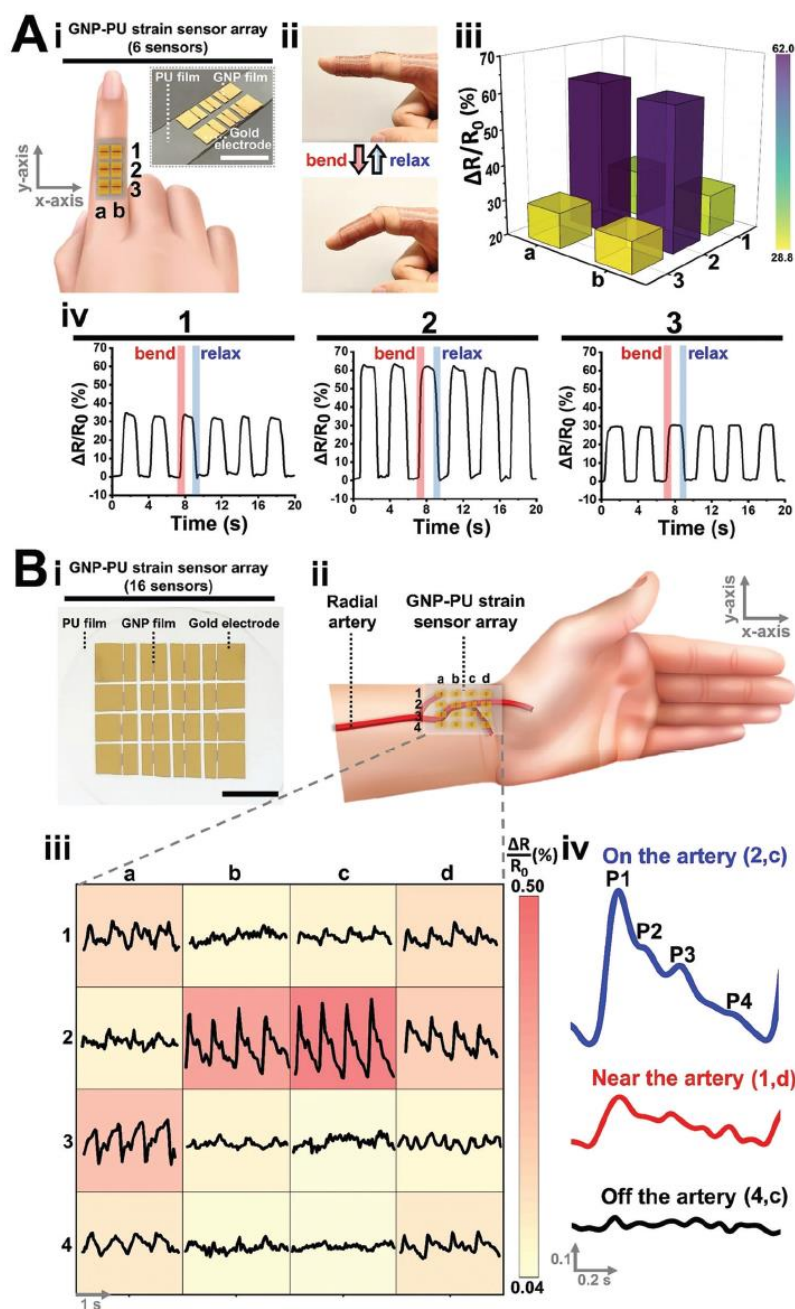


Figure 7. Applications of the GNP-PU strain sensor array. **A**) Spatiotemporal measurement of finger bending: i) schematic illustration of the GNP-PU strain sensor array (2×3) attached to the index finger to show the sensor positions along the x-axis (positions “a” and “b”) and y-axis (positions “1”, “2”, and “3”). The spacing between each active conductive area was ≈ 3 mm along the x-axis and y-axis. The inset shows a photograph of the GNP-PU strain sensor array. ii) Photographs of a volunteer’s index finger with the sensors attached to the finger joint showing the bending–stretching movement of the finger. iii) Spatial distribution of the $\Delta R/R_0$ signals of the GNP-PU strain sensor array during finger bending. iv) $\Delta R/R_0$ responses of the GNP-PU

wearing comfort as it can easily adapt to subtle deformation of the skin.^[35] Furthermore, the biodegradable PU film features much higher stretchability (up to 1000% elongation without break) compared to that of LDPE, PET, and PI substrates.^[32,36] Hence, the biodegradable PU film is also suited for strain sensing with huge strain variations. Similarly, silicone-based substrates, such as PDMS and Ecoflex, also feature a low Young's modulus (0.05–3 MPa) and high stretchability (200–1000% elongation).^[33] Further, PDMS and biodegradable PU substrates possess excellent optical transparency (Figure 1D(iii,iv))^[33] enabling the integration of optical components and making the device invisible during daily use.^[37] However, the inert PDMS substrate shows only poor affinity to the surface of metal nanoparticles and, therefore, it does not support the robust attachment of a GNP layer.^[38] In contrast, the nitrogen atoms of the biodegradable PU substrate enable enhanced interactions with metallic nanomaterials.^[39] For example, it was demonstrated that the interaction between GNPs and PU enables the formation of highly stretchable nanoparticle conductors.^[40] Furthermore, in contrast to silicone-based polymers, the PU substrate used in our present study features better environmental performance due to its biodegradability, as discussed in more detail below.

Printing techniques for the production of patterned sensors can be mainly classified into contact printing and non-contact printing techniques.^[41] Non-contact printing techniques such as inkjet printing and electrohydrodynamic printing can suffer from nozzle clogging due to the use of ink.^[42] In addition, the low printing speed and limited range of viscosity of the ink are potential disadvantages. Further, the use of organic solvents in ink can degrade the chemically non-resistant flexible substrates or can be unfavorable for biomedical applications (e.g., implantable sensors).^[29] Similarly, many previous contact printing techniques also involved the use of organic solvents.^[4b,25d] Therefore, in this study, our aim was to develop a solvent-free and facile contact printing method for the fabrication of patterned GNP-PU strain sensors.

The 9DT crosslinked GNP film was fabricated via facile layer-by-layer spin coating and transferred onto the biodegradable PU substrate to form the active conductive layer of the sensor. The glass substrate which was initially used for the spin-coating process was plasma-treated before depositing the GNP film to enhance its hydrophilicity. Contact angle measurements before ($\approx 56^\circ$) and after ($\approx 49^\circ$) the plasma treatment confirmed increased hydrophilicity. As a result of the spin-coating process the crosslinked GNP film formed a homogeneous layer on the glass slide with well-controlled thickness (Figure 2B). Its bluish color is due to the redshifted localized surface plasmon resonance (LSPR) absorbance peak of the GNPs at ≈ 630 nm (Figure 2C).^[43] In a first simple approach, we obtained the desired size and shape of the GNP film by mechanically removing undesired sections of the film (Figure 2D).^[4b,25d] A hydrophobic PDMS stamp was

then brought in contact with the GNP film. In order to detach the GNP film from the glass substrate a small volume of water was dripped onto the edge of the stamp and quickly dragged into the interfacial region between the GNP film and the hydrophilic glass surface.^[25d,44] After peeling off the glass substrate, the PDMS stamp with the GNP film was just placed onto the biodegradable PU substrate and a heating/cooling cycle was applied to aid the transfer of the GNP film onto the final PU substrate, similar as that reported by Choi et al., who studied the thermally controlled transfer of patterned graphene layers.^[45] It is assumed that the heating/cooling cycle facilitates the transfer process by causing interfacial shear stress between the layers with different thermal expansion. Further, we assume that the above-mentioned interaction between the GNPs and the PU surface facilitates the smooth transfer from the PDMS stamp onto the PU substrate. Note, in contrast to previous studies,^[4b,25d,44b] our present work demonstrates that the transfer of the GNP film onto the PDMS stamp, and from there onto the PU substrate, is feasible without the need of any sacrificial polymer carrier [e.g., PMMA, poly(L-lactic acid) (PLLA)] supporting the GNP film during its transfer (cf. Figure 2D). Omitting such polymer carrier renders the fabrication process less labor- and material-intensive and, hence, environmentally friendlier. Especially, it eliminates the need of removing the polymer carrier with organic solvents before contacting the active layer with electrodes. Further, it is to be noted that the intermediate transfer of the GNP film onto the PDMS stamp was indispensable. Trying to transfer the GNP film directly from the glass slide onto the PU substrate resulted in the formation of holes and cracks within the transferred GNP layer. We attribute this observation to the hydrophilicity of the PU substrate.^[46] When applying the small amount of water to detach the GNP film from the glass surface it is, most likely, also dragged into the interfacial region between the GNP film and the hydrophilic PU surface, preventing the smooth and complete transfer of the GNP film.

The possible interfacial bonding between the 9DT crosslinked GNP film and the PU substrate is illustrated in Figure S11, Supporting Information. The contact angles of the GNP film and PU substrate, measured to evaluate the surface characteristics, were $\approx 40^\circ$ and $\approx 70^\circ$, respectively. The hydrophilicity of the GNP film can be ascribed to the 9DT crosslinkers with free thiol groups exposed at the film surface,^[47] leading to good affinity to water.^[48] The hydrophilicity of the PU film can be ascribed to the polar functional groups (i.e., urethane group and carboxyl group).^[46] Hence, we infer that two kinds of interfacial bonding (i.e., interaction 1 and interaction 2) exist at the interface of the GNP-PU film. Interaction 1 is based on the binding of the nitrogen atoms of the urethane groups to the surface of the GNPs, as reported previously.^[39a] Interaction 2 is based on the hydrogen bonding between the thiol groups of the 9DT crosslinker and the polar functional groups of the PU substrate.^[49]

strain sensor array measured while the finger was cyclically bent and stretched. B) Spatiotemporal measurement of arterial pulse waves: i) photograph of the GNP-PU strain sensor array (4×4). ii) Schematic illustration of the GNP-PU strain sensor array attached on the wrist to show the sensors' positions along the x-axis (positions "a", "b", "c", "d") and y-axis (positions "1", "2", "3", and "4") above the radial artery. The spacing between each active conductive area of the sensor was ≈ 5.4 mm along the x-axis and ≈ 3.2 mm along the y-axis. iii) Spatiotemporal arterial pulse waveform measured with the GNP-PU strain sensor array. iv) Pulse signals measured on the artery, near the artery, and off the artery. Scale bars represent 10 mm in (Ai), (Bi).

3.2. Characterization of the GNP-PU Strain Sensor

Over the past few years, nanomaterials-based strain sensors have often been highlighted because of their ultra-high sensitivity with gauge-factors of $\approx 10^2$ to 10^3 .^[1,4c,50] However, highly sensitive strain sensors usually suffer from a high noise level.^[51] Hence, it is important to consider the signal-to-noise ratio. Furthermore, if the substrate of the sensor is too stiff it cannot follow a subtle deformation of the skin and the signal is easily lost in the background noise.^[15b] As suggested by Boland,^[15b] an ideal strain sensor for healthcare monitoring should have a sufficiently high gauge factor (>7) and low enough Young's modulus (<300 kPa). In general agreement with these requirements, our results show that a GNP-based thin film transducer combined with a soft PU substrate enables accurate measurements of subtle physiological signals despite its rather low gauge factor of ≈ 10 (cf. Figures 4B(i) and 5). In addition, the conductance of the GNP-PU strain sensor was similar to previously published data referring to the 9DT crosslinked GNP films.^[4b,22c,47] The high resistance (several M Ω) of the 9DT crosslinked GNP-based strain sensors was mainly ascribed to the long alkylene chain length (C_9) of the 9DT crosslinker, the low film thickness, and the geometry of used electrode structure.^[4b,22c,47]

A practical strain sensor must possess sufficient durability, that is, it must provide stable response signals during long-term cyclic loading.^[52] In this study, the GNP-PU strain sensor was subjected to 10 000 strain–relaxation cycles and demonstrated excellent repeatability and durability (Figure 4B(ii), and Figure S5, Supporting Information), underlining its high potential for practical applications. The magnified plots of the fatigue test between the beginning cycles (i.e., 0–50 cycles; Figure S5A, Supporting Information) and the ending cycles (i.e., 9900–9950 cycles; Figure S5B, Supporting Information) showed a decrease of resistances, that is, decreasing from 1.631 to 1.624 M Ω for the relaxed GNP-PU sensor. This change is most likely not caused by a network variation of the PU substrate because the cyclic strain/relaxation responses of the PU substrate within the beginning and end cycles were almost the same (Figure S6, Supporting Information). To explore this finding, we investigated the influence of temperature variations on the electrical properties of the GNP-PU sensor (Figure S12, Supporting Information). The resistances decreased with increasing temperature. The resistances, 1.631 and 1.624 M Ω , corresponded to the temperatures of ≈ 24 and ≈ 26 °C, respectively, which is consistent with the monitored temperatures at the beginning and end of the fatigue test. Based on these results, we infer that the decreased resistances in the fatigue test (cf. Figure S5, Supporting Information) were caused by the increase of the environmental temperature. The $\Delta R/R_0$ response of the GNP-PU sensor within a strain range from 0 to 40% can be divided into three regions (Figure 4C(iii)). Within the small strain range from 0 to 3% (region 1), the sensor showed an initial nearly linear increase in resistance with increasing strain (up to $\approx 2\%$). The gauge factor in this region was ≈ 10 (Figure S9, Supporting Information). In accordance with earlier studies, we assign the initial increase in resistance to increasing interparticle distances impeding charge carrier tunneling between neighboring GNPs.^[4a,b,10b,53] Within the middle strain range from $\approx 3\%$ to $\approx 9\%$ (region 2), the gauge factor of the sensor decreased to ≈ 1 . In this region, the surface morphology of the sensor showed the

formation of initial microcracks with random orientation (Figure S8, Supporting Information), which may result from the stress concentration at residual deposition defects or voids in the GNP film when straining.^[8c] The observation of initial microcracks clearly shows that in region 2 the critical strain of the GNP film was reached. Hence, increasing the tensile strain beyond the critical strain induced the formation of microcracks but did not result in further extension of interparticle tunneling distances along the percolating pathways of charge transport. Previously, Park and coworkers studied the formation of microcracks in a strain sensor based on silver nanoparticles on a soft PDMS substrate.^[8c] In general agreement with our findings, their experimental data and theoretical simulations revealed that the formation of microcracks causes a rather moderate increase in resistance with a maximum gauge factor of only 2.05 at 20% tensile strain. However, within the large strain range from 9% to 40% (region 3), the formation of linear cracks in a perpendicular direction to the stretch direction was clearly observable. The number of cracks increased significantly with increasing tensile strain, which is consistent with the literature.^[54] Hence, in this region the response of the sensor is dominated by the disconnection–reconnection process of abundant linear cracks,^[55] which gives rise to the higher gauge factor (≈ 25).

Most of the common flexible substrates (e.g., LDPE, PET, PI, PDMS, Ecoflex) are non-degradable. To evaluate the degradability of the GNP-PU film in this study, the film was placed in distilled water at an accelerated degradation temperature of 74 °C, according to a previously published procedure.^[56] After 17 days the remaining weight of the GNP-PU film was $\approx 58\%$ (Figure 4D). Assuming that the degradation rate is doubled for every 10 °C temperature increase, a period of 17 days at 74 °C corresponds to ≈ 18 months at 24 °C.^[57] The obvious degradation of the PU substrate is attributed to the hydrolyzable polycaprolactone (PCL) diol segment (cf. Figure 1C). Note, we have deliberately chosen the PCL diol as the soft segment for the fabrication of the PU substrate because its hydrolysis is roughly ten times faster than that of polyether diol-based PU.^[58] Furthermore, the degradation products of the PCL diol-based PU do not show any obvious cytotoxicity.^[59] Our own previous works also showed that PCL diol-based PU is biocompatible and well suited for in vitro and in vivo healthcare applications.^[17a] Furthermore, to meet a broad range of various applications, our previous research demonstrated that the degradation rates of PU can be tuned by changing the types of soft segment.^[17a] For instance, the PCL/poly(D,L-lactide) (PDLLA) diol-based PU showed faster degradation than that of the PCL diol-based PU because the released acidic degradation products from PDLLA accelerate the degradation of PCL in vivo.^[17a] In our present study, we also showed that the GNP film can be transferred to the PCL/PDLLA diol-based PU film using our facile contact printing process with high fidelity (Figure S13, Supporting Information).

Biodegradable sensors based on different transduction mechanisms can be categorized into capacitive, piezoelectric, and piezoresistive/resistive types.^[60] All these types of biodegradable sensors have attracted great attention due to their application potential in the emerging fields of eco-friendly wearable electronics and implantable devices.^[12,61] For instance, Koivikko et al. developed eco-friendly capacitive sensors using biodegradable tree leaf skeleton films.^[62] Liu et al. developed disposable

piezoelectric sensors using natural silk films.^[63] However, the drawbacks of the leaf skeleton and silk films are poor stretchability (<5%) and scalability. In addition, the degradation rates are difficult to adjust to meet the requirements of different applications. For example, Curry et al. developed implantable piezoelectric sensors using biodegradable PLLA films.^[56] Hosseini et al. developed wearable piezoelectric sensors using biodegradable glycine-chitosan films.^[64] However, a drawback of the PLLA and glycine-chitosan films is their high Young's modulus (several gigapascals). As mentioned above, the substrate of a strain sensor with high stiffness cannot follow subtle deformations of the skin and the signal is easily lost in the background noise.^[15b] Further, the high Young's modulus of the substrate may cause wearing discomfort.^[135] In another example, Kang et al. developed bioresorbable piezoresistive sensors using a biodegradable poly(lactic-co-glycolic acid) (PLGA) film.^[65] By comparison, Hung et al. demonstrated that the biodegradable PU substrate had a lower Young's modulus and higher dimensional recoverability than the PLGA substrate.^[66] In our present study, the eco-friendly resistive sensors based on the biodegradable PU film feature a low Young's modulus (≈ 17.8 MPa), high stretchability (up to 1000% elongation without break), good durability (10 000 strain-relaxation cycles), and scalability (cf. Figure 6; micrometer- to millimeter-scale square and rectangle geometry, alphabetic characters, and wave and array patterns). Furthermore, by transferring the GNP film onto different types of PU films, the degradation rates could be adjusted.^[17a]

The common materials used as active conductive layer are based on gold, silver, and copper.^[2a] Among them, gold-based materials have the best environmental stability due to their remarkable resistance to corrosion and oxidation.^[67] In addition, nanogold-based materials usually have better biocompatibility than silver/copper-based nanomaterials.^[68] Further, the recyclability and reusability of the active conductive layer are highly desirable. Oestreicher et al. demonstrated that GNP recycling from nanowaste can be achieved through simple procedures and readily available chemical reagents (NaCl, HCl, H₂O₂).^[69]

3.3. Healthcare Applications of the GNP-PU Strain Sensor

The fabricated GNP-PU strain sensors are well suited for non-invasive personalized healthcare applications (Figure 5).^[2b,12,18a,70] For example, the pulse wave signals originating from the faint fluctuation of the radial artery can be used for the long-term assessment of the individual physiological condition and the diagnosis of cardiovascular diseases.^[71] As shown in Figure 5A, the GNP-PU strain sensor can resolve diagnostically detailed signals of the pulse wave (i.e., percussion wave, dicrotic wave, and tricuspid valve opening). As another application, we demonstrated that the GNP-PU strain sensor attached to an N95 (FFP2) face mask enables the well-resolved monitoring of human breathing (Figure 5C). This application can be useful for assessing the breathing resistance of face masks or lung functions of humans.^[72] Furthermore, the subtle physiological signals originating from the movement and vibration of throat muscles can provide a noninvasive assessment of swallowing function and aid patients with vocal problems (Figure 5D).^[73] For example, the wearable GNP-PU strain sensor attached to the human throat

can acquire detailed signals from swallowing and speaking. The acquired swallowing signals are similar to those of hydrogel-based strain or pressure sensors, reported earlier.^[74] The acquired voice signals correspond to stretching/contraction of the laryngeal muscles and enable the distinction of words based on their syllable suggesting the applicability of the GNP-PU strain sensor for voice recognition.^[50]

3.4. Fabrication of the Patterned GNP-PU Strain Sensors

In this study, two methods were used to pattern the GNP film before transferring them via contact printing onto the biodegradable PU substrate: in a first simple approach, we removed undesired sections of the GNP film on the original substrate by manual scratching, similar as described previously (Figure 2D).^[4b] This method, however, is not scalable and not useful for the economic parallel fabrication of sensor devices. Furthermore, it cannot be used to generate complex patterns, which are required for the production of sensor arrays or highly stretchable sensors with a fractal geometry of the sensitive layer.^[6,75] Therefore, we adapted a lithographic process, in which a sacrificial PMMA mask is patterned via deep-UV irradiation.^[31] After depositing the GNP film onto the PMMA mask, the patterned GNP film is obtained via a simple lift-off step (cf. Figure 6). However, initial attempts to transfer the patterned GNP film from the glass substrate onto the PDMS stamp failed. We attributed this problem to residual PMMA on the UV-irradiated areas which prevented the detachment of the GNP film from the glass substrate. Hence, the problem was solved by removing residual PMMA via a short plasma treatment prior to GNP deposition, after which the contact angle on the UV-irradiated sections of the glass substrate decreased from $\approx 66^\circ$ to $\approx 50^\circ$, confirming the increased hydrophilicity of the glass surface.

Based on this process, various patterned GNP films were successfully transferred onto the PDMS stamp and from there onto the biodegradable PU substrate. The examples shown in Figure 6A,B demonstrate the fabrication of patterned GNP films for large-scale and micro-scale flexible electronics.^[2b,76] The examples shown in Figure 6C–E demonstrate the fabrication of patterned GNP films with various promising designs and arrangements.^[77] For example, array patterns are required for the fabrication of sensor arrays to record signals with spatiotemporal resolution.^[7] Further, wave-patterned GNP films are promising for the design of sensors which are subjected to large strain variations.^[6] Furthermore, we note that our process for the fabrication of patterned nanoparticle films on flexible polymer substrates, which is based on straightforward photolithography and facile contact printing, is more clean and efficient than previously reported procedures.^[78]

3.5. Applications of GNP-PU Strain Sensor Arrays for Spatiotemporal Measurements

As mentioned above, strain sensor arrays enable the acquisition of signals with spatiotemporal resolution. Such sensor arrays are extremely useful to monitor and analyze complex actions.^[7,77,79] In this study, we presented GNP-PU strain sensor arrays that

are able to monitor finger bending and to accurately locate arterial lines and acquire well-resolved pulse waveforms (Figure 7). The pulse sensor array features several advantages. First, in contrast to a single element strain sensor, the pulse sensor array enables easy-to-use application because the precise positioning of the sensor is not critical. When attaching the sensor array only roughly above the radial artery, at least one of the sensors will be at a proper position to provide a well-resolved pulse wave signal. For example, the sensor element at coordinates (2,c) of the sensor array shown in Figure 7B provides a pulse wave signal with well-resolved and diagnostically relevant features (i.e., percussion wave P1, tidal wave P2, dicrotic wave P3, tricuspid valve opening P4). Second, the data shown in Figure 7B(ii,iii) suggest that the sensor array can be used to map the position of the radial artery in agreement with anatomical features known from the literature.^[80] Third, the pulse waveforms acquired at different positions of the radial artery (i.e., coordinates (3,a), (2,c), and (2,d)) can be used for personalized pulse diagnosis. For instance, in traditional Chinese medicine (TCM), the practitioner uses three fingers to palpate specific positions of the patient's wrist radial artery (i.e., Cun, Guan, and Chi).^[81] In the diagram of Figure 7B(ii), the coordinates (2,c) correspond to the position Guan, which is slightly below the styloid process of the radius bone. The coordinates (2,d) correspond to the position Cun, which is one finger anterior the Guan. The coordinates (3,a) correspond to the position Chi, which is one finger posterior to the Guan. The acquired pulse waveforms at these three positions are similar to data of the published literature,^[82] which indicates that our spatiotemporal arterial pulse wave map could be useful for the application of pulse wave diagnosis according to traditional Chinese medicine (TCM).

4. Summary and Conclusions

In this study, we fabricated resistive strain sensors by printing patterned GNP films onto flexible and biodegradable PU substrates. Two methods were used to pattern the GNP films, that is, mechanical removal and photolithography. The latter approach is scalable and compatible with standard lithographic fabrication routines. Using this approach, we demonstrated the fabrication of GNP films with various micrometer- to millimeter-scale patterns and transferred them onto the biodegradable PU substrates via clean and eco-friendly contact printing (i.e., without the need of additional organic solvents and chemicals). In addition, we demonstrated that the method can be used to print patterned GNP films onto biodegradable PU substrates of different compositions (i.e., PCL diol-based PU or PCL/PDLLA diol-based PU) with good fidelity. The degradation of the fabricated GNP-PU sensor in water was attributed to the hydrolysis of the polyester diol soft segment of the PU substrate. Combined with the soft PU substrate the GNP-based sensor with a relatively low gauge factor of $\approx 10^1$ enabled the accurate detection of subtle physiological signals, for example, measurements of well-resolved pulse waves and the action of laryngeal muscles during swallowing and speaking. Furthermore, GNP-PU sensor arrays with spatiotemporal strain resolution were fabricated and showed great potential for virtual reality and healthcare applications, such as finger joint flexion detection and pulse wave monitoring.^[12,71]

In conclusion, the presented GNP-PU strain sensors with biodegradability are well suited for the development of wearable eco-friendly electronics which are currently being developed for emerging internet-of-things (IoT) applications, including noninvasive personalized healthcare systems. Another emerging application of biodegradable sensors is their use in implantable electronics.^[18a,61] Implantable electronics with biodegradability and biocompatibility do not need a second surgery after fulfilling their purpose. Further, these materials and devices minimize chronic inflammatory responses during in vivo applications such as tissue engineering and regenerative medicine.^[65,83] Our current study has shown that the GNP films can be transferred onto different types of biodegradable PU films. Hence, GNP-PU strain sensors with tunable biodegradation rates of PU may become promising candidates for implantable electronics for various in vivo applications.^[17a,84] Moreover, implantable strain sensors with anisotropic response characteristics can be designed and fabricated by the facile contact printing method for use in multidirectional strain sensing in the future.^[4d,e]

5. Experimental Section

Synthesis and Characterization of the GNPs: GNPs were synthesized as reported by Peng et al.^[85] with some modifications. Briefly, an orange precursor solution containing chloroauric acid trihydrate (99.99%, Alfa Aesar), 1-dodecylamine (98%, Sigma-Aldrich), and hexane ($\geq 99\%$, VWR Chemicals) was magnetically stirred under N_2 flow at 30 °C. A reducing solution containing *tert*-butylamine-borane complex (98%, Merck), 1-dodecylamine, and hexane was rapidly injected into the precursor solution. After 1 h, ethanol ($\geq 99.9\%$, VWR Chemicals) was used to precipitate the GNPs. The GNPs were then collected by centrifugation, washed with 2-propanol ($\geq 99.5\%$, VWR Chemicals), and finally redispersed in *n*-heptane ($>99\%$, Honeywell). The synthesized GNPs were characterized by TEM (Jeol JEM-1011, acceleration voltage of 100 kV) and UV-vis absorption spectroscopy (Varian Cary 50). Prior to the TEM observation, 1-dodecylamine was exchanged by 1-dodecanethiol to ensure the stability of GNPs under TEM conditions.^[86] The average diameter of GNPs was determined using the ImageJ software.

Fabrication of the GNP Films: The GNP films were fabricated following a layer-by-layer spin-coating procedure described in the authors' previous study with slight modifications.^[4b,22c] Prior to spin-coating, a glass cover slip was sonicated (Bandelin Sonorex RK 255 H) in acetone for 15 min, rinsed with deionized water, and dried under ambient air. The glass slide was then treated with air plasma (Plasma Cleaner PDC-32G, Harrick Plasma) for 12 min. Subsequently, the glass slide was placed onto the center of a spin-coater and rotated at 3000 rpm. Meanwhile, 9DT (97%, Alfa Aesar) was dissolved in methanol ($\geq 99.9\%$, VWR Chemicals). 100 μ L of 9DT linker solution (7.4 mM) was dropped two times onto the rotating glass slide. Subsequently, 10 μ L of GNP solution (particle concentration:^[87] $\approx 9 \mu$ M) and $2 \times 10 \mu$ L of 9DT linker solution were alternately dropped onto the rotating glass slide. The time interval of each deposition was ≈ 30 s. After three repetitions of this cycle, the GNP film with the desired thickness was obtained. The glass slide covered with the GNP film was then immersed in the 9DT linker solution overnight, rinsed with acetone, and dried at ambient air for one day.

To fabricate patterned GNP films, a deep-UV photolithography process was conducted prior to the spin-coating procedure described above. The deep-UV photolithography procedure followed the authors' previous study with some modifications.^[31] First, the glass substrate was sonicated in acetone for 15 min, rinsed with deionized water, and dried under ambient air. Subsequently, the glass was treated with air plasma for 12 min. Meanwhile, PMMA (Mw ≈ 996 kDa, Sigma-Aldrich) was dissolved in chlorobenzene ($\geq 99\%$, Honeywell). The PMMA solution (33 mg mL⁻¹) was spin-coated onto the rotating glass substrate (4000 rpm) for 60 s.

Second, the PMMA-coated glass slide was baked at 60 °C for 10 min and then exposed to a custom-built deep-UV light source (wavelength of ≈ 254 nm) through a custom-designed photomask for 130 min. Third, the PMMA developer [mixture of 2-propanol and 4-methylpentan-2-one ($\geq 98.5\%$, Sigma-Aldrich) in a 3:1 v:v ratio] was prepared. In the first PMMA developing step, the UV-exposed PMMA-coated glass slide was immersed in PMMA developer for 70 s and then washed with 2-propanol for 30 s. Afterward, the PMMA-coated glass slide was treated with air plasma for 2 min and then washed in the second PMMA developing step (i.e., treated with PMMA developer for 70 s and then washed with 2-propanol for 30 s). After the deep-UV photolithography process, the GNP films were deposited onto the PMMA-masked glass slides via the above-described spin-coating procedure. After lift-off by acetone, the patterned GNP films on the glass substrates were obtained. The fabricated patterned GNP films were then immersed in the 9DT linker solution overnight, rinsed with acetone and dried in ambient air for one day.

The water contact angle of the sample surface was measured by a static contact angle analyzer (FTA-1000 B, First Ten Angstrom Company) at 25 °C. Each measurement was performed with a ≈ 5 μL water droplet. Each sample was measured at four different locations and the readings were averaged.

Fabrication and Characterization of the Biodegradable PU Substrates: The detailed synthetic procedure of the PU dispersions has been described previously.^[17a] Briefly, the oligodiols as the soft segment of the biodegradable PU was PCL diol (Mn ≈ 2000 Da, Sigma-Aldrich), or a combination of PCL diol with PDLLA diol (Mn ≈ 2000 Da) in 4:1 molar ratio. The PDLLA diol was synthesized from D,L-lactide (Purac) and 1,3-propanediol (Alfa Aesar). The oligodiols were reacted with IPDI (Evonik Degussa GmbH), 2,2-bis(hydroxymethyl)propionic acid (Sigma-Aldrich), triethylamine (R.D.H.), and ethylenediamine (Tedia) in 1:3.52:1:1:1.52 stoichiometric ratio. Finally, the waterborne biodegradable PU dispersions were obtained with a solid content of ≈ 30 wt%.

To fabricate the biodegradable PU films, the PU dispersions were casted onto single-use plastic petri dishes (Greiner). After drying for three days at ambient air (≈ 25 °C), the films were obtained. The biodegradable PU films described in the main text were made from the PCL diol-based type material (i.e., the soft segment of the PU film was PCL diol only). The fabricated biodegradable PU films were then cut by sharp scissors to obtain the desired sizes. The optical transparency of the biodegradable PU film was examined by absorption spectroscopy (Varian Cary 50). The average roughness of the films was measured by AFM and determined over an area of 4×10 μm^2 using the Gwyddion software package.

Fabrication and Characterization of the GNP-PU Films: The GNP-PU films were fabricated using the facile contact printing process, as shown in Figures 2D and 6. The contact printing process was done manually. The PDMS elastomer (Dow Sylgard 184 Kit Silicone Elastomer, Sigma-Aldrich) was prepared by mixing the base polymer and curing agent in a 10:1 weight ratio and curing for 4 h at 80 °C. The fabricated PDMS elastomer had a thickness of ≈ 5 mm. By cutting the PDMS elastomer with a sharp blade, the PDMS stamp with the appropriate size was obtained. During the contact printing process, bending or squeezing of the PDMS stamp carrying the GNP film should be avoided. The PDMS stamp with the GNP film was placed onto the PU substrate without pressing. For the heating/cooling cycle, the sample was first put onto a hot plate (Präzitherm 2860SR), covered with a glass petri dish (80 mm in diameter), and kept at 60 °C for 3 min. Subsequently, the sample was cooled to 0 °C for 3 min.^[44b]

The surface morphology of GNP films before (i.e., on the glass), during (i.e., on the PDMS stamp), and after contact printing (i.e., on the PU film) was characterized by optical microscopy (Olympus BX51), SEM (Zeiss LEO Gemini 1550, operating voltage of 5 kV), and AFM (Digital Instruments Multimode machine equipped with a AppNano ACTA cantilever, a Veeco 100 μm scanner, and a Nanoscope IV controller). For AFM observation, all scans were conducted in intermittent contact mode. The thickness of the GNP film was investigated by AFM at different film sections and analyzed using the Gwyddion software package.

Fabrication and Characterization of the GNP-PU Strain Sensors: The GNP-PU strain sensors were fabricated by depositing gold electrodes onto the GNP-PU films via PVD (Pfeiffer Classic 250) using shadow masks. The

electrode gap distances for the single element sensor (Figures 4 and 5) and the sensor array (Figure 7) were all ≈ 230 μm . The *I*-*V* curve of the GNP-PU strain sensor was measured using a Keithley 2601A source meter at a sweeping voltage from -5 to 5 V. Resistive strain responses were characterized by bending tests and tensile tests. The bending tests were conducted using a custom-built four-point bending setup, as described in the authors' previous study.^[4b] The GNP-PU strain sensor was fixed onto the circuit board stripe (FR4, thickness of ≈ 0.8 mm) using cyanoacrylate-based adhesive (Pattex). A commercial strain gauge (SGT-1/350-TY11) with a gauge factor of 2.14 was employed as reference sensor. The tensile tests were conducted using a computer-controlled universal tensile machine (Zwick/Roell) with a 10N KAP-TC load cell (Zwick KAP-TC). The dog-bone-shaped PU film with the GNP film at the center of the narrow part was fabricated using the facile contact printing process. The dimensions of the fabricated dog-bone-shaped GNP-PU film are shown in Figure S14, Supporting Information. To electrically connect the GNP-PU strain sensor for the bending tests and tensile tests, thin copper wires were attached to the gold electrodes of the sensor and glued by silver conductive paint. After drying at ambient air, the copper wires were connected to the source meter (Keithley 2601A). The resistances of the GNP-PU strain sensor were recorded by applying a constant voltage (1.0 V) and measuring the resulting current. All the above measurements were performed at ambient conditions. To investigate the influence of temperature variations on the electrical properties of the GNP-PU sensor, the resistance of the sensor was measured at different temperatures (24–36 °C). To this end, the sensor fixed on the circuit board stripe was placed in a custom-built chamber with a heated air flow system. The temperature inside the chamber was recorded using a thermocouple. The resistances of the sensor were recorded using a source meter (Keithley 2601A).

Applications of the GNP-PU Strain Sensors: For monitoring the radial pulse waves and wrist/finger bending as well as swallowing and speaking, the GNP-PU strain sensors were taped onto the wrist and finger joint as well as the throat using medical tape (Hansaplast Classic). The procedures were approved by the Institutional Review Board (IRB) in the Research Ethics Office of National Taiwan University (IRB 202209HM018). For monitoring breathing, the GNP-PU strain sensor was glued onto the face mask using cyanoacrylate-based adhesive (Pattex). All the above measurements were performed at ambient conditions.

Statistical Analysis: The result in Figure 1B was analyzed with Image J software. Other results were processed with OriginPro 2022 software.

Supporting Information

Supporting Information is available from the Wiley Online Library or from the author.

Acknowledgements

This research was supported by the Ministry of Science and Technology of Taiwan (MOST 109-2221-E-002-031-MY3). T.V. acknowledges financial support by the Deutsche Forschungsgemeinschaft (DFG, German Research Foundation), grant number GRK 2536/1. The authors thank Robert Schön and Stefan Werner for their contributions regarding SEM and TEM measurements.

Open access funding enabled and organized by Projekt DEAL.

Conflict of Interest

The authors declare no conflict of interest.

Author Contributions

S.D.W., S.H.H., and T.V. proposed and developed the research idea. S.D.W. performed the experimental design. S.D.W., S.B., and H.S. developed and

optimized the lithographic patterning process. S.D.W. and B.K. developed and optimized the contact printing process. H.S. and B.K. developed the customized test equipment. S.D.W., S.h.H., and T.V. performed the data evaluation and interpretation and wrote the manuscript. S.h.H., H.S., H.W., and T.V. supervised the research.

Data Availability Statement

The data that support the findings of this study are available in the supplementary material of this article.

Keywords

biodegradable polyurethane, eco-friendly electronics, gold nanoparticle, sensor arrays, wearable flexible strain sensors

Received: February 13, 2023

Revised: March 28, 2023

Published online: May 8, 2023

- [1] M. A. U. Khalid, S. H. Chang, *Compos. Struct.* **2022**, *284*, 115214.
- [2] a) H. Liu, Q. Li, S. Zhang, R. Yin, X. Liu, Y. He, K. Dai, C. Shan, J. Guo, C. Liu, C. Shen, X. Wang, N. Wang, Z. Wang, R. Wei, Z. Guo, *J. Mater. Chem. C* **2018**, *6*, 12121; b) Z. Shen, F. Liu, S. Huang, H. Wang, C. Yang, T. Hang, J. Tao, W. Xia, X. Xie, *Biosens. Bioelectron.* **2022**, *211*, 114298.
- [3] W. Gao, H. Ota, D. Kiriya, K. Takei, A. Javey, *Acc. Chem. Res.* **2019**, *52*, 523.
- [4] a) N. Olichwer, E. W. Leib, A. H. Halfar, A. Petrov, T. Vossmeier, *ACS Appl. Mater. Interfaces* **2012**, *4*, 6151; b) B. Ketelsen, M. Yesilmen, H. Schlicke, H. Noei, C.-H. Su, Y.-C. Liao, T. Vossmeier, *ACS Appl. Mater. Interfaces* **2018**, *10*, 37374; c) C.-B. Huang, Y. Yao, V. Montes-García, M.-A. Stoeckel, M. Von Holst, A. Ciesielski, P. Samorà, *Small* **2021**, *17*, 2007593; d) B. Ketelsen, H. Schlicke, V. R. Schulze, S. C. Bittinger, S.-D. Wu, S.-h. Hsu, T. Vossmeier, *Adv. Funct. Mater.* **2023**, *33*, 2210065; e) H.-W. Cheng, S. Yan, G. Shang, S. Wang, C.-J. Zhong, *Biosens. Bioelectron.* **2021**, *186*, 113268; f) N. M. Sangeetha, N. Decorde, B. Viallet, G. Viau, L. Ressler, *J. Phys. Chem. C* **2013**, *117*, 1935; g) H. Moreira, J. Grisolia, N. M. Sangeetha, N. Decorde, C. Farcau, B. Viallet, K. Chen, G. Viau, L. Ressler, *Nanotechnology* **2013**, *24*, 095701.
- [5] H.-N. Barad, H. Kwon, M. Alarcón-Correa, P. Fischer, *ACS Nano* **2021**, *15*, 5861.
- [6] J. A. Fan, W.-H. Yeo, Y. Su, Y. Hattori, W. Lee, S.-Y. Jung, Y. Zhang, Z. Liu, H. Cheng, L. Falgout, M. Bajema, T. Coleman, D. Gregoire, R. J. Larsen, Y. Huang, J. A. Rogers, *Nat. Commun.* **2014**, *5*, 3266.
- [7] S. Baek, Y. Lee, J. Baek, J. Kwon, S. Kim, S. Lee, K.-P. Strunk, S. Stehlin, C. Melzer, S.-M. Park, H. Ko, S. Jung, *ACS Nano* **2022**, *16*, 368.
- [8] a) M. Amjadi, A. Pichitpajongkit, S. Lee, S. Ryu, I. Park, *ACS Nano* **2014**, *8*, 5154; b) W.-W. Jheng, Y.-S. Su, Y.-L. Hsieh, Y.-J. Lin, S.-D. Tzeng, C.-W. Chang, J.-M. Song, W. Kuo, *ACS Appl. Nano Mater.* **2021**, *4*, 1712; c) J. Lee, S. Kim, J. Lee, D. Yang, B. C. Park, S. Ryu, I. Park, *Nanoscale* **2014**, *6*, 11932.
- [9] a) A. F. Carvalho, A. J. S. Fernandes, C. Leitão, J. Deuermeier, A. C. Marques, R. Martins, E. Fortunato, F. M. Costa, *Adv. Funct. Mater.* **2018**, *28*, 1805271; b) C.-W. Jiang, I. C. Ni, S.-D. Tzeng, W. Kuo, *Sci. Rep.* **2015**, *5*, 11939.
- [10] a) Q. Yu, R. Ge, J. Wen, T. Du, J. Zhai, S. Liu, L. Wang, Y. Qin, *Nat. Commun.* **2022**, *13*, 778; b) C. Farcau, H. Moreira, B. Viallet, J. Grisolia, D. Ciuculescu-Pradines, C. Amiens, L. Ressler, *J. Phys. Chem. C* **2011**, *115*, 14494; c) S. W. Lee, H. Joh, M. Seong, W. S. Lee, J. H. Choi, S. J. Oh, *J. Mater. Chem. C* **2017**, *5*, 2442.
- [11] H. J. Park, J.-M. Jeong, S. G. Son, S. J. Kim, M. Lee, H. J. Kim, J. Jeong, S. Y. Hwang, J. Park, Y. Eom, B. G. Choi, *Adv. Funct. Mater.* **2021**, *31*, 2011059.
- [12] T. Tat, G. Chen, X. Zhao, Y. Zhou, J. Xu, J. Chen, *ACS Nano* **2022**, *16*, 13301.
- [13] J. Lu, S. Hu, W. Li, X. Wang, X. Mo, X. Gong, H. Liu, W. Luo, W. Dong, C. Sima, Y. Wang, G. Yang, J.-T. Luo, S. Jiang, Z. Shi, G. Zhang, *ACS Nano* **2022**, *16*, 3744.
- [14] a) X. Ma, Q. Hu, Y. Dai, P. He, X. Zhang, *Sens. Actuators, A* **2022**, *346*, 113834; b) C. M. Boutry, Y. Kaizawa, B. C. Schroeder, A. Chortos, A. Legrand, Z. Wang, J. Chang, P. Fox, Z. Bao, *Nat. Electron.* **2018**, *1*, 314.
- [15] a) V. C. Pinto, T. Ramos, S. Alves, J. Xavier, P. Tavares, P. M. G. P. Moreira, R. M. Guedes, *Procedia Eng.* **2015**, *114*, 635; b) C. S. Boland, *ACS Nano* **2019**, *13*, 13627.
- [16] Z. Liu, C. Li, X. Zhang, B. Zhou, S. Wen, Y. Zhou, S. Chen, L. Jiang, S. Jerrams, F. Zhou, *ACS Sustainable Chem. Eng.* **2022**, *10*, 8788.
- [17] a) S.-h. Hsu, K.-C. Hung, Y.-Y. Lin, C.-H. Su, H.-Y. Yeh, U. S. Jeng, C.-Y. Lu, S. A. Dai, W.-E. Fu, J.-C. Lin, *J. Mater. Chem. B* **2014**, *2*, 5083; b) A. Ni Annaidh, K. Bruyère, M. Destrade, M. D. Gilchrist, M. Otténio, *J. Mech. Behav. Biomed. Mater.* **2012**, *5*, 139.
- [18] a) Y. Song, J. Min, W. Gao, *ACS Nano* **2019**, *13*, 12280; b) X. Lin, F. Li, Y. Bing, T. Fei, S. Liu, H. Zhao, T. Zhang, *Nano-Micro Lett.* **2021**, *13*, 200.
- [19] W. Li, Q. Liu, Y. Zhang, C. a. Li, Z. He, W. C. H. Choy, P. J. Low, P. Sonar, A. K. K. Kyaw, *Adv. Mater.* **2020**, *32*, 2001591.
- [20] C. Wang, C. Linghu, S. Nie, C. Li, Q. Lei, X. Tao, Y. Zeng, Y. Du, S. Zhang, K. Yu, H. Jin, W. Chen, J. Song, *Sci. Adv.* **2020**, *6*, eabb2393.
- [21] M. Su, Y. Song, *Chem. Rev.* **2022**, *122*, 5144.
- [22] a) G. F. Schneider, V. E. Calado, H. Zandbergen, L. M. K. Vandersypen, C. Dekker, *Nano Lett.* **2010**, *10*, 1912; b) Y. Chen, Z. Shu, Z. Feng, L. a. Kong, Y. Liu, H. Duan, *Adv. Funct. Mater.* **2020**, *30*, 2002549; c) H. Schlicke, J. H. Schröder, M. Trebbin, A. Petrov, M. Ijeh, H. Weller, T. Vossmeier, *Nanotechnology* **2011**, *22*, 305303.
- [23] a) C. H. Lee, D. R. Kim, I. S. Cho, N. William, Q. Wang, X. Zheng, *Sci. Rep.* **2012**, *2*, 1000; b) D. S. Wie, Y. Zhang, M. K. Kim, B. Kim, S. Park, Y.-J. Kim, P. P. Irazoqui, X. Zheng, B. Xu, C. H. Lee, *Proc. Natl. Acad. Sci. USA* **2018**, *115*, E7236; c) C. Varnava, *Nat. Electron.* **2018**, *1*, 432.
- [24] a) X. Li, W. Cai, J. An, S. Kim, J. Nah, D. Yang, R. Piner, A. Velamakanni, I. Jung, E. Tutuc, S. K. Banerjee, L. Colombo, R. S. Ruoff, *Science* **2009**, *324*, 1312; b) J. Jiang, Q. Wang, B. Wang, J. Dong, Z. Li, X. Li, Y. Zi, S. Li, X. Wang, *Nano Energy* **2019**, *59*, 545; c) D. Pesquera, E. Khestanova, M. Ghidini, S. Zhang, A. P. Rooney, F. Maccherozzi, P. Riego, S. Farokhipoor, J. Kim, X. Moya, M. E. Vickers, N. A. Stelmashenko, S. J. Haigh, S. S. Dhesi, N. D. Mathur, *Nat. Commun.* **2020**, *11*, 3190.
- [25] a) L. Jiao, B. Fan, X. Xian, Z. Wu, J. Zhang, Z. Liu, *J. Am. Chem. Soc.* **2008**, *130*, 12612; b) S.-W. Hwang, J.-K. Song, X. Huang, H. Cheng, S.-K. Kang, B. H. Kim, J.-H. Kim, S. Yu, Y. Huang, J. A. Rogers, *Adv. Mater.* **2014**, *26*, 3905; c) J. Park, R. Ghosh, M. S. Song, Y. Hwang, Y. Tchoe, R. K. Saroj, A. Ali, P. Guha, B. Kim, S.-W. Kim, M. Kim, G.-C. Yi, *NPG Asia Mater* **2022**, *14*, 40; d) H. Li, J. Wu, X. Huang, Z. Yin, J. Liu, H. Zhang, *ACS Nano* **2014**, *8*, 6563.
- [26] V. E. Calado, G. F. Schneider, A. M. M. G. Theulings, C. Dekker, L. M. K. Vandersypen, *Appl. Phys. Lett.* **2012**, *101*, 103116.
- [27] M.-H. Seo, J.-Y. Yoo, M.-S. Jo, J.-B. Yoon, *Adv. Mater.* **2020**, *32*, 1907082.
- [28] P.-L. Durand, G. Chollet, E. Grau, H. Cramail, *RSC Adv.* **2019**, *9*, 145.
- [29] a) S. D. Razumovskii, G. E. Zaikov, *Mol. Cryst. Liq. Cryst.* **2012**, *556*, 1; b) E. S. Hosseini, S. Dervin, P. Ganguly, R. Dahiya, *ACS Appl. Bio Mater.* **2021**, *4*, 163.
- [30] a) B. Zhuang, S. Li, S. Li, J. Yin, *Carbon* **2021**, *173*, 609; b) J. W. Suk, W. H. Lee, J. Lee, H. Chou, R. D. Piner, Y. Hao, D. Akinwande, R. S. Ruoff, *Nano Lett.* **2013**, *13*, 1462.

- [31] H. Schlicke, S. C. Bittinger, T. Vossmeier, *ACS Appl. Electron. Mater.* **2020**, *2*, 3741.
- [32] G. Carotenuto, S. De Nicola, M. Palomba, D. Pullini, A. Horsewell, T. W. Hansen, L. Nicolais, *Nanotechnology* **2012**, *23*, 485705.
- [33] D. Qi, K. Zhang, G. Tian, B. Jiang, Y. Huang, *Adv. Mater.* **2021**, *33*, 2003155.
- [34] a) C. Qu, J. Hu, X. Liu, Z. Li, Y. Ding, *Materials* **2017**, *10*, 1329; b) Y. Bin, K. Oishi, K. Yoshida, M. Matsuo, *Polym. J.* **2004**, *36*, 888.
- [35] S. F. A. Zaidi, Y. A. Kim, A. Saeed, N. Sarwar, N.-E. Lee, D. H. Yoon, B. Lim, J. H. Lee, *Int. J. Biol. Macromol.* **2022**, *209*, 1665.
- [36] a) W.-Y. Chang, T.-H. Fang, Y.-C. Lin, *Appl. Phys. A* **2008**, *92*, 693; b) R. Panowicz, M. Konarzewski, T. Durejko, M. Szala, M. Łazińska, M. Czerwińska, P. Prasuła, *Materials* **2021**, *14*, 3833.
- [37] E. Roh, B.-U. Hwang, D. Kim, B.-Y. Kim, N.-E. Lee, *ACS Nano* **2015**, *9*, 6252.
- [38] a) N. B. Trung, H. Yoshikawa, E. Tamiya, P. H. Viet, Y. Takamura, T. Ashahi, *Jpn. J. Appl. Phys.* **2012**, *51*, 037001; b) H. SadAbadi, S. Badilescu, M. Packirisamy, R. Wüthrich, *Biosens. Bioelectron.* **2013**, *44*, 77.
- [39] a) S. Phadtare, A. Kumar, V. P. Vinod, C. Dash, D. V. Palaskar, M. Rao, P. G. Shukla, S. Sivaram, M. Sastry, *Chem. Mater.* **2003**, *15*, 1944; b) T. Chen, Y. Xie, Z. Wang, J. Lou, D. Liu, R. Xu, Z. Cui, S. Li, M. Panahi-Sarmad, X. Xiao, *ACS Appl. Polym. Mater.* **2021**, *3*, 5317.
- [40] Y. Kim, J. Zhu, B. Yeom, M. Di Prima, X. Su, J.-G. Kim, S. J. Yoo, C. Uher, N. A. Kotov, *Nature* **2013**, *500*, 59.
- [41] Q. Huang, Y. Zhu, *Adv. Mater. Technol.* **2019**, *4*, 1800546.
- [42] Y. Li, Y. Liu, S. R. A. Bhuiyan, Y. Zhu, S. Yao, *Small Struct.* **2022**, *3*, 2100131.
- [43] a) H. Schlicke, S. Kunze, M. Finsel, E. W. Leib, C. J. Schröter, M. Blankenburg, H. Noei, T. Vossmeier, *J. Phys. Chem. C* **2019**, *123*, 19165; b) T. Ung, L. M. Liz-Marzán, P. Mulvaney, *J. Phys. Chem. B* **2001**, *105*, 3441.
- [44] a) A. E. Wiącek, A. Gozdecka, M. Jurak, K. Przykaza, K. Terpiłowski, *Colloids Surf., A* **2018**, *551*, 185; b) H. Hartmann, J.-N. Beyer, J. Hansen, S. C. Bittinger, M. Yesilmen, H. Schlicke, T. Vossmeier, *ACS Appl. Mater. Interfaces* **2021**, *13*, 40932.
- [45] M. K. Choi, I. Park, D. C. Kim, E. Joh, O. K. Park, J. Kim, M. Kim, C. Choi, J. Yang, K. W. Cho, J.-H. Hwang, J.-M. Nam, T. Hyeon, J. H. Kim, D.-H. Kim, *Adv. Funct. Mater.* **2015**, *25*, 7109.
- [46] S.-H. Hsu, L.-G. Dai, Y.-M. Hung, N.-T. Dai, *Int. J. Nanomed.* **2018**, *13*, 5485.
- [47] Y. Joseph, I. Besnard, M. Rosenberger, B. Guse, H.-G. Nothofer, J. M. Wessels, U. Wild, A. Knop-Gericke, D. Su, R. Schlögl, A. Yasuda, T. Vossmeier, *J. Phys. Chem. B* **2003**, *107*, 7406.
- [48] W. J. Yang, K.-G. Neoh, E.-T. Kang, S. Lay-Ming Teo, D. Rittschof, *Polym. Chem.* **2013**, *4*, 3105.
- [49] I. A. Lobo, P. A. Robertson, L. Villani, D. J. D. Wilson, E. G. Robertson, *J. Phys. Chem. A* **2018**, *122*, 7171.
- [50] C. Wang, J. Zhao, C. Ma, J. Sun, L. Tian, X. Li, F. Li, X. Han, C. Liu, C. Shen, L. Dong, J. Yang, C. Pan, *Nano Energy* **2017**, *34*, 578.
- [51] J. Chen, J. Zheng, Q. Gao, J. Zhang, J. Zhang, O. M. Ormisor, L. Wang, H. Li, *Appl. Sci.* **2018**, *8*, 345.
- [52] H. Souiri, H. Banerjee, A. Jusufi, N. Radacsi, A. A. Stokes, I. Park, M. Sitti, M. Arjadi, *Adv. Intell. Syst.* **2020**, *2*, 2000039.
- [53] a) J. Ivančo, K. Végso, P. Šiffalovič, D. Kostiuk, Y. Halahovets, I. Kláčková, M. Kotlar, Š. Luby, E. Majková, *Key Eng. Mater.* **2015**, *644*, 31; b) J. Herrmann, K.-H. Müller, T. Reda, G. R. Baxter, B. Raguse, G. J. B. d. Groot, R. Chai, M. Roberts, L. Wieczorek, *Appl. Phys. Lett.* **2007**, *91*, 183105.
- [54] Y. Wang, P. Kanjanaboos, E. Barry, S. McBride, X.-M. Lin, H. M. Jaeger, *Nano Lett.* **2014**, *14*, 826.
- [55] a) D. Kang, P. V. Pikhitsa, Y. W. Choi, C. Lee, S. S. Shin, L. Piao, B. Park, K.-Y. Suh, T.-i. Kim, M. Choi, *Nature* **2014**, *516*, 222; b) M. Arjadi, K.-U. Kyung, I. Park, M. Sitti, *Adv. Funct. Mater.* **2016**, *26*, 1678.
- [56] E. J. Curry, K. Ke, M. T. Chorsi, K. S. Wrobel, A. N. Miller, A. Patel, I. Kim, J. Feng, L. Yue, Q. Wu, C.-L. Kuo, K. W.-H. Lo, C. T. Laurencin, H. Ilies, P. K. Purohit, T. D. Nguyen, *Proc. Natl. Acad. Sci. USA* **2018**, *115*, 909.
- [57] J. Janting, J. G. Theander, H. Egesborg, *IEEE Trans. Device Mater. Reliab.* **2019**, *19*, 313.
- [58] R. S. Labow, D. J. Erfle, J. P. Santerre, *Biomaterials* **1996**, *17*, 2381.
- [59] L. Tatai, T. G. Moore, R. Adhikari, F. Malherbe, R. Jayasekara, I. Griffiths, P. A. Gunatillake, *Biomaterials* **2007**, *28*, 5407.
- [60] Y. Li, W. Chen, L. Lu, *ACS Appl. Bio Mater.* **2021**, *4*, 122.
- [61] N. Ashammakhi, A. L. Hernandez, B. D. Unluturk, S. A. Quintero, N. R. de Barros, E. Hoque Apu, A. Bin Shams, S. Ostrovidov, J. Li, C. Contag, A. S. Gomes, M. Holgado, *Adv. Funct. Mater.* **2021**, *31*, 2104149.
- [62] A. Koivikko, V. Sharma, V. Lampinen, K. Yiannacou, V. Sariola, *IEEE Sens. J.* **2021**, *22*, 11241.
- [63] J.-H. Liu, W.-D. Li, J. Jia, C.-Y. Tang, S. Wang, P. Yu, Z.-M. Zhang, K. Ke, R.-Y. Bao, Z.-Y. Liu, Y. Wang, K. Zhang, M.-B. Yang, W. Yang, *Nano Energy* **2022**, *103*, 107787.
- [64] E. S. Hosseini, L. Manjakkal, D. Shakthivel, R. Dahiya, *ACS Appl. Mater. Interfaces* **2020**, *12*, 9008.
- [65] S.-K. Kang, R. K. J. Murphy, S.-W. Hwang, S. M. Lee, D. V. Harburg, N. A. Krueger, J. Shin, P. Gamble, H. Cheng, S. Yu, Z. Liu, J. G. McCall, M. Stephen, H. Ying, J. Kim, G. Park, R. C. Webb, C. H. Lee, S. Chung, D. S. Wie, A. D. Gujar, B. Vernulapalli, A. H. Kim, K.-M. Lee, J. Cheng, Y. Huang, S. H. Lee, P. V. Braun, W. Z. Ray, J. A. Rogers, *Nature* **2016**, *530*, 71.
- [66] K. C. Hung, C. S. Tseng, S. h. Hsu, *Adv. Healthcare Mater.* **2014**, *3*, 1578.
- [67] a) J. Yi, Y. Xianyu, *Adv. Funct. Mater.* **2022**, *32*, 2113012; b) O. Mbanga, E. Cukrowska, M. Gulumian, *Toxicol. Rep.* **2022**, *9*, 788; c) A. A. Keller, A. S. Adeleye, J. R. Conway, K. L. Garner, L. Zhao, G. N. Cherr, J. Hong, J. L. Gardea-Torresdey, H. A. Godwin, S. Hanna, Z. Ji, C. Kaweeteerawat, S. Lin, H. S. Lenihan, R. J. Miller, A. E. Nel, J. R. Peralta-Videa, S. L. Walker, A. A. Taylor, C. Torres-Duarte, J. I. Zink, N. Zuverza-Mena, *NanoImpact* **2017**, *7*, 28.
- [68] a) C. Lasagna-Reeves, D. Gonzalez-Romero, M. A. Barria, I. Olmedo, A. Clos, V. M. S. Ramanujam, A. Urayama, L. Vergara, M. J. Kogan, C. Soto, *Biochem. Biophys. Res. Commun.* **2010**, *393*, 649; b) P. Murawala, S. M. Phadnis, R. R. Bhonde, B. L. V. Prasad, *Colloids Surf., B* **2009**, *73*, 224; c) M. Zhou, B. Wang, Z. Rozynek, Z. Xie, J. O. Fossum, X. Yu, S. Raaen, *Nanotechnology* **2009**, *20*, 505606.
- [69] V. Oestreicher, C. S. García, G. J. A. A. Soler-Illia, P. C. Angelomé, *ChemSusChem* **2019**, *12*, 4882.
- [70] W. Fan, Q. He, K. Meng, X. Tan, Z. Zhou, G. Zhang, J. Yang, Z. L. Wang, *Sci. Adv.* **2020**, *6*, eaay2840.
- [71] K. Meng, X. Xiao, W. Wei, G. Chen, A. Nashalian, S. Shen, X. Xiao, J. Chen, *Adv. Mater.* **2022**, *34*, 2109357.
- [72] H. P. Lee, D. Y. Wang, *Ann. Occup. Hyg.* **2011**, *55*, 917.
- [73] J. Baker, C. Barnett, L. Cavalli, M. Dietrich, L. Dixon, J. R. Duffy, A. Elias, D. E. Fraser, J. L. Freeburn, C. Gregory, K. McKenzie, N. Miller, J. Patterson, C. Roth, N. Roy, J. Short, R. Utianski, M. van Mersbergen, A. Vertigan, A. Carson, J. Stone, L. McWhirter, *J. Neurol., Neurosurg. Psychiatry* **2021**, *92*, 1112.
- [74] a) G. Ge, Y. Zhang, J. Shao, W. Wang, W. Si, W. Huang, X. Dong, *Adv. Funct. Mater.* **2018**, *28*, 1802576; b) H. Wu, H. Qi, X. Wang, Y. Qiu, K. Shi, H. Zhang, Z. Zhang, W. Zhang, Y. Tian, *J. Mater. Chem. C* **2022**, *10*, 8206.
- [75] W. Dong, X. Cheng, X. Wang, H. Zhang, *Appl. Phys. A* **2018**, *124*, 478.
- [76] K. S. Kim, Y. Zhao, H. Jang, S. Y. Lee, J. M. Kim, K. S. Kim, J.-H. Ahn, P. Kim, J.-Y. Choi, B. H. Hong, *Nature* **2009**, *457*, 706.
- [77] W. Wang, L. Qi, *Adv. Funct. Mater.* **2019**, *29*, 1807275.
- [78] W. A. D. M. Jayathilaka, K. Qi, Y. Qin, A. Chinnappan, W. Serrano-García, C. Baskar, H. Wang, J. He, S. Cui, S. W. Thomas, S. Ramakrishna, *Adv. Mater.* **2019**, *31*, 1805921.

- [79] W. Feng, W. Zheng, F. Gao, X. Chen, G. Liu, T. Hasan, W. Cao, P. Hu, *Chem. Mater.* **2016**, *28*, 4278.
- [80] A. R. Bauder, Z. Steinberger, O. B. Amotz, L. S. Levin, I. C. Lin, in *Recipient Vessels in Reconstructive Microsurgery: Anatomy and Technical Considerations* (Eds.: R. Gurunian, R. Djohan), Springer International Publishing, Cham **2021**, p. 149.
- [81] Y. Chu, J. Zhong, H. Liu, Y. Ma, N. Liu, Y. Song, J. Liang, Z. Shao, Y. Sun, Y. Dong, X. Wang, L. Lin, *Adv. Funct. Mater.* **2018**, *28*, 1803413.
- [82] Y. Qiao, J. Jian, H. Tang, S. Ji, Y. Liu, H. Liu, Y. Li, X. Li, F. Han, Z. Liu, T. Cui, G. Gou, L. Jiang, Y. Yang, B. Zhou, T.-L. Ren, J. Zhou, *J. Mater. Chem. A* **2022**, *10*, 4858.
- [83] J. A. Chiong, H. Tran, Y. Lin, Y. Zheng, Z. Bao, *Adv. Sci.* **2021**, *8*, 2101233.
- [84] S.-h. Hsu, C.-M. Tang, H.-J. Tseng, *Biomacromolecules* **2008**, *9*, 241.
- [85] S. Peng, Y. Lee, C. Wang, H. Yin, S. Dai, S. Sun, *Nano Res.* **2008**, *1*, 229.
- [86] H. Schlicke, E. W. Leib, A. Petrov, J. H. Schröder, T. Vossmeier, *J. Phys. Chem. C* **2014**, *118*, 4386.
- [87] W. Haiss, N. T. K. Thanh, J. Aveyard, D. G. Fernig, *Anal. Chem.* **2007**, *79*, 4215.

4. Unpublished work (fourth project): Biocompatible and highly sensitive strain sensor integration in a heart-on-a-chip with 3D cardiomyocyte spheroids

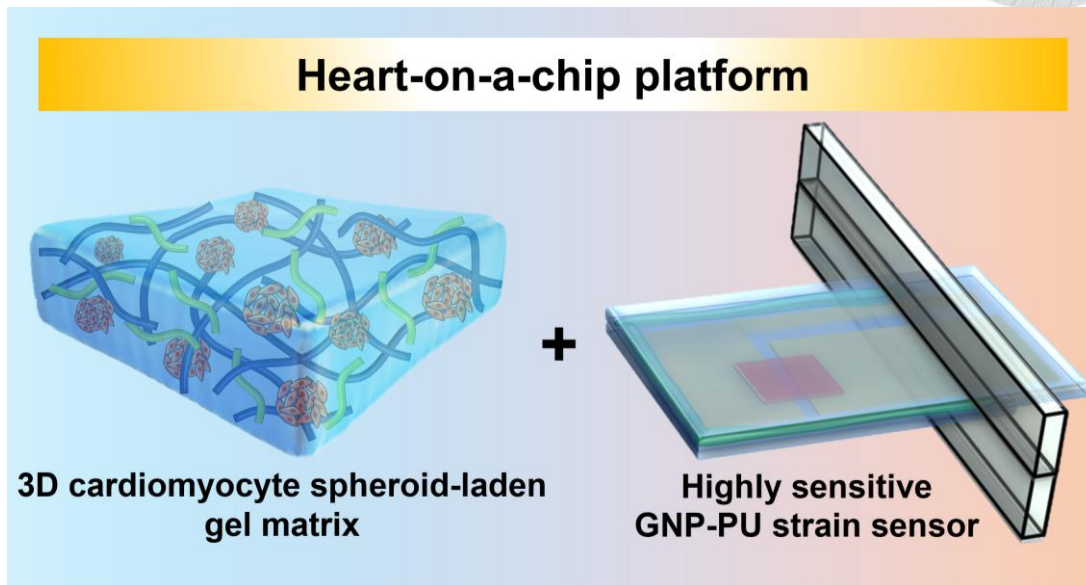
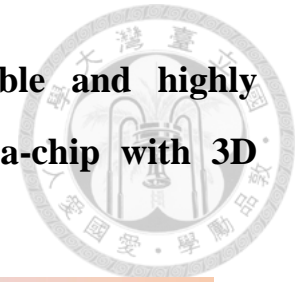


Figure 5. Graphical abstract of the fourth project.

4.1. Introduction

Cardiac diseases, a major threat to human health, require advancements in drug discovery and development for effective treatments [238]. Conventionally, in vivo animal models were the standard for evaluating potential cardiac disease therapeutics [239, 240]. However, due to inter-species differences in non-human proteomes, animal models often fail to predict human cardiotoxicity [241]. To address the problem, heart-on-a-chip platforms have emerged as a promising solution, offering more precise in vitro models that better replicate cardiac physiology in patients [242-244]. The heart-on-a-chip platforms are typically comprised of three key elements: 3D cardiac tissues, ECM, and sensors (**Figure 6**) [245]. 3D cardiac tissues (e.g., cardiomyocyte spheroids), compared to conventional 2D monolayers, offer a more comprehensive replication of the structural and cellular complexity (e.g., cell-cell and cell-ECM interactions), better mimicking the

natural conditions of the human heart [246, 247]. The integration of 3D cardiomyocyte spheroids derived from human induced pluripotent stem cells (hiPSCs) offers a scalable and human-relevant cell source that overcomes limitations of conventional animal models [248, 249]. Further, hiPSC-derived cardiomyocyte spheroids obtained from patients with specific genotypes can mimic human disease phenotypes in vitro, allowing for more precise insights into personalized cardiac physiology [250].

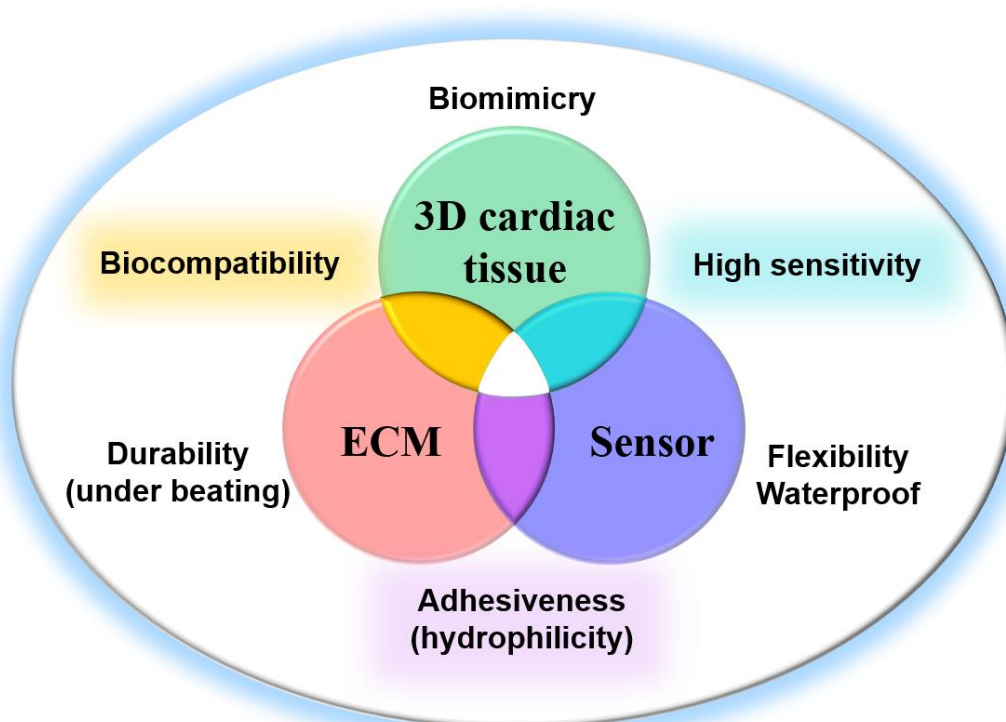
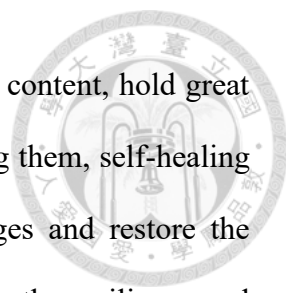


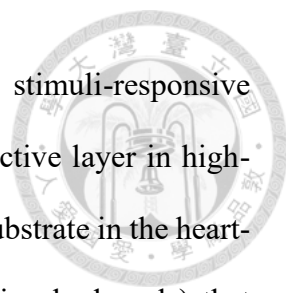
Figure 6. Elements and ideal conditions of heart-on-a-chip platforms for use as in vitro 3D cardiac models.

The ECM in heart-on-a-chip platforms provides a supportive network that mimics the in vivo environment of the human heart for enhancing cell viability and functionality [246]. The ideal ECM must be resilient to cyclic loading forces, which is crucial for proper functionality under continuous mechanical deformations of cardiac tissues [251].



Hydrogels, hydrophilic polymer networks known for the high water content, hold great potential as the ECM for culturing cardiac tissues [251, 252]. Among them, self-healing hydrogels are able to intrinsically and automatically repair damages and restore the original structures and functions, which could be used for enhancing the resilience and structural integrity of the cell-laden matrices [253-256]. Therefore, the employment of suitable self-healing hydrogels with biocompatibility as the ECM to facilitate the sustained development and maturation of cardiomyocyte spheroids is highly desired [257]. In addition, to measure cardiomyocyte contractility for health status assessment, traditional methods often involve optical sensing techniques such as video analysis, laser sensing, atomic force microscopy (AFM), and traction force microscopy (TFM) [258-261]. However, these methods have their own challenges. For instance, optical methods require complex and time-consuming setup procedures, including repeated alignments of microscopes or laser sources [246]. AFM involves direct contact with cardiomyocytes, potentially altering the beating patterns unintentionally [262]. Furthermore, the instruments used in AFM and TFM are costly and complicated to operate [263]. To address these limitations, the development of electrical signal-based contractility sensors has emerged as a promising alternative [264].

Electrical signal-based sensors such as strain and impedance sensors enable facile, real-time, and long-term recording of cardiac contractility [265]. In particular, thin film strain sensors have gained much attention for cardiac sensing due to the flexibility [264, 266]. Thin-film strain sensors are typically composed of two components: an active conductive layer and a flexible substrate [219]. The active conductive layer, consisting of organic and/or inorganic nanomaterials, is responsible for providing functional sensing properties to the strain sensors [176]. Among various metal nanoparticles, GNPs are considered the most appropriate for in vitro and in vivo biomedical applications due to



their biocompatibility [267, 268]. GNP thin films, known for the stimuli-responsive charge transport properties, are commonly used as the active conductive layer in high-performance strain sensors [220, 221, 269]. The role of the flexible substrate in the heart-on-a-chip platform is twofold: it supports the ECM (e.g., self-healing hydrogels) that nurtures 3D cardiac tissues and acts as a structural base for the configuration of the active conductive layer [246, 263, 264]. Therefore, it is important that the flexible substrate possesses compatible surface properties to those of the ECM, ensuring effective integration essential for reliable sensing of cardiac contractility. Meanwhile, the flexible substrate must have good biocompatibility and waterproof properties to maintain cell viability and sensing functionality, respectively, in the cell culture medium at the physiological temperature [263]. Moreover, thin-film strain sensors with high sensitivity are highly desirable for precise monitoring and analysis of cardiac contractility, facilitating noninvasive disease modeling and cardiotoxicity assessment in vitro [264].

In this study, we introduce a new heart-on-a-chip platform, comprising a cell-laden gel matrix and a highly sensitive thin-film strain sensor. The cell-laden gel matrix was constructed from 3D hiPSC-derived cardiomyocyte spheroids embedded within a self-healing chitosan-based hydrogel. The thin-film strain sensor included the GNP thin film as the active conductive layer which was integrated with a biocompatible, flexible PU substrate. A facile, clean, and high-precision contact printing method was used for transferring the GNP film from the glass onto the PU substrate, without the usage of cytotoxic organic solvents or chemical etchants. The fabricated GNP-PU thin-film strain sensors demonstrated high sensitivity (a gauge factor of ~ 50). The developed heart-on-a-chip platform was capable of detecting the contractile behavior of the 3D cardiomyocyte spheroids. Compared with the conventional animal and 2D models, the new heart-on-a-chip platform enables a more accurate and efficient assessment of cardiac contractility,

enhancing the replication of cardiac tissue complexities.



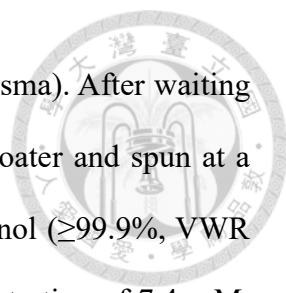
4.2. Materials and methods

4.2.1. Synthesis and characterization of the GNPs

The synthesis of GNPs was adapted from the method described by Peng et al. [161], with certain alterations. Initially, a precursor solution was prepared by mixing chloroauric acid trihydrate (99.99%, Alfa Aesar), 1-dodecylamine (98%, Sigma-Aldrich), and hexane ($\geq 99\%$, VWR Chemicals) and stirring it magnetically under a nitrogen atmosphere at a temperature of 30 °C. Subsequently, a reduction solution containing tert-butylamine-borane complex (98%, Merck), 1-dodecylamine, and hexane was quickly injected into this precursor mixture. One hour later, ethanol ($\geq 99.9\%$, VWR Chemicals) was added to induce the precipitation of the GNPs. These nanoparticles were then isolated by centrifugation, washed with 2-propanol ($\geq 99.5\%$, VWR Chemicals), and dispersed again in n-heptane ($> 99\%$, Honeywell). For characterization, the GNPs were analyzed by TEM, using a Jeol JEM-1011 microscope with an acceleration voltage of 100 kV and ultraviolet-visible (UV-vis) absorption spectroscopy, using a Varian Cary 50 instrument. Before the TEM analysis, 1-dodecylamine was exchanged for 1-dodecanethiol to enhance the stability of the GNPs. The average diameter of the nanoparticles was determined using ImageJ software.

4.2.2. Fabrication and characterization of the GNP-PU film

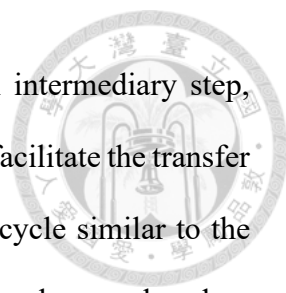
The fabrication of the GNP film was conducted using the layer-by-layer spin-coating technique as described previously [269]. Initially, a glass cover slip was thoroughly cleaned by sonicating (Bandelin Sonorex RK 255 H) it in acetone for 15 min, followed by rinsing with deionized water and air drying. The glass was then subjected to air plasma



treatment for 12 min using a plasma cleaner (PDC-32G, Harrick Plasma). After waiting for one day, the glass slide was positioned at the center of a spin-coater and spun at a speed of 3000 rpm. 9DT (97%, Alfa Aesar) was dissolved in methanol ($\geq 99.9\%$, VWR Chemicals). Then, 100 μL of the 9DT linker solution, with a concentration of 7.4 mM, was dropped twice onto the spinning glass slide. Subsequently, 10 μL of GNP solution (with a particle concentration of $\sim 9 \mu\text{M}$ [270]) and $2 \times 10 \mu\text{L}$ of 9DT linker solution were alternately dropped onto the rotating glass slide. Each deposition step was spaced by ~ 30 s. This cycle was repeated three times to achieve the desired film thickness. Finally, the glass slide covered with the GNP film was immersed overnight in the 9DT linker solution, then cleaned with acetone, and left to dry in ambient air for a day.

The biocompatible PU film was prepared as reported by Brinkman et al. with some modifications [271]. Pellethane 2363 80A (Lubrizol) was first dissolved in THF ($\geq 99.7\%$, VWR Chemicals) to create a 4.5% (w/w) solution. This solution was shaken at room temperature for 6 h to ensure complete dissolution. Subsequently, the solution was passed through a 0.45 μm Teflon filter. The filtered solution was then cast onto the glass petri dish. After the solvent evaporated for one day at 40 $^{\circ}\text{C}$, the resulting film underwent further drying in a vacuum oven for 12 h at 60 $^{\circ}\text{C}$. The dried film was then immersed in methanol for 48 h, with the methanol being replaced every 6 h. Finally, the thoroughly washed film underwent additional drying in a vacuum oven for another 12 h at 60 $^{\circ}\text{C}$.

The GNP-PU film was fabricated using a facile, manually performed contact printing method, as described in our previously published literature [269]. Briefly, a PDMS elastomer was first fabricated by mixing a base polymer with a curing agent in a 10:1 weight ratio, using the Dow Sylgard 184 Kit Silicone Elastomer (Sigma-Aldrich). After curing the mixture for 4 h at 80 $^{\circ}\text{C}$, a PDMS elastomer with a thickness of ~ 5 mm was obtained. The elastomer was then cut with a sharp blade to form a PDMS stamp of



the desired size. The role of the PDMS stamp was to serve as an intermediary step, allowing the GNP film to be transferred from glass to the PU film. To facilitate the transfer of the GNP film onto the final PU substrate, a heating and cooling cycle similar to the method described by Choi et al. was employed [272]. Initially, the sample was placed on a hot plate (Präzitherm 2860SR), covered with a glass petri dish (80 mm diameter), and maintained at 60 °C for 3 min. After that, the sample underwent a cooling process where it was brought down to 0 °C for another 3 min.

The surface morphology of the GNP films was analyzed before (i.e., on the glass) and after contact printing (i.e., on the PU film). This analysis was conducted using optical microscopy (Olympus BX51), scanning electron microscopy (SEM; Zeiss LEO Gemini 1550, at a 5 kV operating voltage), and AFM (Digital Instruments Multimode machine, which included an AppNano ACTA cantilever, a Veeco 100 μm scanner, and a Nanoscope IV controller). For AFM measurements, all scans were conducted in tapping mode and analyzed using the Gwyddion software.

4.2.3. Fabrication and characterization of the GNP-PU strain sensor

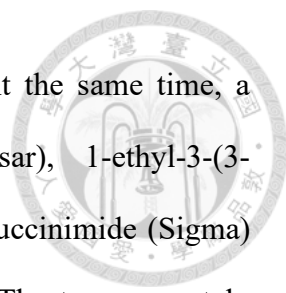
The fabrication of the cantilever-based GNP-PU strain sensor involved a sequential process, as shown in **Figure 10A**. To obtain the GNP-PU strain sensor, gold electrodes were deposited onto the GNP-PU film using the physical vapor deposition (PVD) technique (Pfeiffer Classic 250). The PU (i.e., Pellethane 2363 80A) solution was used as the glue to adhere another PU film onto the GNP-PU strain sensor. To build the cantilever-based GNP-PU strain sensor, the Lab-Tek tissue culture chamber slide (Nunc) was employed and cut to create a slit (width and height of 10.5 mm and 0.6 mm, respectively). The epoxy glue (Wiko Epoxy 05) was used to fix the GNP-PU strain sensor onto the chamber slide. The length and width of the sensor inside the chamber were 12 mm and

10 mm, respectively.

The I-V curve of the GNP-PU strain sensor was measured by employing a Keithley 2601A sourcemeter, using a voltage range from -5 V to 5 V. Resistive strain responses were characterized by the bending tests and cyclic strain-relaxation test. The bending tests were performed with a custom-built four-point bending setup, as previously described [174]. To test the impact of cell culture environments on the GNP-PU strain sensor, the sensor was fully bonded with the PU glue to another PU film and then placed in the cell culture medium (STEMdiff cardiomyocyte maintenance medium) for two days at 37 °C. The GNP-PU strain sensors, before and after medium treatment, were fixed onto the circuit board stripe (FR4, thickness of ~0.8 mm) using 3M Scotch adhesive (4004L 12). For comparison, a commercial strain gauge (SGT-1/350-TY11) with a gauge factor of 2.14 served as the reference sensor. The cyclic strain-relaxation test of the cantilever-based GNP-PU strain sensor was conducted in the cell culture medium using the custom-built bending setup, as shown in **Figure 10Di**. To establish electrical connections to sensors in both the bending and cyclic strain-relaxation tests, copper wires equipped with small crocodile clips were used. These wires were then connected to a sourcemeter (Keithley 2601A). The resistances of the sensors were measured by applying a constant voltage of 1.0 V and recording the resultant current. Both tests were conducted under ambient environmental conditions.

4.2.4. Preparation and characterization of the self-healing hydrogel

The self-healing hydrogel composed of phenol-functionalized chitosan (CS-Ph) and DF-PEG was prepared by following previous literature with modification [53, 273]. To synthesize CS-Ph, chitosan (molecular weight ~145 kDa, degree of deacetylation ~80%, Sigma) was initially dissolved in hydrochloric acid (Showa) and then diluted with a 2(N-

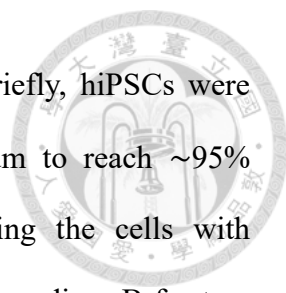


Morpholino)ethanesulfonic acid (MES) buffer solution (Sigma). At the same time, a combination of 3-(4-hydroxyphenyl)propionic acid (Alfa Aesar), 1-ethyl-3-(3-(dimethylamino)propyl)carbodiimide (Alfa Aesar), and N-hydroxysuccinimide (Sigma) was sequentially added to MES buffer under continuous stirring. The two separately prepared solutions were then uniformly mixed and the pH was adjusted to 4. The reaction was carried out in a dark environment at a temperature of 25 °C for 24 h with constant stirring. Post-reaction, the mixture was dialyzed using a dialysis membrane with a 12-14 kDa cutoff in deionized water at least five times to remove the unreacted chemicals. Finally, the purified CS-Ph product was obtained after freeze-drying. The degree of phenolic functionalization of CS-Ph determined by UV-vis spectra was ~12.1%.

For the DF-PEG synthesis, PEG (molecular weight ~ 8 kDa, Sigma) was initially dissolved in anhydrous tetrahydrofuran (Echo). Sequentially, 4-formylbenzoic acid, 4-(dimethylamino)pyridine, and N,N'-dicyclohexylcarbodiimide, all sourced from Sigma, were added to the PEG solution. The mixture was reacted at 25 °C for 48 h. Subsequently, the white precipitate formed during the reaction was removed via filtration. The product, DF-PEG, was obtained as a white solid after it underwent repeated cycles of precipitation in diethyl ether (Echo) and redissolution in THF. The degree of benzaldehyde functionalization of DF-PEG determined by the nuclear magnetic resonance (NMR) spectrum was ~85%. The synthesized CS-Ph and DF-PEG were both dissolved in the cell culture medium (STEMdiff cardiomyocyte maintenance medium). The self-healing hydrogel was produced by mixing the CS-Ph solution (2 wt%) with DF-PEG solution (4 wt%) at the volume ratio of 1:1.

4.2.5. Preparation of 3D cardiomyocyte spheroids

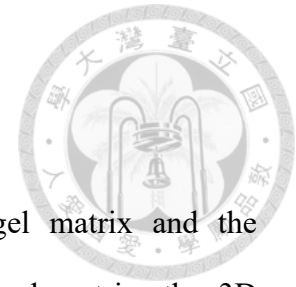
The guideline protocol of the STEMdiff cardiomyocyte differentiation kit was



followed to produce a 2D hiPSC-derived cardiomyocyte sheet. Briefly, hiPSCs were initially cultured on a Matrigel-coated dish with mTeSR1 medium to reach ~95% confluency. The cardiac differentiation began (day 0) by treating the cells with cardiomyocyte differentiation medium A for two days, followed by medium B for two days, and finally medium C for another 4 days. After differentiation, the cells were maintained in STEMdiff cardiomyocyte maintenance medium. The culture environment was a humidified incubator at 37 °C with 5% CO₂, and the medium was refreshed daily. On day 19, the beating 2D hiPSC-derived cardiomyocyte sheet was obtained.

The chitosan-hyaluronan (CS-HA) composite membrane was prepared as previously reported [274], prior to the production of 3D cardiomyocyte spheroids. Briefly, the chitosan (510 kDa, degree of deacetylation ~77%, Sigma) solution was first coated onto the 24-well tissue culture plates. After evaporating the solvent in a laminar flow cabinet overnight, the chitosan membranes were soaked in 0.5 N sodium hydroxide for 30 min and washed thrice with phosphate buffered saline (PBS). Hyaluronan (1800 kDa, SciVision Biotech) solution was then added to the chitosan-coated plates and evaporated in a laminar flow cabinet overnight. Subsequently, the membranes were crosslinked with a 1-ethyl-3-(3-(dimethylamino)propyl)carbodiimide/N-hydroxysuccinimide solution for 48 h. After crosslinking, the fabricated CS-HA membranes were washed thoroughly with PBS thrice to remove any unbound hyaluronan and stored at 4 °C before use.

The 3D cardiomyocyte spheroids were fabricated using the 2D hiPSC-derived cardiomyocyte sheet and the fabricated CS-HA membrane. Initially, the cardiomyocyte sheet was rinsed with Dulbecco's PBS (DPBS) and then dissociated using the STEMdiff dissociation kit. Subsequently, the dissociated single-cell cardiomyocytes were seeded onto the CS-HA membrane with a density of 3.8×10^5 cells per well. After culturing for 3 days, the 3D cardiomyocyte spheroids were obtained.



4.2.6. Construction of the heart-on-a-chip platform

The heart-on-a-chip platform consisted of the cell-laden gel matrix and the cantilever-based GNP-PU strain sensor. To build the cell-laden gel matrix, the 3D cardiomyocyte spheroids were embedded into the self-healing hydrogel with a density of 1×10^7 cells per mL. Subsequently, the cell-laden gel matrix was cultured on the cantilever-based GNP-PU strain sensor for 28 days. The copper wires equipped with small crocodile clips were sterilized and used to connect the sensor and the sourcemeter (Keithley 2601A) for detecting the contractile behavior of cardiomyocyte spheroids. Besides, the cantilever-based control sensor replacing the GNP film with a non-strain-responsive SMD resistor ($\sim 5.1 \text{ M}\Omega$) was fabricated. The carbon conductive adhesive (EM-Tec) and epoxy glue (Wiko Epoxy 05) were used to fix the resistor on the control sensor.

4.3. Results

Figure 7 details the characterization of the two key elements of the strain sensor: GNPs and biocompatible PU. A TEM image of the synthesized GNPs is shown in **Figure 7A**. The TEM images indicated that the GNPs were spherical, with an average diameter of $7.5 \pm 0.6 \text{ nm}$ (**Figure 7B**). Additionally, the UV-vis absorption spectrum of the GNPs showed the localized surface plasmon resonance peak at the wavelength of $\sim 520 \text{ nm}$ (**Figure 7C**). **Figure 7D** illustrates the molecular structure of the biocompatible PU. The PU film, produced by casting, had a thickness of $\sim 230 \mu\text{m}$ and was featured high flexibility, as displayed in **Figure 7E**.

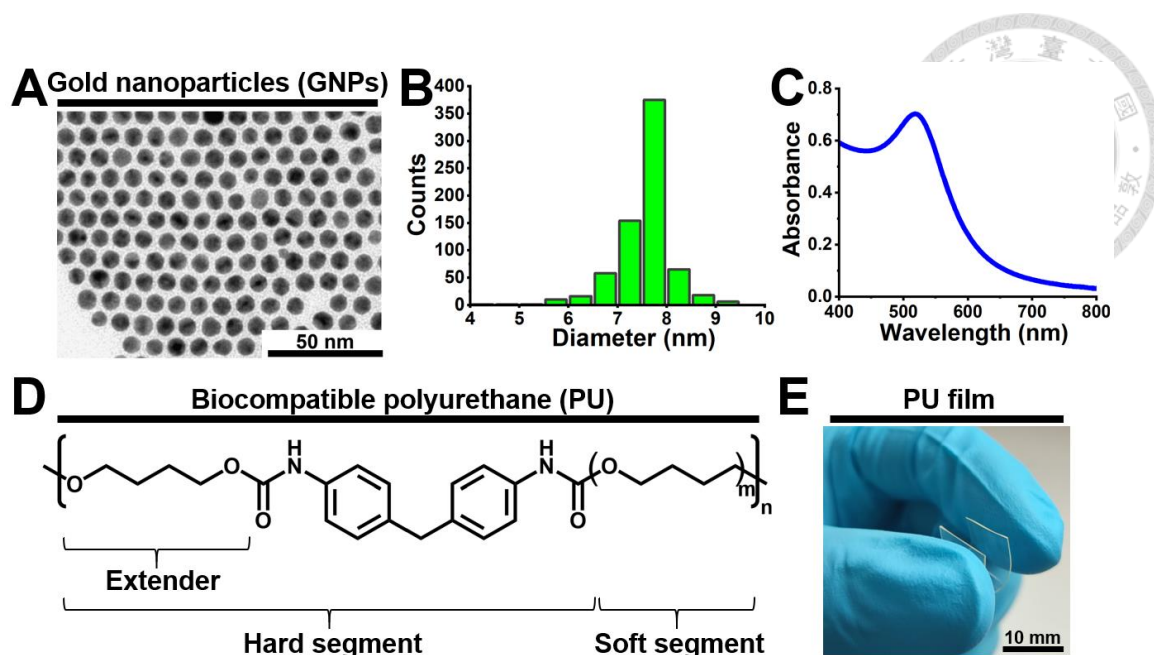


Figure 7. Characteristics of the two components (i.e., GNPs and biocompatible PU) of the strain sensor. (A) TEM image, (B) size distribution histogram, and (C) UV-vis absorption spectrum of GNPs. (D) Chemical structure of the biocompatible PU. (E) Photograph showing flexibility of the biocompatible PU film.

The fabrication of the GNP film on a glass slide was carried out using a layer-by-layer spin-coating process, as shown in **Figure 8A**. During the process, 9DT crosslinker solution and GNP solution were alternately applied onto the spinning glass slide. This spin-coating procedure was repeated for three cycles to complete the fabrication of the crosslinked GNP film. A photograph of the resulting crosslinked GNP film on the glass substrate is shown in **Figure 8B**. The GNP film exhibited a bluish color. For transferring the crosslinked GNP film from the glass substrate to the biocompatible PU film, a facile and clean contact printing method was employed, illustrated in **Figure 8C**. First, the GNP film on the glass substrate was scratched using a sharp blade to create a square shape with a size of 4 mm². Then, a PDMS stamp was applied to the surface of the GNP film to aid the transfer. A small volume of water (~3 μL) was dripped to the interface between the

glass and the GNP film. The GNP film was then transferred onto the PDMS stamp by gently peeling off the glass substrate. Subsequently, the PDMS stamp, now bearing the GNP film, was placed onto the biocompatible PU film. Following a heating and cooling cycle, the PDMS stamp was easily removed, allowing for the successful transfer of the GNP film onto the PU film.

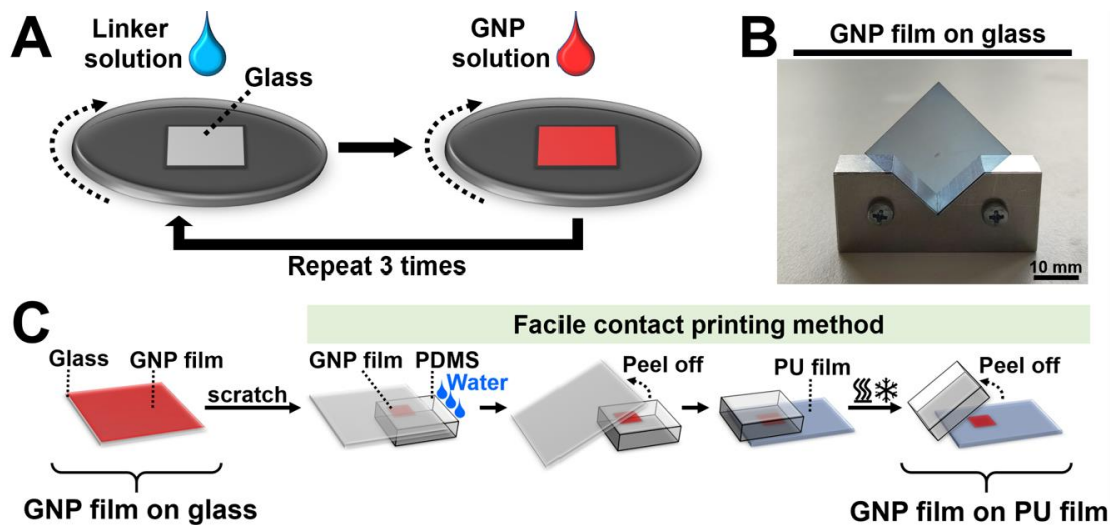


Figure 8. Preparation of the crosslinked GNP film, and printing procedures for transferring the GNP film onto the biocompatible PU film. (A) Layer-by-layer spin-coating deposition of the 9DT crosslinked GNP film. (B) Optical appearance of the fabricated GNP film deposited onto the glass substrate. (C) Schematic illustration showing the facile contact printing method employed for transferring the GNP film onto the PU film.

Figure 9 demonstrates the surface morphology of the GNP film before (i.e., on the glass substrate) and after contact printing (i.e., on the PU film). The optical images in **Figure 9A** show that the geometry of the film remained intact after contact printing, with no visible cracks when transferred onto the PU film. The SEM images in **Figure 9B** display the granular structure of crosslinked GNPs, confirming consistent surface

morphology across both substrates. The 2D/3D AFM images in **Figure 9(C, D)** demonstrate the thickness and surface roughness of the GNP film. The thickness of the GNP film was ~ 22 nm. The PU film exhibited greater roughness than the glass, resulting in higher average roughness for the GNP film on the PU film (~ 11 nm) compared to that on glass (~ 5 nm). Despite this finding, the overall morphology of the GNP film remained unchanged post-printing.

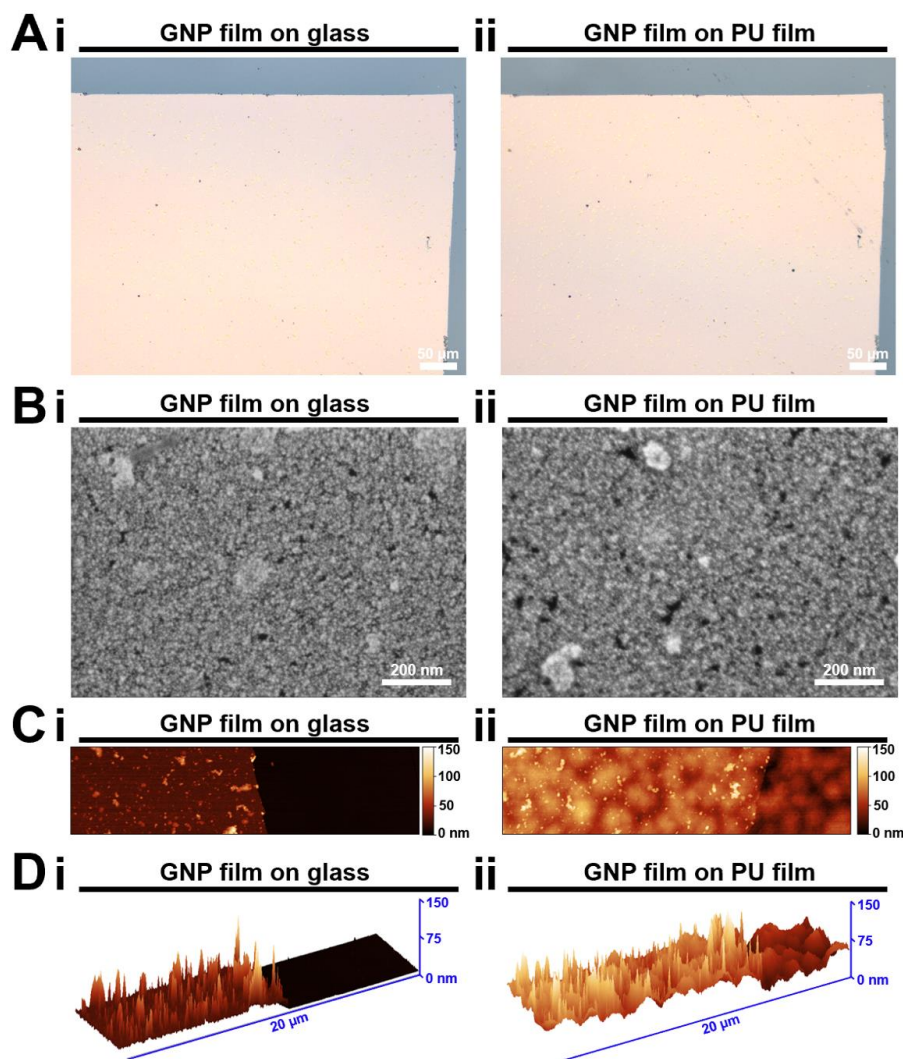


Figure 9. Surface morphology of the GNP film before (i.e., on the glass substrate) and after (i.e., on the PU film) the contact printing process. (A) Optical microscopy images of the GNP film on the (i) glass substrate and (ii) PU film. (B) SEM images of the GNP

film on the (i) glass substrate and (ii) PU film. (C) 2D AFM images of the GNP film on the (i) glass substrate and (ii) PU film. (D) 3D AFM topographic images of the GNP film on the (i) glass substrate and (ii) PU film.



Figure 10A outlines the process used to fabricate the cantilever-based GNP-PU strain sensor. Initially, gold electrodes were applied onto the GNP-PU film through PVD, utilizing a shadow mask. The deposited gold electrodes had a thickness of ~ 100 nm, with a gap of ~ 230 μm between them. Subsequently, a PU glue with a concentration of ~ 35 wt% was employed to bond an additional PU film to the GNP-PU strain sensor. The final step involved fixing the GNP-PU strain sensor in a tissue culture chamber, resulting in the formation of the cantilever-based GNP-PU strain sensor. An image of the completed cantilever-based GNP-PU strain sensor is shown in the figure inset.

Figure 10(B-D) presents the characterization of the GNP-PU strain sensor. The I-V test of the sensor demonstrated ohmic conductivity (**Figure 10B**), with a conductance of ~ 0.39 μS . The resistive responses of the sensor to strain were evaluated through bending and cyclic strain-relaxation tests. In the bending tests (**Figure 10C**), the $\Delta R/R_0$ of the sensor exhibited a nearly linear change with strain. The gauge factor of the sensor, regarded as its sensitivity, is calculated as the slope of the $\Delta R/R_0$ versus strain graph. Results showed that the gauge factor before and after the cell culture medium treatment was ~ 50 and ~ 52 , respectively. During the cyclic strain-relaxation test (**Figure 10D**), the sensor was subjected to 15 strain-relaxation cycles and displayed good repeatability of the sensor's response characteristics.

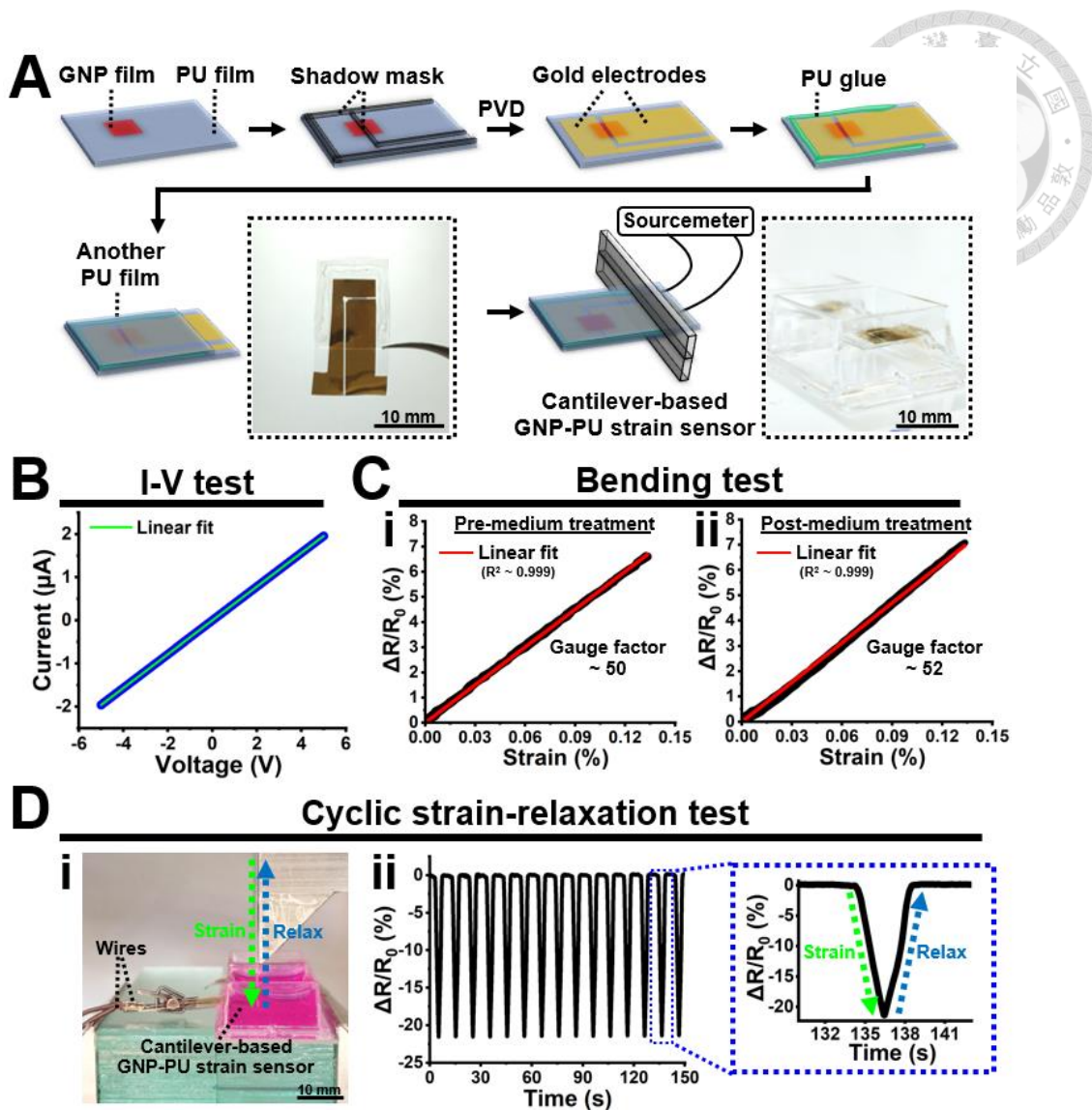
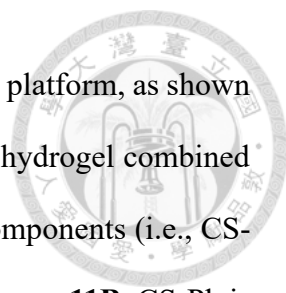


Figure 10. Fabrication and characterization of the cantilever-based GNP-PU strain sensor. (A) Schematic illustration showing the fabrication procedure of the cantilever-based GNP-PU strain sensor. A linear fit to the data is shown as the green solid line. (B) I-V curve of the sensor. (C) Results of bending tests: relationship between $\Delta R/R_0$ and strain of the sensor (i) before and (ii) after the cell culture medium treatment for two days at 37 °C. Linear fits to the data are shown as red solid lines. (D) (i) Setup to conduct 15 strain-relaxation cycles and (ii) results of the cyclic strain-relaxation test on the cantilever-based GNP-PU strain sensor.

To construct the in vitro cardiac model, the cantilever-based GNP-PU strain sensor



was integrated with a cell-laden gel matrix to create a heart-on-a-chip platform, as shown in **Figure 11A**. The cell-laden gel matrix consisted of a self-healing hydrogel combined with cardiomyocyte spheroids. The chemical structures of the two components (i.e., CS-Ph and DF-PEG) within the self-healing hydrogel are presented in **Figure 11B**. CS-Ph is synthesized by the conjugation of phloretic acid to chitosan through carbodiimide chemistry, while DF-PEG is synthesized via Steglich esterification. The self-healing hydrogel is then fabricated using CS-Ph as the main chain and DF-PEG as the crosslinker, forming dynamic Schiff base linkages.

The rheological properties of the fabricated chitosan-based self-healing hydrogel are shown in **Figure 11C**. In the time sweep, the gel point [crossover point of the storage (G') modulus and the loss (G'') modulus] occurred before the rheological analysis, indicating the fast gelling property of the self-healing hydrogel (**Figure 11Ci**). The G' value of the hydrogel underwent a significant increase in the initial gelling stage. After ~ 500 s, this value became stabilized, eventually reaching a steady state of ~ 400 Pa. Meanwhile, the G'' value of the hydrogel oscillated with time. In the frequency sweep, the hydrogel exhibited low frequency dependence of G' and G'' , indicating the inherent solid-like relaxation behavior (**Figure 11Cii**). In the strain sweep, the critical strain point for transitioning from the gel state to sol state (i.e., structural damage) was $\sim 320\%$ (**Figure 11Ciii**). The self-healing property of the hydrogel was assessed by applying strains alternately, switching between a high strain that exceeded the critical strain point and a lower strain of 1% (**Figure 11Civ**). Below 1% strain, G' was higher than G'' and both moduli remained constant over time. At the higher strains of 500% , a G' - G'' crossover had occurred, indicating a sol state with G'' greater than G' . Upon strain reversal, the values of G' and G'' quickly returned to their initial levels. This repeatable rheological behavior after several damaging-healing cycles confirmed the self-healing nature of the chitosan-

based hydrogel.

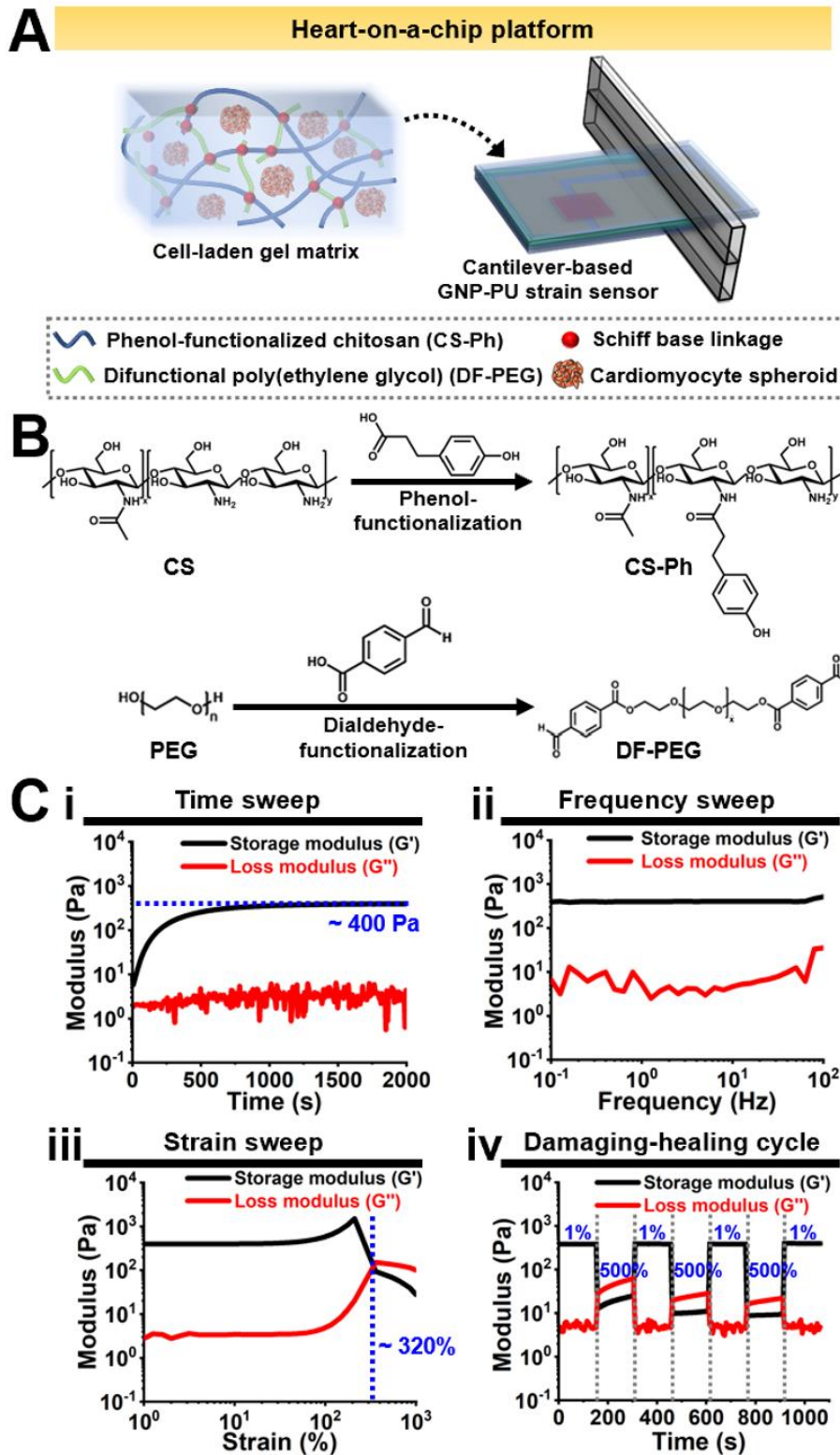
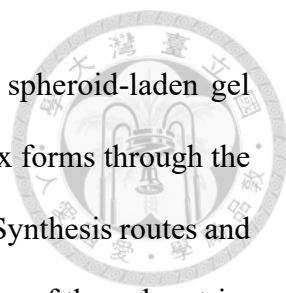


Figure 11. Characterization of the gel matrix within the in vitro 3D cardiac model. (A)



The in vitro 3D cardiac model is composed of the cardiomyocyte spheroid-laden gel matrix and the cantilever-based GNP-PU strain sensor. The gel matrix forms through the reaction of CS-Ph and DF-PEG via dynamic Schiff base linkage. (B) Synthesis routes and chemical structures of CS-Ph and DF-PEG. (C) Rheological properties of the gel matrix. (i) Time-dependent moduli after sample loading, measured at 1% strain and 1 Hz. (ii) Frequency-dependent moduli after gel stabilization, measured at 1% strain. (iii) Strain-dependent moduli after gel stabilization, measured at 1 Hz. (iv) Damaging-healing cycles measured at 1 Hz through the continuous step strain changes.

The fabrication process of the 3D cardiomyocyte spheroids is illustrated in **Figure 12A**. Initially, hiPSCs were grown according to the procedure outlined in the commercially available cardiomyocyte differentiation kit, and the hiPSCs underwent differentiation to form a 2D cardiomyocyte sheet. Subsequently, the cardiomyocyte sheet was dissociated into single-cell cardiomyocytes and seeded onto the CS-HA membrane (0 h), as shown in **Figure 12B**. After further culture for 72 h, the individual cardiomyocytes spontaneously assembled into the 3D and beating cardiomyocyte spheroids. The 3D spheroids formed had diameters ranging approximately between 90 to 150 μm .

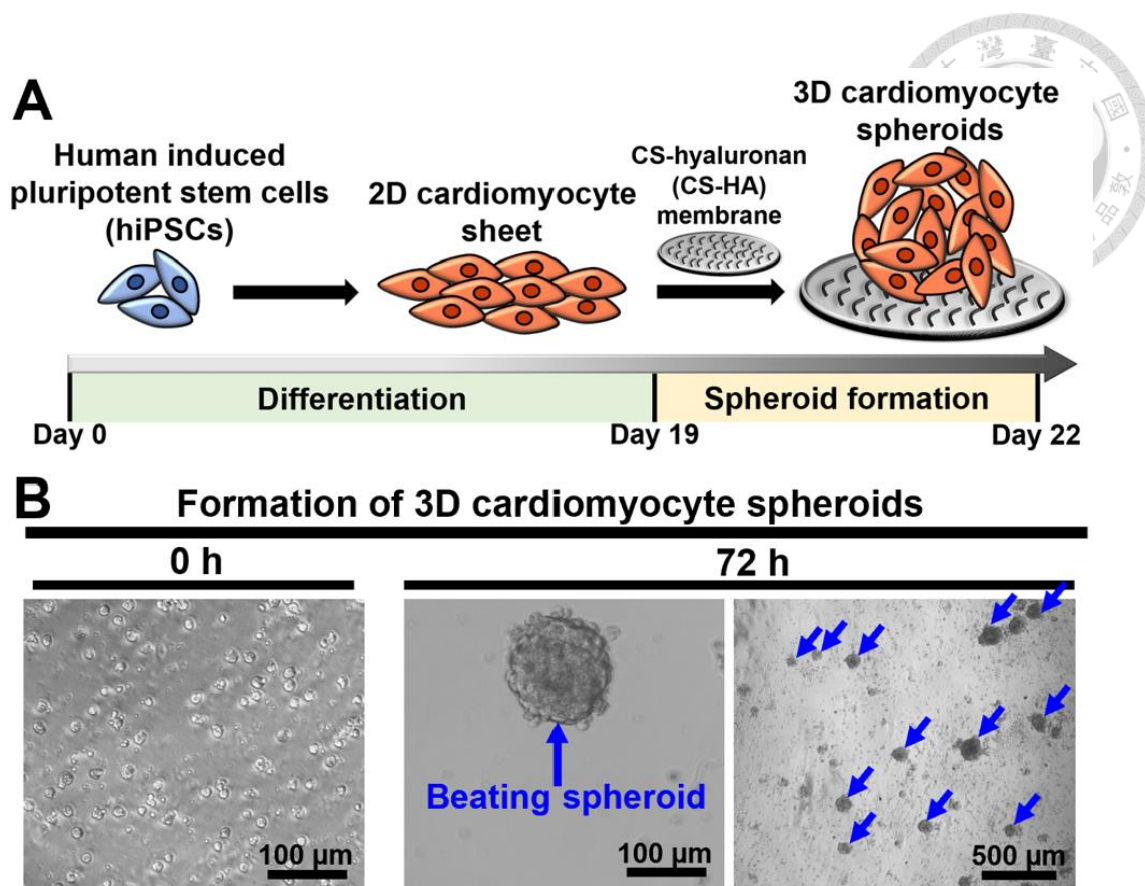
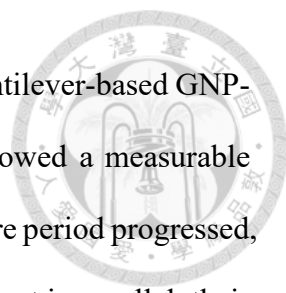


Figure 12. Preparation of 3D cardiomyocyte spheroids. (A) Schematic illustration of the timeline of differentiation from hiPSCs to a 2D cardiomyocyte sheet. Subsequently, the 2D cardiomyocyte sheet was dissociated and self-assembled into 3D cardiomyocyte spheroids on the CS-HA plate. (B) Optical microscopy images of the formation of 3D cardiomyocyte spheroids on the CS-HA plate at 0 and 72 h.

The heart-on-a-chip platform comprising the cell-laden gel matrix and the cantilever-based GNP-PU strain sensor is shown in **Figure 13A**. This platform, serving as the *in vitro* cardiac model, captured the contraction/relaxation of 3D hiPSC-derived cardiomyocyte spheroids embedded in the self-healing hydrogel. The detection of the cardiac contractile behavior was accomplished using the cantilever-based GNP-PU strain sensor, which was operated using a sourcemeter for precise measurement. **Figure 13B** shows the real-time $\Delta R/R_0$ signal traces of contraction and relaxation characteristics of



cardiomyocyte spheroids measured at days 7, 14, and 28 using the cantilever-based GNP-PU strain sensor. Initially, the cultured cardiomyocyte spheroids showed a measurable beating rate at an early stage of the culture period (day 7). As the culture period progressed, the beating rate of the cardiomyocyte spheroids gradually decreased, yet in parallel, their contraction force increased. By day 28, the contraction force stabilized at its highest level. To ensure that the $\Delta R/R_0$ signals in Figure 13B originated from strain-induced responses rather than electrophysiological signals from cardiac contractions, a cantilever-based control sensor has been specifically designed and fabricated (**Figure 13Ci**). This control sensor was modified from the standard design by replacing the GNP film with a non-strain-responsive resistor. The experiment demonstrated that for cardiomyocyte spheroids cultured on the cantilever-based control sensor over 28 days, no $\Delta R/R_0$ signal was detected by the sourcemeter (**Figure 13Cii**). This result confirms that the $\Delta R/R_0$ signals in Figure 13B indeed resulted from strain changes caused by the contractile behavior of cardiomyocytes.

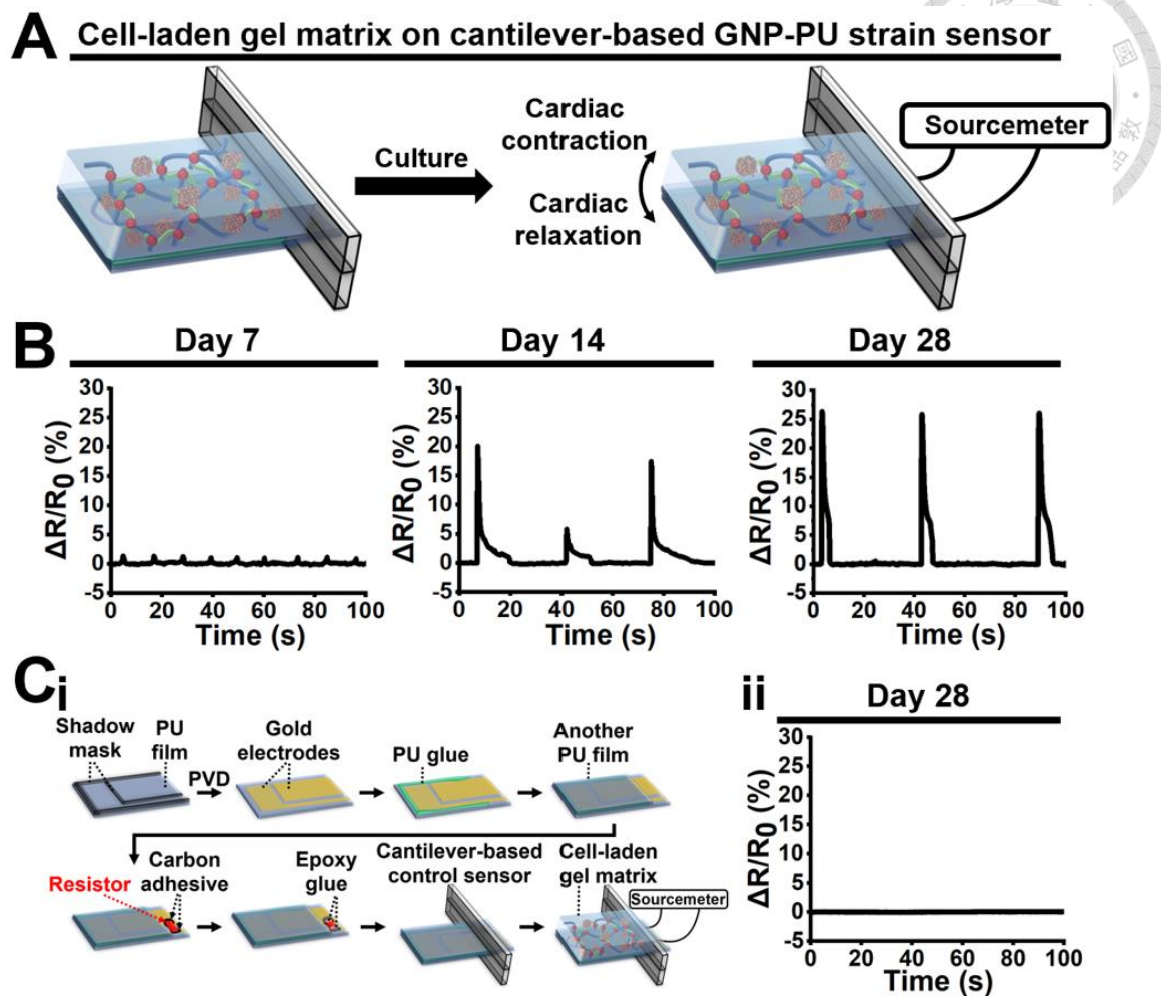
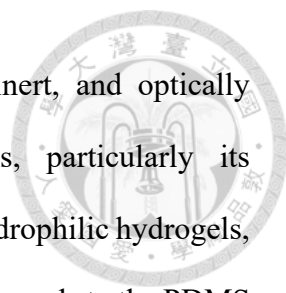


Figure 13. The in vitro 3D cardiac model. (A) Schematic illustration showing the application of the cantilever-based GNP-PU strain sensor to measure the contraction/relaxation of cardiomyocyte spheroids within the gel matrix. (B) $\Delta R/R_0$ signals of the cantilever-based GNP-PU strain sensor at 7, 14, and 28 days. (C) (i) Fabrication procedure of the cantilever-based control sensor. The design concept of the control sensor is to substitute the GNP film with a non-strain-responsive resistor, with the aim to confirm that the results in (B) are attributed to the strain behavior of cardiomyocyte spheroids. (ii) $\Delta R/R_0$ signal of the cantilever-based control sensor at day 28.

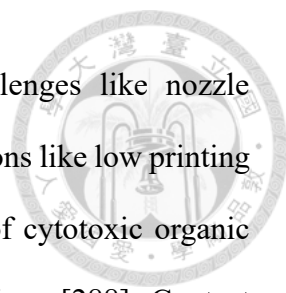
4.4. Discussion

PDMS is one of the most popular flexible substrates used in heart-on-a-chip



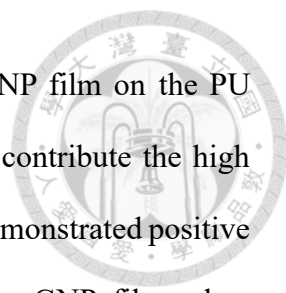
platforms due to its advantages of being non-toxic, chemically inert, and optically transparent [263]. However, PDMS presents some limitations, particularly its hydrophobic surface [275], which hampers effective bonding with hydrophilic hydrogels, thereby impeding the adherence of cardiomyocyte spheroid-laden hydrogels to the PDMS substrate. Further, the inert nature of PDMS leads to poor affinity towards metal nanoparticle surfaces, which is detrimental for the robust attachment of the active conductive GNP layer [276, 277]. An additional drawback of PDMS is its high absorption rate of small molecule chemicals, a factor that is particularly significant in drug screening applications [263]. In contrast, Pellethane 2363 80A, a thermoplastic type of PU, offers distinct advantages over PDMS. Notably, it exhibits superior resistance to water and chemicals as well as biocompatibility and processability, making it a promising biomaterial for medical applications [278-280]. The flexible substrate fabricated from Pellethane 2363 80A was hydrophilic (contact angle $\sim 60^\circ$) [281]. Therefore, in this study, the PU substrate demonstrated good adherence with cell-laden chitosan-based hydrogels, facilitating reliable sensing of cardiac contractility. Furthermore, the nitrogen atoms present in the PU substrate promote enhanced interactions with metallic nanomaterials [282, 283]. For instance, Kim et al. demonstrated that the interaction between GNPs and PU results in the formation of highly stretchable nanoparticle conductors [284]. In our previously published study, eco-friendly GNP-PU strain sensors showed high stretchability and good durability [269].

The process of fabricating thin-film strain sensors involves the integration of the active conductive layer with the flexible substrate, a critical step that ensures the functionality and reliability of the sensors [264, 269]. To integrate these two components, printing methods have been developed [285]. The methods are broadly categorized into contact and non-contact types [286]. Non-contact printing methods, such as inkjet



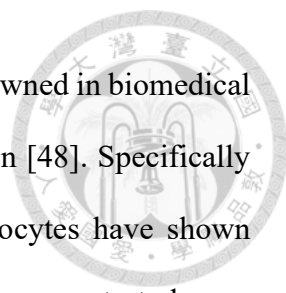
printing and electrohydrodynamic printing, often encounter challenges like nozzle clogging due to ink usage [287]. These methods also face the limitations like low printing speeds and a limited range of ink viscosity. Furthermore, the use of cytotoxic organic solvents in inks could be disadvantageous for biomedical applications [288]. Contact printing methods, including the peel-and-stick process and PMMA-mediated transfer printing, also involve the use of organic solvents [174, 184, 190, 193, 221]. Other common contact printing methods, such as the wedging transfer process, can induce undesirable cracks or wrinkles during the transfer, potentially degrading the performance of the sensors [176, 182]. The lift-off by etching method, which involves the use of chemical etchants, can negatively impact the organic components of the active layer or lead to undesired changes in the properties of the flexible substrate [188, 189]. In this study, we employed a solvent-free and facile contact printing method, previously reported by our group, to fabricate the GNP-PU strain sensors for use in the heart-on-a-chip platform (**Figure 8C**) [269].

The gauge factor of a strain sensor, which is important for evaluating its sensitivity, is calculated based on the changes in resistance induced by mechanical strain. Strain sensors that possess a high gauge factor and a low Young's modulus are highly advantageous for precise sensing [234]. Herein, the Young's modulus of the PU film was ~ 4.1 MPa based on the commercial data sheet, which is considered low enough for sensing applications [269]. The fabricated GNP-PU strain sensor exhibited higher sensitivity (gauge factor ~ 50 ; **Figure 10C**) than our previously published eco-friendly GNP-PU strain sensors (gauge factor ~ 13) made from biodegradable, waterborne PU film [269]. We attribute the higher sensitivity of the GNP-PU strain sensor in this study to the rippled surface topology of the PU film [**Figure 9(Cii, Dii)**]. This unique rippled structure resulted from the phase separation between the soft and hard segments of Pellethane [289].



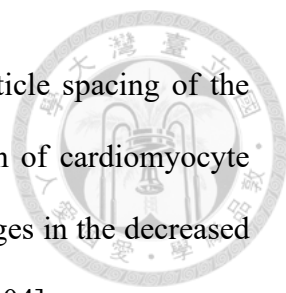
During stretching, localized stress concentration occurred in the GNP film on the PU substrate, potentially forming nanoscale cracks at junctions, which contribute the high sensitivity of the GNP-PU strain sensor [225, 290, 291]. The sensor demonstrated positive resistive changes due to the increased interparticle spacing of the GNP film when subjected to bending in a four-point bending setup (**Figure 10C**). To use the sensor in heart-on-a-chip platforms, the highly sensitive GNP-PU strain sensor was designed in a cantilever format, serving as an efficient monitoring platform for detecting cardiac contractility (**Figure 11A**) [264]. The contraction of cardiomyocytes generates surface stress that causes mechanical deformation of the flexible cantilevers [246], which can be monitored by the embedded strain sensors. In the cantilever-based GNP-PU strain sensor, the GNP film was positioned on one side of the upper PU film, while the opposite side of the PU film made contact with cardiomyocytes. Therefore, during the cyclic strain-relaxation test (**Figure 10D**), the sensor exhibited negative resistive responses when strain was applied by the bending setup, due to the reduced interparticle spacing of the GNP film.

Hydrogels with tunable elastic moduli have been applied in combination with flexible cantilevers, serving as the ECM and enhancing contraction-induced cantilever deflections [246, 252, 292-294]. Chitosan, a natural biomaterial, is often utilized in cardiac regeneration due to good biocompatibility, biodegradability, and antimicrobial properties [295, 296]. Through chemical modification, chitosan can be tailored to enable customized properties. For instance, chitosan functionalization with phenol enhances its water solubility at neutral pH and accelerates the crosslinking rates, aiding in avoiding the use of acidic solution and ensuring more uniform cell distribution within the CS-Ph hydrogel [53, 273, 297]. Further, integration of chitosan with other biomaterials can improve the functionality, such as the self-healing property, which enhances the resilience



and structural integrity of the hydrogel [257]. PEG hydrogels are renowned in biomedical field for the biocompatibility and capability of chemical modification [48]. Specifically for cardiac applications, PEG hydrogels embedded with cardiomyocytes have shown preserved sarcomeric integrity and t-tubular structure [298]. In the present study, we prepared a chitosan-based hydrogel composed of CS-Ph and DF-PEG (**Figure 11B**), following our group's previously published literature, to serve as the ECM for supporting cardiomyocyte spheroids [53]. The chitosan-based hydrogel demonstrated fast-gelling and self-healing properties (**Figure 11C**) as well as tunable moduli [53, 297]. The self-healing property was associated with the breaking and reforming of reversible dynamic Schiff base linkages in the hydrogels [53, 273].

Among the various methods for generating 3D spheroids, the use of CS-HA membranes coated on culture plates is particularly notable due to its simplicity and cost-effectiveness [299]. HA, a major component of the ECM in the human body, is a natural anionic polymer extensively used in biomedical applications based on its biocompatibility [300]. Previous studies have shown that the carboxyl groups of HA can graft with the amine groups of chitosan, which can promote the formation of 3D spheroids from 2D stem cells [274, 301]. The developed 3D biomimetic spheroids can be applied in various biomedical fields in vitro such as regenerative medicine, disease modeling, and drug screening [302, 303]. In our present study, we have successfully utilized CS-HA membranes to facilitate the self-assembly of 2D cardiomyocytes into 3D beating cardiomyocyte spheroids (**Figure 12**). We have further developed the heart-on-a-chip platform as the in vitro cardiac model for evaluating the contractile behavior of cardiomyocyte spheroids by integrating the cell-laden chitosan-based self-healing hydrogel with the cantilever-based GNP-PU strain sensor. The results showed that the sensor exhibited positive resistive responses due to the contractile behavior of



cardiomyocyte spheroids, which caused an increase in the interparticle spacing of the GNP film. Moreover, the results indicated the increased maturation of cardiomyocyte spheroids with an increasing culture period, as reflected by the changes in the decreased beating rate and the increased contractility (**Figure 13B**) [263, 280, 304].

In addition to cardiomyocytes, the human heart also comprises various essential supporting cells, including cardiac fibroblasts, endothelial cells, smooth muscle cells, and immune cells [305]. These supporting cells are vital for key heart functions such as maintaining heart homeostasis, facilitating heart repair, producing ECM, and ensuring nutrient delivery [305-307]. Therefore, co-culturing cardiomyocytes with supporting cells in 3D in vitro cardiac models is important for a more comprehensive understanding of the complex cellular interactions [246, 263, 308]. Our group's previously published literature has demonstrated the effectiveness of the CS-HA membrane as a 3D co-culture platform, which holds promise for the co-culture of cardiomyocytes and supporting cells in the future [299, 309, 310]. In addition, multimaterial 3D printing technology enables the facile fabrication of customized heart-on-a-chip platforms [280]. In our present study, the PU substrate, GNP film, and the chitosan-based self-healing hydrogel have shown potential for 3D printability, as previously reported [53, 172, 280]. The 3D bioprintability and photo-responsiveness of the chitosan-based hydrogel provides the possibility for the creation of unidirectional microfilament networks using filament light biofabrication, which can guide cells to form aligned tissues [53, 252]. Moreover, the self-healing property of the chitosan-based hydrogel could facilitate accurate spatial positioning and merging of bioprinted cardiomyocyte spheroids for the development of in vitro drug and disease model [256].

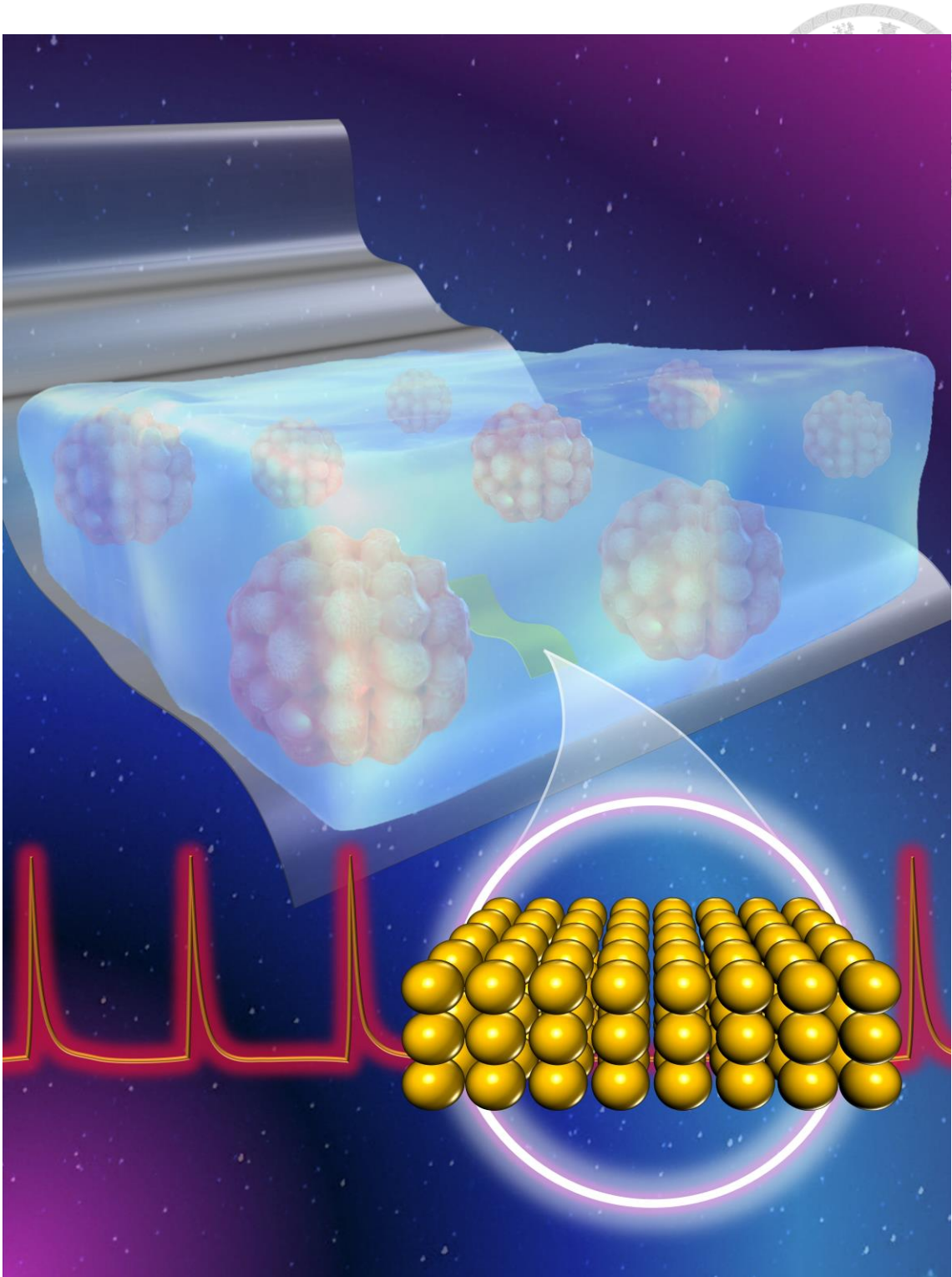


Figure 14. Graphic art of the fourth project.

5. Conclusion and outlook

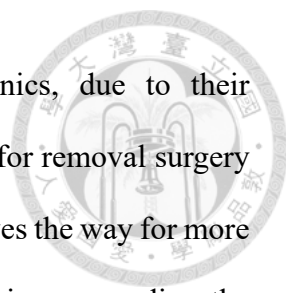
In concluding this dissertation, which spans the interconnected realms of materials science, biofabrication, flexible electronics, and tissue engineering, I reflect on the significant strides I have made and look forward to the promising avenues yet to be explored. My research journey, marked by the development of groundbreaking biomaterials such as the smart PUGG hydrogel, alongside the novel contact printing method and sensing applications such as wearable electronics and the heart-on-a-chip platform, highlights the immense potential that interdisciplinary collaboration holds in revolutionizing healthcare.

The innovative smart PUGG hydrogel, a central element of my doctoral work, has shown remarkable properties in self-healing, environmental responsiveness, and biocompatibility. These features make it highly suitable for a broad range of biomedical applications. The success of this hydrogel in high-resolution 3D bioprinting and its potential in the realm of 4D bioprinting for minimally invasive surgery and biobanking underscore its vast capabilities. The versatility of the PUGG hydrogel extends beyond its technical strengths to its adaptability in various medical applications. Having proven effective in laboratory settings, the next critical step involves applying this hydrogel in animal models for minimally invasive surgical procedures. This phase is vital as it will provide key insights into the performance of the hydrogel in live, dynamic environments, closely simulating human physiological conditions. These animal experiments are designed to thoroughly evaluate the effectiveness of the hydrogel in supporting tissue repair and its safety in surgical settings. They will allow for a detailed assessment of the interaction of hydrogel with living tissues, its biodegradation process, and its overall impact on the healing process. Results from these studies are expected to be crucial in demonstrating the appropriateness of hydrogel for human medical use. Additionally, these

animal studies will offer an opportunity to refine the composition and application methods of the hydrogel. Based on the outcomes, adjustments and improvements will be made to ensure that the hydrogel meets the rigorous standards required for human medical applications, focusing on safety and efficacy.

The study of recombinant spider silk hydrogel stands as a significant breakthrough in biomimetic biomaterials, particularly noted for its self-healing properties. This research has laid the groundwork for future advancements in the design and optimization of self-healing biomaterials, like PU block copolymers, for fundamental research and functional applications. However, the limitation of the recombinant spider silk hydrogel was the relatively low G' . Addressing this, future research directions include developing a series of recombinant spider silk hydrogels with tunable mechanical properties. This development aims to expand the scope of their biomedical applications, adapting them to a wider range of needs and scenarios. Moreover, there are plans to innovate further by incorporating different biomaterials into the recombinant spider silk hydrogels. The goal here is to create multi-intelligent hydrogels that possess a variety of functionalities. Such advancements will not only enhance the utility of these hydrogels in biomedical applications but also open new avenues for research into smart biomaterials.

In the realm of eco-friendly wearable electronics, the flexible GNP-PU strain sensor has been successfully developed using a facile and clean contact printing method. This sensor has made significant strides in health monitoring, capable of securely attaching to the skin and monitoring subtle physiological signals (e.g., mapping of arterial lines and sensing pulse waveforms) and large-strain movements (e.g., finger bending). Future efforts will focus on extending its use beyond wearable devices to implantable sensors for comprehensive health management. The adaptability of these sensors, demonstrated by their successful application on various biodegradable PU films, positions them as

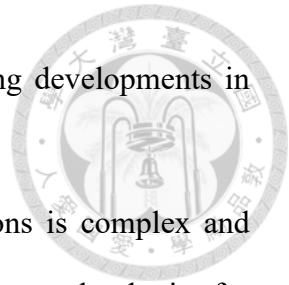


promising candidates for implantable electronics. These electronics, due to their biodegradability and biocompatibility, can be used without the need for removal surgery and are less likely to cause chronic inflammation. This innovation paves the way for more advanced applications in tissue engineering and regenerative medicine, expanding the potential of implantable sensors in medical technology.

The fabricated heart-on-a-chip platform represents a significant step forward in cardiac research, combining a 3D gel matrix laden with hiPSC-derived cardiomyocyte spheroids and the GNP-PU cantilever-based strain sensor. The fabrication of this strain sensor, using the developed clean contact printing method, ensures its biocompatibility, a crucial aspect for in vitro models. This heart-on-a-chip platform, equipped with a high gauge factor GNP-PU strain sensor, has proven its ability to detect the contractile behavior of cardiomyocyte spheroids. This capability opens up several promising avenues for future research and applications. One key area is in drug testing and cardiac disease modeling, where this platform can provide a more accurate and ethical alternative to traditional methods. It offers a highly controlled environment for studying the effects of pharmaceutical compounds on cardiomyocytes, potentially accelerating drug discovery and reducing reliance on animal testing. Another potential direction is the further development and refinement of the heart-on-a-chip platform for personalized medicine. By using patient-specific hiPSCs, the platform could be customized to model individual cardiac conditions, aiding in the development of tailored treatments and therapies. Additionally, the success of the GNP-PU strain sensor in this model paves the way for its application in other types of organ-on-a-chip platforms. This could lead to the creation of more comprehensive multi-organ systems, offering deeper insights into complex inter-organ interactions and systemic responses to treatments. Overall, the heart-on-a-chip project not only underscores the importance of interdisciplinary research in advancing

healthcare technology but also sets a foundation for groundbreaking developments in cardiac research, drug testing, and personalized medicine.

The journey from laboratory research to real-world applications is complex and challenging. A critical part of my future work will involve scaling these technologies for commercial use. This process will ensure that the benefits of my research reach a wider audience, particularly those in need of advanced healthcare solutions. Navigating this path will require attention to ethical and regulatory standards, ensuring patient safety and compliance with medical guidelines. In summary, this dissertation represents a significant step in the convergence of multiple scientific fields towards enhancing healthcare technologies. The future, as I envision it, is filled with opportunities to further these advancements, making a tangible impact on patient care and medical research.





6. Bibliography

- [1] Peppas, N. A.; Hilt, J. Z.; Khademhosseini, A.; Langer, R. Hydrogels in Biology and Medicine: From Molecular Principles to Bionanotechnology. *Advanced Materials* **2006**; 18 (11): 1345-1360.
- [2] Ahmed, E. M. Hydrogel: Preparation, characterization, and applications: A review. *Journal of Advanced Research* **2015**; 6 (2): 105-121.
- [3] Hoffman, A. S. Hydrogels for biomedical applications. *Advanced Drug Delivery Reviews* **2012**; 64: 18-23.
- [4] Hennink, W. E.; van Nostrum, C. F. Novel crosslinking methods to design hydrogels. *Advanced Drug Delivery Reviews* **2012**; 64: 223-236.
- [5] Lei, L.; Bai, Y.; Qin, X.; Liu, J.; Huang, W.; Lv, Q. Current Understanding of Hydrogel for Drug Release and Tissue Engineering. *Gels* **2022**; 8 (5): 301.
- [6] Li, L.; Yu, F.; Zheng, L.; Wang, R.; Yan, W.; Wang, Z.; Xu, J.; Wu, J.; Shi, D.; Zhu, L.; Wang, X.; Jiang, Q. Natural hydrogels for cartilage regeneration: Modification, preparation and application. *Journal of Orthopaedic Translation* **2019**; 17: 26-41.
- [7] Islam, M. M.; Shahrzaman, M.; Biswas, S.; Nurus Sakib, M.; Rashid, T. U. Chitosan based bioactive materials in tissue engineering applications-A review. *Bioactive Materials* **2020**; 5 (1): 164-183.
- [8] Andreatza, R.; Morales, A.; Pieniz, S.; Labidi, J. Gelatin-Based Hydrogels: Potential Biomaterials for Remediation. *Polymers* **2023**; 15 (4).
- [9] Catoira, M. C.; Fusaro, L.; Di Francesco, D.; Ramella, M.; Boccafoschi, F. Overview of natural hydrogels for regenerative medicine applications. *Journal of Materials Science: Materials in Medicine* **2019**; 30 (10): 115.
- [10] Dragan, E. S. Design and applications of interpenetrating polymer network

hydrogels. A review. *Chemical Engineering Journal* **2014**; 243: 572-590.

[11] Slaughter, B. V.; Khurshid, S. S.; Fisher, O. Z.; Khademhosseini, A.; Peppas, N. A. Hydrogels in regenerative medicine. *Advanced Materials* **2009**; 21 (32-33): 3307-3329.

[12] Vasile, C.; Pamfil, D.; Stoleru, E.; Baican, M. New Developments in Medical Applications of Hybrid Hydrogels Containing Natural Polymers. *Molecules* **2020**; 25 (7).

[13] El-Husseiny, H. M.; Mady, E. A.; Hamabe, L.; Abugomaa, A.; Shimada, K.; Yoshida, T.; Tanaka, T.; Yokoi, A.; Elbadawy, M.; Tanaka, R. Smart/stimuli-responsive hydrogels: Cutting-edge platforms for tissue engineering and other biomedical applications. *Materials Today Bio* **2022**; 13: 100186.

[14] Kopecek, J. Hydrogels: From soft contact lenses and implants to self-assembled nanomaterials. *Journal of Polymer Science Part A: Polymer Chemistry* **2009**; 47 (22): 5929-5946.

[15] Bordbar-Khiabani, A.; Gasik, M. Smart Hydrogels for Advanced Drug Delivery Systems. *International Journal of Molecular Sciences* **2022**; 23 (7).

[16] Schild, H. G. Poly(N-isopropylacrylamide): experiment, theory and application. *Progress in Polymer Science* **1992**; 17 (2): 163-249.

[17] Sood, N.; Bhardwaj, A.; Mehta, S.; Mehta, A. Stimuli-responsive hydrogels in drug delivery and tissue engineering. *Drug Delivery* **2016**; 23 (3): 748-770.

[18] Roy, D.; Brooks, W. L. A.; Sumerlin, B. S. New directions in thermoresponsive polymers. *Chemical Society Reviews* **2013**; 42 (17): 7214-7243.

[19] Qiu, Y.; Park, K. Environment-sensitive hydrogels for drug delivery. *Advanced Drug Delivery Reviews* **2001**; 53 (3): 321-339.

[20] Stuart, M. A. C.; Huck, W. T. S.; Genzer, J.; Müller, M.; Ober, C.; Stamm, M.; Sukhorukov, G. B.; Szleifer, I.; Tsukruk, V. V.; Urban, M.; Winnik, F;

Zauscher, S.; Luzinov, I.; Minko, S. Emerging applications of stimuli-responsive polymer materials. *Nature Materials* **2010**; 9 (2): 101-113.

[21] Taylor, M. J.; Tomlins, P.; Sahota, T. S. Thermoresponsive Gels. *Gels* **2017**; 3 (1).

[22] Chatterjee, S.; Hui, P. C.-I. Review of Applications and Future Prospects of Stimuli-Responsive Hydrogel Based on Thermo-Responsive Biopolymers in Drug Delivery Systems. *Polymers* **2021**; 13 (13): 2086.

[23] Van Hoorick, J.; Gruber, P.; Markovic, M.; Tromayer, M.; Van Erps, J.; Thienpont, H.; Liska, R.; Ovsianikov, A.; Dubruel, P.; Van Vlierberghe, S. Cross-Linkable Gelatins with Superior Mechanical Properties Through Carboxylic Acid Modification: Increasing the Two-Photon Polymerization Potential. *Biomacromolecules* **2017**; 18 (10): 3260-3272.

[24] Klouda, L.; Mikos, A. G. Thermoresponsive hydrogels in biomedical applications. *European Journal of Pharmaceutics and Biopharmaceutics* **2008**; 68 (1): 34-45.

[25] Hsieh, C.-T.; Hsu, S.-h. Double-Network Polyurethane-Gelatin Hydrogel with Tunable Modulus for High-Resolution 3D Bioprinting. *ACS Applied Materials & Interfaces* **2019**; 11 (36): 32746-32757.

[26] Wang, Y. J.; Jeng, U. S.; Hsu, S. h. Biodegradable Water-Based Polyurethane Shape Memory Elastomers for Bone Tissue Engineering. *ACS Biomaterials Science & Engineering* **2018**; 4 (4): 1397-1406.

[27] Ndlovu, S. P.; Ngece, K.; Alven, S.; Aderibigbe, B. A. Gelatin-Based Hybrid Scaffolds: Promising Wound Dressings. *Polymers* **2021**; 13 (17).

[28] Li, L.; Scheiger, J. M.; Levkin, P. A. Design and Applications of Photoresponsive Hydrogels. *Advanced Materials* **2019**; 31 (26): 1807333.

[29] Tomatsu, I.; Peng, K.; Kros, A. Photoresponsive hydrogels for biomedical applications. *Advanced Drug Delivery Reviews* **2011**; 63 (14): 1257-1266.

[30] Li, W.; Guan, Q.; Li, M.; Saiz, E.; Hou, X. Nature-inspired strategies for the synthesis of hydrogel actuators and their applications. *Progress in Polymer Science* **2023**; 140: 101665.

[31] Whitaker, C. M.; Derouin, E. E.; O'Connor, M. B.; Whitaker, C. K.; Whitaker, J. A.; Snyder, J. J.; Kaufmann, N. R.; Gilliard, A. N.; Reitmayer, A. K. Smart hydrogel sensor for detection of organophosphorus chemical warfare nerve agents. *Journal of Macromolecular Science, Part A* **2017**; 54 (1): 40-46.

[32] Van Den Bulcke A I, B. B. D. R. N. S. E. H. C. M.; Berghmans, H. Structural and rheological properties of methacrylamide modified gelatin hydrogels. *Biomacromolecules* **2000**; 1 (1): 31-38.

[33] Yue, K.; Trujillo-de Santiago, G.; Alvarez, M. M.; Tamayol, A.; Annabi, N.; Khademhosseini, A. Synthesis, properties, and biomedical applications of gelatin methacryloyl (GelMA) hydrogels. *Biomaterials* **2015**; 73: 254–271.

[34] Nichol, J. W.; Koshy, S. T.; Bae, H.; Hwang, C. M.; Yamanlar, S.; Khademhosseini, A. Cell-laden microengineered gelatin methacrylate hydrogels. *Biomaterials* **2010**; 31 (21): 5536-5544.

[35] Tomal, W.; Ortyl, J. Water-Soluble Photoinitiators in Biomedical Applications. *Polymers* **2020**; 12 (5).

[36] Choi, J. R.; Yong, K. W.; Choi, J. Y.; Cowie, A. C. Recent advances in photocrosslinkable hydrogels for biomedical applications. *BioTechniques* **2019**; 66 (1): 40-53.

[37] Rouillard A D, B. C. M. L. J. Y. P. W. J. T. Y. B. L. J.; Kirby, B. J. Methods for photocrosslinking alginate hydrogel scaffolds with high cell viability. *Tissue Engineering* **2011**; 17 (2): 173-179.

[38] Occhetta, P.; Visone, R.; Russo, L.; Cipolla, L.; Moretti, M.; Rasponi, M. VA-086 methacrylate gelatine photopolymerizable hydrogels: A parametric study for

highly biocompatible 3D cell embedding. *Journal of Biomedical Materials Research Part A* **2015**; 103 (6): 2109–2117.

[39] White, S. R.; Sottos, N. R.; Geubelle, P. H.; Moore, J. S.; Kessler, M. R.; Sriram, S. R.; Brown, E. N.; Viswanathan, S. Autonomic healing of polymer composites. *Nature* **2001**; 409 (6822): 794-797.

[40] Toohey, K. S.; Sottos, N. R.; Lewis, J. A.; Moore, J. S.; White, S. R. Self-healing materials with microvascular networks. *Nature Materials* **2007**; 6 (8): 581-585.

[41] Syrett, J. A.; Becer, C. R.; Haddleton, D. M. Self-healing and self-mendable polymers. *Polymer Chemistry* **2010**; 1 (7): 978-987.

[42] Murphy, E. B.; Wudl, F. The world of smart healable materials. *Progress in Polymer Science* **2010**; 35 (1): 223-251.

[43] Harada, A.; Takashima, Y.; Nakahata, M. Supramolecular Polymeric Materials via Cyclodextrin–Guest Interactions. *Accounts of Chemical Research* **2014**; 47 (7): 2128-2140.

[44] Liu, Y.; Hsu, S.-h. Synthesis and biomedical applications of self-healing hydrogels. *Frontiers in Chemistry* **2018**; 6: 449.

[45] Zou, W.; Dong, J.; Luo, Y.; Zhao, Q.; Xie, T. Dynamic Covalent Polymer Networks: from Old Chemistry to Modern Day Innovations. *Advanced Materials* **2017**; 29 (14): 1606100.

[46] Devi V. K, A.; Shyam, R.; Palaniappan, A.; Jaiswal, A. K.; Oh, T.-H.; Nathanael, A. J. Self-Healing Hydrogels: Preparation, Mechanism and Advancement in Biomedical Applications. *Polymers* **2021**; 13 (21).

[47] Saini, A. K.; Carlin, C. M.; Patterson, H. H. Confirmation of the presence of imine bonds in thermally cured polyimides. *Journal of Polymer Science Part A: Polymer Chemistry* **1993**; 31 (11): 2751-2758.

[48] Xu, J.; Liu, Y.; Hsu, S.-h. Hydrogels Based on Schiff Base Linkages for Biomedical Applications. *Molecules* **2019**; 24 (16).

[49] Liu, Y.; Hsu, Y.-H.; Huang, A. P.-H.; Hsu, S.-h. Semi-Interpenetrating Polymer Network of Hyaluronan and Chitosan Self-Healing Hydrogels for Central Nervous System Repair. *ACS Applied Materials & Interfaces* **2020**; 12 (36): 40108-40120.

[50] Han, L.; Lu, X.; Wang, M.; Gan, D.; Deng, W.; Wang, K.; Fang, L.; Liu, K.; Chan, C. W.; Tang, Y. A mussel-inspired conductive, self-adhesive, and self-healable tough hydrogel as cell stimulators and implantable bioelectronics. *Small* **2017**; 13 (2): 1601916.

[51] Zhou, X.; Li, Y.; Chen, S.; Fu, Y.-n.; Wang, S.; Li, G.; Tao, L.; Wei, Y.; Wang, X.; Liang, J. F. Dynamic agent of an injectable and self-healing drug-loaded hydrogel for embolization therapy. *Colloids and Surfaces B: Biointerfaces* **2018**; 172: 601-607.

[52] Duceac, I. A.; Coseri, S. Chitosan Schiff-Base Hydrogels—A Critical Perspective Review. *Gels* **2022**; 8 (12).

[53] Liu, Y.; Wong, C.-W.; Chang, S.-W.; Hsu, S.-h. An injectable, self-healing phenol-functionalized chitosan hydrogel with fast gelling property and visible light-crosslinking capability for 3D printing. *Acta Biomaterialia* **2021**; 122: 211-219.

[54] Tseng, T. C.; Tao, L.; Hsieh, F. Y.; Wei, Y.; Chiu, I. M.; Hsu, S. h. An Injectable, Self-Healing Hydrogel to Repair the Central Nervous System. *Advanced Materials* **2015**; 27 (23): 3518–3524.

[55] Ke, R.; Lin, Z.; Zhang, H.; Zhou, S. Research Progress in Intrinsic Self-healing Polyurethane Materials Based on Dynamic Reversible Non-covalent Bonds. *Journal of Physics: Conference Series* **2022**; 2324 (1): 012007.

[56] Diesendruck, C. E.; Sottos, N. R.; Moore, J. S.; White, S. R. Biomimetic Self-

Healing. *Angewandte Chemie International Edition* **2015**; 54 (36): 10428-10447.

[57] Xie, Z.; Hu, B.-L.; Li, R.-W.; Zhang, Q. Hydrogen Bonding in Self-Healing Elastomers. *ACS Omega* **2021**; 6 (14): 9319-9333.

[58] Ding, D.; Guerette, P. A.; Fu, J.; Zhang, L.; Irvine, S. A.; Miserez, A. From Soft Self-Healing Gels to Stiff Films in Suckerin-Based Materials Through Modulation of Crosslink Density and β -Sheet Content. *Advanced Materials* **2015**; 27 (26): 3953-3961.

[59] Zhang, G.; Ngai, T.; Deng, Y.; Wang, C. An Injectable Hydrogel with Excellent Self-Healing Property Based on Quadruple Hydrogen Bonding. *Macromolecular Chemistry and Physics* **2016**; 217 (19): 2172-2181.

[60] Shin, M.; Lee, H. Gallol-Rich Hyaluronic Acid Hydrogels: Shear-Thinning, Protein Accumulation against Concentration Gradients, and Degradation-Resistant Properties. *Chemistry of Materials* **2017**; 29 (19): 8211-8220.

[61] Wei, H.; Du, S.; Liu, Y.; Zhao, H.; Chen, C.; Li, Z.; Lin, J.; Zhang, Y.; Zhang, J.; Wan, X. Tunable, luminescent, and self-healing hybrid hydrogels of polyoxometalates and triblock copolymers based on electrostatic assembly. *Chemical Communications* **2014**; 50 (12): 1447-1450.

[62] Li, J.; Su, Z.; Ma, X.; Xu, H.; Shi, Z.; Yin, J.; Jiang, X. In situ polymerization induced supramolecular hydrogels of chitosan and poly(acrylic acid-acrylamide) with high toughness. *Materials Chemistry Frontiers* **2017**; 1 (2): 310-318.

[63] Sun, T. L.; Kurokawa, T.; Kuroda, S.; Ihsan, A. B.; Akasaki, T.; Sato, K.; Haque, M. A.; Nakajima, T.; Gong, J. P. Physical hydrogels composed of polyampholytes demonstrate high toughness and viscoelasticity. *Nature Materials* **2013**; 12 (10): 932-937.

[64] Löwenberg, C.; Balk, M.; Wischke, C.; Behl, M.; Lendlein, A. Shape-Memory Hydrogels: Evolution of Structural Principles To Enable Shape Switching of Hydrophilic

Polymer Networks. *Accounts of Chemical Research* **2017**; 50 (4): 723-732.

[65] Xia, Y.; He, Y.; Zhang, F.; Liu, Y.; Leng, J. A Review of Shape Memory Polymers and Composites: Mechanisms, Materials, and Applications. *Advanced Materials* **2021**; 33 (6): 2000713.

[66] Korde, J. M.; Kandasubramanian, B. Naturally biomimicked smart shape memory hydrogels for biomedical functions. *Chemical Engineering Journal* **2020**; 379: 122430.

[67] Shiblee, M. N. I.; Ahmed, K.; Kawakami, M.; Furukawa, H. 4D Printing of Shape-Memory Hydrogels for Soft-Robotic Functions. *Advanced Materials Technologies* **2019**; 4 (8): 1900071.

[68] Biswas, M. C.; Chakraborty, S.; Bhattacharjee, A.; Mohammed, Z. 4D Printing of Shape Memory Materials for Textiles: Mechanism, Mathematical Modeling, and Challenges. *Advanced Functional Materials* **2021**; 31 (19): 2100257.

[69] Thakur, S., Shape memory polymers for smart textile applications. In *Textiles for advanced applications*, InTech: 2017; pp 323-336.

[70] Jandyal, A.; Chaturvedi, I.; Wazir, I.; Raina, A.; Ul Haq, M. I. 3D printing – A review of processes, materials and applications in industry 4.0. *Sustainable Operations and Computers* **2022**; 3: 33-42.

[71] Melchels, F. P. W. Celebrating three decades of stereolithography. *Virtual and Physical Prototyping* **2012**; 7 (3): 173-175.

[72] Huang, J.; Qin, Q.; Wang, J. A Review of Stereolithography: Processes and Systems. *Processes* **2020**; 8 (9).

[73] Tian, Y.; Chen, C.; Xu, X.; Wang, J.; Hou, X.; Li, K.; Lu, X.; Shi, H.; Lee, E.-S.; Jiang, H. B. A Review of 3D Printing in Dentistry: Technologies, Affecting Factors, and Applications. *Scanning* **2021**; 2021: 9950131.

[74] Rahim, T. N. A. T.; Abdullah, A. M.; Md Akil, H. Recent Developments in Fused

Deposition Modeling-Based 3D Printing of Polymers and Their Composites. *Polymer Reviews* **2019**; 59 (4): 589-624.

[75] Kruth, J. P.; Mercelis, P.; Van Vaerenbergh, J.; Froyen, L.; Rombouts, M. Binding mechanisms in selective laser sintering and selective laser melting. *Rapid prototyping journal* **2005**; 11 (1): 26-36.

[76] Ziaee, M.; Crane, N. B. Binder jetting: A review of process, materials, and methods. *Additive Manufacturing* **2019**; 28: 781-801.

[77] Gibson, I.; Rosen, D. W.; Stucker, B.; Khorasani, M.; Rosen, D.; Stucker, B.; Khorasani, M., Additive manufacturing technologies. Springer: 2021; Vol. 17, pp 23-51.

[78] Three-Dimensional Scaffolds for Tissue Engineering Applications: Role of Porosity and Pore Size. *Tissue Engineering Part B: Reviews* **2013**; 19 (6): 485-502.

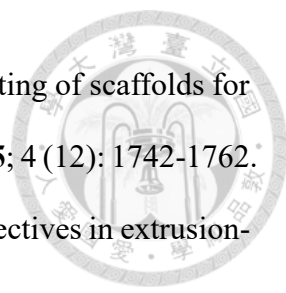
[79] Massie, A. B.; Kuricka, L. M.; Segev, D. L. Big Data in Organ Transplantation: Registries and Administrative Claims. *American Journal of Transplantation* **2014**; 14 (8): 1723-1730.

[80] Sykes, M. Developing pig-to-human organ transplants. *Science* **2022**; 378 (6616): 135-136.

[81] Takemoto, S. K.; Zeevi, A.; Feng, S.; Colvin, R. B.; Jordan, S.; Kobashigawa, J.; Kupiec-Weglinski, J.; Matas, A.; Montgomery, R. A.; Nickerson, P. National conference to assess antibody-mediated rejection in solid organ transplantation. *American Journal of Transplantation* **2004**; 4 (7): 1033-1041.

[82] Iram, D.; a Riaz, R.; Iqbal, R. K. 3D Bioprinting: An attractive alternative to traditional organ transplantation. *Biomed Sci Eng* **2019**; 5 (1): 007-018.

[83] Murphy, S. V.; Atala, A. 3D bioprinting of tissues and organs. *Nature Biotechnology* **2014**; 32 (8): 773-785.

- 
- [84] Do, A. V.; Khorsand, B.; Geary, S. M.; Salem, A. K. 3D printing of scaffolds for tissue regeneration applications. *Advanced Healthcare Materials* **2015**; 4 (12): 1742-1762.
- [85] Ozbolat, I. T.; Hospodiuk, M. Current advances and future perspectives in extrusion-based bioprinting. *Biomaterials* **2016**; 76: 321-343.
- [86] Annabi, N.; Tamayol, A.; Uquillas, J. A.; Akbari, M.; Bertassoni, L. E.; Cha, C.; Camci-Unal, G.; Dokmeci, M. R.; Peppas, N. A.; Khademhosseini, A. 25th anniversary article: Rational design and applications of hydrogels in regenerative medicine. *Advanced Materials* **2014**; 26 (1): 85-124.
- [87] Unagolla, J. M.; Jayasuriya, A. C. Hydrogel-based 3D bioprinting: A comprehensive review on cell-laden hydrogels, bioink formulations, and future perspectives. *Applied Materials Today* **2020**; 18: 100479.
- [88] Chaterji, S.; Kwon, I. K.; Park, K. Smart polymeric gels: Redefining the limits of biomedical devices. *Progress in Polymer Science* **2007**; 32 (8): 1083-1122.
- [89] Cooperstein, M. A.; Canavan, H. E. Assessment of cytotoxicity of (N-isopropyl acrylamide) and Poly(N-isopropyl acrylamide)-coated surfaces. *Biointerphases* **2013**; 8 (1): 19.
- [90] Martina, M.; Hutmacher, D. W. Biodegradable polymers applied in tissue engineering research: a review. *Polymer International* **2007**; 56 (2): 145-157.
- [91] Asim, S.; Tabish, T. A.; Liaqat, U.; Ozbolat, I. T.; Rizwan, M. Advances in Gelatin Bioinks to Optimize Bioprinted Cell Functions. *Advanced Healthcare Materials* **2023**; 12 (17): 2203148.
- [92] Piao, Y.; You, H.; Xu, T.; Bei, H.-P.; Piwko, I. Z.; Kwan, Y. Y.; Zhao, X. Biomedical applications of gelatin methacryloyl hydrogels. *Engineered Regeneration* **2021**; 2: 47-56.
- [93] Wang, H.; Bi, S.; Shi, B.; Ma, J.; Lv, X.; Qiu, J.; Wei, Y. Recent Advances

in Engineering Bioinks for 3D Bioprinting. *Advanced Engineering Materials* **2023**; 25 (19): 2300648.

[94] Candal, M. V.; Calafel, I.; Fernández, M.; Aranburu, N.; Aguirresarobe, R. H.; Gerrica-Echevarria, G.; Santamaría, A.; Müller, A. J. Study of the interlayer adhesion and warping during material extrusion-based additive manufacturing of a carbon nanotube/biobased thermoplastic polyurethane nanocomposite. *Polymer* **2021**; 224: 123734.

[95] Wang, Y.; Adokoh, C. K.; Narain, R. Recent development and biomedical applications of self-healing hydrogels. *Expert Opinion on Drug Delivery* **2018**; 15 (1): 77–91.

[96] Heidarian, P.; Kouzani, A. Z.; Kaynak, A.; Paulino, M.; Nasri-Nasrabadi, B. Dynamic Hydrogels and Polymers as Inks for Three-Dimensional Printing. *ACS Biomaterials Science & Engineering* **2019**; 5 (6): 2688–2707.

[97] Pekkanen, A. M.; Mondschein, R. J.; Williams, C. B.; Long, T. E. 3D Printing Polymers with Supramolecular Functionality for Biological Applications. *Biomacromolecules* **2017**; 18 (9): 2669–2687.

[98] Rammal, H.; GhavamiNejad, A.; Erdem, A.; Mbeleck, R.; Nematollahi, M.; Emir Diltemiz, S.; Alem, H.; Darabi, M. A.; Ertas, Y. N.; Caterson, E. J.; Ashammakhi, N. Advances in biomedical applications of self-healing hydrogels. *Materials Chemistry Frontiers* **2021**; 5 (12): 4368-4400.

[99] Giwa, S.; Lewis, J. K.; Alvarez, L.; Langer, R.; Roth, A. E.; Church, G. M.; Markmann, J. F.; Sachs, D. H.; Chandraker, A.; Wertheim, J. A.; Rothblatt, M.; Boyden, E. S.; Eidbo, E.; Lee, W. P. A.; Pomahac, B.; Brandacher, G.; Weinstock, D. M.; Elliott, G.; Nelson, D.; Acker, J. P.; Uygun, K.; Schmalz, B.; Weegman, B. P.; Tocchio, A.; Fahy, G. M.; Storey, K. B.; Rubinsky, B.; Bischof,

J.; Elliott, J. A. W.; Woodruff, T. K.; Morris, G. J.; Demirci, U.; Brockbank, K. G. M.; Woods, E. J.; Ben, R. N.; Baust, J. G.; Gao, D.; Fuller, B.; Rabin, Y.; Kravitz, D. C.; Taylor, M. J.; Toner, M. The promise of organ and tissue preservation to transform medicine. *Nature Biotechnology* **2017**; 35 (6): 530-542.

[100] Lee, J.; Kim, G. A cryopreservable cell-laden GelMa-based scaffold fabricated using a 3D printing process supplemented with an in situ photo-crosslinking. *Journal of Industrial and Engineering Chemistry* **2020**; 85: 249-257.

[101] Mazur, P. Cryobiology: The Freezing of Biological Systems. *Science* **1970**; 168 (3934): 939-949.

[102] Pan, H. M.; Chen, S.; Jang, T.-S.; Han, W. T.; Jung, H.-d.; Li, Y.; Song, J. Plant seed-inspired cell protection, dormancy, and growth for large-scale biofabrication. *Biofabrication* **2019**; 11 (2): 025008.

[103] Baust, J. M.; Corwin, W. L.; VanBuskirk, R.; Baust, J. G., Biobanking: The Future of Cell Preservation Strategies. In *Biobanking in the 21st Century*, Karimi-Busheri, F., Ed. Springer International Publishing: Cham, 2015; pp 37-53.

[104] Mazur, P.; Leibo, S. P.; Chu, E. H. Y. A two-factor hypothesis of freezing injury: Evidence from Chinese hamster tissue-culture cells. *Experimental Cell Research* **1972**; 71 (2): 345-355.

[105] Gao, B.; Yang, Q.; Zhao, X.; Jin, G.; Ma, Y.; Xu, F. 4D Bioprinting for Biomedical Applications. *Trends in Biotechnology* **2016**; 34 (9): 746-756.

[106] Liu, Y.; Shaw, B.; Dickey, M. D.; Genzer, J. Sequential self-folding of polymer sheets. *Science Advances* **2017**; 3 (3): e1602417.

[107] Zhang, Y.; Gao, H.; Wang, H.; Xu, Z.; Chen, X.; Liu, B.; Shi, Y.; Lu, Y.; Wen, L.; Li, Y. Radiopaque highly stiff and tough shape memory hydrogel microcoils for permanent embolization of arteries. *Advanced Functional Materials* **2018**;

28 (9): 1705962.

[108] Miao, S.; Castro, N.; Nowicki, M.; Xia, L.; Cui, H.; Zhou, X.; Zhu, W.; Lee, S.-j.; Sarkar, K.; Vozzi, G.; Tabata, Y.; Fisher, J.; Zhang, L. G. 4D printing of polymeric materials for tissue and organ regeneration. *Materials Today* **2017**; 20 (10): 577–591.

[109] Kirillova, A.; Maxson, R.; Stoychev, G.; Gomillion, C. T.; Ionov, L. 4D biofabrication using shape-morphing hydrogels. *Advanced Materials* **2017**; 29 (46): 1703443.

[110] Szycher, M., Szycher's handbook of polyurethanes. CRC press: 1999; pp 87-132.

[111] Linke, W. A.; Stockmeier, M. R.; Ivemeyer, M.; Hossler, H.; Mundel, P. Characterizing titin's I-band Ig domain region as an entropic spring. *Journal of Cell Science* **1998**; 111 (11): 1567-1574.

[112] Srichatrapimuk, V. W.; Cooper, S. L. Infrared thermal analysis of polyurethane block polymers. *Journal of Macromolecular Science, Part B* **1978**; 15 (2): 267-311.

[113] Linliu, K.; Chen, S.-A.; Yu, T. L.; Lin, T.-L.; Lee, C.-H.; Kai, J.-J.; Chang, S.-L.; Lin, J. S. A small-angle X-ray scattering study of microphase separation transition of polyurethanes: Effect of hard segments. *Journal of Polymer Research* **1995**; 2 (1): 63-70.

[114] Huang, S.-L.; Chao, M.-S.; Ruaan, R.-C.; Lai, J.-Y. Microphase separated structure and protein adsorption of polyurethanes with butadiene soft segment. *European Polymer Journal* **2000**; 36 (2): 285-294.

[115] Akindoyo, J. O.; Beg, M. D. H.; Ghazali, S.; Islam, M. R.; Jeyaratnam, N.; Yuvaraj, A. R. Polyurethane types, synthesis and applications – a review. *RSC Advances* **2016**; 6 (115): 114453-114482.

[116] Esposito Corcione, C.; Prinari, P.; Cannoletta, D.; Mensitieri, G.; Maffezzoli, A. Synthesis and characterization of clay-nanocomposite solvent-based polyurethane adhesives. *International Journal of Adhesion and Adhesives* **2008**; 28 (3): 91-100.

[117] Sonnenschein, M. F., Polyurethanes: science, technology, markets, and trends. John Wiley & Sons: 2021; pp 207-254.

[118] Gupta, R. K.; Mishra, A. K., Eco-friendly waterborne polyurethanes: synthesis, properties, and applications. CRC Press: 2022; pp 31-45.

[119] Hsu, S.-h.; Hung, K.-C.; Lin, Y.-Y.; Su, C.-H.; Yeh, H.-Y.; Jeng, U. S.; Lu, C.-Y.; Dai, S. A.; Fu, W.-E.; Lin, J.-C. Water-based synthesis and processing of novel biodegradable elastomers for medical applications. *Journal of Materials Chemistry B* **2014**; 2 (31): 5083-5092.

[120] Santamaria-Echart, A.; Ugarte, L.; Arbelaiz, A.; Gabilondo, N.; Corcuera, M. A.; Eceiza, A. Two different incorporation routes of cellulose nanocrystals in waterborne polyurethane nanocomposites. *European Polymer Journal* **2016**; 76: 99-109.

[121] Wu, G. H.; Hsu, S. H. Synthesis of water-based cationic polyurethane for antibacterial and gene delivery applications. *Colloids and Surfaces B: Biointerfaces* **2016**; 146: 825-832.

[122] Cavaco, L. I.; Melo, J. A., Polyurethane: Properties, Structure, and Applications. Nova Science: 2012; pp 1-16.

[123] Jin, X.; Dong, J.; Guo, X.; Ding, M.; Bao, R.; Luo, Y. Current advances in polyurethane biodegradation. *Polymer International* **2022**; 71 (12): 1384-1392.

[124] Ho, L.; Hsu, S. h. Cell reprogramming by 3D bioprinting of human fibroblasts in polyurethane hydrogel for fabrication of neural-like constructs. *Acta Biomaterialia*

2018; 70: 57–70.

[125] Labow, R. S.; Erfle, D. J.; Santerre, J. P. Elastase-induced hydrolysis of synthetic solid substrates: poly(ester-urea-urethane) and poly(ether-urea-urethane).

Biomaterials **1996**; 17 (24): 2381-2388.

[126] Magnin, A.; Pollet, E.; Phalip, V.; Avérous, L. Evaluation of biological degradation of polyurethanes. *Biotechnology Advances* **2020**; 39: 107457.

[127] Liu, J.; He, J.; Xue, R.; Xu, B.; Qian, X.; Xin, F.; Blank, L. M.; Zhou, J.; Wei, R.; Dong, W.; Jiang, M. Biodegradation and up-cycling of polyurethanes: Progress, challenges, and prospects. *Biotechnology Advances* **2021**; 48: 107730.

[128] Pedersen, D. D.; Kim, S.; Wagner, W. R. Biodegradable polyurethane scaffolds in regenerative medicine: Clinical translation review. *Journal of Biomedical Materials Research Part A* **2022**; 110 (8): 1460-1487.

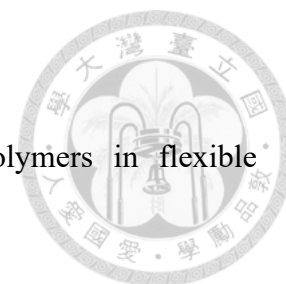
[129] Bat, E.; Zhang, Z.; Feijen, J.; Grijpma, D. W.; Poot, A. A. Biodegradable elastomers for biomedical applications and regenerative medicine. *Regenerative medicine* **2014**; 9 (3): 385-398.

[130] Zhang, F.; King, M. W. Biodegradable Polymers as the Pivotal Player in the Design of Tissue Engineering Scaffolds. *Advanced Healthcare Materials* **2020**; 9 (13): 1901358.

[131] Guelcher, S. A. Biodegradable polyurethanes: synthesis and applications in regenerative medicine. *Tissue Engineering Part B: Reviews* **2008**; 14 (1): 3-17.

[132] Hsu, S.-h.; Xu, J.; Lin, S.-H.; Wu, S.-D.; Cheng, Q.-P.; Wong, C.-W. Creative transformation of biomedical polyurethanes: from biostable tubing to biodegradable smart materials. *Journal of Polymer Research* **2022**; 29 (2): 70.

[133] Wendels, S.; Avérous, L. Biobased polyurethanes for biomedical applications.



Bioactive Materials **2021**; 6 (4): 1083-1106.

[134] Ouyang, J. Application of intrinsically conducting polymers in flexible electronics. *SmartMat* **2021**; 2 (3): 263-285.

[135] Hsiao, S.-H.; Hsu, S.-h. Synthesis and Characterization of Dual Stimuli-Sensitive Biodegradable Polyurethane Soft Hydrogels for 3D Cell-Laden Bioprinting. *ACS Applied Materials & Interfaces* **2018**; 10 (35): 29273-29287.

[136] Huang, C. T.; Kumar Shrestha, L.; Ariga, K.; Hsu, S. h. A graphene–polyurethane composite hydrogel as a potential bioink for 3D bioprinting and differentiation of neural stem cells. *Journal of Materials Chemistry B* **2017**; 5 (44): 8854–8864.

[137] Pinchuk, L. A review of the biostability and carcinogenicity of polyurethanes in medicine and the new generation of 'biostable' polyurethanes. *Journal of Biomaterials Science* **1995**; 6 (3): 225-267.


[138] Gunatillake, P. A.; Dandeniya, L. S.; Adhikari, R.; Bown, M.; Shanks, R.; Adhikari, B. Advancements in the Development of Biostable Polyurethanes. *Polymer Reviews* **2019**; 59 (3): 391-417.

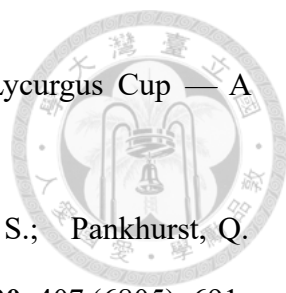
[139] Ulrich, H.; Bonk, H. Emerging biomedical applications of polyurethane elastomers. *Journal of Cellular Plastics* **1983**; 19 (2): 83-88.

[140] Daniel, M.-C.; Astruc, D. Gold Nanoparticles: Assembly, Supramolecular Chemistry, Quantum-Size-Related Properties, and Applications toward Biology, Catalysis, and Nanotechnology. *Chemical Reviews* **2004**; 104 (1): 293-346.

[141] Corti, C. W.; Holliday, R. J. Commercial aspects of gold applications: From materials science to chemical science. *Gold Bulletin* **2004**; 37 (1): 20-26.

[142] Goodman, P. Current and future uses of gold in electronics. *Gold Bulletin* **2002**; 35 (1): 21-26.

- 
- [143] Eustis, S.; El-Sayed, M. A. Why gold nanoparticles are more precious than pretty gold: Noble metal surface plasmon resonance and its enhancement of the radiative and nonradiative properties of nanocrystals of different shapes. *Chemical Society Reviews* **2006**; 35 (3): 209-217.
- [144] Murray, C.; Norris, D. J.; Bawendi, M. G. Synthesis and characterization of nearly monodisperse CdE (E= sulfur, selenium, tellurium) semiconductor nanocrystallites. *Journal of the American Chemical Society* **1993**; 115 (19): 8706-8715.
- [145] Weller, H. Colloidal Semiconductor Q-Particles: Chemistry in the Transition Region Between Solid State and Molecules. *Angewandte Chemie International Edition in English* **1993**; 32 (1): 41-53.
- [146] Schmid, G., Nanoparticles: from theory to application. John Wiley & Sons: 2011; pp 49-368.
- [147] Daniel, M.-C.; Astruc, D. Gold nanoparticles: assembly, supramolecular chemistry, quantum-size-related properties, and applications toward biology, catalysis, and nanotechnology. *Chemical Reviews* **2004**; 104 (1): 293-346.
- [148] Mirkin, C. A.; Letsinger, R. L.; Mucic, R. C.; Storhoff, J. J., In *Spherical Nucleic Acids*, Jenny Stanford Publishing: 2020; pp 3-11.
- [149] Loweth, C. J.; Caldwell, W. B.; Peng, X.; Alivisatos, A. P.; Schultz, P. G. DNA-Based Assembly of Gold Nanocrystals. *Angewandte Chemie International Edition* **1999**; 38 (12): 1808-1812.
- [150] Alivisatos, P. The use of nanocrystals in biological detection. *Nature Biotechnology* **2004**; 22 (1): 47-52.
- [151] Sperling, R. A.; Rivera Gil, P.; Zhang, F.; Zanella, M.; Parak, W. J. Biological applications of gold nanoparticles. *Chemical Society Reviews* **2008**; 37 (9): 1896-1908.

- 
- [152] Freestone, I.; Meeks, N.; Sax, M.; Higgitt, C. The Lycurgus Cup — A Roman nanotechnology. *Gold Bulletin* **2007**; 40 (4): 270-277.
- [153] Wagner, F. E.; Haslbeck, S.; Stievano, L.; Calogero, S.; Pankhurst, Q. A.; Martinek, K. P. Before striking gold in gold-ruby glass. *Nature* **2000**; 407 (6805): 691-692.
- [154] Louis, C.; Pluchery, O., Gold nanoparticles for physics, chemistry and biology. World Scientific: 2017; pp 1-31.
- [155] Turkevich, J.; Stevenson, P. C.; Hillier, J. A study of the nucleation and growth processes in the synthesis of colloidal gold. *Discussions of the Faraday Society* **1951**; 11: 55-75.
- [156] Brust, M.; Walker, M.; Bethell, D.; Schiffrin, D. J.; Whyman, R. Synthesis of thiol-derivatised gold nanoparticles in a two-phase Liquid–Liquid system. *Journal of the Chemical Society, Chemical Communications* **1994**; (7): 801-802.
- [157] Schulz, F.; Friedrich, W.; Hoppe, K.; Vossmeier, T.; Weller, H.; Lange, H. Effective PEGylation of gold nanorods. *Nanoscale* **2016**; 8 (13): 7296-7308.
- [158] Leff, D. V.; Brandt, L.; Heath, J. R. Synthesis and Characterization of Hydrophobic, Organically-Soluble Gold Nanocrystals Functionalized with Primary Amines. *Langmuir* **1996**; 12 (20): 4723-4730.
- [159] Chen, F.; Li, X.; Hihath, J.; Huang, Z.; Tao, N. Effect of Anchoring Groups on Single-Molecule Conductance: Comparative Study of Thiol-, Amine-, and Carboxylic-Acid-Terminated Molecules. *Journal of the American Chemical Society* **2006**; 128 (49): 15874-15881.
- [160] Joseph, Y.; Besnard, I.; Rosenberger, M.; Guse, B.; Nothofer, H.-G.; Wessels, J. M.; Wild, U.; Knop-Gericke, A.; Su, D.; Schlögl, R.; Yasuda, A.; Vossmeier, T. Self-Assembled Gold Nanoparticle/Alkanedithiol Films: Preparation,

Electron Microscopy, XPS-Analysis, Charge Transport, and Vapor-Sensing Properties.

The Journal of Physical Chemistry B **2003**; 107 (30): 7406-7413.

[161] Peng, S.; Lee, Y.; Wang, C.; Yin, H.; Dai, S.; Sun, S. A facile synthesis of monodisperse Au nanoparticles and their catalysis of CO oxidation. *Nano Research* **2008**; 1 (3): 229-234.

[162] Ghosh, S. K.; Pal, T. Interparticle Coupling Effect on the Surface Plasmon Resonance of Gold Nanoparticles: From Theory to Applications. *Chemical Reviews* **2007**; 107 (11): 4797-4862.

[163] Barber, D. J.; Freestone, I. C. An investigation of the origin of the colour of the Lycurgus Cup by analytical transmission electron microscopy. *Archaeometry* **1990**; 32 (1): 33-45.

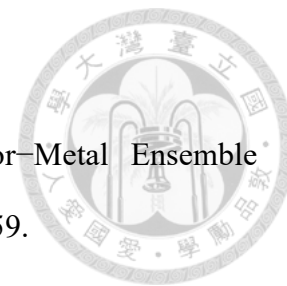
[164] Horvath, H. Gustav Mie and the scattering and absorption of light by particles: Historic developments and basics. *Journal of Quantitative Spectroscopy and Radiative Transfer* **2009**; 110 (11): 787-799.

[165] Link, S.; El-Sayed, M. A. Spectral Properties and Relaxation Dynamics of Surface Plasmon Electronic Oscillations in Gold and Silver Nanodots and Nanorods. *The Journal of Physical Chemistry B* **1999**; 103 (40): 8410-8426.

[166] Tauran, Y.; Brioude, A.; Coleman, A. W.; Rhimi, M.; Kim, B. Molecular recognition by gold, silver and copper nanoparticles. *World journal of biological chemistry* **2013**; 4 (3): 35.

[167] Jain, P. K.; Huang, W.; El-Sayed, M. A. On the Universal Scaling Behavior of the Distance Decay of Plasmon Coupling in Metal Nanoparticle Pairs: A Plasmon Ruler Equation. *Nano Letters* **2007**; 7 (7): 2080-2088.

[168] Sönnichsen, C.; Reinhard, B. M.; Liphardt, J.; Alivisatos, A. P. A molecular ruler based on plasmon coupling of single gold and silver nanoparticles. *Nature*



Biotechnology **2005**; 23 (6): 741-745.

[169] Wohltjen, H.; Snow, A. W. Colloidal Metal–Insulator–Metal Ensemble Chemiresistor Sensor. *Analytical Chemistry* **1998**; 70 (14): 2856-2859.

[170] Terrill, R. H.; Postlethwaite, T. A.; Chen, C.-h.; Poon, C.-D.; Terzis, A.; Chen, A.; Hutchison, J. E.; Clark, M. R.; Wignall, G. Monolayers in three dimensions: NMR, SAXS, thermal, and electron hopping studies of alkanethiol stabilized gold clusters. *Journal of the American Chemical Society* **1995**; 117 (50): 12537-12548.

[171] Schmid, G. The role of big metal clusters in nanoscience. *Journal of the Chemical Society, Dalton Transactions* **1998**; 7: 1077-1082.

[172] Ketelsen, B.; Tjarks, P. P.; Schlicke, H.; Liao, Y.-C.; Vossmeier, T. Fully Printed Flexible Chemiresistors with Tunable Selectivity Based on Gold Nanoparticles. *Chemosensors* **2020**; 8 (4): 116.

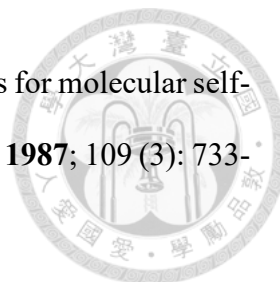
[173] Schulz, F.; Lokteva, I.; Parak, W. J.; Lehmkuhler, F. Recent Notable Approaches to Study Self-Assembly of Nanoparticles with X-Ray Scattering and Electron Microscopy. *Particle & Particle Systems Characterization* **2021**; 38 (9): 2100087.

[174] Ketelsen, B.; Yesilmen, M.; Schlicke, H.; Noei, H.; Su, C.-H.; Liao, Y.-C.; Vossmeier, T. Fabrication of Strain Gauges via Contact Printing: A Simple Route to Healthcare Sensors Based on Cross-Linked Gold Nanoparticles. *ACS Applied Materials & Interfaces* **2018**; 10 (43): 37374-37385.

[175] Saha, K.; Agasti, S. S.; Kim, C.; Li, X.; Rotello, V. M. Gold Nanoparticles in Chemical and Biological Sensing. *Chemical Reviews* **2012**; 112 (5): 2739-2779.

[176] Schlicke, H.; Schröder, J. H.; Trebbin, M.; Petrov, A.; Ijeh, M.; Weller, H.; Vossmeier, T. Freestanding films of crosslinked gold nanoparticles prepared via layer-by-layer spin-coating. *Nanotechnology* **2011**; 22 (30): 305303.

[177] Nuzzo, R. G.; Zegarski, B. R.; Dubois, L. H. Fundamental studies of the



chemisorption of organosulfur compounds on gold (111). Implications for molecular self-assembly on gold surfaces. *Journal of the American Chemical Society* **1987**; 109 (3): 733-740.

[178] Schlicke, H.; Leib, E. W.; Petrov, A.; Schröder, J. H.; Vossmeier, T. Elastic and Viscoelastic Properties of Cross-Linked Gold Nanoparticles Probed by AFM Bulge Tests. *The Journal of Physical Chemistry C* **2014**; 118 (8): 4386-4395.

[179] Olichwer, N.; Meyer, A.; Yesilmen, M.; Vossmeier, T. Gold nanoparticle superlattices: correlating chemiresistive responses with analyte sorption and swelling. *Journal of Materials Chemistry C* **2016**; 4 (35): 8214-8225.

[180] Yan, C.; Arfaoui, I.; Goubet, N.; Pileni, M.-P. Soft Supracrystals of Au Nanocrystals with Tunable Mechanical Properties. *Advanced Functional Materials* **2013**; 23 (18): 2315-2321.

[181] Schlicke, H.; Rebber, M.; Kunze, S.; Vossmeier, T. Resistive pressure sensors based on freestanding membranes of gold nanoparticles. *Nanoscale* **2016**; 8 (1): 183-186.

[182] Schneider, G. F.; Calado, V. E.; Zandbergen, H.; Vandersypen, L. M. K.; Dekker, C. Wedging Transfer of Nanostructures. *Nano Letters* **2010**; 10 (5): 1912-1916.

[183] Chen, Y.; Shu, Z.; Feng, Z.; Kong, L. a.; Liu, Y.; Duan, H. Reliable Patterning, Transfer Printing and Post-Assembly of Multiscale Adhesion-Free Metallic Structures for Nanogap Device Applications. *Advanced Functional Materials* **2020**; 30 (32): 2002549.

[184] Lee, C. H.; Kim, D. R.; Cho, I. S.; William, N.; Wang, Q.; Zheng, X. Peel-and-Stick: Fabricating Thin Film Solar Cell on Universal Substrates. *Scientific Reports* **2012**; 2 (1): 1000.

[185] Wie, D. S.; Zhang, Y.; Kim, M. K.; Kim, B.; Park, S.; Kim, Y.-J.;

Irazoqui, P. P.; Zheng, X.; Xu, B.; Lee, C. H. Wafer-recyclable, environment-friendly transfer printing for large-scale thin-film nanoelectronics. *Proceedings of the National Academy of Sciences* **2018**; 115 (31): E7236-E7244.



[186] Varnava, C. Peel-and-stick circuits. *Nature Electronics* **2018**; 1 (8): 432-432.

[187] Li, X.; Cai, W.; An, J.; Kim, S.; Nah, J.; Yang, D.; Piner, R.; Velamakanni, A.; Jung, I.; Tutuc, E.; Banerjee, S. K.; Colombo, L.; Ruoff, R. S. Large-Area Synthesis of High-Quality and Uniform Graphene Films on Copper Foils. *Science* **2009**; 324 (5932): 1312-1314.

[188] Jiang, J.; Wang, Q.; Wang, B.; Dong, J.; Li, Z.; Li, X.; Zi, Y.; Li, S.; Wang, X. Direct lift-off and the piezo-phototronic study of InGaN/GaN heterostructure membrane. *Nano Energy* **2019**; 59: 545-552.

[189] Pesquera, D.; Khestanova, E.; Ghidini, M.; Zhang, S.; Rooney, A. P.; Maccherozzi, F.; Riego, P.; Farokhipoor, S.; Kim, J.; Moya, X.; Vickers, M. E.; Stelmashenko, N. A.; Haigh, S. J.; Dhessi, S. S.; Mathur, N. D. Large magnetoelectric coupling in multiferroic oxide heterostructures assembled via epitaxial lift-off. *Nature Communications* **2020**; 11 (1): 3190.

[190] Jiao, L.; Fan, B.; Xian, X.; Wu, Z.; Zhang, J.; Liu, Z. Creation of Nanostructures with Poly(methyl methacrylate)-Mediated Nanotransfer Printing. *Journal of the American Chemical Society* **2008**; 130 (38): 12612-12613.

[191] Hwang, S.-W.; Song, J.-K.; Huang, X.; Cheng, H.; Kang, S.-K.; Kim, B. H.; Kim, J.-H.; Yu, S.; Huang, Y.; Rogers, J. A. High-Performance Biodegradable/Transient Electronics on Biodegradable Polymers. *Advanced Materials* **2014**; 26 (23): 3905-3911.

[192] Park, J.; Ghosh, R.; Song, M. S.; Hwang, Y.; Tchoe, Y.; Saroj, R. K.; Ali, A.; Guha, P.; Kim, B.; Kim, S.-W.; Kim, M.; Yi, G.-C. Individually

addressable and flexible pressure sensor matrixes with ZnO nanotube arrays on graphene.

NPG Asia Materials **2022**; 14 (1): 40.

[193] Li, H.; Wu, J.; Huang, X.; Yin, Z.; Liu, J.; Zhang, H. A Universal, Rapid Method for Clean Transfer of Nanostructures onto Various Substrates. *ACS Nano* **2014**; 8 (7): 6563-6570.

[194] Calado, V. E.; Schneider, G. F.; Theulings, A. M. M. G.; Dekker, C.; Vandersypen, L. M. K. Formation and control of wrinkles in graphene by the wedging transfer method. *Applied Physics Letters* **2012**; 101 (10): 103116.

[195] Seo, M.-H.; Yoo, J.-Y.; Jo, M.-S.; Yoon, J.-B. Geometrically Structured Nanomaterials for Nanosensors, NEMS, and Nanosieves. *Advanced Materials* **2020**; 32 (35): 1907082.

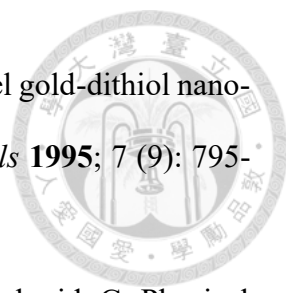
[196] Durand, P.-L.; Chollet, G.; Grau, E.; Cramail, H. Versatile cross-linked fatty acid-based polycarbonate networks obtained by thiol-ene coupling reaction. *RSC Advances* **2019**; 9 (1): 145-150.

[197] Razumovskii, S. D.; Zaikov, G. E. Degradation as a Method of Modification of Polymeric Products. *Molecular Crystals and Liquid Crystals* **2012**; 556 (1): 1-24.

[198] Hosseini, E. S.; Dervin, S.; Ganguly, P.; Dahiya, R. Biodegradable Materials for Sustainable Health Monitoring Devices. *ACS Applied Bio Materials* **2021**; 4 (1): 163-194.

[199] Zhuang, B.; Li, S.; Li, S.; Yin, J. Ways to eliminate PMMA residues on graphene — superclean graphene. *Carbon* **2021**; 173: 609-636.

[200] Suk, J. W.; Lee, W. H.; Lee, J.; Chou, H.; Piner, R. D.; Hao, Y.; Akinwande, D.; Ruoff, R. S. Enhancement of the Electrical Properties of Graphene Grown by Chemical Vapor Deposition via Controlling the Effects of Polymer Residue. *Nano Letters* **2013**; 13 (4): 1462-1467.

- 
- [201] Brust, M.; Schiffrin, D. J.; Bethell, D.; Kiely, C. J. Novel gold-dithiol nano-networks with non-metallic electronic properties. *Advanced Materials* **1995**; 7 (9): 795-797.
- [202] van Staveren, M. P. J.; Brom, H. B.; de Jongh, L. J.; Schmid, G. Physical properties of metal cluster compounds II: Dc-conductivity of the high-nuclearity gold cluster compound Au₅₅(PPh₃)₁₂Cl₆. *Solid State Communications* **1986**; 60 (4): 319-322.
- [203] Abeles, B.; Sheng, P.; Coutts, M. D.; Arie, Y. Structural and electrical properties of granular metal films. *Advances in Physics* **1975**; 24 (3): 407-461.
- [204] Neugebauer, C. A.; Webb, M. B. Electrical Conduction Mechanism in Ultrathin, Evaporated Metal Films. *Journal of Applied Physics* **2004**; 33 (1): 74-82.
- [205] Joseph, Y.; Guse, B.; Vossmeier, T.; Yasuda, A. Gold Nanoparticle/Organic Networks as Chemiresistor Coatings: The Effect of Film Morphology on Vapor Sensitivity. *The Journal of Physical Chemistry C* **2008**; 112 (32): 12507-12514.
- [206] Wessels, J. M.; Nothofer, H.-G.; Ford, W. E.; von Wrochem, F.; Scholz, F.; Vossmeier, T.; Schroedter, A.; Weller, H.; Yasuda, A. Optical and Electrical Properties of Three-Dimensional Interlinked Gold Nanoparticle Assemblies. *Journal of the American Chemical Society* **2004**; 126 (10): 3349-3356.
- [207] Wuelfing, W. P.; Green, S. J.; Pietron, J. J.; Cliffel, D. E.; Murray, R. W. Electronic Conductivity of Solid-State, Mixed-Valent, Monolayer-Protected Au Clusters. *Journal of the American Chemical Society* **2000**; 122 (46): 11465-11472.
- [208] Cui, X. D.; Primak, A.; Zarate, X.; Tomfohr, J.; Sankey, O. F.; Moore, A. L.; Moore, T. A.; Gust, D.; Nagahara, L. A.; Lindsay, S. M. Changes in the Electronic Properties of a Molecule When It Is Wired into a Circuit. *The Journal of Physical Chemistry B* **2002**; 106 (34): 8609-8614.
- [209] Cui, X. D.; Zarate, X.; Tomfohr, J.; Sankey, O. F.; Primak, A.; Moore,

A. L.; Moore, T. A.; Gust, D.; Harris, G.; Lindsay, S. M. Making electrical contacts to molecular monolayers. *Nanotechnology* **2002**; 13 (1): 5.

[210] Likharev, K. K. Single-electron devices and their applications. *Proceedings of the IEEE* **1999**; 87 (4): 606-632.

[211] Vossmeier, T.; Stolte, C.; Ijeh, M.; Kornowski, A.; Weller, H. Networked Gold-Nanoparticle Coatings on Polyethylene: Charge Transport and Strain Sensitivity. *Advanced Functional Materials* **2008**; 18 (11): 1611-1616.

[212] Olichwer, N.; Leib, E. W.; Halfar, A. H.; Petrov, A.; Vossmeier, T. Cross-Linked Gold Nanoparticles on Polyethylene: Resistive Responses to Tensile Strain and Vapors. *ACS Applied Materials & Interfaces* **2012**; 4 (11): 6151-6161.


[213] Steinecker, W. H.; Rowe, M. P.; Zellers, E. T. Model of Vapor-Induced Resistivity Changes in Gold-Thiolate Monolayer-Protected Nanoparticle Sensor Films. *Analytical Chemistry* **2007**; 79 (13): 4977-4986.

[214] Herrmann, J.; Müller, K.-H.; Reda, T.; Baxter, G. R.; Raguse, B.; Groot, G. J. J. B. d.; Chai, R.; Roberts, M.; Wiczorek, L. Nanoparticle films as sensitive strain gauges. *Applied Physics Letters* **2007**; 91 (18): 183105.

[215] Han, J.-H.; Min, S. J.; Kim, J. H.; Min, N. K. Reciprocating Arc Silicon Strain Gauges. *Sensors* **2023**; 23 (3): 1381.

[216] Khalid, M. A. U.; Chang, S. H. Flexible strain sensors for wearable applications fabricated using novel functional nanocomposites: A review. *Composite Structures* **2022**; 284: 115214.

[217] Liu, H.; Li, Q.; Zhang, S.; Yin, R.; Liu, X.; He, Y.; Dai, K.; Shan, C.; Guo, J.; Liu, C.; Shen, C.; Wang, X.; Wang, N.; Wang, Z.; Wei, R.; Guo, Z. Electrically conductive polymer composites for smart flexible strain sensors: a critical review. *Journal of Materials Chemistry C* **2018**; 6 (45): 12121-12141.

- 
- [218] Shen, Z.; Liu, F.; Huang, S.; Wang, H.; Yang, C.; Hang, T.; Tao, J.; Xia, W.; Xie, X. Progress of flexible strain sensors for physiological signal monitoring. *Biosensors and Bioelectronics* **2022**; 211: 114298.
- [219] Gao, W.; Ota, H.; Kiriya, D.; Takei, K.; Javey, A. Flexible Electronics toward Wearable Sensing. *Accounts of Chemical Research* **2019**; 52 (3): 523-533.
- [220] Huang, C.-B.; Yao, Y.; Montes-García, V.; Stoeckel, M.-A.; Von Holst, M.; Ciesielski, A.; Samorì, P. Highly Sensitive Strain Sensors Based on Molecules–Gold Nanoparticles Networks for High-Resolution Human Pulse Analysis. *Small* **2021**; 17 (8): 2007593.
- [221] Ketelsen, B.; Schlicke, H.; Schulze, V. R.; Bittinger, S. C.; Wu, S.-D.; Hsu, S.-h.; Vossmeier, T. Nanoparticle-Based Strain Gauges: Anisotropic Response Characteristics, Multidirectional Strain Sensing, and Novel Approaches to Healthcare Applications. *Advanced Functional Materials* **2023**; 33 (7): 2210065.
- [222] Barad, H.-N.; Kwon, H.; Alarcón-Correa, M.; Fischer, P. Large Area Patterning of Nanoparticles and Nanostructures: Current Status and Future Prospects. *ACS Nano* **2021**; 15 (4): 5861-5875.
- [223] Fan, J. A.; Yeo, W.-H.; Su, Y.; Hattori, Y.; Lee, W.; Jung, S.-Y.; Zhang, Y.; Liu, Z.; Cheng, H.; Falgout, L.; Bajema, M.; Coleman, T.; Gregoire, D.; Larsen, R. J.; Huang, Y.; Rogers, J. A. Fractal design concepts for stretchable electronics. *Nature Communications* **2014**; 5 (1): 3266.
- [224] Baek, S.; Lee, Y.; Baek, J.; Kwon, J.; Kim, S.; Lee, S.; Strunk, K.-P.; Stehlin, S.; Melzer, C.; Park, S.-M.; Ko, H.; Jung, S. Spatiotemporal Measurement of Arterial Pulse Waves Enabled by Wearable Active-Matrix Pressure Sensor Arrays. *ACS Nano* **2022**; 16 (1): 368-377.
- [225] Jheng, W.-W.; Su, Y.-S.; Hsieh, Y.-L.; Lin, Y.-J.; Tzeng, S.-D.; Chang,

C.-W.; Song, J.-M.; Kuo, W. Gold Nanoparticle Thin Film-Based Strain Sensors for Monitoring Human Pulse. *ACS Applied Nano Materials* **2021**; 4 (2): 1712-1718.

[226] Lee, J.; Kim, S.; Lee, J.; Yang, D.; Park, B. C.; Ryu, S.; Park, I. A stretchable strain sensor based on a metal nanoparticle thin film for human motion detection. *Nanoscale* **2014**; 6 (20): 11932-11939.

[227] Yu, Q.; Ge, R.; Wen, J.; Du, T.; Zhai, J.; Liu, S.; Wang, L.; Qin, Y. Highly sensitive strain sensors based on piezotronic tunneling junction. *Nature Communications* **2022**; 13 (1): 778.

[228] Park, H. J.; Jeong, J.-M.; Son, S. G.; Kim, S. J.; Lee, M.; Kim, H. J.; Jeong, J.; Hwang, S. Y.; Park, J.; Eom, Y.; Choi, B. G. Fluid-Dynamics-Processed Highly Stretchable, Conductive, and Printable Graphene Inks for Real-Time Monitoring Sweat during Stretching Exercise. *Advanced Functional Materials* **2021**; 31 (21): 2011059.

[229] Tat, T.; Chen, G.; Zhao, X.; Zhou, Y.; Xu, J.; Chen, J. Smart Textiles for Healthcare and Sustainability. *ACS Nano* **2022**; 16 (9): 13301-13313.

[230] Lu, J.; Hu, S.; Li, W.; Wang, X.; Mo, X.; Gong, X.; Liu, H.; Luo, W.; Dong, W.; Sima, C.; Wang, Y.; Yang, G.; Luo, J.-T.; Jiang, S.; Shi, Z.; Zhang, G. A Biodegradable and Recyclable Piezoelectric Sensor Based on a Molecular Ferroelectric Embedded in a Bacterial Cellulose Hydrogel. *ACS Nano* **2022**; 16 (3): 3744-3755.

[231] Boutry, C. M.; Kaizawa, Y.; Schroeder, B. C.; Chortos, A.; Legrand, A.; Wang, Z.; Chang, J.; Fox, P.; Bao, Z. A stretchable and biodegradable strain and pressure sensor for orthopaedic application. *Nature Electronics* **2018**; 1 (5): 314-321.

[232] Ma, X.; Hu, Q.; Dai, Y.; He, P.; Zhang, X. Disposable sensors based on biodegradable polylactic acid piezoelectret films and their application in wearable

electronics. *Sensors and Actuators A: Physical* **2022**; 346: 113834.

[233] Pinto, V. C.; Ramos, T.; Alves, S.; Xavier, J.; Tavares, P.; Moreira, P. M. G. P.; Guedes, R. M. Comparative Failure Analysis of PLA, PLA/GNP and PLA/CNT-COOH Biodegradable Nanocomposites thin Films. *Procedia Engineering* **2015**; 114: 635-642.

[234] Boland, C. S. Stumbling through the Research Wilderness, Standard Methods To Shine Light on Electrically Conductive Nanocomposites for Future Healthcare Monitoring. *ACS Nano* **2019**; 13 (12): 13627-13636.

[235] Liu, Z.; Li, C.; Zhang, X.; Zhou, B.; Wen, S.; Zhou, Y.; Chen, S.; Jiang, L.; Jerrams, S.; Zhou, F. Biodegradable Polyurethane Fiber-Based Strain Sensor with a Broad Sensing Range and High Sensitivity for Human Motion Monitoring. *ACS Sustainable Chemistry & Engineering* **2022**; 10 (27): 8788-8798.

[236] Ní Annaidh, A.; Bruyère, K.; Destrade, M.; Gilchrist, M. D.; Otténio, M. Characterization of the anisotropic mechanical properties of excised human skin. *Journal of the Mechanical Behavior of Biomedical Materials* **2012**; 5 (1): 139-148.

[237] Song, Y.; Min, J.; Gao, W. Wearable and Implantable Electronics: Moving toward Precision Therapy. *ACS Nano* **2019**; 13 (11): 12280-12286.

[238] Benjamin, E. J.; Muntner, P.; Alonso, A.; Bittencourt, M. S.; Callaway, C. W.; Carson, A. P.; Chamberlain, A. M.; Chang, A. R.; Cheng, S.; Das, S. R. Heart disease and stroke statistics—2019 update: a report from the American Heart Association. *Circulation* **2019**; 139 (10): e56-e528.

[239] Doggrell, S. A.; Brown, L. Rat models of hypertension, cardiac hypertrophy and failure. *Cardiovascular research* **1998**; 39 (1): 89-105.

[240] Keßler, M.; Rottbauer, W.; Just, S. Recent progress in the use of zebrafish for novel cardiac drug discovery. *Expert Opinion on Drug Discovery* **2015**; 10 (11): 1231-



1241.

[241] Passier, R.; van Laake, L. W.; Mummery, C. L. Stem-cell-based therapy and lessons from the heart. *Nature* **2008**; 453 (7193): 322-329.

[242] Cardiovascular Organ-on-a-Chip Platforms for Drug Discovery and Development. *Applied In Vitro Toxicology* **2016**; 2 (2): 82-96.

[243] Mastikhina, O.; Moon, B.-U.; Williams, K.; Hatkar, R.; Gustafson, D.; Mourad, O.; Sun, X.; Koo, M.; Lam, A. Y. L.; Sun, Y.; Fish, J. E.; Young, E. W. K.; Nunes, S. S. Human cardiac fibrosis-on-a-chip model recapitulates disease hallmarks and can serve as a platform for drug testing. *Biomaterials* **2020**; 233: 119741.

[244] Criscione, J.; Rezaei, Z.; Hernandez Cantu, C. M.; Murphy, S.; Shin, S. R.; Kim, D.-H. Heart-on-a-chip platforms and biosensor integration for disease modeling and phenotypic drug screening. *Biosensors and Bioelectronics* **2023**; 220: 114840.

[245] Chen, X.; Liu, S.; Han, M.; Long, M.; Li, T.; Hu, L.; Wang, L.; Huang, W.; Wu, Y. Engineering Cardiac Tissue for Advanced Heart-On-A-Chip Platforms. *Advanced Healthcare Materials* **2024**; 13 (1): 2301338.

[246] Dou, W.; Malhi, M.; Zhao, Q.; Wang, L.; Huang, Z.; Law, J.; Liu, N.; Simmons, C. A.; Maynes, J. T.; Sun, Y. Microengineered platforms for characterizing the contractile function of in vitro cardiac models. *Microsystems & Nanoengineering* **2022**; 8 (1): 26.

[247] Ergir, E.; Oliver-De La Cruz, J.; Fernandes, S.; Cassani, M.; Niro, F.; Pereira-Sousa, D.; Vrbský, J.; Vinarský, V.; Perestrelo, A. R.; Debellis, D.; Vadovičová, N.; Uldrijan, S.; Cavalieri, F.; Pagliari, S.; Redl, H.; Ertl, P.; Forte, G. Generation and maturation of human iPSC-derived 3D organotypic cardiac microtissues in long-term culture. *Scientific Reports* **2022**; 12 (1): 17409.

[248] Thavandiran, N.; Dubois, N.; Mikryukov, A.; Massé, S.; Beca, B.;

Simmons, C. A.; Deshpande, V. S.; McGarry, J. P.; Chen, C. S.; Nanthakumar, K.; Keller, G. M.; Radisic, M.; Zandstra, P. W. Design and formulation of functional pluripotent stem cell-derived cardiac microtissues. *Proceedings of the National Academy of Sciences* **2013**; 110 (49): E4698-E4707.

[249] Smits, A. M.; van Vliet, P.; Metz, C. H.; Korfage, T.; Sluijter, J. P. G.; Doevendans, P. A.; Goumans, M.-J. Human cardiomyocyte progenitor cells differentiate into functional mature cardiomyocytes: an in vitro model for studying human cardiac physiology and pathophysiology. *Nature Protocols* **2009**; 4 (2): 232-243.

[250] Freund, C.; Mummery, C. L. Prospects for pluripotent stem cell-derived cardiomyocytes in cardiac cell therapy and as disease models. *Journal of Cellular Biochemistry* **2009**; 107 (4): 592-599.

[251] Li, Z.; Guan, J. Hydrogels for Cardiac Tissue Engineering. *Polymers* **2011**; 3 (2): 740-761.

[252] Liu, H.; Chansoria, P.; Delrot, P.; Angelidakis, E.; Rizzo, R.; Rütscche, D.; Applegate, L. A.; Loterie, D.; Zenobi-Wong, M. Filamented Light (FLight) Biofabrication of Highly Aligned Tissue-Engineered Constructs. *Advanced Materials* **2022**; 34 (45): 2204301.

[253] Song, X.; Wang, X.; Zhang, J.; Shen, S.; Yin, W.; Ye, G.; Wang, L.; Hou, H.; Qiu, X. A tunable self-healing ionic hydrogel with microscopic homogeneous conductivity as a cardiac patch for myocardial infarction repair. *Biomaterials* **2021**; 273: 120811.

[254] Jing, X.; Mi, H.-Y.; Napiwocki, B. N.; Peng, X.-F.; Turng, L.-S. Mussel-inspired electroactive chitosan/graphene oxide composite hydrogel with rapid self-healing and recovery behavior for tissue engineering. *Carbon* **2017**; 125: 557-570.

[255] Fang, Y.; Guo, Y.; Wu, B.; Liu, Z.; Ye, M.; Xu, Y.; Ji, M.; Chen,

L.; Lu, B.; Nie, K.; Wang, Z.; Luo, J.; Zhang, T.; Sun, W.; Xiong, Z. Expanding Embedded 3D Bioprinting Capability for Engineering Complex Organs with Freeform Vascular Networks. *Advanced Materials* **2023**; 35 (22): 2205082.

[256] Daly, A. C.; Davidson, M. D.; Burdick, J. A. 3D bioprinting of high cell-density heterogeneous tissue models through spheroid fusion within self-healing hydrogels. *Nature Communications* **2021**; 12 (1): 753.

[257] Bertsch, P.; Diba, M.; Mooney, D. J.; Leeuwenburgh, S. C. G. Self-Healing Injectable Hydrogels for Tissue Regeneration. *Chemical Reviews* **2023**; 123 (2): 834-873.

[258] Beussman, K. M.; Rodriguez, M. L.; Leonard, A.; Taparia, N.; Thompson, C. R.; Sniadecki, N. J. Micropost arrays for measuring stem cell-derived cardiomyocyte contractility. *Methods* **2016**; 94: 43-50.

[259] Oyunbaatar, N.-E.; Dai, Y.; Shanmugasundaram, A.; Lee, B.-K.; Kim, E.-S.; Lee, D.-W. Development of a Next-Generation Biosensing Platform for Simultaneous Detection of Mechano- and Electrophysiology of the Drug-Induced Cardiomyocytes. *ACS Sensors* **2019**; 4 (10): 2623-2630.

[260] Pesl, M.; Pribyl, J.; Acimovic, I.; Vilotic, A.; Jelinkova, S.; Salykin, A.; Lacampagne, A.; Dvorak, P.; Meli, A. C.; Skladal, P.; Rotrekl, V. Atomic force microscopy combined with human pluripotent stem cell derived cardiomyocytes for biomechanical sensing. *Biosensors and Bioelectronics* **2016**; 85: 751-757.

[261] Colin-York, H.; Fritzsche, M. The future of traction force microscopy. *Current Opinion in Biomedical Engineering* **2018**; 5: 1-5.

[262] Sun, N.; Yazawa, M.; Liu, J.; Han, L.; Sanchez-Freire, V.; Abilez, O. J.; Navarrete, E. G.; Hu, S.; Wang, L.; Lee, A.; Pavlovic, A.; Lin, S.; Chen, R.; Hajjar, R. J.; Snyder, M. P.; Dolmetsch, R. E.; Butte, M. J.; Ashley, E. A.; Longaker, M. T.; Robbins, R. C.; Wu, J. C. Patient-Specific Induced Pluripotent Stem

Cells as a Model for Familial Dilated Cardiomyopathy. *Science Translational Medicine* **2012**; 4 (130): 130ra47.

[263] Yang, Q.; Xiao, Z.; Lv, X.; Zhang, T.; Liu, H. Fabrication and Biomedical Applications of Heart-on-a-chip. *International Journal of Bioprinting* **2021**; 7 (3): 370.

[264] Cho, K. W.; Lee, W. H.; Kim, B.-S.; Kim, D.-H. Sensors in heart-on-a-chip: A review on recent progress. *Talanta* **2020**; 219: 121269.

[265] Choi, S.; Han, S. I.; Jung, D.; Hwang, H. J.; Lim, C.; Bae, S.; Park, O. K.; Tschabrunn, C. M.; Lee, M.; Bae, S. Y.; Yu, J. W.; Ryu, J. H.; Lee, S.-W.; Park, K.; Kang, P. M.; Lee, W. B.; Nezafat, R.; Hyeon, T.; Kim, D.-H. Highly conductive, stretchable and biocompatible Ag–Au core–sheath nanowire composite for wearable and implantable bioelectronics. *Nature Nanotechnology* **2018**; 13 (11): 1048-1056.

[266] Lee, J.; Cho, H. R.; Cha, G. D.; Seo, H.; Lee, S.; Park, C.-K.; Kim, J. W.; Qiao, S.; Wang, L.; Kang, D.; Kang, T.; Ichikawa, T.; Kim, J.; Lee, H.; Lee, W.; Kim, S.; Lee, S.-T.; Lu, N.; Hyeon, T.; Choi, S. H.; Kim, D.-H. Flexible, sticky, and biodegradable wireless device for drug delivery to brain tumors. *Nature Communications* **2019**; 10 (1): 5205.

[267] Kadhim, R. J.; Karsh, E. H.; Taqi, Z. J.; Jabir, M. S. Biocompatibility of gold nanoparticles: In-vitro and In-vivo study. *Materials Today: Proceedings* **2021**; 42: 3041-3045.

[268] Alkilany, A. M.; Lohse, S. E.; Murphy, C. J. The Gold Standard: Gold Nanoparticle Libraries To Understand the Nano–Bio Interface. *Accounts of Chemical Research* **2013**; 46 (3): 650-661.

[269] Wu, S.-D.; Hsu, S.-h.; Ketelsen, B.; Bittinger, S. C.; Schlicke, H.; Weller, H.; Vossmeier, T. Fabrication of Eco-Friendly Wearable Strain Sensor Arrays via

Facile Contact Printing for Healthcare Applications. *Small Methods* **2023**; 7 (9): 2300170.

[270] Haiss, W.; Thanh, N. T. K.; Aveyard, J.; Fernig, D. G. Determination of Size and Concentration of Gold Nanoparticles from UV–Vis Spectra. *Analytical Chemistry* **2007**; 79 (11): 4215-4221.

[271] Brinkman, E.; Poot, A.; Beugeling, T.; Van der Does, L.; Bantjes, A. Surface modification of copolyether-urethane catheters with poly (ethylene oxide). *The International journal of artificial organs* **1989**; 12 (6): 390-394.

[272] Choi, M. K.; Park, I.; Kim, D. C.; Joh, E.; Park, O. K.; Kim, J.; Kim, M.; Choi, C.; Yang, J.; Cho, K. W.; Hwang, J.-H.; Nam, J.-M.; Hyeon, T.; Kim, J. H.; Kim, D.-H. Thermally Controlled, Patterned Graphene Transfer Printing for Transparent and Wearable Electronic/Optoelectronic System. *Advanced Functional Materials* **2015**; 25 (46): 7109-7118.

[273] Lin, S.-H.; Papadakis, C. M.; Kang, J.-J.; Lin, J.-M.; Hsu, S.-h. Injectable Phenolic-Chitosan Self-Healing Hydrogel with Hierarchical Micelle Architectures and Fast Adhesiveness. *Chemistry of Materials* **2021**; 33 (11): 3945-3958.

[274] Huang, Y.-J.; Hsu, S.-h. Acquisition of epithelial–mesenchymal transition and cancer stem-like phenotypes within chitosan-hyaluronan membrane-derived 3D tumor spheroids. *Biomaterials* **2014**; 35 (38): 10070-10079.

[275] Zhou, J.; Ellis, A. V.; Voelcker, N. H. Recent developments in PDMS surface modification for microfluidic devices. *ELECTROPHORESIS* **2010**; 31 (1): 2-16.

[276] Trung, N. B.; Yoshikawa, H.; Tamiya, E.; Viet, P. H.; Takamura, Y.; Ashahi, T. Propitious Immobilization of Gold Nanoparticles on Poly(dimethylsiloxane) Substrate for Local Surface Plasmon Resonance Based Biosensor. *Japanese Journal of Applied Physics* **2012**; 51 (3R): 037001.

[277] SadAbadi, H.; Badilescu, S.; Packirisamy, M.; Wüthrich, R. Integration of

gold nanoparticles in PDMS microfluidics for lab-on-a-chip plasmonic biosensing of growth hormones. *Biosensors and Bioelectronics* **2013**; 44: 77-84.

[278] Taylor, J. E.; Laity, P. R.; Freeburn, S.; Wong, S. S.; Norris, K.; Khunkamchoo, P.; Cable, M.; Andrews, G.; Johnson, A. F.; Cameron, R. E. Effect of processing route and acetone pre-treatment on the biostability of pellethane materials used in medical device applications. *Biomaterials* **2005**; 26 (33): 6467-6476.

[279] Chernonosova, V.; Gostev, A.; Murashov, I.; Chelobanov, B.; Karpenko, A.; Laktionov, P. Assessment of Electrospun Pellethane-Based Scaffolds for Vascular Tissue Engineering. *Materials* **2021**; 14 (13): 3678.

[280] Lind, J. U.; Busbee, T. A.; Valentine, A. D.; Pasqualini, F. S.; Yuan, H.; Yadid, M.; Park, S.-J.; Kotikian, A.; Nesmith, A. P.; Campbell, P. H.; Vlassak, J. J.; Lewis, J. A.; Parker, K. K. Instrumented cardiac microphysiological devices via multimaterial three-dimensional printing. *Nature Materials* **2017**; 16 (3): 303-308.

[281] Brinkman, E.; Poot, A.; Beugeling, T.; Van Der Does, L.; Bantjes, A. Surface Modification of Copolyether-Urethane Catheters with Poly(Ethylene Oxide). *The International journal of artificial organs* **1989**; 12 (6): 390-394.

[282] Phadtare, S.; Kumar, A.; Vinod, V. P.; Dash, C.; Palaskar, D. V.; Rao, M.; Shukla, P. G.; Sivaram, S.; Sastry, M. Direct Assembly of Gold Nanoparticle “Shells” on Polyurethane Microsphere “Cores” and Their Application as Enzyme Immobilization Templates. *Chemistry of Materials* **2003**; 15 (10): 1944-1949.

[283] Chen, T.; Xie, Y.; Wang, Z.; Lou, J.; Liu, D.; Xu, R.; Cui, Z.; Li, S.; Panahi-Sarmad, M.; Xiao, X. Recent Advances of Flexible Strain Sensors Based on Conductive Fillers and Thermoplastic Polyurethane Matrixes. *ACS Applied Polymer Materials* **2021**; 3 (11): 5317-5338.

[284] Kim, Y.; Zhu, J.; Yeom, B.; Di Prima, M.; Su, X.; Kim, J.-G.; Yoo,

S. J.; Uher, C.; Kotov, N. A. Stretchable nanoparticle conductors with self-organized conductive pathways. *Nature* **2013**; 500 (7460): 59-63.

[285] Yi, J.; Xianyu, Y. Gold Nanomaterials-Implemented Wearable Sensors for Healthcare Applications. *Advanced Functional Materials* **2022**; 32 (19): 2113012.

[286] Huang, Q.; Zhu, Y. Printing Conductive Nanomaterials for Flexible and Stretchable Electronics: A Review of Materials, Processes, and Applications. *Advanced Materials Technologies* **2019**; 4 (5): 1800546.

[287] Li, Y.; Liu, Y.; Bhuiyan, S. R. A.; Zhu, Y.; Yao, S. Printed Strain Sensors for On-Skin Electronics. *Small Structures* **2022**; 3 (2): 2100131.

[288] Rastin, H.; Mansouri, N.; Tung, T. T.; Hassan, K.; Mazinani, A.; Ramezanpour, M.; Yap, P. L.; Yu, L.; Vreugde, S.; Losic, D. Converging 2D Nanomaterials and 3D Bioprinting Technology: State-of-the-Art, Challenges, and Potential Outlook in Biomedical Applications. *Advanced Healthcare Materials* **2021**; 10 (22): 2101439.

[289] McLean, R. S.; Sauer, B. B. Tapping-Mode AFM Studies Using Phase Detection for Resolution of Nanophases in Segmented Polyurethanes and Other Block Copolymers. *Macromolecules* **1997**; 30 (26): 8314-8317.

[290] Zhou, Y.; Lian, H.; Li, Z.; Yin, L.; Ji, Q.; Li, K.; Qi, F.; Huang, Y. Crack engineering boosts the performance of flexible sensors. *VIEW* **2022**; 3 (5): 20220025.

[291] Kang, D.; Pikhitsa, P. V.; Choi, Y. W.; Lee, C.; Shin, S. S.; Piao, L.; Park, B.; Suh, K.-Y.; Kim, T.-i.; Choi, M. Ultrasensitive mechanical crack-based sensor inspired by the spider sensory system. *Nature* **2014**; 516 (7530): 222-226.

[292] McCain, M. L.; Agarwal, A.; Nesmith, H. W.; Nesmith, A. P.; Parker, K. K. Micromolded gelatin hydrogels for extended culture of engineered cardiac tissues.

Biomaterials **2014**; 35 (21): 5462-5471.

[293] Wang, J.; Liu, Q.; Gong, J.; Wan, Z.; Zhou, J.; Chang, C.; Zhang, D. Micropatterned Hydrogels with Highly Ordered Cellulose Nanocrystals for Visually Monitoring Cardiomyocytes. *Small* **2022**; 18 (45): 2202235.

[294] Tijore, A.; Irvine, S. A.; Sarig, U.; Mhaisalkar, P.; Baisane, V.; Venkatraman, S. Contact guidance for cardiac tissue engineering using 3D bioprinted gelatin patterned hydrogel. *Biofabrication* **2018**; 10 (2): 025003.

[295] Beleño Acosta, B.; Advincula, R. C.; Grande-Tovar, C. D. Chitosan-Based Scaffolds for the Treatment of Myocardial Infarction: A Systematic Review. *Molecules* **2023**; 28 (4): 1920.

[296] Kazemi Asl, S.; Rahimzadegan, M.; Ostadrahimi, R. The recent advancement in the chitosan hybrid-based scaffolds for cardiac regeneration after myocardial infarction. *Carbohydrate Polymers* **2023**; 300: 120266.

[297] Gong, T.-Y.; Hsu, S.-h.; Chang, S.-W.; Chou, C.-C. Effects of the Degree of Phenol Substitution on Molecular Structures and Properties of Chitosan-Phenol-Based Self-Healing Hydrogels. *ACS Biomaterials Science & Engineering* **2023**; 9 (11): 6146-6155.

[298] Crocini, C.; Walker, C. J.; Anseth, K. S.; Leinwand, L. A. Three-dimensional encapsulation of adult mouse cardiomyocytes in hydrogels with tunable stiffness. *Progress in Biophysics and Molecular biology* **2020**; 154: 71-79.

[299] Wong, C.-W.; Han, H.-W.; Tien, Y.-W.; Hsu, S.-h. Biomaterial substrate-derived compact cellular spheroids mimicking the behavior of pancreatic cancer and microenvironment. *Biomaterials* **2019**; 213: 119202.

[300] Toole, B. P. Hyaluronan: from extracellular glue to pericellular cue. *Nature Reviews Cancer* **2004**; 4 (7): 528-539.

[301] Hsu, S.-h.; Huang, G.-S. Substrate-dependent Wnt signaling in MSC differentiation within biomaterial-derived 3D spheroids. *Biomaterials* **2013**; 34 (20): 4725-4738.

[302] Chang, P.-H.; Chao, H.-M.; Chern, E.; Hsu, S.-h. Chitosan 3D cell culture system promotes naïve-like features of human induced pluripotent stem cells: A novel tool to sustain pluripotency and facilitate differentiation. *Biomaterials* **2021**; 268: 120575.

[303] Andrysiak, K.; Stępniewski, J.; Dulak, J. Human-induced pluripotent stem cell-derived cardiomyocytes, 3D cardiac structures, and heart-on-a-chip as tools for drug research. *Pflügers Archiv - European Journal of Physiology* **2021**; 473 (7): 1061-1085.

[304] Kim, D.-S.; Choi, Y. W.; Shanmugasundaram, A.; Jeong, Y.-J.; Park, J.; Oyunbaatar, N.-E.; Kim, E.-S.; Choi, M.; Lee, D.-W. Highly durable crack sensor integrated with silicone rubber cantilever for measuring cardiac contractility. *Nature Communications* **2020**; 11 (1): 535.

[305] Litviňuková, M.; Talavera-López, C.; Maatz, H.; Reichart, D.; Worth, C. L.; Lindberg, E. L.; Kanda, M.; Polanski, K.; Heinig, M.; Lee, M.; Nadelmann, E. R.; Roberts, K.; Tuck, L.; Fasouli, E. S.; DeLaughter, D. M.; McDonough, B.; Wakimoto, H.; Gorham, J. M.; Samari, S.; Mahbubani, K. T.; Saeb-Parsy, K.; Patone, G.; Boyle, J. J.; Zhang, H.; Zhang, H.; Viveiros, A.; Oudit, G. Y.; Bayraktar, O. A.; Seidman, J. G.; Seidman, C. E.; Nosedá, M.; Hubner, N.; Teichmann, S. A. Cells of the adult human heart. *Nature* **2020**; 588 (7838): 466-472.

[306] Pinto, A. R.; Ilinykh, A.; Ivey, M. J.; Kuwabara, J. T.; D'Antoni, M. L.; Debuque, R.; Chandran, A.; Wang, L.; Arora, K.; Rosenthal, N. A.; Tallquist, M. D. Revisiting Cardiac Cellular Composition. *Circulation Research* **2016**; 118 (3): 400-409.

[307] Zhou, P.; Pu, W. T. Recounting Cardiac Cellular Composition. *Circulation Research* **2016**; 118 (3): 368-370.

[308] Beauchamp, P.; Jackson, C. B.; Ozhathil, L. C.; Agarkova, I.; Galindo, C. L.; Sawyer, D. B.; Suter, T. M.; Zuppinger, C. 3D Co-culture of hiPSC-Derived Cardiomyocytes With Cardiac Fibroblasts Improves Tissue-Like Features of Cardiac Spheroids. *Frontiers in Molecular Biosciences* **2020**; 7: 1-14.

[309] Yeh, H. Y.; Hsieh, F. Y.; Hsu, S. h. Self-patterning of adipose-derived mesenchymal stem cells and chondrocytes cocultured on hyaluronan-grafted chitosan surface. *Biointerphases* **2016**; 11 (1): 011011.

[310] Han, H.-W.; Hsu, S.-h. Chitosan derived co-spheroids of neural stem cells and mesenchymal stem cells for neural regeneration. *Colloids and Surfaces B: Biointerfaces* **2017**; 158: 527-538.



7. Appendix

7.1. Supporting information

This section contains the Supporting information relating to the publications in the section 3.

7.1.1. Publication 1 (first project): 4D bioprintable self-healing hydrogel with shape memory and cryopreserving properties

The supporting information for "Shin-Da Wu and Shin-hsu Hsu. 4D bioprintable self-healing hydrogel with shape memory and cryopreserving properties. *Biofabrication* **2021**; 13: 045029" is available at the following DOI: <https://doi.org/10.1088/1758-5090/ac2789>

7.1.2. Publication 3 (third project): Fabrication of eco-friendly wearable strain sensor arrays via facile contact printing for healthcare applications

Reprinted from “Shin-Da Wu, Shan-hui Hsu, Bendix Ketelsen, Sophia C. Bittinger, Hendrik Schlicke, Horst Weller, and Tobias Vossmeier. Fabrication of Eco-friendly Wearable Strain Sensor Arrays via Facile Contact Printing for Healthcare Applications. *Small Methods* **2023**; 7(9): 2300170.” with permission from WILEY-VCH.

small methods



Supporting Information

for *Small Methods*, DOI 10.1002/smtd.202300170

Fabrication of Eco-Friendly Wearable Strain Sensor Arrays via Facile Contact Printing for Healthcare Applications

*Shin-Da Wu, Shan-hui Hsu**, Bendix Ketelsen, Sophia C. Bittinger, Hendrik Schlicke, Horst Weller and Tobias Vossmeier*

Supporting Information



Fabrication of Eco-friendly Wearable Strain Sensor Arrays via Facile Contact Printing for Healthcare Applications

Shin-Da Wu^{1,2}, Shan-hui Hsu^{1,3,*}, Bendix Ketelsen², Sophia C. Bittinger²,

Hendrik Schlicke⁴, Horst Weller^{2,4}, and Tobias Vossmeier^{2,*}

¹ Institute of Polymer Science and Engineering, National Taiwan University, No. 1,
Sec. 4 Roosevelt Road, Taipei 10617, Taiwan

² Institute of Physical Chemistry, University of Hamburg, Grindelallee 117, 20146
Hamburg, Germany

³ Institute of Cellular and System Medicine, National Health Research Institutes,
Miaoli, Taiwan

⁴ Fraunhofer Center for Applied Nanotechnology CAN, Grindelallee 117, 20146
Hamburg, Germany

Pages: 15

Supplemental Figures: 14 (Figure S1-Figure S14)

*** Corresponding author:**

Tobias Vossmeier (ORCID: 0000-0001-9738-3826)

E-mail: tobias.vossmeier@chemie.uni-hamburg.de

Shan-hui Hsu (ORCID: 0000-0003-3399-055X)

E-mail: shhsu@ntu.edu.tw

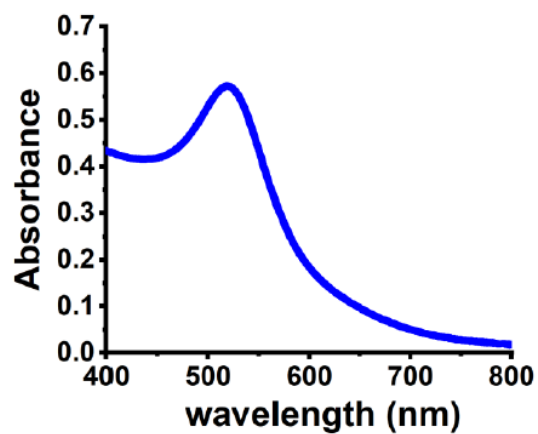


Figure S1. The UV-vis absorbance spectrum of GNPs synthesized in this study.

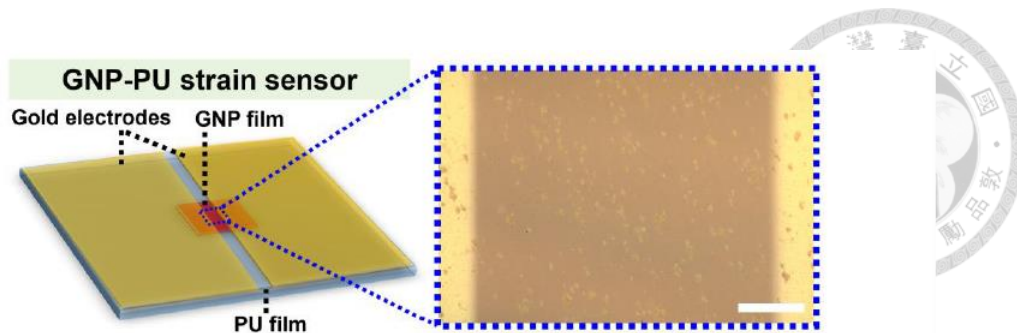


Figure S2. Schematic illustration of the GNP-PU strain sensor. The optical microscopy (OM) image shows that the gap between the two gold electrodes was $\sim 230 \mu\text{m}$. Scale bar represents $50 \mu\text{m}$.

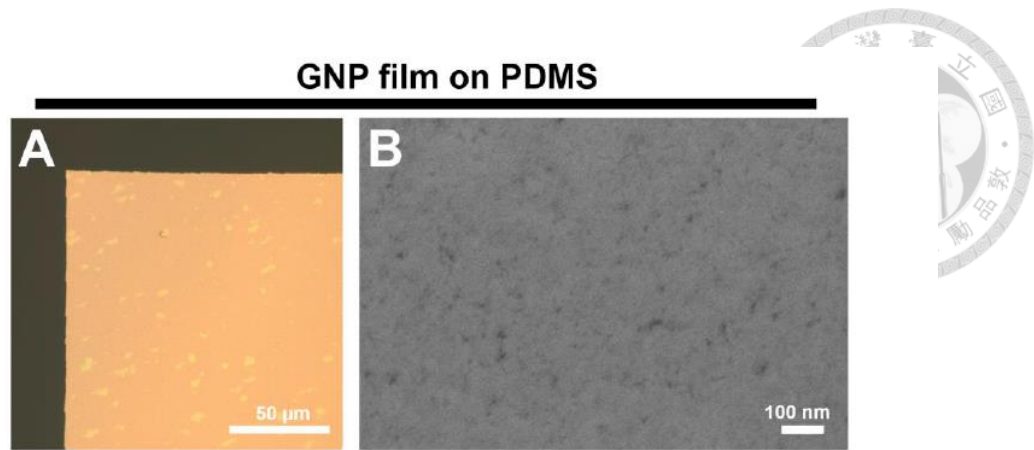


Figure S3. GNP film after transfer onto the PDMS stamp. The (A) OM image and (B) SEM image show the surface morphology of the GNP film.

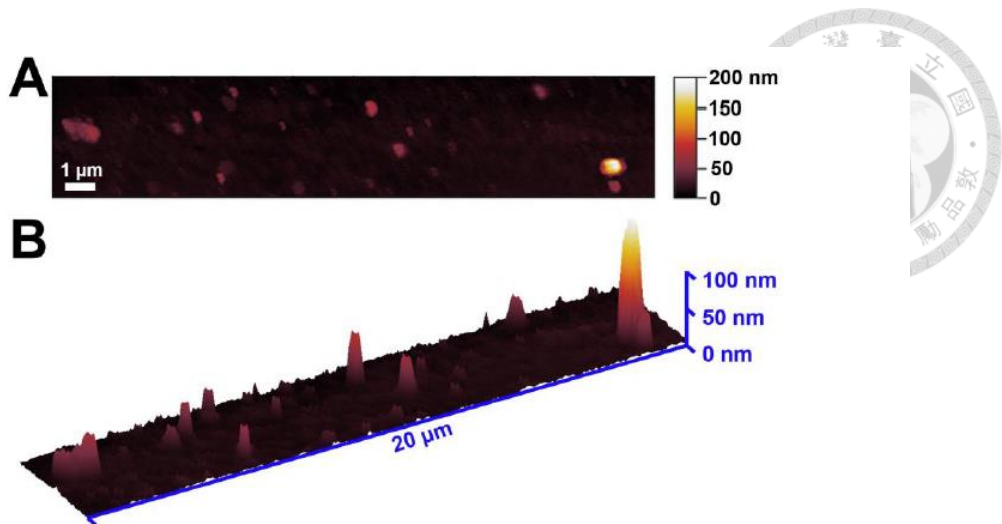


Figure S4. Surface morphology of the PU film. (A) Two-dimensional AFM image of the PU film. (B) Three-dimensional AFM image of the PU film.

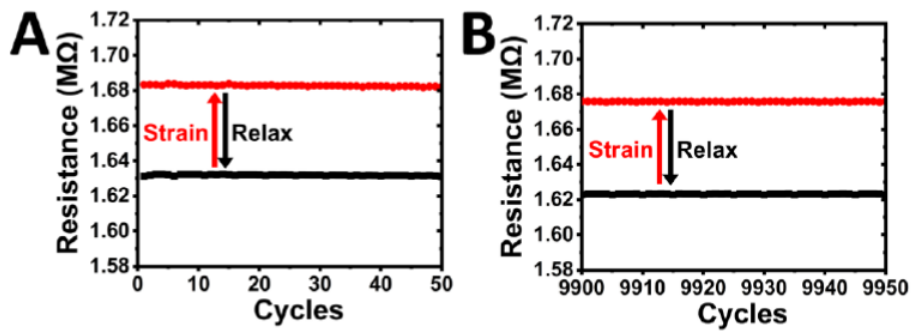


Figure S5. Magnified plots of the fatigue test (Figure 4Bii) at (A) 0-50 cycles and (B) 9900-9950 cycles.

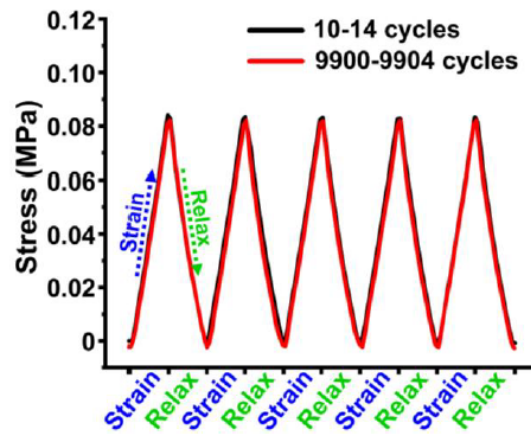


Figure S6. Cyclic strain/relaxation responses of the PU substrate under applied strains of 0-0.5% and 0.5-0%. The black line showed 10-14 cycles. The red line showed 9900-9904 cycles.

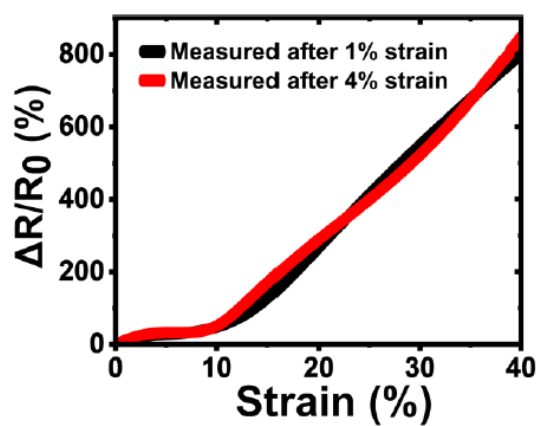


Figure S7. Plots of two tensile tests conducted after prestraining the sensor to 1% and 4%. $\Delta R/R_0$ was measured as a function of applied strain from 0 to 40% at a tension rate of 10 mm min^{-1} .

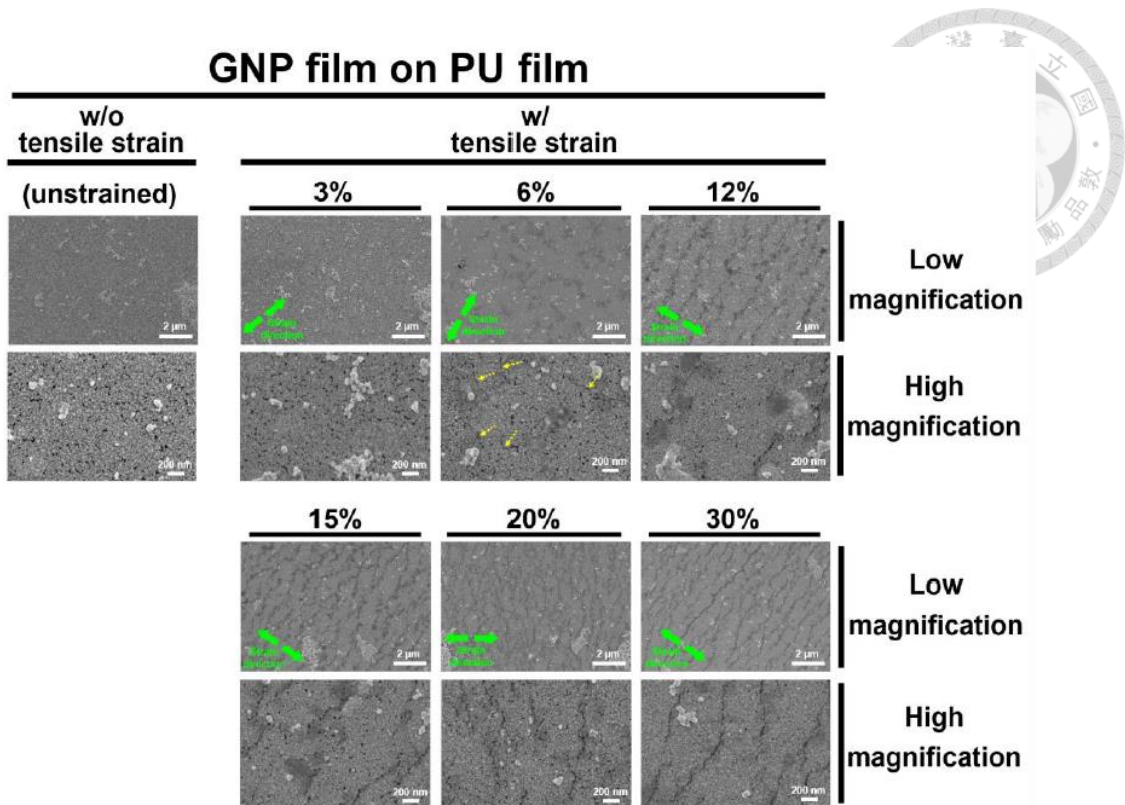


Figure S8. Low and high magnification SEM images of the GNP film after applying tensile strain of 0% (unstrained), 3%, 6%, 12%, 15%, 20%, and 30%. The green solid arrows indicate the strain directions. The yellow dotted arrows indicate the initial microcracks.

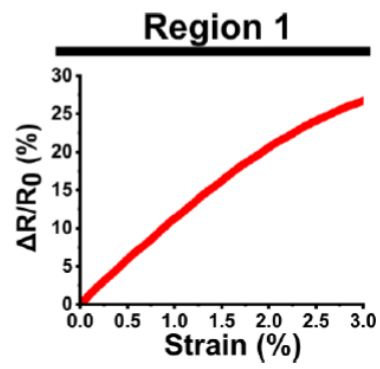


Figure S9. The magnified plot of the tensile test (Figure 4Ciii) within the low strain range from 0 to 3%.

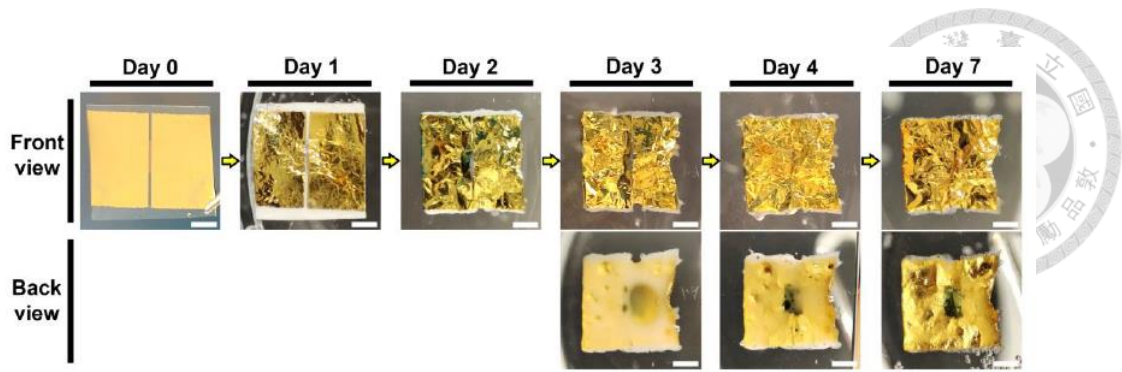


Figure S10. Optical images showing the degradation of the GNP-PU strain sensor on different days in distilled water at an accelerated-degradation temperature of 74 °C. Scale bars represent 2 mm.

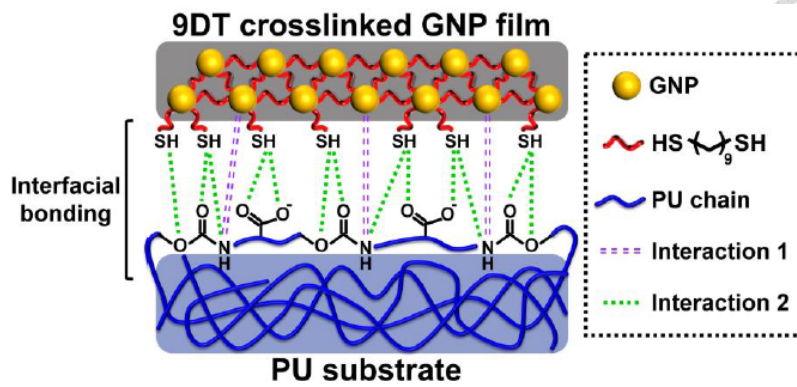


Figure S11. Schematic illustration of the interfacial bonding between the 9DT crosslinked GNP film and the PU substrate.

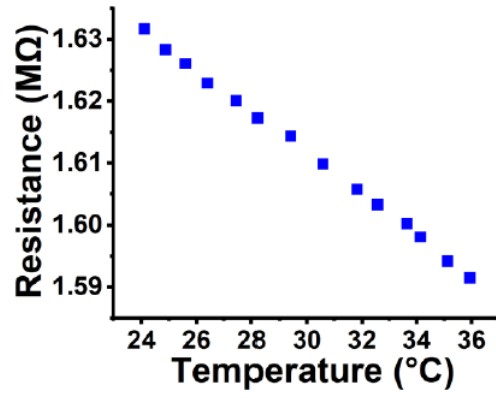


Figure S12. Temperature-dependent resistance of the GNP-PU strain sensor in the temperature range of 24-36 °C.

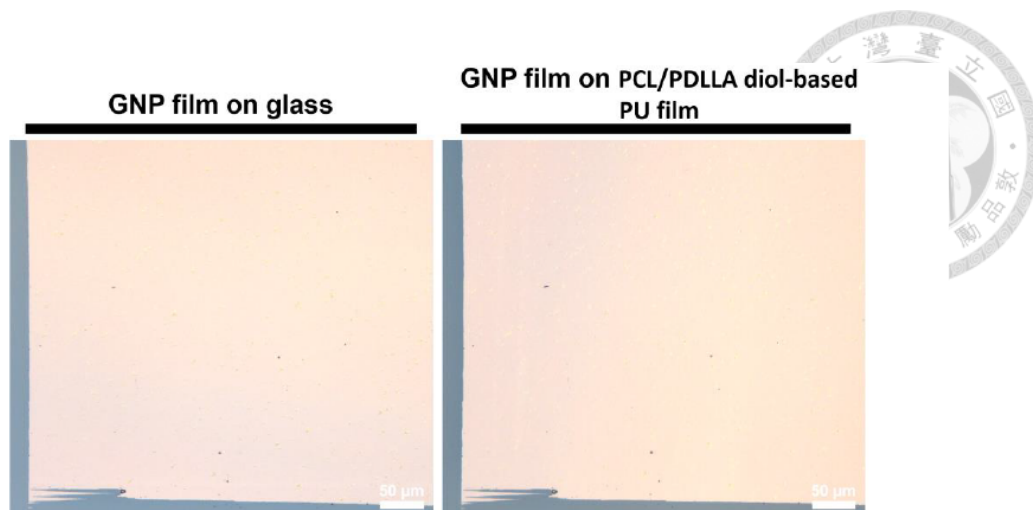


Figure S13. Optical images showing the GNP film before (*i.e.*, GNP film was on the glass) and after the transferring printing process. In this case, the GNP film was transferred to a different type of PU, which has a chemical composition different from the PU used in the main text. Here, the PU has the soft segment of PCL and PDLLA from the reactants PCL diol and PDLLA diol.

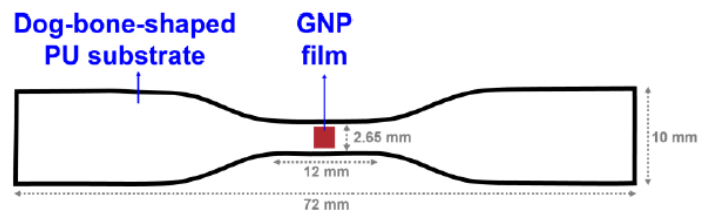


Figure S14. The fabricated dog-bone-shaped GNP-PU film.



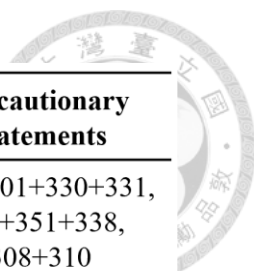
7.2. Safety

7.2.1. List of hazardous substances according to GHS

The chemicals utilized in this study are listed in **Table 1.**, which provides their respective classifications under the globally harmonized system (GHS), as well as the applicable hazard and precautionary statements.

Table 1. List of chemicals and GHS classifications.

Substance	GHS symbol	Hazardous statements	Precautionary statements
Acetone	02, 07	225, 319, 336	210, 233, 305+351+338
Borane tert-butylamine complex	06, 09	301+311, 315, 319, 411	264, 273, 301+310, 302+352+312 305+351+338
Chlorobenzene	02, 07, 09	226, 332, 315, 411	260, 262, 273, 403
1-Dodecylamine	05, 07, 08, 09	304, 314, 335, 373, 410	261, 273, 280, 301+310, 305+351+338
Ethanol	02, 07	225, 319	210, 280, 310
Heptane	02, 07, 08, 09	225, 304, 315, 336, 410	210, 261, 273, 310+301, 331, 501
Hexane	02, 07, 08, 09	225, 304, 315, 361f, 373, 336, 411	210, 240, 273, 310+301, 331, 302+352, 403+235
Methanol	02, 06, 08	225, 317	210, 260, 280, 301+310, 311
1,9-Nonanedithiol	07	315, 319, 335	261, 305+351+338
Oleylamine	05, 07, 08, 09	302, 304, 314, 335, 373, 410	260, 280, 301+310, 303+361+353, 304+310+340, 305+351+338
1-Propanol	02, 05, 07	225, 318, 336	210, 233, 240, 280, 303+361+353, 310, 305+351+338, 370+378, 501



Substance	GHS symbol	Hazardous statements	Precautionary statements
Sodium hydroxide	05	290, 314	280, 301+330+331, 305+351+338, 308+310
4-Methy-2-pentanone	02, 07	225, 332, 335, 319	210, 305+351+338, 304+340
Triammonium citrate	07	315, 319, 335	261, 305+351+338



GHS 01



GHS 02



GHS 03



GHS 04



GHS 05



GHS 06



GHS 07



GHS 08



GHS 09

7.2.2. CMR substance

Substances that are carcinogenic, mutagenic, or toxic to reproduction are called CMR.

The CMR substance used in this study is listed in **Table 2.**

Table 2. List of the CMR substance.

CAS number	Substance	Usage and Amount
110-54-3	n-Hexane	GNP synthesis (30mL)

8. Acknowledgement



The journey through the joint doctoral program has been akin to running a marathon. This endeavor would not have been possible without the guidance and support of many. I am deeply grateful to my three esteemed supervisors - Prof. Shan-hui Hsu at National Taiwan University, and Prof. Dr. Horst Weller and PD Dr. Tobias Vossmeier at the University of Hamburg. Through invaluable teachings, rigorous training, and steadfast encouragement, they have equipped me with the foundational knowledge and skills that will serve me well into the future. It is with a deep sense of gratitude that I sincerely appreciate the significant and indispensable roles my supervisors have played in my doctoral period. I extend my thanks to all the laboratory partners at National Taiwan University, 韓皓偉博士、黃翠薇博士、曾庭箴博士、謝政田博士、劉藝博士、徐俊鵬博士、堃志、照庭、昱仁、何琳、仁德、佩玟、宗翰、苡庭、昆哲、鈺傑、子為、世和、哉羽、廷杰、乾溥、佩旋, for their companionship and shared wisdom. I also appreciate all the laboratory partners at the University of Hamburg, Dr. Hendrik Schlicke, Dr. Bendix Ketelsen, Chi-Yin Liu, Hauke Hartmann, Sophia Bittinger, Finn Dobschall, Svenja Kunze, and Ahir Bose, for their companionship and assistance. I am also thankful to Robert Schön and Stefan Werner for their contributions in SEM and TEM measurements. In addition, my appreciation goes out to 曾清秀教授、廖昭仰教授、吳亘承教授、莊偉綜教授、戴念梓醫師、胡瑜峰醫師、嵐雅、郁文、佩君、若甄 for their collaborative efforts and contributions. I also thank the Ministry of Science and Technology of Taiwan and the National Synchrotron Radiation Research Center of Taiwan for their financial support and resources. My deep gratitude extends to all my oral defense examiners, Prof. Shan-hui Hsu, Prof. Dr. Horst Weller, PD Dr. Tobias Vossmeier, Prof. Dr. Volker Abetz, Prof. Shu-Wei Chang, Prof. Jia-Shing Yu, for the participation and guidance. Lastly, my appreciation is reserved for my family, whose unwavering support

and belief in my abilities have been my constant source of strength and inspiration.



9. Declaration on oath

“I hereby declare on oath that this doctoral dissertation is written independently and solely by my own based on the original work of my PhD and has not been used other than the acknowledged resources and aids. The submitted written version corresponds to the version on the electronic storage medium. I declare that the present dissertation was prepared maintaining the Rules of Good Scientific Practice of the German Research Foundation and it has never been submitted in the present form or similar to any other University or board of examiners.”

31.1.2024 Shin-Da Wu

Date, Signature